Chem Soc Rev

REVIEW ARTICLE

View Article Online
View Journal | View Issue

Cite this: *Chem. Soc. Rev.*, 2024, **53**, 2435

Penetrant-induced plasticization in microporous polymer membranes

Katherine Mizrahi Rodriguez, †[a] Sharon Lin, †[b] Albert X. Wu,[b] Kayla R. Storme,[c] Taigyu Joo,[b] Aristotle F. Grosz,[b] Naksha Roy,[b] Duha Syar,[b] Francesco M. Benedetti[b] and Zachary P. Smith *[b]

Penetrant-induced plasticization has prevented the industrial deployment of many polymers for membrane-based gas separations. With the advent of microporous polymers, new structural design features and unprecedented property sets are now accessible under controlled laboratory conditions, but property sets can often deteriorate due to plasticization. Therefore, a critical understanding of the origins of plasticization in microporous polymers and the development of strategies to mitigate this effect are needed to advance this area of research. Herein, an integrative discussion is provided on seminal plasticization theory and gas transport models, and these theories and models are compared to an exhaustive database of plasticization characteristics of microporous polymers. Correlations between specific polymer properties and plasticization behavior are presented, including analyses of plasticization pressures from pure-gas permeation tests and mixed-gas permeation tests for pure polymers and composite films. Finally, an evaluation of common and current state-of-the-art strategies to mitigate plasticization is provided along with suggestions for future directions of fundamental and applied research on the topic.

Received 4th May 2023

DOI: 10.1039/d3cs00235g

rsc.li/chem-soc-rev

1. Introduction

Separations of gas and vapor mixtures play a significant role in many chemical processes.[1] To meet these demands, various unit operations can be used, but distillation is by far the most common. In fact, there are over 40 000 distillation columns in the United States, which is a testament to their versatility.[2] Distillation can operate over a wide range of pressures from

[a] *Department of Materials Science and Engineering, Massachusetts Institute of Technology, Cambridge, MA 02139, USA*
[b] *Department of Chemical Engineering, Massachusetts Institute of Technology, Cambridge, MA 02139, USA. E-mail: zpsmith@mit.edu*
[c] *Department of Chemistry, Massachusetts Institute of Technology, Cambridge, MA 02139, USA*
† These authors contributed equally to this work and are co-first authors.

Katherine Mizrahi Rodriguez

Katherine Mizrahi Rodriguez is a co-founder at Osmoses Inc., where she works on the commercialization of breakthrough membrane technology. She has a PhD in Materials Science and Engineering from MIT, where she evaluated the gas transport properties of membranes under industrially realistic conditions. Katherine has been recognized as a NSF Graduate Research fellow, a Ford Foundation predoctoral fellow, a GEM fellow, an NSF I-Corps co-entrepreneurial lead, and a Kavanaugh Postdoctoral Fellow.

Sharon Lin

Sharon Lin obtained her PhD in Chemical Engineering from MIT in 2021, where she worked under the guidance of Zachary P. Smith to understand the effects of free volume modification on the gas separation performance of polymer membranes. She is currently a Materials Scientist at Pascal Technologies, Inc., where she is developing materials for sustainable heating and cooling.

0.14 bar (*e.g.*, ethylbenzene/styrene) to nearly 21 bar (*e.g.*, propylene/propane) and is capable of separating feeds with high volumetric flowrates and various components that cover a range of relative volatilities from only 1.17 (*o*-xylene/*m*-xylene) to 81.2 (water/ethylene glycol).[2] Distillation provides a convenient and time-tested solution to separate a diversity of chemicals in a continuous manner with high purity.

However, distillation has an enormous environmental footprint, resulting in the consumption of approximately 25% of all industrial energy use.[3] The key issue is that distillation operates based on phase changes, and this separation mechanism requires vast energy inputs. In 2021, the industrial sector consumed approximately 55% of energy use worldwide. In the United States, industrial energy consumption was fractionally smaller, but still substantial at 24% of total energy consumption.[4] These percentages are projected to increase in coming years.[5,6] In addition, the heat required to power thermally-driven separations often comes from natural gas and petroleum. For this reason, thermally-driven separations in the industrial sector in the United States produce about 20% of total carbon dioxide emissions.[6] This number is projected to increase to 25% by 2050.[6]

As such, engineers and scientists have worked to find alternative technologies that achieve similar separation performance while simultaneously offering energy efficiency. Pressure swing adsorption (PSA) and thermal swing adsorption (TSA) are commonly practiced in industry, but they operate in a semi-continuous fashion, requiring pressurization–depressurization cycles that increase operational complexity. Absorption processes, like amine absorption, are another alternative. However, absorbents can degrade, thereby requiring a reclaimer to address contaminant buildup and volatility issues.[7,8]

The use of membranes provides an alternative separation strategy that avoids these limitations. Compared to other separation techniques, membrane-based separations offer reduced indirect CO_2 emissions, modularity, low cost, and a continuous operation, while avoiding the need for toxic absorbents.[9] If such non-thermally driven technology was adopted by the petroleum, chemical, and paper manufacturing industries, it is estimated that 100 million tons of CO_2 emissions could be eliminated and

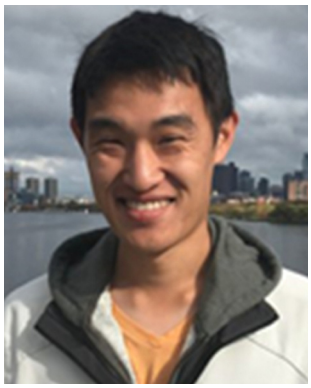

Albert X. Wu

Albert X. Wu received his PhD in Chemical Engineering from MIT under the supervision of Prof. Zachary P. Smith, where his research focused on the synthesis, transport characterization, and sorption modeling of highly fluorinated polymer materials for gas separations. He is currently a researcher at 3M working on technology development and full-scale implementation of advanced water treatment processes.

Kayla R. Storme

Kayla Roberta Storme received her BSc degree in Biochemistry from the University of Illinois at Chicago in 2018. In 2019, she started her PhD at the MIT Department of Chemistry working in the labs of Professor Timothy M. Swager and Professor Zachary P. Smith. Her thesis focuses on the design, synthesis, and characterization of polymers for gas separations. Kayla has been recognized as an NSF Graduate Research fellow and an NSF I-Corps Entrepreneurial Lead.

Taigyu Joo

Taigyu Joo is a graduate student at MIT. He obtained his bachelor's degree in Chemical Engineering from Carnegie Mellon University in 2018 and a master's degree in Chemical Engineering Practice from MIT in 2021. Under the guidance of Professor Zachary P. Smith, his doctoral research focuses on understanding the physical aging behaviors and the rational design of post-synthetic modification strategies for microporous polymer membranes used in gas separation applications.

Aristotle F. Grosz

Aristotle F. Grosz is a PhD candidate in the Department of Chemical Engineering at MIT under the supervision of Professor Zachary P. Smith. His research focuses on enhancing gas separation performance and plasticization resistance in polymeric membranes by tuning the extent of backbone fluorination. Aristotle received his bachelor's degree in Chemical and Biomolecular Engineering from the Georgia Institute of Technology and master's degree in Chemical Engineering Practice from MIT.

4 billion USD in energy savings could be recovered annually in the United States alone.[3]

Membrane-based gas separations have been implemented commercially in a wide range of applications such as hydrogen recovery, nitrogen and oxygen production, natural gas treatment, vapor recovery, and hydrocarbon separations.[7,10] The gas separations market expanded from 0.150 billion USD in 2002 to approximately 1.5 billion USD in 2017, and it is projected to reach 2.61 billion USD by 2022.[10–12] While this market growth indicates that membrane-based gas separations have successfully emerged as a promising platform technology, the technique still has significant limitations relative to conventional unit operations. Notably, a considerable number of studies have shown upper bound trade-off relationships between permeability and selectivity for membranes.[13–18] From a materials perspective, permeability and selectivity property sets need to be improved under realistic conditions to displace legacy separation processes, and these efforts remain a primary barrier for deploying membrane technology.[19–24]

Polymers of intrinsic microporosity (PIMs) contain persistent intrinsic micropores smaller than 2 nm and have gained significant interest in the field.[25,26] For example, PIM-1—the first microporous ladder polymer studied for gas separations—contains a ladder-type backbone that hinders chain rotation and a spirobisindane moiety that contorts polymer chains and introduces configurational free volume.[25,26] Such features lead to high permeability while maintaining moderate selectivity. So far, many sub-classes of PIMs, including PIM-polyimides,[27,28] Tröger's base PIMs,[28–33] and triptycene-based PIMs,[28,29,34] among others,[35–39] have been developed with exceptional upper

Naksha Roy

Naksha Roy graduated from MIT with a Bachelor's of Science in Chemical Engineering in 2022. During her time at MIT, she was as an undergraduate researcher at the Smith Lab, working on the development of polymer-metal organic framework (MOF) materials for energy-efficient separations. She received the AIChE 2021 First Place Award in Separations I and the 2022 NESACS Phyllis A. Brauner Award for her research presentations.

Duha Syar

Duha Syar graduated from MIT with a Bachelor of Science in Chemical Engineering in 2023. During her time at MIT, she was an undergraduate researcher in the Smith Lab. She is currently pursuing her PhD in Chemical Engineering at the University of California Berkeley.

Francesco M. Benedetti

Dr Francesco Benedetti is a Co-Founder and serves as CEO at Osmoses, a venture backed technology company commercializing solutions for industrial gas separations. Benedetti earned his PhD in chemical engineering from the University of Bologna, Italy, and worked as a Postdoctoral Associate at MIT. His research focused on developing structure/property relationships for new glassy polymer membranes for gas separations, with particular emphasis on evaluating the effect of mixed-gas permeation and competitive sorption on transport. He received the MIT Energy Fellowship, the Activate Fellowship, and was an NSF I-Corps Entrepreneurial Lead.

Zachary P. Smith

Zachary P. Smith is an Associate Professor and the Robert N. Noyce Career Development Chair of Chemical Engineering at MIT. His research focuses on the molecular-level design, synthesis, and characterization of polymers and inorganic materials for applications in membrane and adsorption-based separations. Prof. Smith has co-authored over 60 peer-reviewed papers and has been recognized with various awards, including the DoE Early Career Award, NSF CAREER Award, and ONR Young Investigator Award. He served as a committee member in writing the 2019 National Academies of Sciences, Engineering, and Medicine report on A Research Agenda for Transforming Separation Science. Prof. Smith serves on the Board of Directors for the North American Membrane Society and is on the Editorial Advisory Boards of Macromolecules and Polymer. He is a co-founder of Osmoses Inc., a startup aiming to commercialize membrane technology.

bound performance. Despite these many advancements, the operational stability of PIMs is still a key challenge. Of note, stability issues frequently manifest themselves in the form of physical aging and plasticization. Physical aging is the prolonged temporal relaxation of all solid-state non-equilibrium glassy polymers. More precisely, the specific volume of a polymer decreases as subtle macromolecular motions kinetically drive the polymer packing structure into a denser, lower energy state. This phenomenon results in decreased permeability.[10,40,41] On the other hand, plasticization results in the increase of polymer chain translational motion in the presence of strongly sorbing gases resulting in decreased size-sieving ability and increased gas flux.[42] Physical aging rates and plasticization generally increase with decreasing membrane thickness, making these phenomena especially challenging to control for industrial applications.[43–47] Thus, stability remains a major hindrance for industries to implement membranes as their primary separation technique.

Developing a fundamental understanding of plasticization is critical to further advance membranes as a platform technology for energy-efficient gas separations. Strong plasticization resistance is required in many industrial separation processes, especially those involving highly condensable gases and vapors. For example, natural gas treatment constitutes a large portion of the current gas separation market. However, gas wells frequently reach pressures exceeding 50 bar and contain high levels of known plasticizers, including CO_2 and H_2S.[48,49] Membranes for olefin/paraffin separations, such as ethylene/ethane and propylene/propane, are also susceptible to plasticization since these industrial gas feeds are usually at 8–11 bar and at temperatures that result in high gas-phase activities.[11] Under these aggressive operating conditions, plasticization often leads to a substantial deterioration in gas selectivity.[11,50,51]

In addition to existing applications, there are many emerging applications for membranes beyond olefin/paraffin separations, but membrane materials need improved performance and stability to address these potential markets. For example, hydrogen recovery from steam methane reforming, in which CO_2 is separated from syngas after a water–gas shift reaction, is known to be economically more favorable when the separation is performed at high reactor effluent pressures (usually about 50 bar).[52,53] Vapor separations like dehydration of organic solvents are also attractive applications for membranes due to difficulties in separating azeotropic mixtures using traditional methods like distillation. However, strong interactions between polymers and penetrants like water and ethanol can plasticize membranes, causing reduced overall diffusion selectivity.[54–56] To address plasticization issues in many of these industrial processes, various methods have been developed to reduce chain mobility in polymers, and thus, increase resistance toward plasticization. Some common approaches include crosslinking, increasing chain interactions through polymer functionalization, adding fillers, blending, grafting, and UV or thermal treatments.[57]

While the concept of penetrant-induced plasticization in polymers has been recognized since the earliest days of the polymer field and its appreciation in membrane applications can date back to at least the 1960s,[58–60] developing a fundamental understanding of this phenomena for emerging materials is still an evolving theme in the literature. The timeline in Fig. 1 shows some of the major efforts and studies that have contributed to the understanding of penetrant-induced plasticization behavior for membrane materials. These are summarized in more detail in Table 1. Interestingly, early research efforts coincided closely with the first commercialization efforts of gas separation membranes in the late 1970s.[61] Beginning in the 1980s, many membrane researchers made efforts to develop a fundamental understanding of penetrant-induced plasticization effects, especially by studying how changes in membrane transport relate to polymer mobility and chain dynamics. Based on these early studies, the general approach in recent years has transitioned to developing mitigation strategies, which have been bolstered by computational modeling and the synthesis and design of new types of plasticization-resistant polymers. Of note, a significant effort has been placed on studying the effects of plasticization on new, high-performance membrane materials.

Plasticization has been a focus of many experimental studies, but there are few reviews on this topic.[49,57,92–99] Hence, this review focuses on plasticization studies in the membrane field with a particular emphasis on new microporous polymer membranes and experimental techniques used to mitigate these effects. It should be noted that there are some limited examples where plasticization is beneficial for a separation. These examples are briefly discussed in Section 5.1.4.[85,100] However, this review primarily focuses on applications where

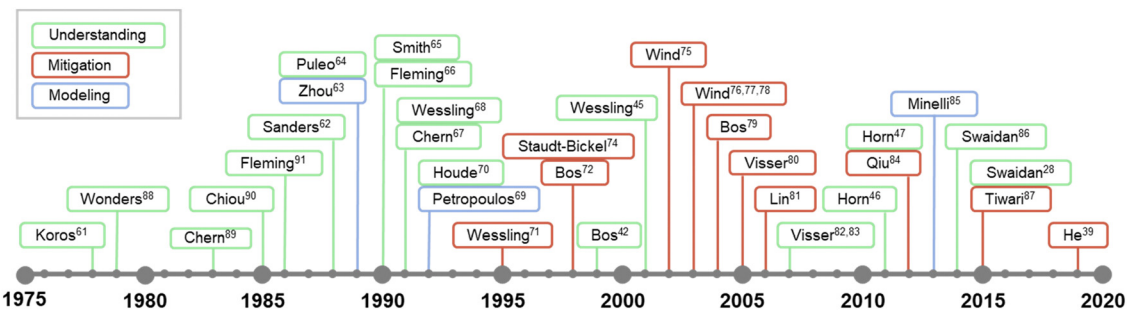

Fig. 1 Abridged timeline highlighting some major studies on penetrant-induced plasticization behavior in the membrane field.[28,39,45–47,61–91]

it is undesirable. Section 2 of this review describes gas transport theory in microporous polymer membranes, as well as penetrant properties and their relationship to plasticization. Section 3 describes polymer chain mobility and translational cooperativity, their relation to plasticization, and methods to measure these parameters, while Section 4 discusses plasticization mitigation strategies in more detail. Section 5 reviews and discusses all plasticization data for microporous polymers that have been recorded to date, highlighting the best-performing polymers and discussing common characteristics that lead to enhanced plasticization resistance. Finally, Section 6 summarizes the current research progress and future directions for the understanding and development of microporous polymers that are plasticization-resistant.

2. Gas transport and plasticization phenomena

Glassy polymers are viscous metastable solids.[101,102] Over time, contractive forces drive these non-equilibrium materials to a lower energy state, resulting in polymer chain reorganization to form denser polymer structures.[103–105] Viewed another way, excess free volume in glassy polymers can be envisioned as a fluid trapped in a viscous polymer solid, which "bubbles" to the surface of a polymer film, analogously resulting in a denser polymer structure over time.[106,107] Regardless of the physical picture, polymer chains are constantly in motion and intimately influenced by free volume.[108]

Plasticization is broadly defined as the increase in polymer chain mobility in the presence of condensable diluents.[10,109–111]

Table 1 Selected studies that have contributed to the understanding of penetrant-induced plasticization behavior for membrane materials

Year	Author	Highlights	Ref.	# of citations
1978	Koros	Observed hysteresis in sorption following high-pressure CO_2 exposure in semi-crystalline glassy polymer	61	244
1979	Wonders	Observed membrane transport property changes after high-pressure CO_2 exposure in glassy polymer	62	169
1983	Chern	Membrane materials with high T_g and rigid backbone structure will be more plasticization resistant	63	124
1985	Chiou	Suppression of T_g at high CO_2 pressure	64	304
1986	Fleming	Glassy polymers show a markedly different response to external CO_2 pressure compared to rubbery polymers	65	271
1988	Sanders	Plasticization of glassy polymer, indicated by sorption kinetics and T_g depression, does not necessarily increase permeability with higher CO_2 feed pressure	66	159
1989	Zhou	Examination of plasticization effects using dual-mode sorption model with partial immobilization	67	53
1989	Puleo	High CO_2 sorption swells cellulose acetate matrix, which disrupts interchain interactions and increases Langmuir sorption capacity	68	239
1990	Smith	Dissolved CO_2 enhances penetrant mobility in glassy polymers	69	20
1990	Fleming	Comparison of hysteresis behavior of sorption and volume dilation at high CO_2 pressure implies that polymers with high initial swelling exhibit more pronounced history-dependent behavior	70	32
1991	Chern	Glassy polymers with high T_g can still show a large plasticization effect	71	20
1991	Wessling	Sorption kinetics and dilation kinetics are different	72	155
1992	Petropoulos	Development of a model to describe the effect of plasticization on gas permeation	73	21
1992	Houde	Increase in CO_2 permeability with pressure is caused by increased intersegmental spacing under high CO_2 pressure	74	51
1995	Wessling	A new experimental method and model to study sorption induced dilation kinetics	75	46
1998	Bos	Stabilization of plasticization by high temperature thermal treatment	76	275
1999	Bos	Polymers under study plasticized at the same critical CO_2 concentration of 36 ± 7 $cm_{(STP)}^3$ cm^{-3}	42	461
1999	Staudt-Bickel	Incorporation of polar groups and crosslinks can reduce plasticization effect	78	349
2001	Wessling	Plasticization effects are more pronounced for sub-micron thick polyimide films	45	104
2002	Wind	Diol chemical crosslinking strategy to mitigate plasticization	79	233
2003	Wind	Thermal annealing and covalent cross-linking reduce polymer swelling at high CO_2 feed pressures	80	154
2003	Wind	Mitigation of plasticization by chemically crosslinking with various diol crosslinker sizes	81	160
2003	Wind	Thermal annealing and diol crosslinking to mitigate plasticization in gas mixtures	82	318
2004	Bos	Blending a less plasticizable polymer with a highly plasticizable polymer can suppress plasticization	83	137
2005	Visser	Introducing an inert gas to CO_2 feed suppresses plasticization through competitive sorption	84	129
2006	Lin	When diffusion selectivity is undesired, strong plasticization can be beneficial to separation performance	85	684
2007	Visser	Polymers require different levels of CO_2 concentrations to reach the plasticization point	86	157
2007	Visser	Any gas can exhibit non-Fickian diffusion and induce irreversible sorption relaxations once a critical level of volume dilation is reached	87	71
2011	Horn	The competing effects between plasticization and aging is balanced, with physical aging predominating in polymers with less CO_2 sorption	46	41
2011	Qiu	Sub-T_g thermal crosslinking of copolyimide to mitigate plasticization	88	217
2012	Horn	Plasticization effects in glassy polymers depend on film thickness, especially for sub-micron thick films	47	65
2013	Minelli	Use of the Non-Equilibrium Lattice Fluid (NELF) model to predict permeability with plasticization effect	89	75
2014	Swaidan	Not only intrachain rigidity but also a balance between interchain rigidity and interchain spacing is important for reducing plasticization in PIMs	90	87
2015	Swaidan	Intrachain rigidity, crucial to PIM designs, does not solely mitigate plasticization	28	232
2015	Tiwari	Glassy perfluorinated polymers show higher plasticization resistance compared to other glassy polymers	91	46
2019	He	Development of exceptionally high plasticization resistant materials can be achieved using ladder side chains on flexible backbones	39	51

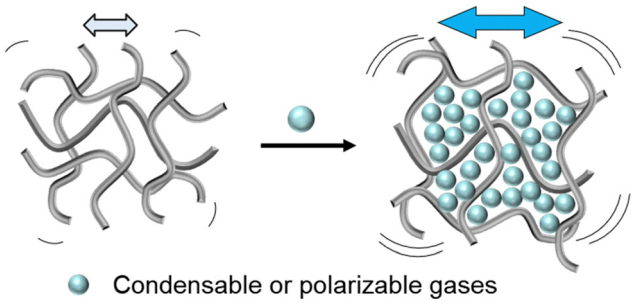

Fig. 2 Pictorial representation of plasticization, which involves increased polymer backbone mobility and chain spacing caused by incorporation of condensable or polarizable gases. This phenomenon is illustrated by showing an increase in chain mobility (arrows and vibrations) caused from a decrease in polymer–polymer interactions and increase in polymer–penetrant interactions.

Thus, this phenomenon correlates directly with a lowering of the glass transition temperature of the polymer.[112–114] In the gas separations field, plasticization often refers to the observation of increased permeability when a polymer is subjected to high concentrations of certain gases (Fig. 2).[7,64,72] The increase in permeability is not necessarily a result of increased free volume, but instead, lower activation energies of diffusion.[72] Therefore, plasticization is often more severe for larger gases because these gases benefit more significantly from reduced activation energies and show more significant increases in stochastic diffusive jump steps.[72,115] This section provides a short summary of (1) common penetrant properties, (2) transport metrics and models used to understand polymer–gas interactions and plasticization, and (3) common tests and principles used to evaluate plasticization in polymers.

2.1. Penetrant properties and their relation to plasticization

Heuristically, plasticization of polymer membranes correlates with condensability or polarizability of penetrants in a mixture. The more strongly sorbing the penetrant, the higher the expected degree of plasticization. Because this phenomenon relates to the interactions between polymer and penetrant, certain thermodynamic lattice models such as the Flory–Huggins, Sanchez-Lacombe, and non-equilibrium lattice fluid (NELF) are particularly useful for quantifying interactions in polymer systems. In the case of rubbery polymers without the consideration of unoccupied free volume, the Flory–Huggins model can be used to describe the activity of the penetrant as a function of penetrant volume fraction:[116]

$$\ln(a_s) = \ln(\phi_s) + \left(1 - \frac{V_s}{V_p}\right)(1 - \phi_s) + \chi(1 - \phi_s)^2 \quad (1)$$

where a_s is the activity of the penetrant, ϕ_s is the volume fraction of the penetrant, V_p and V_s are the molar volume of the polymer and solvent, respectively, and χ is the Flory–Huggins interaction parameter.[116,117] The parameter χ represents the degree of interaction between the polymer and penetrant and can be experimentally determined by solubility measurements,[118] light scattering in polymer blends,[119,120] or considering solubility parameters δ_i:[118,119,121]

$$\chi = 0.34 + \frac{v_s}{RT}(\delta_s - \delta_p)^2 \quad (2)$$

where v_s is the molar volume of solvent, and δ_i (where i refers to either the polymer or solvent) can be found from:

$$\delta_i^2 = \frac{\Delta H_i^{vap}}{v_i} \quad (3)$$

where ΔH_i^{vap} is the heat of vaporization of species i, and v_i is the molar volume of i.

Since the heat of vaporization of a polymer cannot be found experimentally, an alternative method of finding the solubility parameter of polymers is as follows:[122]

$$\delta_p^2 = \frac{\sum_j \Delta e_j}{\sum_j \Delta v_j} \quad (4)$$

where Δe_j represents group contributions to molar cohesive energy, and Δv_j the group contributions to molar volume. Alternatively, it is also possible to use molecular simulations to predict enthalpies of mixing and use the results to compute solubility parameters.[123]

In the context of plasticization, as interactions between the polymer and gas increase, the activity of the gas in the matrix will likewise increase, making the polymer–gas system more susceptible to plasticization. Such trends also apply in more complex models of polymer systems that include free volume, such as Sanchez–Lacombe and NELF, as will be discussed later in this section.

Several properties that correlate with gas sorption of common gases relevant for membrane separations are tabulated in Table 2.[124] Generally, larger penetrants have higher sorption in polymers,[125] but there are notable exceptions for highly polarizable gases such as CO_2, H_2S, and H_2O, among others. Penetrants with higher gas–polymer interactions are more likely to induce plasticization.

2.2. Transport theory for gas separation membranes

Permeability and selectivity are the two primary material properties to evaluate membrane performance. Permeability (P) is defined as:

$$P = \frac{Nl}{\Delta p} \quad (5)$$

where N is the gas flux, l is the membrane thickness, and Δp is the transmembrane pressure.[134] Under the framework of the sorption–diffusion model, permeability can be described as the product of the effective diffusion coefficient, D, and the effective sorption coefficient, S:[135,136]

$$P = DS \quad (6)$$

The ideal selectivity for a binary mixture is defined as the ratio of the pure-gas permeability of the more permeable gas to that of the less permeable gas. Using the sorption–diffusion

Table 2 Properties of gases that are frequently considered for membrane applications.[87,124,126–128] The categories of "No plasticization expected" and "Plasticization observed" are general guidelines for most literature studies

	Gas	Critical temperature[129] (K)	Critical volume[113,129] ($cm^3\ mol^{-1}$)	Kinetic (Å)	Lennard-Jones well depth[131–133] (K)
No plasticization expected	He	5.19	57.3	2.551	10.2
	H_2	33.2	64.9	2.89	59.7
	Ne	44.4	41.7	2.82	33.9
	N_2	126.2	89.3	3.64	71.4
	CO	134.5	90.1	3.76	91.7
	Ar	150.9	74.57	3.542	116.8
	O_2	154.6	73.5	3.46	106.7
	CH_4	190.6	98.6	3.8	148.6
	Kr	209.4	91.2	3.655	162.6
Plasticization observed	C_2H_4	282.5	131.1	3.9	224.7
	Xe	289.7	118	4.047	226.1
	CO_2	304.2	91.9	3.3	195.2
	C_2H_6	305.3	147	4.443	215.7
	C_3H_6	365.2	184.6	4.5	298.9
	C_3H_8	369.9	200	4.3	237.1
	H_2S	373.3	87.7	3.6	301.1
	i-C_4H_{10}	407.7	259	5	330.1
	n-C_4H_{10}	426	255	4.3	531.4
	SO_2	430.3	122.2	3.6	—
	H_2O	647	55.9	2.65	809.1

model, selectivity can be written as the product of the diffusion and sorption selectivities:

$$\alpha_{i,j} = \frac{P_i}{P_j} = \frac{D_i}{D_j}\frac{S_i}{S_j} \tag{7}$$

In mixed-gas tests, the selectivity is defined as:

$$\alpha_{i,j} = \frac{y_i/y_j}{x_i/x_j} \tag{8}$$

where x_i is the concentration of gas species i in the feed, and y_i is the concentration of i in the permeate. Unlike pure-gas tests, mixture experiments are critical for evaluating the effects of plasticization under more realistic conditions. These experiments can also be used to elucidate additional complex phenomena such as competitive sorption effects, which are discussed in more depth in Section 5.2.

Diffusion selectivity and sorption selectivity highlight primary metrics by which separation performance can be improved. Increases in diffusion selectivity are commonly targeted by forming polymers with denser packing structures. Increases in sorption selectivity are commonly targeted through incorporation of functional groups with strong gas affinity, such as amine or carboxylic acid groups for CO_2.[38,137–139]

Because permeability is the product of diffusion and sorption, it is important to evaluate both of these terms to elucidate structure–property behavior, especially for understanding plasticization. We begin by first considering gas sorption. One of the most widely used models to describe sorption in glassy polymers is the dual mode sorption (DMS) model,[140,141] where the pressure dependence of penetrant concentration (C, $cm_{STP}^3\ cm_{pol}^{-3}$) in a polymer is the sum of sorption into Henry and Langmuir modes:

$$C = k_d p + \frac{C'_H bp}{1+bp} \tag{9}$$

where k_d is the Henry's constant ($cm_{STP}^3\ cm_{pol}^{-3}\ atm^{-1}$), C'_H is the Langmuir capacity constant ($cm_{STP}^3\ cm_{pol}^{-3}$), and b is the Langmuir affinity constant (atm^{-1}). This phenomenological model is particularly helpful for understanding plasticization in glassy polymers because it envisions sorption as occurring in hypothetical equilibrium and non-equilibrium domains. For a polymer above its T_g (*i.e.*, in its rubbery state), the linear portion of the DMS model is often sufficient for describing sorption in a polymer without volume dilation. For a polymer below its T_g (*i.e.*, in its glassy state), a second population of sorption (the Langmuir mode) accounts for excess sorption into non-equilibrium free volume. Koros extended the DMS model to mixtures, where competitive sorption effects are captured *via* a combined Langmuir sorption term for a binary *i*–*j* system:[141,142]

$$C_i = k_{d,i}p_i + \frac{b_i p_i}{1 + b_i p_i + b_j p_j} \tag{10}$$

The mixed-gas extension to the DMS model has shown good mixed-gas predictions using parameters derived from pure gas tests.[143]

The DMS model has also been extended to envision hypothetical and discrete modes of diffusion through what is known as the partial immobilization model. This model asserts that each sorption "mode" contributes its own diffusivity. "Partial immobility" refers to the theory that penetrant molecules sorbed in the Langmuir mode are partially immobile and therefore have some contribution to the overall permeation, whereas the remainder of diffusing molecules belonging to the Henry's mode are fully mobile.[144,145] In its initial conception, the partial immobilization model did not address the effects of plasticization, by virtue of considering D as invariant with respect to penetrant concentration.[144] Addressing plasticization *via* the partial immobilization model became possible when extended by Stern and Saxena, who implemented D as an exponential

function of penetrant concentration.[146] Zhou and Stern extend the model further by describing each of the aforementioned modes' diffusivities as their own individual exponential function, in order to demonstrate the effects of plasticization on mass transport in a single mode.[67] Other studies demonstrate a clear dependency between diffusivity and free volume:[147]

$$D = A\exp\left(-\gamma\frac{v^*}{v_f}\right) \quad (11)$$

where v^* is the volume required for diffusive displacement, v_f is free volume, and A and γ are constants.

More rigorous models have also been developed to quantitatively describe and predict the sorption of gases in glassy polymers. Specifically, the Flory–Huggins[116] and Sanchez–Lacombe[148] lattice fluid framework was extended by Doghieri and Sarti for glassy polymers[104,149] using the so-called non-equilibrium lattice fluid (NELF) model, which is capable of reproducing isotherms under relevant mixture conditions using one fitted binary interaction parameter determined from pure-gas measurements.[150,151] Of note, the NELF model can account for plasticization effects through incorporation of a swelling parameter that describes the change in polymer density (ρ) as a function of penetrant pressure:

$$\rho = \rho^0(1 - k_{sw}p) \quad (12)$$

where ρ^0 is the initial polymer density and k_{sw} (atm^{-1}) is the swelling coefficient.[89,149] The swelling coefficient can be determined through dilation experiments, described in more detail in Section 3, or through fitting of sorption isotherms. In this way, the NELF model has been applied broadly to predicting sorption isotherms even when plasticization plays a role.[89,150]

2.3. Effect of penetrant-induced plasticization on gas transport

Penetrant concentration inside a polymer membrane is proportional to feed pressure, so increasing pressure can exacerbate plasticization effects. A commonly used approach to evaluate plasticization in a polymer membrane is a high-pressure pure-gas permeation test, in which gas permeability is monitored while increasing upstream pressure in a stepwise fashion.[28,66,82,152] These pressure steps are held for a predetermined time that is sufficiently above the expected time-lag of the gas. However, because the time scale for diffusion and the time scale for plasticization are vastly different, the results of these high-pressure tests will be highly dependent on the length of the hold time set at each pressure step.[66,153–155] Standard methods to run these tests involve using the same hold time for all pressures or, alternatively, running each pressure point until some metric of steady state has been achieved, such as tracking time intervals when the variation in permeation is $<1\%$.[156] In all cases, plasticization phenomena (*e.g.*, the plasticization pressure) will be highly dependent on the experimental procedure, making it difficult to compare performance across samples from different studies. As such, reporting hold times is needed to gain a deeper understanding of plasticization kinetics and behavior.

Permeability isotherms have a dependence on pressure.[89] Representative isotherms for glassy polymers are illustrated in Fig. 3, including those for the following cases:

Type I: non-plasticizing penetrants that have low sorption

Type II: non-plasticizing penetrants that have moderate sorption, which can saturate the Langmuir mode

Type III: highly-sorbing penetrants, where the permeability initially decreases due to sorption into the Langmuir mode before it increases at higher pressure due to plasticization

Type IV: highly plasticizing penetrants that have very high sorption, inducing a significant plasticization effect in the polymer matrix even at low pressures

Of note, Type IV is equivalent to the plasticization behavior of rubbery polymers.[157,158] When observed in traditional glassy polymers, this finding indicates that plasticization is severe and that the T_g of the polymer may have been suppressed below the testing temperature, thereby eliminating Langmuir sorption behavior. In the parlance of the membrane-based gas separation literature, plasticization during a pure-gas permeation test is often reported when permeability begins to rise with increasing feed pressure. The minimum value in permeability is the "plasticization pressure," as shown in isotherm Fig. 3c.[42,72] Fundamentally, the plasticization pressure results from an increase in the diffusivity of penetrants at high pressures, which exactly balances the decrease in sorption for glassy polymers.[84,86] Beyond this pressure, increases in diffusivity dominate and permeability increases. However, the plasticization pressure alone does not provide any indication of the changes in gas selectivity or permeability of non-plasticization gases that would co-permeate in a real application. Therefore,

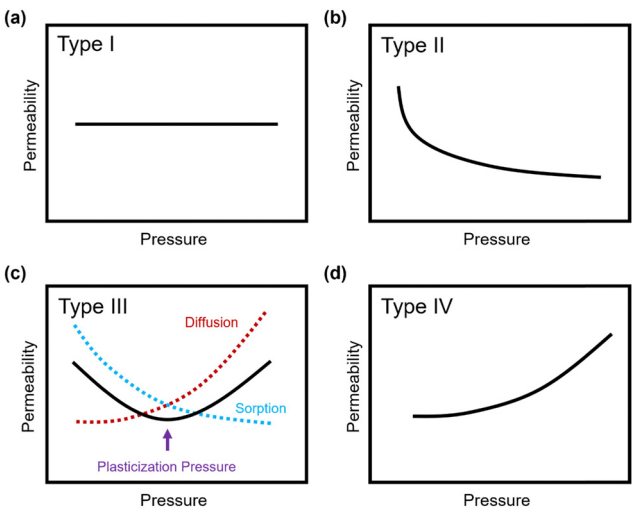

Fig. 3 Illustration of 4 different cases of permeability trends for glassy polymers,[89] in which the penetrants are: (a) non-plasticizing with low sorption, (b) non-plasticizing with moderate sorption, (c) highly-sorbing, where the permeability dependence initially decreases with increasing pressure due to saturation of the Langmuir mode, followed by increasing permeability at higher pressures due to enhanced diffusion, and (d) highly plasticizing with very high sorption. (c) also depicts the plasticization pressure as the point at which the increase in diffusion overtakes the decrease in sorption.

pure-gas experiments are useful for screening fundamental plasticization behavior, but inadequate at predicting property sets under realistic conditions.

A more comprehensive approach to evaluating plasticization involves monitoring permeability isotherms during high-pressure mixed-gas experiments. These experiments can also be used to track emergent phenomena for co-permeating species, such as competitive sorption effects that are discussed in detail in Section 5.2. For mixed-gas experiments, the plasticization pressure is often reported as the onset of an increase in the permeability of the less permeable gas.[28,159] To illustrate these effects, Fig. 4 presents transport metrics used to identify plasticization for a gas mixture of CO_2 and CH_4. In this case, the response of the less condensable penetrant (*i.e.*, CH_4) is an unambiguous indicator of plasticization. An increase in the diffusivity from the pure- to mixed-gas case (Fig. 4a) indicates plasticization, resulting in a concomitant decrease in diffusion selectivity, and frequently, in permselectivity for mixtures (Fig. 4c). Conversely, if the diffusivity of CH_4 is largely unchanged between the pure- and mixed-gas cases (Fig. 4b), the permselectivity of the mixed-gas case will be higher than that of the pure-gas case due to competitive sorption (Fig. 4d).[160] In this way, mixture testing can be used to decouple the role of competitive sorption and plasticization for gas separation membranes. In addition to laboratory experiments, molecular dynamics (MD) simulations can be used to understand the plasticization behavior of microporous polymers.[161–164]

In addition to pure- and mixed-gas permeation testing, permeation and sorption hysteresis curves are also used to examine the effect of plasticization and conditioning after a high-pressure test, as shown in Fig. 5.[46,165–167] Because the free

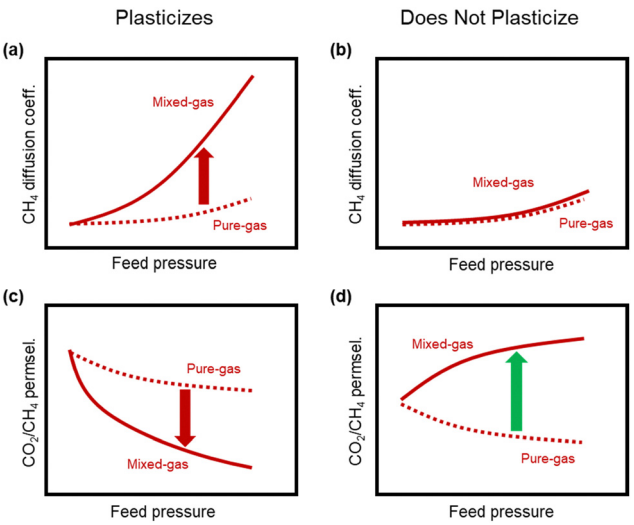

Fig. 4 Representations of the effect of plasticization on CH_4 diffusion and CO_2/CH_4 permselectivity in pure- and mixed-gas experiments. (a) and (b) represent the change in CH_4 diffusion coefficients between the pure- and mixed-gas cases for a polymer that plasticizes and does not plasticize, respectively. The change in CO_2/CH_4 permselectivity between the pure- and mixed-gas cases for a polymer that plasticizes and does not plasticize are represented in (c) and (d), respectively. Note that competitive effects are ignored for (a) and (b).

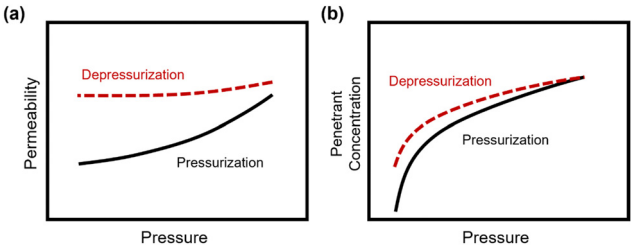

Fig. 5 Hysteresis curves during pressurization and depressurization steps of (a) permeation and (b) sorption tests.

volume architecture of a polymer changes during plasticization, pressurization and depressurization steps can be compared to quantify the performance change after exposure to certain gases. Hysteresis tests for sorption have shown that sorption of penetrants can increase after polymer plasticization, as indicated by a higher equilibrium concentration of penetrant during depressurization steps.[87] While the polymer structure can, over an extended period of time, return to its equilibrium state, plasticization effects often can be detrimental over the time scale relevant for industrial applications. In practice, membranes are operated continuously and can experience variability in feed compositions. Thus, the complex nature of plasticization and the variations in environmental conditions can result in pronounced effects over time during membrane operation.

It should also be noted that dimensional changes of polymers are rarely evaluated over identical testing conditions,[72,87,168–170] and desorption from truly microporous materials requires more energy than sorption,[171] so a multifaceted approach of considering hysteresis along with mixed-gas testing is best for evaluating details on plasticization and conditioning, and for identifying their relative contributions.[72,172] By doing so, the net consequences of changes in permeability can be evaluated.[82]

3. Polymer chain cooperativity and its relation to plasticization

Section 2 discussed chemical and thermodynamic properties of gases and how parameters such as condensability and size can influence plasticization behavior. This section highlights the role of the polymer matrix and how polymer chain cooperativity relates to plasticization. Pertinent concepts including polymer chain cooperativity and the glass transition temperature (T_g) are reviewed, and a summary of characterization techniques commonly employed to understand relaxation phenomena in glassy polymers is provided.

3.1. Polymer chain cooperativity and the glass transition temperature

As a polymer is cooled from its equilibrium rubbery state, it will experience an apparent continuous phase transition with respect to volume, entropy, and enthalpy. At temperatures below this transition, several important polymer characteristics become apparent, including decreased configurational entropy and the

absence of cooperative polymer chain translation under relevant timescales.[173–175] As the more liquid-like rubbery polymer transforms into a more solid-like glassy polymer, it becomes trapped in a *meta*-stable and hence, non-equilibrium state.[175] While the origins of the T_g represent an active and ongoing topic of research and debate within the scientific community,[175–177] the T_g is generally viewed as a pseudo-second-order phase transition of kinetic origin that is influenced by the processing and thermal history of the sample.[173,174]

Because of their disordered nature in the solid-state, glassy polymers are characterized by the presence of localized domains with distinct chain dynamics. These domains experience molecular level fluctuations in conformation, a phenomenon termed dynamic heterogeneity.[175,178] Chain cooperativity describes the collective motion of polymer segments as they spontaneously switch from one conformation to another in the glassy state.[178] Above the T_g, large energy fluctuations lead to large-scale cooperative changes in the configuration of polymer chains that are observed as liquid-like flow. Due to dynamic heterogeneity, the T_g is often characterized by diverging relaxation times and broad or non-exponential response functions with respect to temperature when evaluating spectroscopic or relaxation experiments.[178,179] Around the T_g, liquid-like flow is significantly minimized. Below the T_g, transient polymer chain dynamics can also allow for changes in the macroscopic packing structure, although these changes are significantly slowed and become dependent on nascent driving forces that develop during vitrification, such as those created by excess non-equilibrium free volume. Of particular relevance to this review, these macroscopic changes also depend on environmental stimuli (*e.g.*, penetrant-induced plasticization).

3.1.1 Backbone chain mobility, chemical structure, and the T_g. When in contact with highly condensable gases (*e.g.*, CO_2, H_2S, C_3H_6, and C_3H_8) at high pressures, polymer chains can reorganize, often resulting in increased overall gas permeability and decreased permselectivity. In other words, in the presence of condensable gases, an increase in chain mobility is observed with a concomitant reduction in the T_g.[180] The T_g of a polymer will also define its ideal working conditions for certain applications. At ambient conditions, polymers with a glass transition temperature below room temperature (*e.g.*, polydimethylsiloxane (PDMS) and polyethylene glycol (PEG)) are in their rubbery state, while polymers with a T_g above room temperature (*e.g.*, cellulose acetate (CA) and polymers of intrinsic microporosity (PIMs)) are in their glassy state.[181] All microporous polymers considered in this review are glassy. However, because of the wide array of chemistries accessible through organic synthesis, the range of glass transition temperatures covered by many glassy polymers varies widely. For example, CA has a T_g between 185–205 °C and PIMs actually decompose around 400–500 °C, which is potentially below their glass transition temperatures, although there is some uncertainty in evaluating the T_g of these polymers in the literature.[182–184] From a chemical design perspective, some generalizations apply when relating the T_g to the structure of a polymer:[108,182]

1. Backbone rigidity. As backbone intrachain mobility decreases, the T_g typically increases. Polymers with aromatic backbones tend to have a higher T_g than polymers with flexible backbones such as those composed of single-bonded chains. Examples of high T_g structures include aromatic polyimides, polymers with fused-rings, and ladder polymers such as PIMs.

2. Side group rigidity. Polymers with rigid side chains that impede reorganization typically have a higher T_g than polymers with small or no sidechains. A classic example of this effect is the difference in T_g between polystyrene (T_g = 100 °C) and polyethylene (T_g = −125 °C). Conversely, addition of flexible side groups to rigid chains can result in a decreased T_g because flexible side chains can act as plasticizers. A classic example here is for the poly(methyl methacrylate) (PMMA), poly(ethyl methacrylate) (PEMA), and poly(propyl methacrylate) (PPMA) series, where T_g decreases from 105 °C for PMMA to 43 °C for PPMA, which corresponds to the increasing length of the flexible aliphatic side chain.

3. Intermolecular interactions. Interchain rigidity induced by strongly interacting backbones or side group chemistries results in higher glass transition temperatures than similar backbones without interacting chemistries. These intermolecular interactions (*e.g.*, hydrogen bonding, π–π stacking, *etc.*) can reduce cooperative chain motion, and will be discussed in this review as a feature with promise for mitigating plasticization effects.

A summary of glass transition temperatures for select polymers including some commodity and commercial gas separation polymers are provided in Fig. 6, where the state of the polymer at room temperature is used to distinguish rubbery from glassy polymers. Among glassy polymers, the T_g of cellulose acetate is dependent on the degree of acetyl substitutions. For aromatic polyimides, the monomers selected for synthesis can yield glass transition temperatures ranging widely from 200–400 °C, where some polyimides are considered traditional glassy polymers and others are considered microporous and referred to as PIM-PIs. Microporous PIM-PIs have characteristic rigid and contorted backbone structures. The majority of the summarized glass transition temperatures in Fig. 6 were collected through standard experimental techniques such as differential scanning calorimetry (DSC) and dynamic mechanical analysis (DMA), which will be discussed in detail later in this section.

For the past decade, chemists have focused on developing increasingly rigid backbone structures to increase fractional free volume (FFV) and molecular diffusion through polymer films. Through this effort, solution-processable microporous polymers with ultrahigh free volume and measurable Brunauer–Emmett–Teller (BET) surface areas were developed. In many cases, the ultrahigh backbone stiffness and limited chain mobility in microporous polymers can sometimes result in T_g values well above the degradation temperature of the materials. In these cases, standard techniques such as DSC and DMA do not identify a T_g, and specialized methods such as molecular dynamics (MD) simulations[183] and flash calorimetry[184,185] are required, as is the case for the PIMs shown in Fig. 6. While variations in glass transition temperatures derived from simulation and ultrafast DSC methods warrant investigation that is beyond the scope of

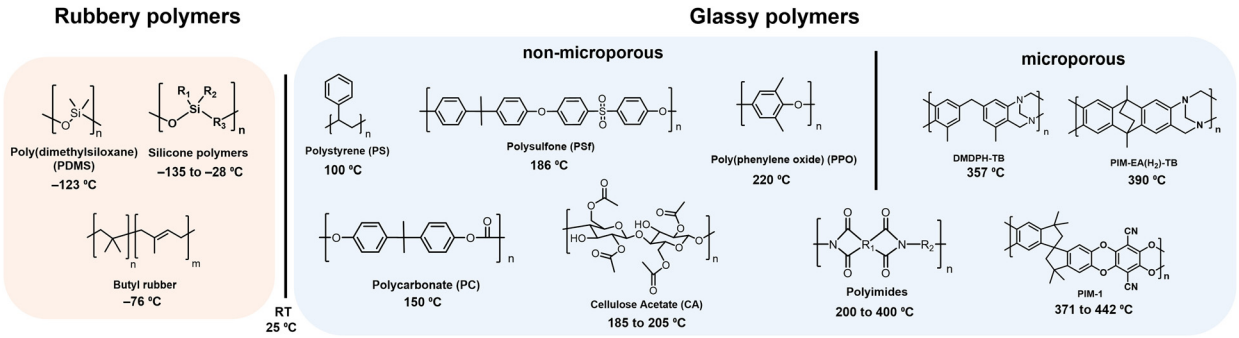

Fig. 6 Approximate values for the T_g of representative polymers including PDMS,[108] butyl rubber,[186] PS,[186] PC,[186] PSf,[187] CA,[68] PPO,[186] polyimides,[188] DMDPH-TB,[185] PIM-1,[184] PIM-EA-TB.[185] For CA, cellulose diacetate is shown as the example. Polymers with glass transition temperatures below room temperature (RT, 25 °C) are considered rubbery, while those with glass transition temperatures above room temperature are considered glassy. Among glassy polymers, a line is drawn between examples of microporous polymers and traditional glassy polymers, where polyimides can be designated as traditional polyimides or microporous PIM-PIs, depending on the structure.

this review, both methods have proved valuable in accessing approximate T_g values where traditional techniques fall short.

3.1.2. Free volume theory. When a polymer solution is processed into a solid-state film or powder, inefficient packing of polymer chains generates spaces devoid of electron density often referred to as free volume. The free volume (V_{free}) is a material property that is typically defined as:[189]

$$V_{free} = V - V_0 \quad (13)$$

where V is the experimentally derived specific volume of the polymer ($cm^3\ g^{-1}$) and V_0 is the volume occupied by polymer chains ($cm^3\ g^{-1}$). When considering molecular transport through a film, V_0 includes the volume occupied by the polymer chains called hard core volume (the temperature-independent volume in Fig. 7) and the nearby free volume occupied by polymer segment vibrations (the sloped line above the hard core volume in Fig. 7). The latter is referred to as interstitial volume and is the effective volume that originates from solid-state packing.[189] Interstitial volume is not often correlated with gas transport properties because the energy required for redistribution of the polymer chains is too large to contribute to molecular transport.[190] Therefore, the "free volume" responsible for gas transport refers to the free volume that can continuously redistribute within polymer matrix by random thermal fluctuations (above the interstitial volume line in Fig. 7).[118,191]

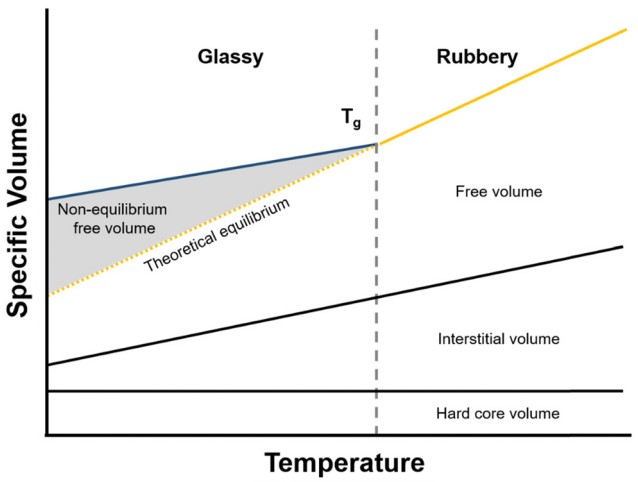

Fig. 7 Polymer volume as a function of temperature. The shaded area indicates non-equilibrium free volume.

As mentioned in the previous section, when a polymer is cooled from the rubbery state, it will eventually traverse a glass transition. Below this temperature, cooperative polymer chain mobility becomes exceedingly unfavorable, trapping the polymer in a non-equilibrium and *meta*-stable state.[192] This behavior is reflected schematically in Fig. 7, where the specific volume of the polymer with respect to temperature changes slope with decreasing temperature and correspondingly deviates from the theoretical equilibrium volume (dashed line). The deviation from equilibrium packing results in the formation of non-equilibrium free volume (shaded area in Fig. 7), which is sometimes referred to as "excess free volume". In the context of the dual-mode sorption model, non-equilibrium free volume provides an additional mode of gas sorption, the "Langmuir mode" discussed in Section 2, and generally results in an order-of-magnitude increase in sorption coefficients for glassy polymers compared to those of rubbery polymers.[193] For highly rigid microporous materials, non-equilibrium packing effects can be even more significant and result in large improvements in sorption capacity.[194]

Fractional free volume (FFV) in a polymer can be correlated with transport properties of diffusing molecules in a polymer film:[190,195]

$$FFV = \frac{V_{free}}{V} = \frac{V - V_0}{V} \quad (14)$$

Hence, free volume theory is widely used in the gas separation field to describe molecular diffusion and predict transport behavior of gas penetrants. Estimation of FFV requires an approximation of V_0, typically calculated using group contribution theory.[196,197] While group contribution theory is commonly used due to its simplicity, it has several limitations that have recently come under debate.[198,199] Our group recently re-visited and updated group-contribution theory for FFV calculations

with a particular focus on the structural groups that compose microporous polymers.[200] Information on other characterization methods used to determine free volume experimentally can be found elsewhere.[195,201–203]

The relationship between free volume and diffusion coefficients of gas molecules in polymers is commonly shown as an exponential correlation:

$$D = A \times \exp\left(-\frac{B}{\mathrm{FFV}}\right) \quad (15)$$

where A and B are gas and polymer specific constants, respectively.[204] This equation demonstrates that polymers with larger free volume elements yield higher diffusivity of gas penetrants.[195,204] The relevance of free volume in gas transport through membranes is further emphasized when such plots are generated using families of polymers with similar backbone structures.[7] Stronger correlations are observed when structurally related polymers (*e.g.*, polysulfones, polycarbonates, polyimides, *etc.*) are compared directly, while large scatter is observed when such correlations are drawn with extensive sets of polymer structures.[205] In addition to diffusivity, the amount of free volume is also known to influence gas sorption, and the exceptional gas transport performance of PIMs are often attributed to their very high sorption coefficients resulting from their high free volume structure.[15,194,206,207] For example, PIM-1 and PIM-7 showed high CH_4 sorption coefficients of 14 and 9 $cm^3\ cm^{-3}\ atm^{-1}$, respectively, compared to conventional polymers that typically showed CH_4 sorption coefficients below 4 $cm^3\ cm^{-3}\ atm^{-1}$. These high uptakes arise from the high free volume of the polymers and contribute to improved performance that can sometimes surpass the Robeson upper bound.[194]

Importantly, the effect of plasticization on free volume is seldom studied because of the difficulty in obtaining *in situ* measurements of FFV for a polymer experiencing plasticization. However, dilatometry and ellipsometry experiments have shown that polymers that sorb condensable penetrants show a decrease in density and increase in free volume.[80,91,208] Additionally, molecular simulations have indicated the same type of volume expansion: using cyclical Monte Carlo and molecular dynamics simulations through a ''sorption–relaxation cycle'', experiments can be used to predict to what extent a polymer matrix has physically expanded, correlating to lower density and thus higher free volume.[168,209,210]

3.1.3. The dependence of T_g on free volume, molecular weight, and polymer blends. In addition to chemical structure, the T_g also depends on factors including blend composition, molecular weight, and free volume. Such dependencies inform our understanding of polymer relaxation in membranes made using different synthetic or processing approaches.

3.1.3.1. Dependence of T_g on free volume. The Doolittle equation[211] is often used to describe the relationship between viscosity and FFV in liquids[212–214] and rubbery polymers:[215]

$$\ln(\eta) = \ln(A) + B \times \frac{V - V_f}{V} = \ln(A) + B' \times \left(\frac{1}{f} - 1\right) \quad (16)$$

where A, B, and B' are constants, η is the viscosity, V is the total volume, and V_f is the free volume. A linear dependence between fractional free volume (f) and temperature can be expressed as follows:[216]

$$f = f_g + \alpha_f(T - T_g) \quad (17)$$

where f_g is the free volume at the glass transition temperature (T_g) and α_f is the coefficient of thermal expansion. The Doolittle equation can then be re-written as:

$$\ln(\eta) = \ln(A) + B' \times \left(\frac{1}{f_g + \alpha_f(T - T_g)}\right) \quad (18)$$

and after some mathematical rearrangement:

$$\ln(\eta) = \ln(A) + \frac{C}{T - T_0} \quad (19)$$

where $C = B'/\alpha_f$ and $T_0 = T_g - \frac{f_g}{\alpha_f}$. This equation is known as the Vogel–Fulcher–Tamman–Hesse (VFTH) equation, which correlates polymer relaxation times to temperature primarily through their dependence on free volume. The three parameters required in the VFTH equation can be simplified into two variables by incorporating a reference viscosity (η_{ref}) at a reference temperature (T_{ref}), which can be described using a modified version of eqn (18) with T_{ref} instead of T_g: $f = f_{ref} + \alpha_f(T - T_{ref})$ The resulting relationship is known as the Williams–Landel–Ferry (WLF) equation:[217]

$$\log\left(\frac{\eta}{\eta_{ref}}\right) = -\frac{C_1(T - T_{ref})}{C_2 + (T - T_{ref})} \quad (20)$$

where $C_1 = \frac{B'}{2.303 \times f_{ref}}$ and $C_2 = \frac{f_{ref}}{\alpha_f}$ are WLF coefficients, and $\frac{\eta}{\eta_{ref}} = \alpha_T$ is the WLF shift factor.

For a polymer glass above its T_g, the WLF equation is a universal function widely used to describe the temperature dependence of properties of viscoelastic materials.[218] The WLF shift factor is a direct consequence of time-temperature superposition (TTS), where a relaxation process occurring at a long time scale is equivalent to one occurring at a low temperature and *vice versa*. By running tests over a range of temperatures and/or frequencies, TTS allows for the determination of a large range of viscoelastic properties. As a result, viscoelastic tests such as dynamic mechanical analysis (DMA) can provide useful information on polymer mobility and the glass transition by scanning across a large range of temperatures and timescales and identifying temperatures where phase transitions and relaxation processes occur. In turn, this information can be used to better understand polymer chain dynamics and relaxation processes associated with plasticization phenomena.

3.1.3.2. Dependence of T_g on molecular weight. The Flory–Fox relationship describes the dependence of T_g on polymer molecular weight:[108,219]

$$T_g = T_{g(M_n \to \infty)} - \frac{A}{M_n} \quad (21)$$

where A is an empirical constant and M_n is the number average molecular weight. Large variations in molecular weight result in changes in molecular mobility and T_g. As the M_n of the polymer increases, the second term in the Flory–Fox relationship decreases, resulting in T_g values close to the upper limit at an infinite M_n. At very low molecular weights (*e.g.*, for oligomers), the subtracted term predicts a reduction in T_g. This general dependence of T_g on molecular weight is related to free volume, where shorter polymer chains have more chain ends, thereby increasing overall free volume.[220,221] The presence of other low molecular weight components or impurities, such as plasticizers, can similarly increase the free volume of the polymer matrix and lower the T_g. However, if the molecular weight is high enough, the inverse relationship between T_g and M_n renders T_g essentially independent of M_n. In the context of gas separations, because polymers need to have high molecular weights to cast strong and ductile films for testing, variations in T_g related to polymer molecular weight are rarely significant.

3.1.3.3. Dependence of T_g on blend or copolymer composition. While many new microporous polymers have been developed in the last decades, their sophisticated chemistries can often result in low molecular weight, decreased mechanical integrity, and expensive or time-consuming multistep syntheses. Blending offers a time- and cost-effective alternative to tune the separation performance and mechanical properties of membranes,[222] including properties related to plasticization, as will be discussed in detail in Section 4.[223–226] Additionally, copolymerization can also serve as a method to engineer gas-separation properties. In both of these approaches, understanding the dependence of T_g on blend or copolymer composition can assist in selecting the appropriate polymer blend combinations.

For miscible polymer blends and random copolymers, the Fox equation describes the general dependence of T_g on composition:[227]

$$\frac{1}{T_g} = \frac{w_1}{T_{g,1}} + \frac{w_2}{T_{g,2}} \quad (22)$$

where w_i and $T_{g,i}$ are the mass fraction and T_g of component i, respectively. The accuracy of the Fox equation increases when the difference in glass transition temperatures of the components is small and when the two components have weak intermolecular interactions.

3.1.4. Sub-T_g transitions. In addition to the glass transition temperature, there are several other thermal transitions that occur below T_g and are usually referred to as sub-T_g transitions. Sub-T_g transitions can play a role in polymer dynamics associated with physical aging, plasticization, and molecular diffusion. The T_g is referred to as an α transition, and subsequent transitions are referred to as β transitions, γ transitions, and so on. Fig. 8 illustrates an idealized representation of the dynamic mechanical spectrum of an amorphous polymer with γ, β, and α relaxations.[228] Each of these transitions is associated with molecular motions of progressively smaller molecular units of the polymer chain (α > β > γ). More specifically, the γ transition is often associated with localized bond movement,

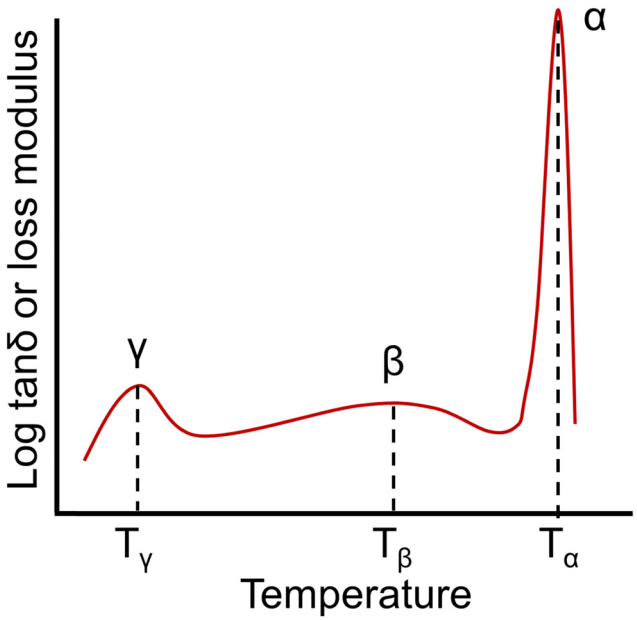

Fig. 8 An example of a dynamic mechanical spectrum of an amorphous polymer with γ, β, and α (T_g) relaxations.

the β transition with localized group movement, and finally, the α transition is the traditional T_g where large-scale cooperative motion occurs. While the γ and β transitions are usually found to be local and non-cooperative in nature, there is some debate on the molecular mechanisms involved in these transitions.[229–234]

A number of studies have indicated that the presence of residual water in a polymer can affect γ relaxations, resulting in changes to the location and intensity of these features.[235–237] From a molecular perspective, the γ transition is most commonly associated with phenyl ring oscillations.[238,239] The β relaxation has been associated with short-range motions that may be precursors to segmental polymer mobility occurring at the T_g. For instance, β relaxations in aromatic compounds have often been associated with the ring flipping of para-phenylene groups.[239] The temperature range and magnitude of some sub-T_g transitions can also be affected by factors such as film preparation methods, thermal history, and moisture absorption.[228]

Several characterization techniques are used to identify the temperatures at which sub-T_g relaxations occur. These tests include dynamic mechanical analysis (DMA), broadband dielectric spectroscopy (BDS), and thermally stimulated discharge current (TSC) measurements.[228] For example, Comer *et al.* investigated dynamic relaxation characteristics of Matrimid® polyimide using both dielectric and dynamic mechanical tests.[240] DMA storage and loss moduli were obtained at a number of frequencies from 0.1–30 Hz, and at discrete temperatures ranging from −150 °C to 425 °C. Additionally, dielectric spectroscopy data, such as the dielectric constant and dielectric loss, were recorded for frequencies from 1 Hz–1 MHz at 10 °C isothermal intervals from −150 °C to 300 °C, which approaches the T_g. As shown in Fig. 9a, two sub-T_g relaxations in Matrimid® were identified at −112 °C (T_γ) and 80 °C (T_β). Through Starkweather analysis[241,242] of the activation energies for each transition, the

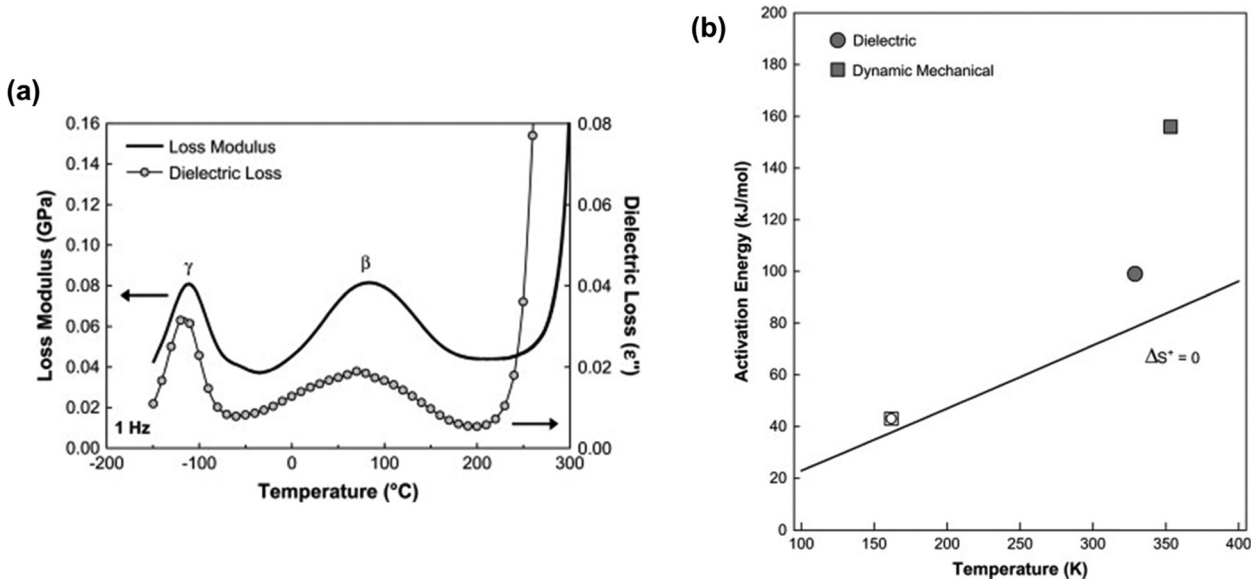

Fig. 9 (a) Dynamic mechanical loss modulus (GPa) and dielectric loss *vs.* temperature (°C) at a frequency of 1 Hz for Matrimid® polyimide. Two sub-glass relaxations are observed at −112 °C (T_γ) and 80 °C (T_β). (b) Apparent activation energy (kJ mol^{-1}) *vs.* relaxation temperature (K) at 1 Hz for γ transition (open symbols) and β transition (filled symbols) based on dynamic mechanical analysis (squares) and dielectric spectroscopy (circles). Reprinted with permission from ref. 240 (Copyright Elsevier, 2009).

authors found that the γ transition was close to the zero-entropy limit and non-cooperative in nature, while the β transition showed more cooperative character, which is indicated by the larger variation between the activation energies in Fig. 9b. Performing similar in-depth analyses of sub-T_g relaxation processes in microporous materials would allow for better fundamental understanding of mechanisms relevant in relaxation-related phenomena like CO_2 induced plasticization.

3.2. Techniques to measure chain cooperativity

Common characterization techniques used to measure chain mobility are reviewed in this section, including methods to determine the T_g and methods to characterize inter and intra-chain cooperativity. Typical advantages and disadvantages of each method are summarized in Table 3.

3.2.1. The glass transition temperature. This section provides a brief overview of methods commonly used to identify the T_g including differential scanning calorimetry (DSC), dynamic mechanical analysis (DMA), and dielectric spectroscopy (DS).

3.2.1.1. Differential scanning calorimetry (DSC). Differential scanning calorimetry (DSC) is a thermoanalytical characterization technique used to study thermal transitions such as glass transition temperatures, melting and boiling points, and crystallization temperatures.[243] DSC instruments can be classified into two types: heat-flux and power-compensated.[243,244] A typical heat-flux DSC instrument consists of two pans heated in a chamber: one pan contains the material of interest and a second reference pan is typically empty or contains a well-characterized sample.[244,245] As the pans are heated, transitions such as T_g, melting, and degradation will manifest as differences in the heat flow (q) required to maintain a constant temperature ramp.[244,245] The DSC heat flow, q, is defined as:

$$q = \frac{\Delta T}{R} \tag{23}$$

where ΔT is the temperature difference between the sample and the reference, and R is the resistance of the plate on which the pans sit. Using the temperature difference due to the specific heat (C_p) of the materials, the heat-flux DSC system can determine the enthalpy change of a sample:[243]

$$\Delta H = C_p \Delta T \tag{24}$$

where ΔH is the enthalpy.[243] In a power-compensated DSC, the sample and reference pans are heated in separate furnaces and the difference in power needed to keep the samples at the same temperature is plotted against time or temperature.[243,244]

When evaluating a DSC curve, exothermic processes (*e.g.*, crystallization) require a reduction in heat flow to keep the temperature constant, while endothermic processes (*e.g.*, melting, evaporation) require an influx of heat flow. Conventional DSC plots show endothermic reactions as valleys and exothermic reactions as peaks (*i.e.*, "Exo up"), as shown in Fig. 10.[246] The crystallization temperature, T_{cryst}, is an exothermic process shown as a peak on Fig. 10, while the melting temperature, T_m, is an endothermic process represented as a valley. The reported values for T_m and T_{cryst} are commonly defined as the temperature in the middle of the peak/valley.

The heat capacity (C_p) of a polymer increases as the polymer traverses the glass transition to the rubbery state.[243] Two heating/cooling cycles are usually conducted where the polymer is heated to 50–100 °C above T_g or 30 °C above T_m, and the second cycle is usually reported as it does not depend as much

Table 3 Characterization methods used to measure chain cooperativity

Technique	Parameters	Information	Advantages	Disadvantages
Differential scanning calorimetry (DSC)	C_p, q	T_g, T_m, T_c	Requires small sample amounts and easy to use. Accurate temperature reading and analysis. Specialized DSCs reach high temperatures & heating rates. Provides information on reactions.	Gas can diffuse out of non-hermetically sealed pans over time for concentration dependent experiments. Pressure dependent tests have large signal variation. Difficult to decouple when more than one reaction or transition occurs.
Dynamic mechanical analysis (DMA)	E', E'', tan(δ), and stress–strain response	T_g (T_α), T_β, T_γ, T_m, E, ε_f, σ^*	Provides information on major and minor thermal transitions. Allows for rapid scanning of modulus *vs.* time, temperature, strain, or frequency.	Variation in calculation of T_g from E', E'', or tan(δ) caused by differences in testing parameters such as clamp types, sample dimension, scan rate, *etc.* Need continuous films for testing.
Dielectric spectroscopy (DS)	$\varepsilon(f)$, ε'', ε'	T_g, T_β, T_γ	Accepts a broad f range ($\sim 10^{-6}$ Hz to $\sim 10^{12}$ Hz) Flexible sample type from liquids to rubbery or glassy solids. Accesses information on miscibility and reaction rates.	Long test times when $f < 0.01$ Hz. DS only captures relaxations of dipoles making non-polar or non-ionic samples difficult to test. Conductivity can often obscure other relaxations in the system. Challenging to de-convolute multiple relaxations.
Relaxation NMR experiments	Intensity, chemical shift (ppm)	T_1, $T_{1,\rho}$	Provides information on mobility of individual chemical shifts. Can be performed in film or powder with small quantities of material.	Overlapping chemical signals are difficult to deconvolute. Fitting of relaxation time can be heavily user dependent. Does not provide information about T_g.
Dilation experiments	Dimensions, capacitance, or wavelength	$\tau_{R,I}$, $M_{R,I}$; $M_{F,\infty}$, $\frac{\Delta V}{V_0}$, k_{sw}	Can be performed using different techniques depending on sample thickness. Provides information for kinetic and NELF sorption modeling. Real-time measurement of changes in sample due to plasticization. Provides absorbed penetrant concentration data.	Dimension tests in thin films are affected by substrate surface (ellipsometry). Parameters derived from fittings can vary widely (ellipsometry).

on the processing history of the polymer or the residual presence of solvent or impurities.[243,245] The first cycle should be run at temperatures below the degradation temperature of the polymer. As shown in Fig. 10, while the T_g occurs over a range of temperatures, the T_g is usually identified as the midpoint of the inclined region in the curve.[247]

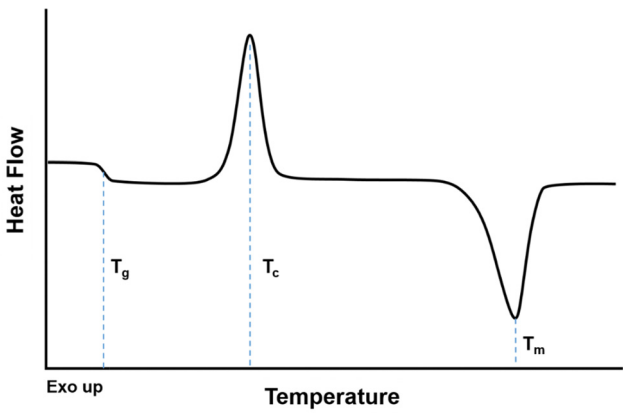

Fig. 10 Reference DSC curve with common thermal transitions observed in a semi-crystalline polymer.

In addition to the traditional DSCs, specialized DSC techniques have emerged in the last decades including microelectromechanical systems (MEMS) DSC,[248] infrared (IR) heated DSC,[249] modulated-temperature (MT) DSC,[250] and pressure perturbation calorimetry (PPC).[251] A particularly interesting example is the IR-heated DSC, also referred to as rapid-heating DSC, as it can heat up at a rate up to 2000 °C per minute.[243] High heating rates are sub-categorized as fast-scan DSC (100–300 °C per minute), Hyper-DSC (300–750 °C per minute), and Ultra-Fast or Flash DSC (up to 2 400 000 °C per minute). Ultra-fast or flash DSC allows ultra-glassy materials to be studied as structural changes can be more easily observed at higher heating rates. For instance, this method is particularly useful in analyzing polymers with rigid backbones like PIM-1 and PIM-EA-TB, which have degradation temperatures below their T_g.[184,185]

In the context of plasticization, high-pressure DSC can be also used to limit desorption of condensable gases from the sample and evaluate the effects of plasticization on the T_g.[252,253] Specifically, pressure-controlled DSC, or pressure

perturbation calorimetry (PPC), can be used to apply a pressure to the sample cell and subsequently determine differences in heat absorbed and released.[253] PPC has been useful for measuring temperature differentials in response to pressure change in proteins.[243] However, a major limitation of high-pressure DSCs is the appearance of noisy data even at baseline pressures.[252] As pressure is increased, the noise increases due to phase transitions of condensable gases that occur above their critical pressures, making the data difficult to interpret.[252,253]

Despite such limitations, DSC has been used to investigate the effect of CO_2 plasticization on the T_g. In a typical experiment, a pressure-controlled hermetic cell is used and the polymer film is equilibrated at the CO_2 pressure of interest.[252] Thicker membranes help to minimize fractional loss of CO_2 through diffusion before reaching the T_g and retain a high content of CO_2 in the polymer.[64,252] The total time between removing the polymer from the sorption chamber to sealing the pan is kept short to minimize desorption before testing.[64] Erratic fluctuation in the DSC curve above T_g can sometimes reflect evidence of CO_2 desorption.[64] Thus, in these specialized experiments, it is important to limit CO_2 desorption while also reaching a high enough heating rate and temperature to clearly observe the T_g without polymer degradation.[64] Moreover, initial scans may feature sub-T_g changes associated with processing history, which make the second heating curve a more useful metric for determining T_g.

For certain polymers, as CO_2 sorption increases with increasing pressure, a steady reduction in the T_g has been documented.[64,254] Chiou, Barlow, and Paul demonstrated this effect for poly(methyl methacrylate) (PMMA) evaluated at various CO_2 pressures, where there is a clear decrease in T_g with increasing CO_2 concentration (Fig. 11).[64] On the other hand, crystallization and the addition of fillers to the polymer matrix (*i.e.*, mixed-matrix membranes) have been shown to increase T_g.[64,254] As such, DSC can be an effective tool to study the effects of plasticization and provide insight into thermal transitions (*i.e.*, T_g, T_m, and T_{cryst}).

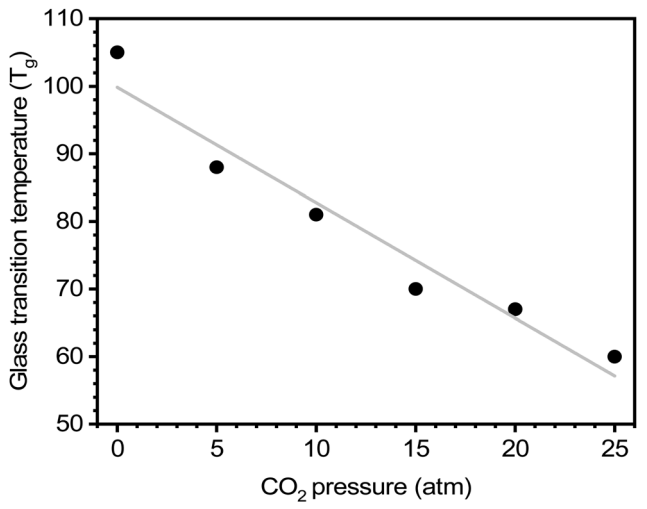

Fig. 11 Glass transition temperature (T_g) plotted against CO_2 sorption equilibration pressure for a sample of PMMA. Black circles represent collected data, which were then fit through linear regression (gray line).[64] The T_g data was redrawn from ref. 64 with permission from Wiley, copyright 1985.

3.2.1.2. Dynamic mechanical analysis (DMA). Dynamic mechanical analysis (DMA) is generally used to investigate the viscoelastic properties of materials by extracting stress–strain information of samples at controlled frequencies.[255] Parameters such as temperature and the frequency of the measurement are often varied to obtain a comprehensive range of data for the materials using the concept of time-temperature superposition discussed earlier in this section. DMA data can then be used to determine properties of the sample such as T_g, mechanical damping parameters ($\tan(\delta)$), and other mechanical properties such as the storage (E') and loss moduli (E'') and, in tensile tests, the Young's modulus, a measure of a material's stiffness.[235,240,256–263] In the presence of highly condensable gases like CO_2, glassy polymers susceptible to plasticization often swell to accommodate additional volume from the gas, leading to increases in polymer chain mobility that result in a depression in the effective T_g.[42,64,66,113,264–266] Therefore, the changing T_g in the presence of CO_2 can be indicative of the tendency of a polymer to increase chain mobility and, thus, be affected by plasticization.

In a typical DMA experiment to measure T_g, a piece of polymer film is clamped and subjected to a sinusoidal oscillating load while the material response (stress or strain) is recorded as a function of time, temperature, and frequency.[267] Tests in which temperature is varied are known as "temperature sweep tests", while those in which frequency is varied are referred to as "frequency sweep tests". In an ideal elastic material, the stress and strain will be in phase with each other, while in an ideal viscous material, the stress and strain will be 90° out of phase with each other.[268] The stress (σ) at any time, t, can be written as:

$$\sigma = \sigma_0 \sin(\omega t) \tag{25}$$

where σ_0 is the maximum stress achieved and ω is the frequency of oscillation.[255] Similarly, the strain (ϵ) can be written as:

$$\epsilon = \epsilon_0 \sin(\omega t + \delta) \tag{26}$$

where ϵ_0 is the maximum strain achieved and δ is the phase angle between stress and strain.[268] Therefore, in an ideal elastic material, $\delta = 0$, while in an ideal viscous material, $\delta = 90°$.[268] Fig. 12 depicts the three strain responses that can occur when a sinusoidal stress is applied to a material.

The storage modulus (E'), which is a measure of the stored energy in a material (*i.e.*, the elastic portion), and loss modulus (E''), which is a measure of the energy lost as heat (*i.e.*, the viscous portion) can be defined as follows:[268]

$$E' = \frac{\sigma_0}{\epsilon_0}\cos(\delta) \tag{27}$$

$$E'' = \frac{\sigma_0}{\epsilon_0}\sin(\delta) \tag{28}$$

In addition, the tangent of the phase angle, which is also referred to as the damping factor, can be expressed as the ratio of the loss modulus to the storage modulus:[269]

$$\tan(\delta) = \frac{E''}{E'} \tag{29}$$

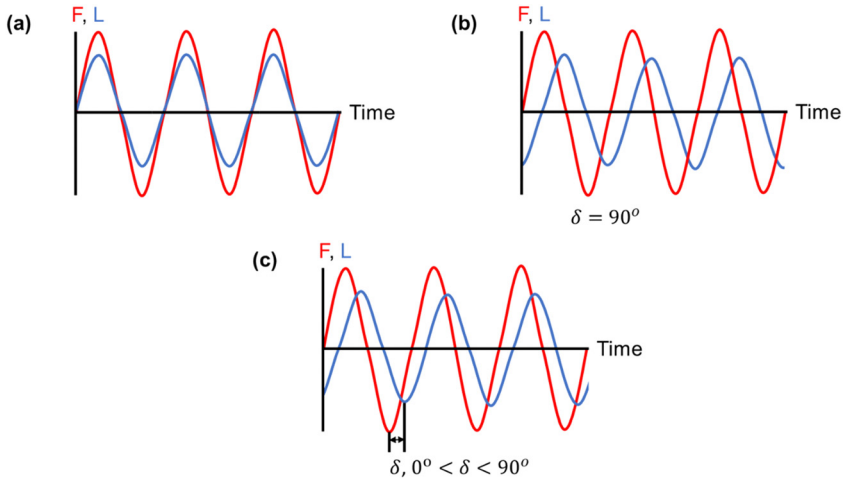

Fig. 12 Three strain responses (L) to applied stress (F): (a) an ideal elastic material, (b) an ideal viscous material, and (c) a viscoelastic material, in which the strain response lies in between that of an ideal elastic and an ideal viscous material.[255]

Below the T_g, the material acts as a "rigid" solid with a very high storage modulus, but when the T_g is traversed, the material enters a more "rubbery"-like state, which is indicated by a sharp decrease in E' and a peak in both E'' and $\tan(\delta)$.[270] Fig. 13a depicts an idealized E' scan of a polymer material as a function of temperature. As temperature increases, transitions (*e.g.*, sub-T_g and T_g) will occur as indicated by sharp decreases in E'. An example scan of both E' and E'' as functions of temperature is shown in Fig. 13b for a Matrimid® polyimide. The T_g is clearly indicated by the drop in E' and peak in E'' (which is labeled as α in the graph), while both β and γ transitions are also present and labeled accordingly.[240]

Since the glass transition of a polymer is a macromolecular relaxation process, the frequency (rate) of DMA tests can influence the onset of transitions. Comer *et al.* ran a series of DMA tests on an HAB-6FDA polyimide that was thermally-rearranged at 300 °C for 1 h over a frequency range of 0.1 to 30 Hz.[261] As seen in Fig. 14, the sub-glass transition temperatures (γ and β), as well as the glass transition temperature (labeled α) exhibited an increased response with increasing frequency, implying that these transitions are kinetic motional processes that are influenced by changes in testing frequency.[261] However, above the glass transition, the dynamic mechanical scan becomes independent of frequency, indicating that the polymer is in an equilibrium (and not *meta*-stable) state. The increase in the modulus starting at around 330 °C is associated with a stiffening of the polymer backbone from thermal rearrangement, while the increase in modulus at 450 °C is attributed to the beginning of thermal degradation.[261]

Several studies have reported mechanical properties of polymers in the presence of different concentrations of CO_2. Examples include those from Al-Enezi *et al.*, in which a high-pressure three-point bend testing cell was used to monitor the mechanical properties of polycarbonate (PC), polysulfone (PSf), and polymethyl methacrylate (PMMA) at CO_2 pressures of up to 120 bar.[271] It was found that all polymer samples generally experienced similar deformations at lower temperatures when exposed to more CO_2, which can be attributed to CO_2 "softening" the samples.[271] Ulrich *et al.* generated tensile stress–strain curves for polycarbonate films exposed to CO_2 and found that increasing CO_2 concentration led to a depression of yield stress (the stress at which a material will experience permanent

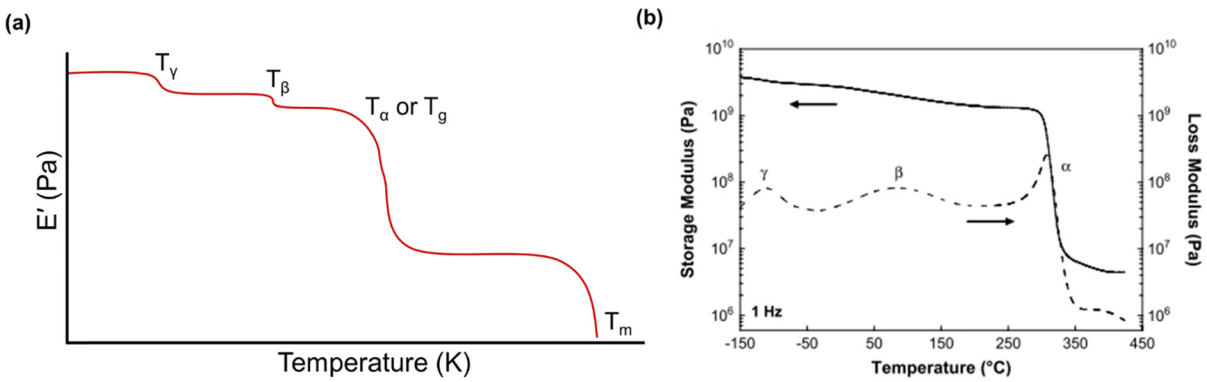

Fig. 13 (a) An idealized temperature scan of a polymer.[255] Regions of transitions are labeled. (b) Storage modulus (solid line) and loss modulus (dashed line) of Matrimid® polyimide.[240] Reproduced with permission from ref. 240 (Copyright Elsevier, 2009).

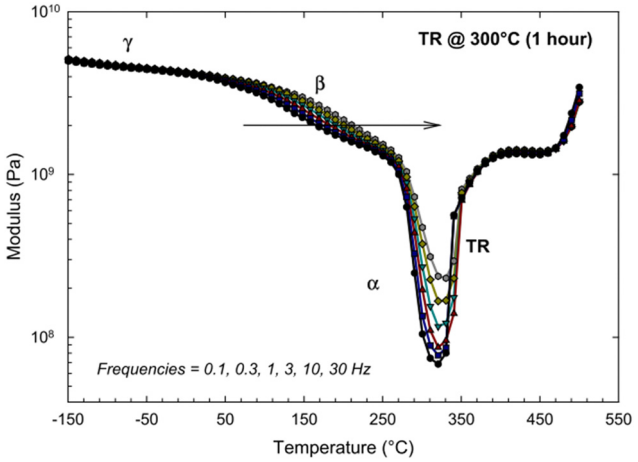

Fig. 14 Dynamic mechanical analysis of a thermally-rearranged HAB-6FDA polyimide at different test frequencies.[261] Reprinted with permission from ref. 261 (Copyright Elsevier, 2013).

deformation).[268,272] Flichy *et al.* conducted indentation experiments of PMMA in a CO_2 atmosphere up to 160 bar, reporting that the hardness of PMMA (as well as its T_g) was reduced as CO_2 pressure increased.[273] In addition, Wang *et al.* measured the Young's modulus, which is a measure of stiffness, of polystyrene as CO_2 pressure was increased from 1 to 1050 bar and found that both the Young's modulus and the T_g of polystyrene reached a minimum at a CO_2 pressure of 200 bar.[180] The authors attributed this finding to two competing effects that occur during CO_2 pressurization.[180] The first effect, plasticization, causes decreases in both Young's modulus and T_g. The second effect, which is caused by increasing hydrostatic pressure, leads to an increase in stiffness of the polymer,[180] and thus increases in Young's modulus and T_g.

A few studies have used DMA measurements directly to determine the effects of plasticizers such as CO_2 on polymer properties. Fried *et al.* analyzed the effects of sorbed CO_2 on the dynamic mechanical response of polysulfone (PSf), polycarbonate (PC), and polyetherimide (PEI).[264] DMA results for unconditioned samples and samples conditioned at ~30 bar of CO_2 for 30 h are shown in Fig. 15. In all three cases, E' exhibited a sharp decrease at a lower temperature for conditioned samples, indicating a lower T_g.[264] The peak associated with T_g in the E'' scans was also broader and occured at a lower temperature for all three conditioned samples.[264] The low-temperature secondary relaxation (γ) was also enhanced in magnitude and occurred at lower temperatures for all three conditioned samples, which suggests that sorbed CO_2 increases chain separation and allows for more chain mobility.[264]

Minelli *et al.* demonstrated through DMA that the presence of CO_2 decreases the magnitude of E' and increased tan(δ) for three different glassy polymers (PSf, PMMA, and Matrimid®) that were in equilibrium with CO_2 at different pressures.[274] The three polymers were chosen based on their different permeability behaviors in response to increased CO_2 feed pressures (Fig. 16a). PSf showed a continuously decreasing trend in permeability up to a CO_2 feed pressure of 30 bar,[275] PMMA displayed an increasing permeability even at low feed pressures,[276] and Matrimid® showed a plasticization pressure of approximately 11 bar.[277] In Fig. 16b–d, the change in storage moduli as the amount of sorbed CO_2 increases is shown for PSf, PMMA, and Matrimid®, respectively.[274] For all three polymers considered, the storage modulus decreases with increasing amount of CO_2 dissolved into the material, demonstrating that CO_2 decreased the elastic response of all three polymers.[274] As shown in Fig. 16e, tan(δ) for all three polymers increases with increasing CO_2 pressure, indicating an enhancement in the viscous response relative to the elastic response of the three polymers, as well as enhanced mobility and relaxation of polymer chains.[274]

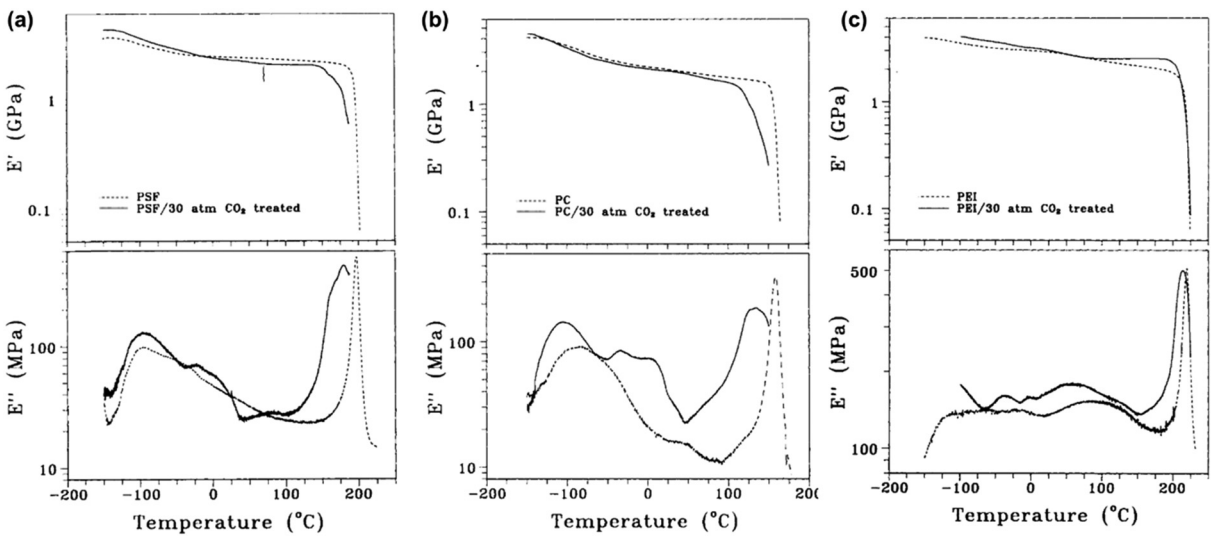

Fig. 15 Plot of E' and E'' for (a) PSf, (b) PC, and (c) PEI.[264] Dotted lines represent data for unconditioned samples, while solid lines represent data for conditioned samples at ~30 bar of CO_2 for 30 h. Runs were performed at a frequency of 1 Hz. Reprinted with permission from ref. 264 (Copyright Wiley-VCH, 1980).

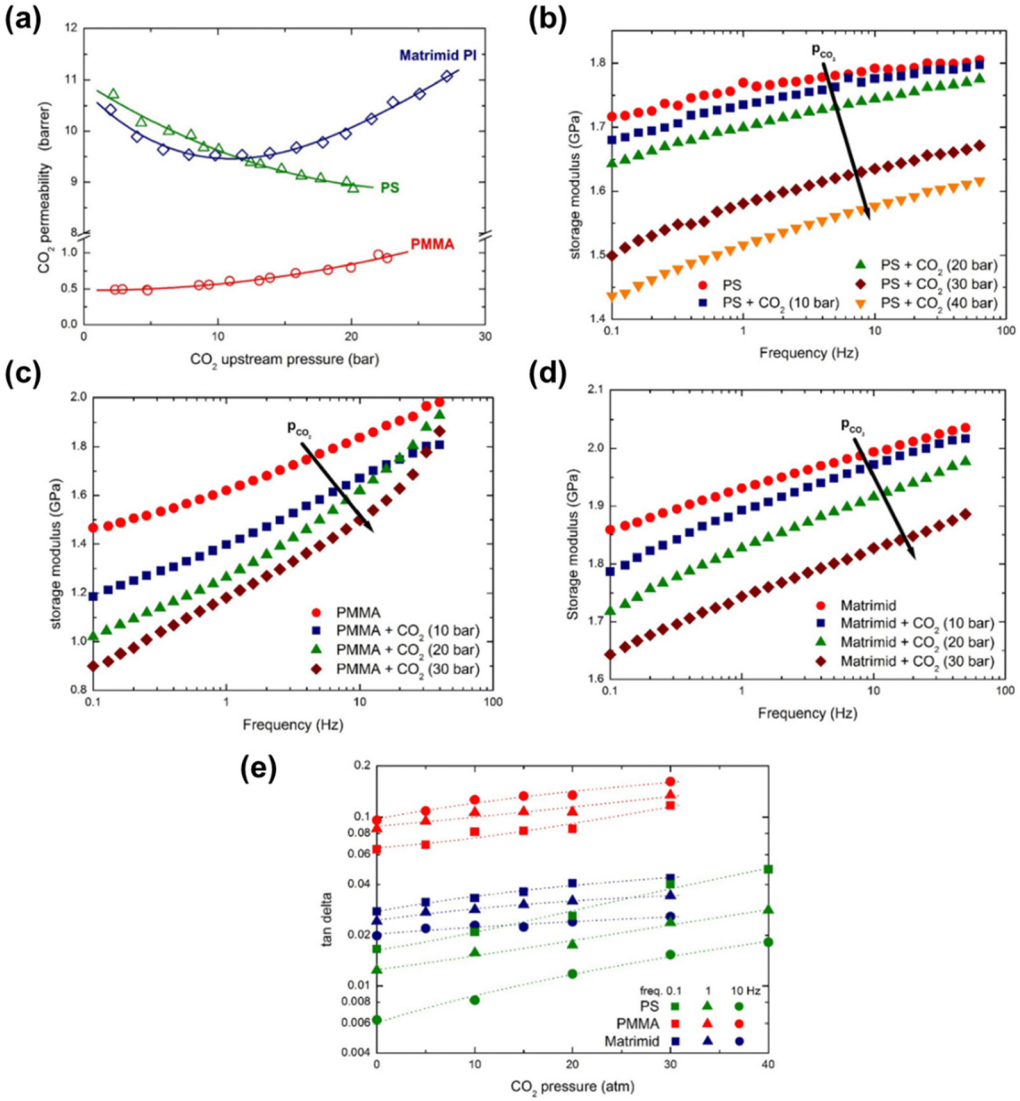

Fig. 16 (a) CO_2 permeability as a function of CO_2 feed pressure for PSf (labeled PS in figures), PMMA, and Matrimid®.[274–277] (b)–(d) depicts the storage modulus at various CO_2 pressures for PSf, PMMA, and Matrimid®, respectively, at varying test frequencies from 0.1 to 50 Hz. (e) tan(δ) as a function of CO_2 mass fraction for PSf, PMMA, and Matrimid® at a test frequency of 0.1 Hz.[274] Reprinted with permission from ref. 274 (Copyright Elsevier, 2019).

In regard to microporous polymers, DMA measurements are commonly used to determine T_g or other mechanical properties, but to the best of our knowledge, there have not been any direct DMA studies on microporous polymers in a CO_2 environment. However, a recent study by Číhal *et al.* analyzed the behavior of PIM-1 films exposed to vapor methanol and dimethyl carbonate (DMC) using DMA and found that E' remained comparable to that of untreated PIM-1 until exposure to DMC-rich vapor mixtures or mixtures at higher degrees of saturation (63% of the dew point pressure), where E' decreased.[278] This finding indicated that the binary mixture acted as a plasticizer.[278] Since DMA is a useful technique to determine the mechanical properties of polymer membranes, as well as the changes in such properties when exposed to different environments (such as CO_2 or other condensable gases), continued DMA tests on microporous polymers will be useful to elucidate important structural and functional correlations with plasticization.

3.2.1.2. Dielectric spectroscopy. Dielectric spectroscopy is a versatile experimental technique used to examine molecular relaxation processes, such as the T_g and sub-T_g transitions, or phase transitions, including the melting temperature in a crystalline material. Dielectric spectroscopy is also one of only a few analytical techniques that can survey a wide range of behavior for a single material, spanning low viscosity liquids to rubbery solids to hard glassy solids.[279] Additionally, dielectric spectroscopy can also be used to understand mixture miscibility and polymerization reaction rates.[279]

In a typical dielectric spectroscopy experiment for a polymer film, a thin sample is placed in contact with two or more electrodes while a time-varying sinusoidal voltage is applied. Although there are several electrode-sample configurations for polymer system measurements,[279] the most commonly used geometry is the parallel-plate arrangement. Pictured in Fig. 17 are two parallel-plate electrodes that sandwich a thin, flat sample,

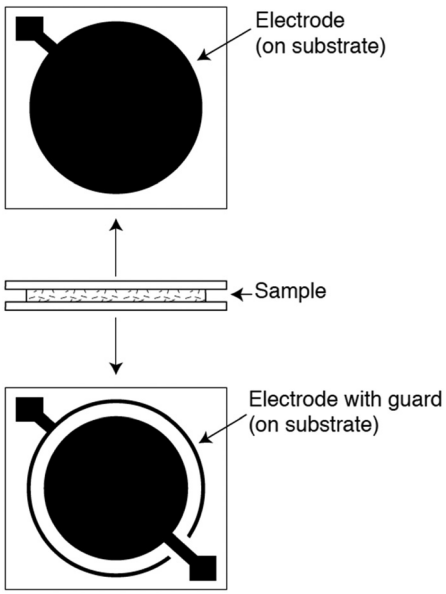

Fig. 17 Parallel-plate arrangement for dielectric spectroscopy. Two parallel plates sandwich a thin, flat sample. A guard ring is used to minimize edge effects. Reprinted with permission from ref. 279 (Copyright Wiley, 2006).

and a guard ring that minimizes fringing or edge effects. After a voltage is applied, the complex permittivity, also known as the dielectric constant, is measured as a function of frequency. To determine various properties of a given polymer, the measurement can be performed as a function of temperature and time at fixed frequencies. By surveying a broad frequency range (from $\sim 10^{-6}$ Hz to $\sim 10^{12}$ Hz) and variations in temperature, molecular responses on different length scales can be observed.[280] However, there is no single instrument that can cover this entire frequency range, thereby requiring multiple instruments to extract the most in-depth information. Common types of dielectric instrument techniques along with their typical frequency coverage are discussed by Schultz.[279]

In a time-varying or oscillating electric field, dielectric spectroscopy helps to measure the complex dielectric permittivity, $\varepsilon^*(f)$, which is represented by a complex number:

$$\varepsilon^*(f) = \varepsilon'(f) - i^*\varepsilon''(f) \quad (30)$$

where f is the frequency, i is the imaginary unit, ε' is the real part of the permittivity, and ε'' is the imaginary part of the permittivity or the dielectric loss factor. Function $\varepsilon(f)$ depends on several processes, including fluctuations of molecular dipoles, propagation of charge carriers, and additional polarization caused by separation of charges at interfaces.[280] The dielectric loss factor, ε'', is related to the energy absorbed by the polymer. A more in-depth discussion of phenomena that contribute to values of complex permittivity when analyzing dielectric data has been covered by Schultz.[279] In general, a peak in the imaginary part ε'' and a step-like decrease of the real portion ε' with increasing frequency characterizes relaxation processes in polymers.[281] Further analysis of dielectric relaxation data with respect to frequency can reveal additional information. For instance, though several models have been applied for the frequency domain data, the Havriliak–Negami (HN) equation fits a wide range of data:[282]

$$\varepsilon_{HN} = \varepsilon_\infty + \frac{\Delta\varepsilon}{\left[1 + (i\omega\tau_{HN})^{\beta_{HN}}\right]^{\gamma_{HN}}} \quad (31)$$

where ε_∞ is the real part for $\omega \gg 1/\tau_{HN}$, $\Delta\varepsilon$ is the dielectric strength, ω is the radial frequency ($\omega = 2\pi f$), τ_{HN} is the relaxation time that corresponds to the frequency of maximal dielectric loss f_{max}, and β_{HN} and γ_{HN} are shape parameters which describe the symmetric and asymmetric broadening of relaxation peaks.[283]

Many studies have used dielectric spectroscopy and analysis to determine T_g and sub-T_g relaxations in various polymers, including PIM-1, DL-polylactic acid (PLA), and polystyrene (PS).[240,280,284,285] For example, Konnertz *et al.* investigated the molecular mobility of PIM-1 by using dielectric spectroscopy.[284] The complex dielectric permittivity was measured in a frequency range from 10^{-1}–10^6 Hz using a parallel-plate geometry, and a temperature program with several heating and cooling cycles in the range of −100 to 250 °C was applied (depicted in Fig. 18a) to analyze the influence of temperature on sample structure and dynamics. Fig. 18b illustrates the dielectric spectra ($\log \varepsilon''$ *vs.* temperature) at a fixed frequency of 1000 Hz for the different heating and cooling runs performed, and a distinct relaxation peak is observed around 187 °C. Further analysis suggested that this relaxation process in PIM-1, denoted β^*, demonstrates a non-cooperative character due to a linear van't Hoff behavior, compared to the exponential dependence typically observed for cooperative segmental relaxation processes.[284] This relaxation can be attributed to π–π stacking in the polymer backbone that leads to local intermolecular agglomerates. Because PIM-1 can be susceptible to factors like physical aging and, therefore, lose its separation performance, Konnertz *et al.* investigated the molecular mobility of solution-cast nanocomposite films of PIM-1 and polyhedral oligomeric silsesquioxane with phenethyl substituents (PhE-POSS) as nanofillers using dielectric spectroscopy.[280] The same frequency range and temperature program from an earlier PIM-1 study was used.[284] Fig. 19 shows the dielectric spectra for the second heating run for pure PIM-1, pure PhE-POSS and selected composites at 1000 Hz. Though only a β relaxation (due to π–π stacking) is observed for pure PIM-1, composites with higher wt% of PhE-POSS (*i.e.*, PIM-1 with 15 wt% PhE-POSS and 30 wt% PhE-POSS) begin to show a weak but distinct second relaxation process, which the authors attributed to the α relaxation observed in pure PhE-POSS. Thus, these two studies helped to demonstrate that the addition of a secondary component, such as nanofillers or plasticizing agents, to an existing polymer can lead to changes in the T_g and sub-T_g relaxation processes. Dielectric spectroscopy is a useful way to observe, measure, and analyze these molecular dynamic changes in composites or pristine materials.

3.2.2. Intra and interchain mobility. In addition to measuring the T_g, relaxation studies using nuclear magnetic resonance

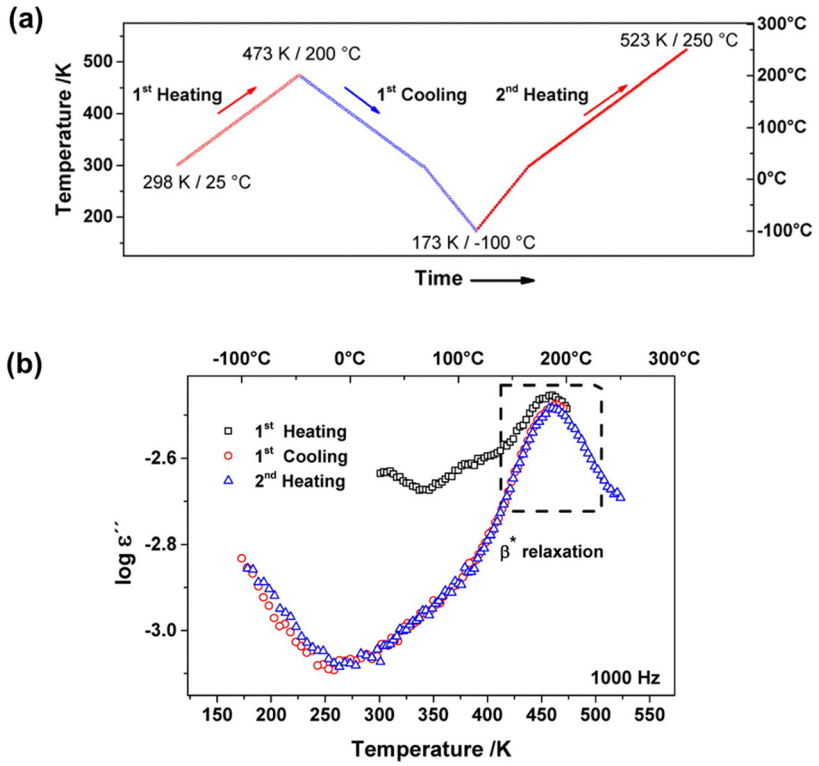

Fig. 18 (a) Heating/cooling cycles in the range of −100 to 250 °C of the dielectric measurements on PIM-1. (b) Dielectric spectra (log ε'' *vs.* temperature) at a fixed frequency of f = 1000 Hz for the different heating and cooling runs for PIM-1. Reprinted with permission from ref. 284 (Copyright American Chemical Society, 2020).

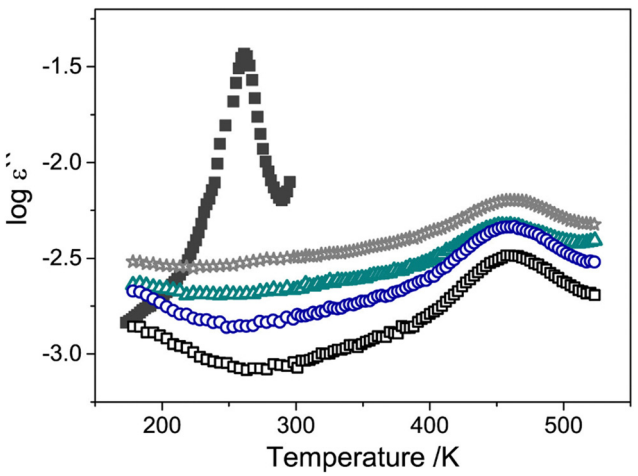

Fig. 19 Dielectric spectra (log ε'' *vs.* temperature) for pure PIM-1 (unfilled black squares), of PIM-1 with 1 wt% PhE-POSS (unfilled blue circles), 7.5 wt% PhE-POSS (unfilled green triangles), 30 wt% PhE-POSS (unfilled gray stars) and pure PhE-POSS (filled dark gray squares) at a frequency of 1000 Hz. Reprinted with permission from ref. 280 (Copyright Elsevier, 2020).

(NMR) and dilation studies can provide useful information on the mobility of polymer chains in a solid-state film before and after plasticization. On one hand, NMR experiments can probe chain dynamics at a molecular level, while dilation experiments can reveal dimensional changes in a film upon exposure to a plasticizing gas. A description of these methods and examples of their use in probing chain motion and plasticization is described in this section.

3.2.2.1. NMR relaxation experiments. Solid-state magic angle spinning (MAS) NMR can provide in-depth information on the energetics of polymer chain motion and even individual atom-specific motions through spin–lattice relaxation experiments. These studies help evaluate subtle variations in localized, molecular-level dynamics, which can correlate with gas transport phenomena.[69] In general, NMR relaxation experiments evaluate the process through which an excited magnetic state returns to its equilibrium state. Specifically, the spin–lattice relaxation time (T_1) is the process where an excited spin returns to equilibrium along the axis of the applied magnetic field. Spin–lattice relaxation can also be measured using a spin-lock, which is referred to as the spin–lattice relaxation in the rotating frame ($T_{1\rho}$) that forms a rotating magnetic field perpendicular to the applied field. Because NMR signals are associated with specific atoms in an organic molecule, both T_1 and $T_{1\rho}$ can resolve relaxation times for individual atoms or clusters of similar atoms in a polymer chain. This feature enables analysis of mobility for atoms on side chains or atoms on the polymer backbone and provides information on both the intra and interchain mobility of polymer chains in a solid-state film. Generally, when thinking of polymer chain dynamics, longer relaxation times indicate less chain mobility. Detailed information on the fundamental theory and common procedures to conduct NMR relaxation experiments can be found elsewhere.[286–288]

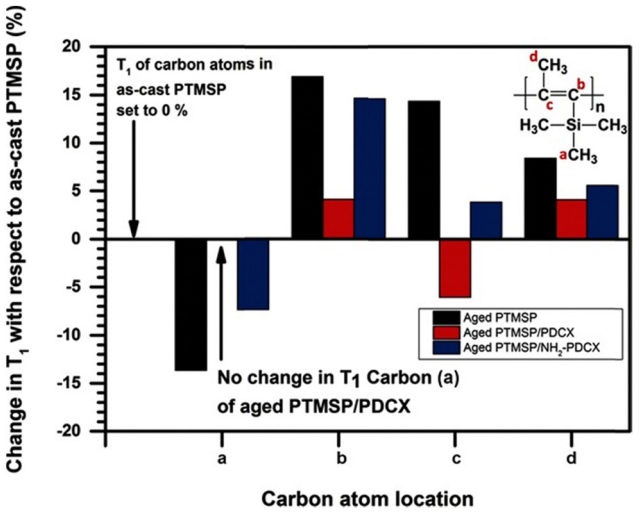

Fig. 20 Change in T_1 relaxation times for carbon atoms in PTMSP before and after adding a hypercrosslinked additive (α-dichloro-*p*-xylene, *p*-DCX) or its amine-functional counterpart. Reprinted with permission from ref. 291 (Copyright Wiley, 2016).

In the context of gas separations, NMR experiments have been used to elucidate (1) the evolution of chain mobility as a function of CO_2 content, (2) the mechanism for densification of polymer chains over time in mixed-matrix membranes (MMMs), and (3) the influence of plasticizing solvents or small molecules on the overall chain dynamics. In general, decreases in T_1 or $T_{1\rho}$ as a function of physical aging time, additive concentration, or plasticizer content indicate increased mobility and higher local free volume, while increases in T_1 or $T_{1\rho}$ suggest reduced chain mobility, higher local packing density or increased secondary interactions.[289]

Because of the relationship between relaxation times and packing density, NMR has been used to study physical aging mechanisms in films.[290] For instance, in work by Lau *et al.*, ^{13}C solid state NMR was used to understand how addition of a hypercrosslinked additive (α-dichloro-*p*-xylene, *p*-DCX) helped reduce aging of poly(1-trimethylsilyl-1-propyne, PTMSP).[291] In that study, the relative change in T_1 values for the carbon atoms was evaluated over time. As shown in Fig. 20, films with added *p*-DCX showed little change in T_1 over time while the pristine PTMSP polymer had a 13% increase in T_1 values for the side chains and reduced mobility for the backbone, which was attributed to the collapse of free volume and hindered chain motion.[291] Similar ^{13}C-NMR T_1 studies have been performed with PIM-1-based MMMs based on different additives such as PAF-1,[292] hydroxyl-functionalized *p*-DCX,[293] and functionalized silica nanoparticles.[294] These studies have revealed some characteristics of particle–polymer interactions that may help or hinder chain mobility. NMR analysis has also been used to elucidate the effect of casting solvent and particle–solvent interactions on the resulting solid-state chain mobility, such as in cases where the same polymer was cast using solvents of different polarity,[293] or where increases in chain mobility arose after solvent treatments or conditioning[289] (*e.g.*, methanol in PTMSP). While not as frequently applied in the context of plasticization, the measurement of T_1 relaxation over time is inherently similar to the chain dynamics that occur on exposure to plasticizing agents, such as low molecular weight diluents and condensable gases, and may provide useful information on the mechanisms affecting such processes.

In addition to relaxation experiments as a function of time, T_1 or $T_{1\rho}$ experiments have also been used to probe the atom mobility as a function of plasticizer content. For instance, Koval'aková *et al.* evaluated how a small plasticizing agent, glycerol triacetate (TAC), affected the relaxation of polylactic acid (PLA)[295] using solid-state ^{13}C and ^{1}H-NMR experiments. In this case, the presence of plasticizers led to an increase in mobility (decrease in ^{13}C T_1 values) of PLA chains at room temperature. In separate studies, $T_{1\rho}$ values measured at frequencies in the mid-kilohertz range have been used to probe relaxations associated with cooperative main-chain motions in polymers.[69] In one instance, Sefcik and Schaefer performed ^{13}C NMR tests as a function of CO_2 pressure from vacuum to ~1 bar and observed a reduction in $T_{1\rho}$ values, indicating increased mobility with increasing pressure.[296] In subsequent work, Sefcik and Schaefer investigated the role of the tricresyl phosphate plasticizer on the mobility of poly(vinyl chloride) (PVC) and related these correlations to time-lag diffusion.[297] The diffusion coefficients decreased when concentrations of the plasticizer were below 15%, while diffusion coefficients and relaxation rates increased at concentrations above 15%. The authors suggested that these similarities in trends may indicate a close relationship between main-chain molecular motions and gas diffusion. To complement this work, Smith and Moll performed deuterium (^{2}H) NMR T_1 studies as a function of CO_2 pressures ranging from vacuum to ~35 bar for polycarbonate, a polyester carbonate, and polystyrene.[69] As shown in Fig. 21, relaxation times were found to consistently decrease with increasing CO_2 pressures, indicating increased main-chain motions once again.

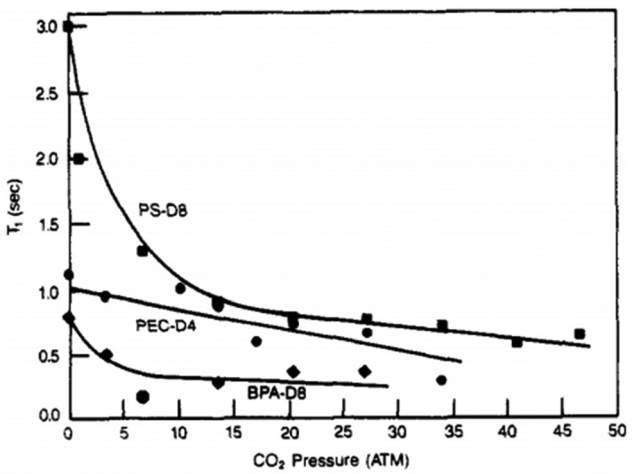

Fig. 21 Dependence of ^{2}H-NMR T_1 values on CO_2 pressure for polystyrene (PS-d_8), polyester carbonate (PEC-d_4), and bisphenol A polycarbonate (BPA-d_8). Reprinted with permission from ref. 69. (Copyright American Chemical Society, 1990).

Here, the authors considered two hypotheses: that (1) the microscopic dynamic processes (oscillatory motions and phenyl ring flips) assist in diffusion, or that (2) CO_2 gas plasticizes the film leading to increased chain motion and diffusion. Importantly, they also note that relative frequency of diffusion (correlation times $\sim 10^{12}$ s^{-1}) is much shorter than the slow relaxations probed by NMR (10^6–10^7 s^{-1}). Therefore, diffusion and NMR relaxation may be independent but both can still suggest how CO_2 alters the dynamics of the films. Taken together, these examples showcase the utility of NMR relaxation experiments in understanding intra and interchain motions in relation to plasticization. Applying such analyses to microporous materials would assist in revealing clear structure–property relationships and understanding the molecular origins of plasticization, especially in rigid microporous polymers with ultrahigh glass transition temperatures, where sub-T_g motions can influence plasticization effects.

3.2.2.2. Dilation experiments. As discussed in Section 2, sorption tests can reveal information on interaction parameters when using models such as the NELF model, but an additional consideration is dilation of the membrane—the physical expansion of the polymer matrix when forming a mixture of the polymer and penetrant.[65] This volume expansion has been correlated with the increase of diffusivity related to plasticization.[72] Dilation experiments have been used as tools to (1) estimate molar volume of the sorbed penetrant,[65,150,298] (2) differentiate Fickian and non-Fickian diffusion in polymer chains,[72,87,168] and (3) validate thermodynamic model predictions (such as the k_{sw} swelling parameter used in the NELF model).[65,87,150,298]

Dilation experiments are typically performed sequentially through equilibration with a gaseous atmosphere at discrete pressure steps. Additionally, dimensional changes are recorded for the polymer film as it comes into equilibrium, typically using the assumption of isotropic expansion[65,298] to measure volume changes at different sorption equilibrium conditions. These experiments can be performed using a variety of methods such as dilatometry and spectroscopic ellipsometry. Dilatometry measures the change in size of a single dimension using either a camera or a capacitance sensor.[65,72,168] For spectroscopic ellipsometry, light of a certain wavelength is refracted through a thin polymer sample attached to a reflective substrate, and the changes in the polarization state of the dispersed waves collected by the detector can be fitted to an appropriate model to obtain thickness and refractive index of the sample.[299] The key assumption in spectroscopic ellipsometry is that the measured refractive index of a mixture is based on the refractive indices of both the polymer and penetrant, and can be linked to the individual density of the polymer and penetrant through the Clausius–Mosotti equation.[47,300–302] Using volume change data, a dilation isotherm can be created, measuring the fractional volume change from the starting volume (*i.e.*, $\Delta V/V_0$) *versus* pressure p.

Dilation experiments have been used to estimate the partial molar volume of the penetrant[150,298] based on its thermodynamic definition:

$$\bar{v}_i = \left(\partial V/\partial n_i\right)_{T,p,n_{j\neq i}} \tag{32}$$

Using $\Delta V/V_0$ data from the dilation isotherm, the penetrant partial molar volume is found using the following equation:

$$\bar{v}_1 = V_{STP}\left(\frac{d}{dp}\left(\frac{\Delta V}{V_0}\right) + \beta\right)\frac{dp}{dc} \tag{33}$$

where V_{STP} is the volume of an ideal gas at STP, β is the isothermal compressibility of the polymer, p is the pressure of the penetrant, and c is the concentration of penetrant in the polymer.

Hysteretic behavior seen in sorption isotherms of plasticized polymers is also observed in dilation experiments, where the fractional volume change due to an external penetrant ($\Delta V/V_0$) is higher for depressurizataion curves than the pressurizing curves.[65,72,87] Importantly, the treatment history and conditioning of the polymer play a role in dilation.[65] The changes to the polymer matrix caused by dilation at high pressures remain for additional time that is dictated by a relaxation time inherent to the polymer structure and morphology.[303,304] For example, Ogieglo *et al.* leveraged *in situ* spectroscopic ellipsometry to investigate high-pressure CO_2 sorption (0–45 bar) for ultrathin films of microporous polymers including PIM-1, AO-PIM-1, a Tröger's base PIM, and PIM-6FDA-OH.[305] As shown in Fig. 22a and b, the PIMs showed typical hysteretic behavior for glassy polymers and swelled significantly more than the non-microporous polystyrene. However, PIMs with higher CO_2 affinity, PIM-6FDA-OH and Tröger's base PIM, showed higher swelling of about 15% at 45 bar compared to PIM-1 and AO-PIM-1. The hysteretic behavior of ultrathin PIM-1 films (7–128 nm) was also investigated (Fig. 22c). As film thickness decreased, the shape of the sorption isotherms changed to reflect a more rubbery-like isotherm (*i.e.*, the slope of the desorption curve increased). Moreover, the maximum swelling increased to 18% for the 7 nm film, about three times that of the 128 nm thick film. Thin films appeared to have a higher susceptibility to plasticization, which corresponded to an apparent T_g reduction of 200 °C.

Dilation experiments can also be used to gain insight into the kinetics of gas sorption in plasticized polymers. In these cases, a distinction between Fickian and non-Fickian diffusion must be made.[87,168,303] While Fickian diffusion describes the transport behavior expected for molecular diffusion using Crank's solution,[72,306] non-Fickian diffusion needs to be considered if dimensional changes occur to the polymer during an experiment. As proposed by Berens and Hopfenberg,[72,87,303] penetrant uptake can be modeled as a two-component relaxational process: the relatively fast matrix response to Fickian diffusion and the slower, relaxational motions of the polymer matrix during dilation. Newns proposed a viscoelastic functional form to model this uptake behavior, which can be found at this reference.[307] This model was designed to match viscoelastic phenomena with a distribution of relaxation times.[72,303,307] Information on the final mass uptake at steady-state ($M_{F,\infty}$), the maximum sorbed masses for the corresponding relaxational mode ($M_{R,i}$), and time constants (τ_i) can be obtained by fitting the Newns equations to transient pressure-decay data provided by sorption experiments. Dilation experiments to capture experimental data on volume dilation *versus* penetrant pressure can also be used to calculate a

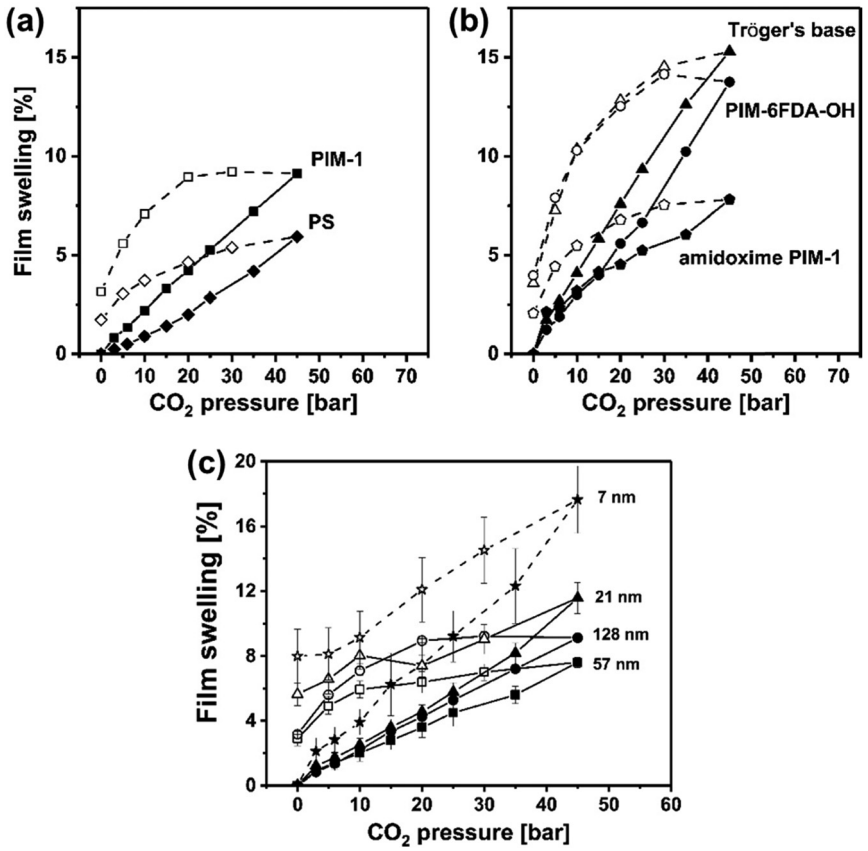

Fig. 22 Film swelling *versus* CO_2 pressure for (a) PS (112 nm) and PIM-1 (128 nm), (b) Tröger's base PIM (105 nm), PIM-6FDA-OH (132 nm), and AO-PIM-1, (135 nm), and (c) PIM-1 films of different thicknesses. Filled and unfilled symbols indicate sorption and de-sorption curves, respectively. Reprinted with permission from ref. 305 (Copyright American Chemical Society, 2018).

swelling coefficient, k_{sw}, used for the NELF model. Doing so constrains fitting for the NELF model with one less variable required, significantly improving model predictions.[150]

In addition to enabling evaluation of the various fundamental phenomena reviewed above, ellipsometry can be used to further investigate thin films and even the thin selective layers of hollow-fiber membranes,[308,309] which are critical considerations for industrial deployment. As demonstrated in Fig. 22c, thin films exhibit vastly different swelling and plasticization behavior than bulk membrane samples.[303,305,307] However, ellipsometry experiments can be challenging for certain membrane geometries, preventing widespread adoption of this technique in literature reports.

4. Approaches to mitigate plasticization

In general, there are three primary approaches that researchers pursue to mitigate the effects of plasticization in microporous polymers: (1) engineering the polymer backbone or sidechain chemistry to induce rigidity, (2) applying post-synthetic modification such as crosslinking, and (3) developing composites, blends, and copolymers. Fig. 23 provides an overview of these approaches. When analyzing the success of each approach, the figure of merit is often the plasticization pressure and/or changes in permeability and selectivity between pure- and mixed-gas measurements. These approaches and their resulting trends will be discussed in more detail in Section 5 and compared across an extensive dataset of literature collected from all microporous polymer reports to date. It should also be noted that some reports included in this section performed mixed-gas tests at low pressures (*e.g.*, 1 bar partial pressure CO_2). While these sorts of mixed-gas tests do not necessarily provide information relevant to penetrant-induced plasticization effects, they are still valuable as they often reveal information related to competitive sorption. Therefore, we have decided to include these reports in this section but generally recommend that high pressure mixed-gas permeation experiments be run when evaluating stability to plasticization.

4.1. Novel syntheses of polymer structures to induce rigidity

Previous studies on non-microporous polymers such as polyimides[92–94,310,311] have demonstrated successful plasticization resistance through the restriction of chain mobility *via* crosslinking,[78,312,313] addition of polar moieties,[314–316] and formation of charge transfer complexes (CTCs).[76,316–318] These methods specifically aim to increase the interchain rigidity of polymers, while, in other cases, researchers have looked to increase the intrachain rigidity of polymers. The differences between interchain and intrachain rigidity are depicted in Fig. 24. Interchain rigidity

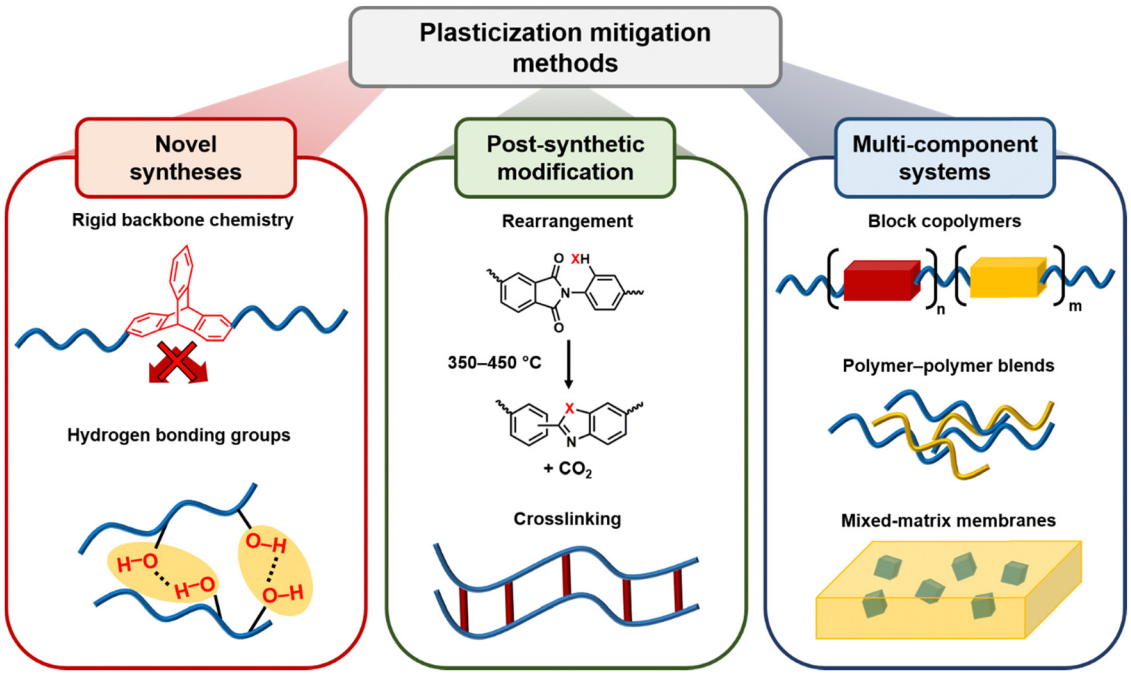

Fig. 23 Methods employed to mitigate plasticization in polymer membranes.

results from physical or chemical interactions between chains, while intrachain rigidity results from mobility restrictions within a single chain.[90]

The seminal work by Budd and McKeown in 2004 on polymers of intrinsic microporosity (PIMs)[25,319] and subsequent development of many microporous polymers that contain rigid and contorted backbones[26,103] has prompted researchers to pursue microporous polymer chemistries for gas separations and plasticization resistance. In particular, increasing the intrachain rigidity of PIMs with addition of bridged-bicyclic contortion centers such as triptycene[29,320–324] and Tröger's base (TB) has led to improved gas separation properties.[33,35,325,326]

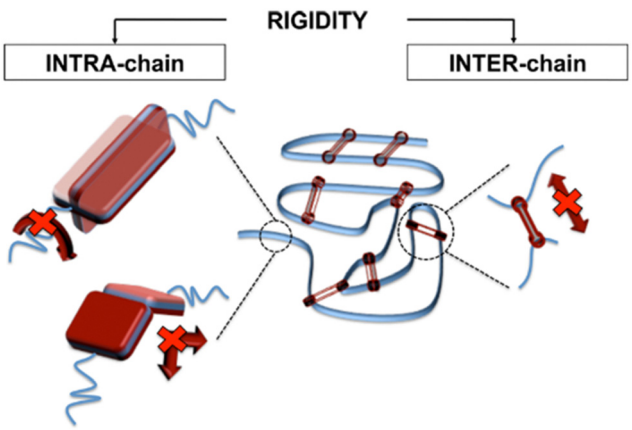

Fig. 24 Classification of polymer rigidity into intrachain and interchain rigidity. The blue ribbons represent polymer chains, red segments feature areas of rigidity, and red arrows represent regions of polymer chain movement that are restricted. Adapted with permission from ref. 90 (Copyright American Chemical Society, 2014).

4.1.1. Intrachain rigidity. A classic synthetic example of applying the concept of intrachain rigidity comes from Lasseuguette *et al.*, who studied gas transport properties of PIM-EA(H_2)-TB, a PIM-containing TB polymer (Fig. 25).[30] Over the pure-gas pressure range tested (1–20 bar), no plasticization pressure was observed, suggesting plasticization resistance due to the rigidity of the polymer structure.[30] Williams *et al.* synthesized PIM-MP-TB (Fig. 25), a TB-based polymer containing the structural unit methanopentacene (MP), which is designed to increase rigidity in the polymer chain.[327] In mixed-gas studies (52.1 : 47.9 vol% CO_2/CH_4), they found that while CO_2 permeability was constant up to a total feed pressure of 6 bar, CH_4 permeability increased slightly and CO_2/CH_4 selectivity decreased with increasing feed pressure.[327] The presence of CO_2 in the mixture likely induced dilation of the polymer matrix, which would allow CH_4 to permeate more easily.[327] However, in a 10 : 90 vol% CO_2/N_2 mixture, both CO_2 and N_2 permeability, as well as CO_2/N_2 selectivity, remained fairly constant up to a total feed pressure of 6 bar.[327] This result could be attributed to the presence of less CO_2 in the CO_2/N_2 mixture, which would not induce as much swelling. Wang *et al.* synthesized two microporous polymers containing a diamine analogue of TB, known as Hünlich's base (HB), to create 6FDA-HB and TDAi3-HB (Fig. 25).[328] While the calculated pure-gas CO_2/CH_4 selectivity decreased from a feed pressure of 2 bar to 15 bar for both polymers, no obvious CO_2-induced plasticization was observed since the permeabilities of both CO_2 and CH_4 did not increase with increasing feed pressure.[328] While these structures show promising initial results, additional studies including mixed-gas tests would be helpful in determining whether the addition of HB onto a polymer backbone can mitigate plasticization more than that of TB.

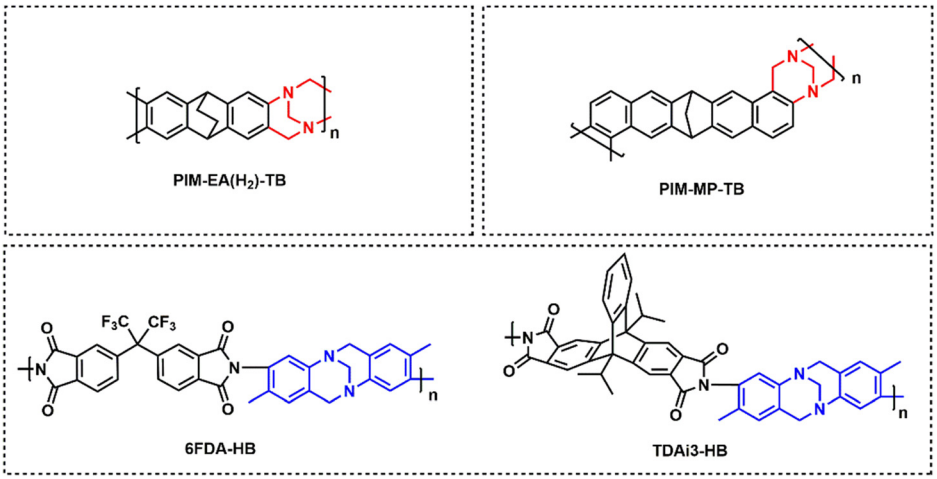

Fig. 25 Chemical structures of polymers of intrinsic microporosity containing Tröger's base (red) or Hünlich's base (blue), for studies that reported pure-gas pressurization studies and/or mixed-gas permeation.[30,327,328]

Another highly rigid and fused structural component that has been used to increase intrachain rigidity in polymers is triptycene (Fig. 26).[20,22,23,25,33–43] Thus, the effects of incorporating triptycene, along with other iptycene structures, on plasticization resistance has been investigated. Swaidan *et al.* compared the C_3H_6/C_3H_8 gas transport properties of KAUST-PI-1 and PIM-PI-1 (Fig. 26) for a feed mixture of 50 : 50 C_3H_6/C_3H_8 and a C_3H_6 partial pressure of 1.0 to 2.5 bar. KAUST-PI-1 experienced a 33% increase in C_3H_6 permeability while PIM-PI-1 experienced a 7% increase.[329] Over this same pressure range, there were also a decrease in C_3H_6/C_3H_8 selectivity (7 to 5 for KAUST-PI-1 and 3.4 to 2 for PIM-PI-1).[329] However, KAUST-PI-1 both exceeded PIM-PI-1 in terms of C_3H_6 permeability and C_3H_6/C_3H_8 selectivity for the entire pressure range studied.[329] In addition, mixed-gas data for KAUST-PI-1 was on the C_3H_6/C_3H_8 pure-gas upper bound, while pure-gas data exceeded the upper bound.[329,330] Another triptycene-containing polymer, PMDA-DAT (Fig. 26), was also studied for its plasticization resistance.[331] pure-gas permeability measurements found that PMDA-DAT had a CO_2 plasticization pressure of around 15 bar.[331] PIM-TMN-Trip, another PIM with a triptycene unit in the backbone, did not show obvious CO_2-induced plasticization effects when exposed to a feed mixture of 22.2 vol% CO_2, 6.8 vol% O_2, 70.2 vol% N_2, and 2220 ppm SO_2 over a trans-membrane pressure difference from 1 to 4 bar.[332] However, as the CO_2 partial pressure was limited to less than 4 bar, plasticization may not have been observed, which would necessitate tests at higher feed pressures, if required for the application.

Triptycene and an extended iptycene were compared in the forms of 6FDA-DAT1 and 6FDA-DAT2, respectively (Fig. 26), and it was found that 6FDA-DAT2 contained larger micropores due to the bulkier nature of the extended iptycene.[333] In terms of gas transport properties, both polymers experienced CO_2-induced plasticization when exposed to a mixture feed of 50 : 50 CO_2/CH_4 up to a CO_2 partial pressure of 16 bar, as evident from the increase in both CO_2 and CH_4 permeability with increasing feed pressure.[333]

Several other studies have shown that solely increasing the intrachain rigidity to mitigate plasticization may not be effective.[28,90,334–336] In 2014, Swaidan *et al.* examined the gas transport properties of two triptycene-based intrinsically microporous polyimides, KAUST-PI-1 (TPDA-TMPD) and KAUST-PI-5 (TPDA-6FpDA) (Fig. 26).[90] When comparing the degrees of torsional freedom at 35 °C for the characteristic highlighted bonds in Fig. 27a and Fig. 27b, it was found that KAUST-PI-5, which contains the 6FpDA diamine, exhibits more torsional freedom due to (a) the non-substituted *N*-phenyl-imide bond and (b) the single bonds between the phenyl rings. Thus, it was expected that KAUST-PI-1 would exhibit higher plasticization resistance due to its increased backbone rigidity and reduced rotational mobility.

While the more flexible KAUST-PI-5 exhibited a plasticization pressure at 10 bar CO_2 partial pressure in both pure- and mixed-gas (50 : 50 CO_2/CH_4 mixture) tests, KAUST-PI-1 showed significant effects from plasticization, as indicated by an immediate rise in CO_2 permeability with pressure in both pure- and mixed-gas tests.[90] Thus, it was concluded that intrachain rigidity alone is insufficient to mitigate plasticization and, instead, intrachain flexibility could actually result in changes in polymer conformation to help suppress plasticization. In the case of KAUST-PI-5, for example, flexible backbones can coplanarize and assume a denser packing configuration, leading to interchain interactions that subsequently restrict chain mobility.[90] Thus, establishing a balance between intrachain and interchain rigidity can lead to plasticization-resistant membranes.

In 2015, Swaidan *et al.* continued this study by comparing the effects of plasticization on gas transport properties in PIM-1 and two triptycene-based ladder polymers, TPIM-1 and TPIM-2 (Fig. 26).[28] When comparing the degrees of torsional freedom at 35 °C for representative PIMs, it was found that TPIM-1 contains higher intrachain rigidity compared to PIM-1 due to the presence of the rigid triptycene group in its backbone (Fig. 28).[28] However, when measuring mixed-gas permeability (50 : 50 CO_2/CH_4 mixture) at 10 bar CO_2 partial pressure, TPIM-1 experienced a 93%

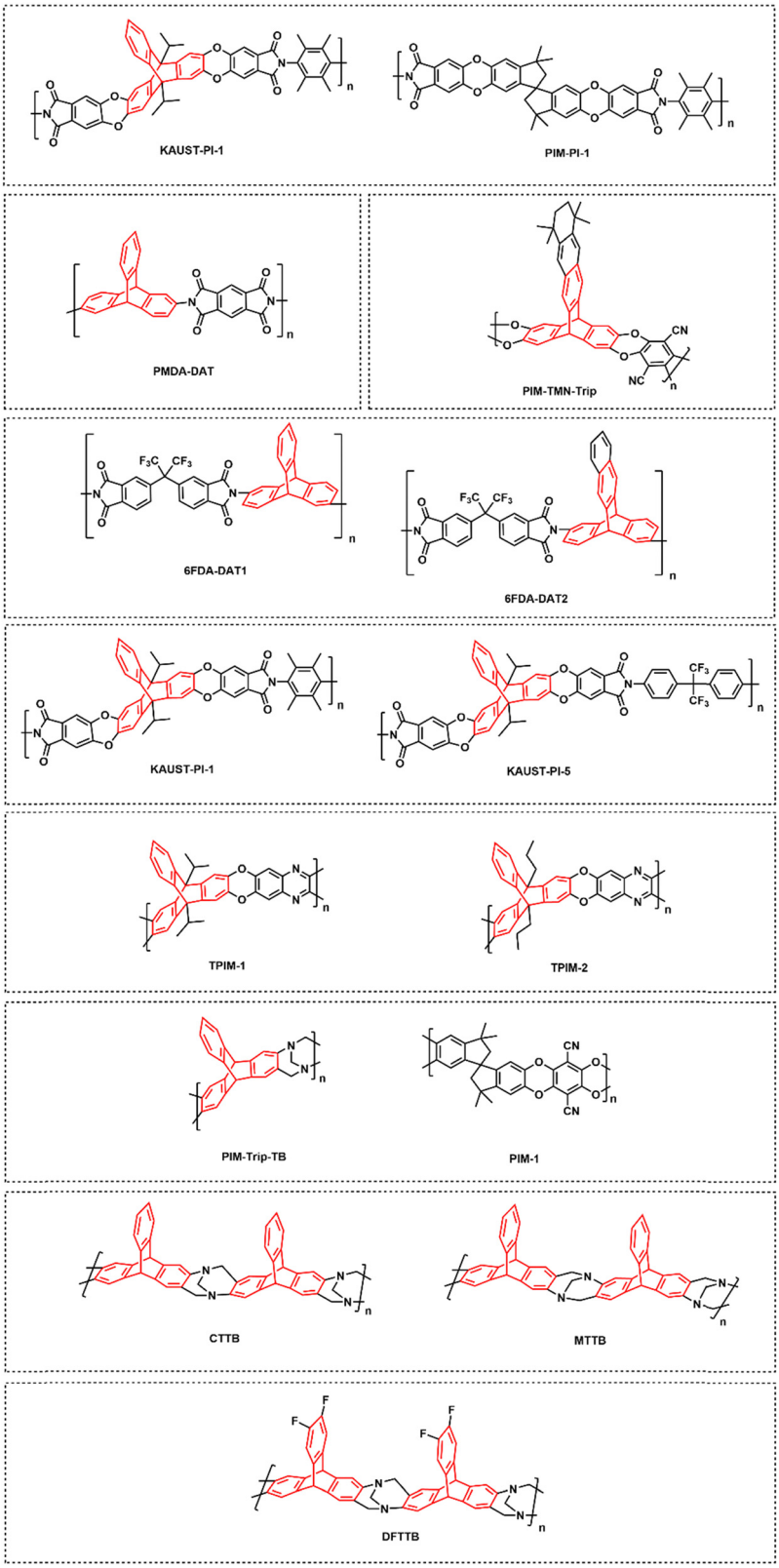

Fig. 26 Chemical structures of polymers of intrinsic microporosity containing triptycene (red) and analogous structures, for studies that reported pure-gas pressurization studies and/or mixed-gas permeation.[20,22,23,33–43]

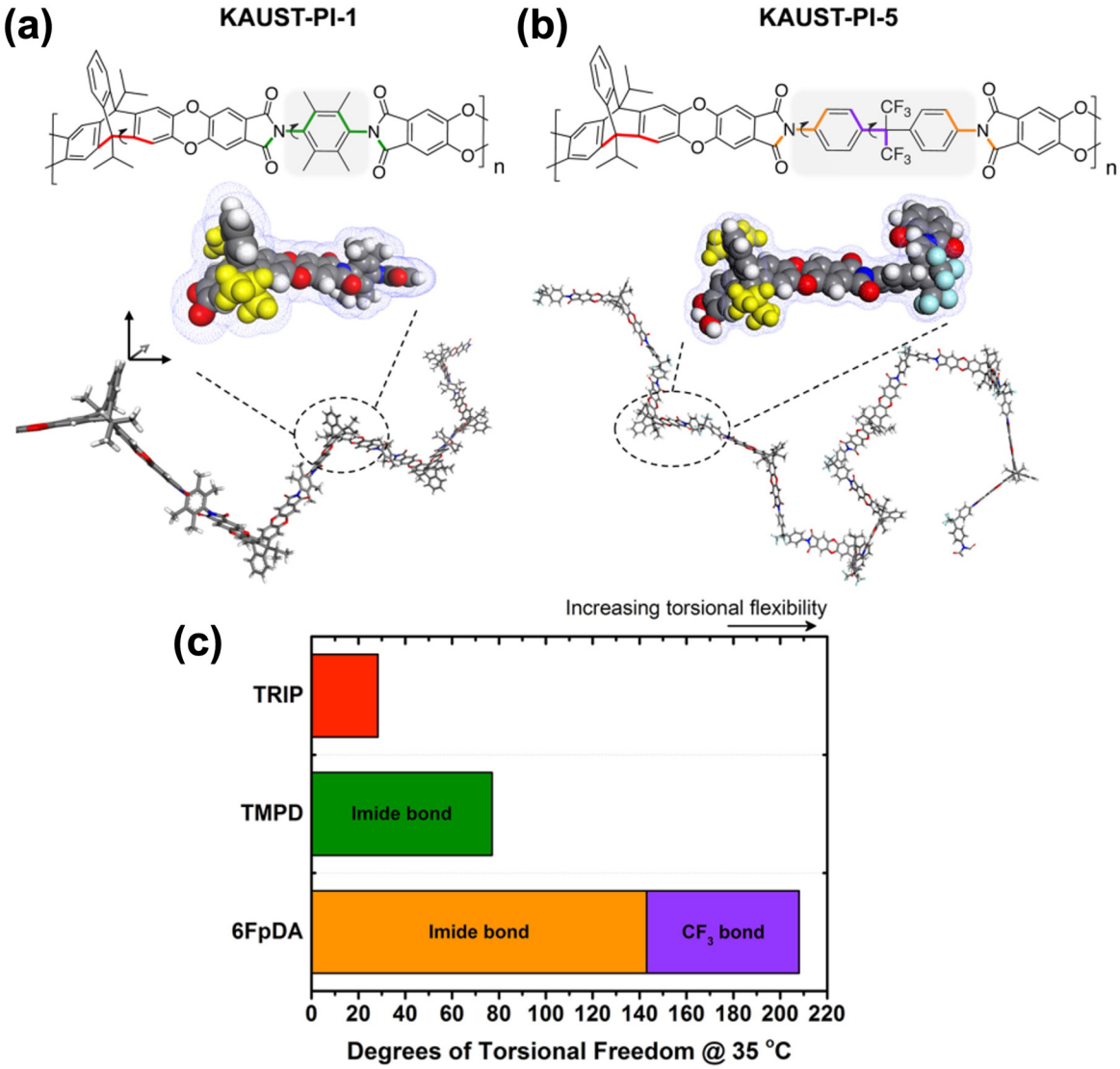

Fig. 27 Energy-minimized structures (forcite module, materials studio 7.0, accelrys) of (a) KAUST-PI-1 (TPDA-TMPD), and (b) KAUST-PI-5 (TPDA-6FpDA). (c) Degrees of torsional freedom at 35 °C are measured for bonds of interest highlighted in red, green, orange, and purple. Adapted with permission from ref. 90 (Copyright American Chemical Society, 2014).

increase in CH_4 permeability compared to pure-gas permeability at a feed pressure of 10 bar, while PIM-1 experienced a 62% increase.[28] This increase in CH_4 permeability is an indication of CO_2-induced plasticization despite the high intrachain rigidity of TPIM-1. TPIM-2, instead, plasticized less readily than TPIM-1, showing less than a 10% increase in CH_4 permeability from the pure- to mixed-gas test up to a CO_2 partial pressure of 15 bar.[28] The authors investigated the potential origin of this difference in plasticization susceptibility through transport analysis. TPIM-1 possessed higher O_2 permeability and O_2/N_2 selectivity than TPIM-2, suggesting a highly ultra-microporous, size-sieving pore structure with a significant amount of pores around the sizes of O_2 and N_2 at 3–4 Å.[28] If such pores are dilated during exposure to CO_2 at higher pressures, both CO_2 (d_k = 3.3 Å) and CH_4 (d_k = 3.8 Å) diffusivities will be significantly affected.[15,28] This hypothesis is illustrated further in Fig. 29.

Genduso *et al.* also examined the effects of intrachain rigidity on plasticization resistance by conducting mixed-gas permeability experiments on PIM-Trip-TB, PIM-1, and 6FDA-mPDA (Fig. 26).[334] At ~10 bar CO_2 partial fugacity in a 50 : 50 mol% CO_2/CH_4 mixture, it was found that the CH_4 diffusion coefficients for PIM-1 and PIM-Trip-TB were 1.4 and 2.2 times higher than those for 6FDA-mPDA.[334] From this result, the authors concluded that intrachain rigidity alone found in PIM structures cannot suppress CO_2-induced plasticization.[334]

Zhu *et al.* synthesized and characterized two different regioisomers of triptycene-containing TB-based polymers, CTTB and MTTB, with ITTB being a 50 : 50 mixture of the two (Fig. 26), and found that there was a 30–50% increase in CO_2 and CH_4 permeability for all three polymers compared to pure-gas experiments at feed pressures from 2 to 16 bar.[335] Although CTTB, MTTB, and ITTB possessed both triptycene and TB, the polymers still

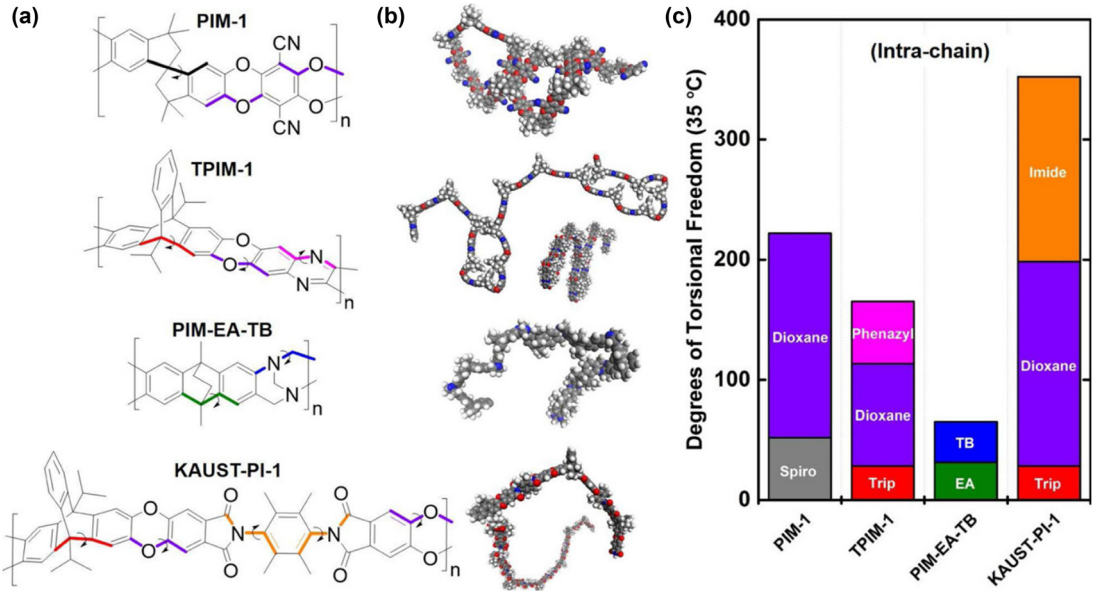

Fig. 28 (a) Chemical structures, (b) energy-minimized chain conformations developed from Materials Studio, Accelrys, 7.0, and (c) degrees of torsional freedom at 35 °C in one repeat unit. Adapted with permission from ref. 28 (Copyright American Chemical Society, 2015).

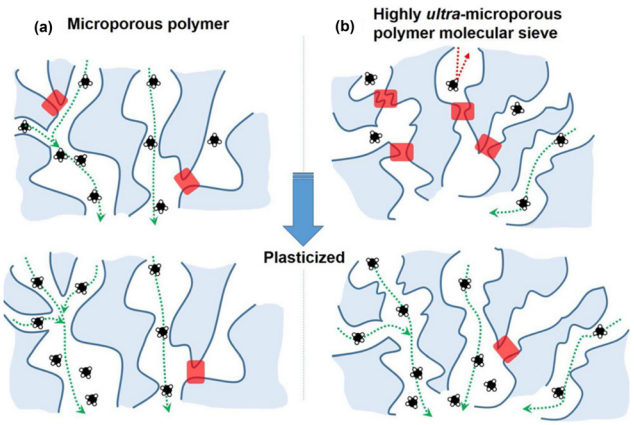

Fig. 29 A schematic detailing a higher sensitivity of high ultra-microporous polymers to CO_2-induced plasticization. Adapted with permission from ref. 28 (Copyright American Chemical Society, 2015).

experienced CO_2-induced plasticization,[335] solidifying the hypothesis that intrachain rigidity alone may not suppress plasticization.

Ma *et al.* generated a fluorine-functionalized triptycene-containing TB-based polymer known as DFTTB (Fig. 26).[336] When increasing the upstream pure-gas CO_2 pressure, the CO_2 permeability of DFTTB decreased around 4% from 2 to 5 bar.[336] However, from 5 to 15 bar, DFTTB experienced an approximately 30% increase in CO_2 permeability.[336] When mixed-gas tests (50 : 50 CO_2/CH_4 mixture) were conducted from a feed pressure of 2 to 20 bar on DFTTB, the CO_2/CH_4 selectivity decreased from 28.1 to 18.9, and the CH_4 permeability increased from 82 barrer to 119 barrer, once again indicating CO_2-induced plasticization in structures with intrachain rigidity.[336] Still, at a CO_2 partial pressure of 10 bar, DFTTB exhibited a CO_2/CH_4 selectivity of 18.9 and a CO_2 permeability of 2253 barrer, which lies above the 2018 CO_2/CH_4 mixed-gas upper bound[337] and renders DFTTB as a promising candidate for natural gas purification.[336]

The effects of additional chemical moieties on intrachain rigidity and gas transport properties have also been studied. Using superacid-catalyzed hydroxyalkylation Friedel–Crafts polymerization, Cai *et al.* synthesized a series of microporous polymers named SACP-1 (BET surface area = 307 $m^2\ g^{-1}$), SACP-2 (BET surface area = 273 $m^2\ g^{-1}$), and SACP-3 (BET surface area = 568 $m^2\ g^{-1}$) (Fig. 30).[338] When mixed-gas tests (50 : 50 vol% CO_2/CH_4) were performed with total feed pressures ranging from 4 to 40 bar, it was found that while SACP-1 and SACP-2 experienced a 34% and 40% decrease in CO_2/CH_4 selectivity, respectively, SACP-3 experienced only a 29% decrease in CO_2/CH_4 permselectivity.[338] The authors ascribed the superior plasticization resistance of SACP-3 to its increased chain rigidity from the presence of spirobisindane moieties, as well as its micropore architecture, which consists of micropores larger than the kinetic diameter of CH_4.[338] Dilation of these micropores would thus not affect CH_4 permeability as much.[338]

Chen *et al.* studied the plasticization resistance of PIM-PBOI-3 (Fig. 30) before and after thermal annealing at 400 °C.[339] Both the unannealed and thermally-annealed PIM-PBOI-3 exhibited a pure-gas CO_2 plasticization pressure of ~10 bar, but the CO_2/CH_4 selectivity of the annealed PIM-PBOI-3 decreased by only 13.8% from 28.6 at a feed pressure of 1 bar to 24.7 at a feed pressure of 30 bar.[339] In contrast, the CO_2/CH_4 selectivity of the unannealed PIM-PBOI-3 dropped by ~40.9% from 23.2 at a feed pressure of 1 bar to ~13.7 at a feed pressure of 30 bar.[339] The authors attributed the improved plasticization resistance of the thermally-annealed PIM-PBOI-3 to potential crosslinking,[339] which is a plasticization mitigation method that will be discussed in further detail in Section 4.2.2.

The gas transport properties of PIM-ABAs, which contain difluorenylanthracene-based moieties, synthesized by Han

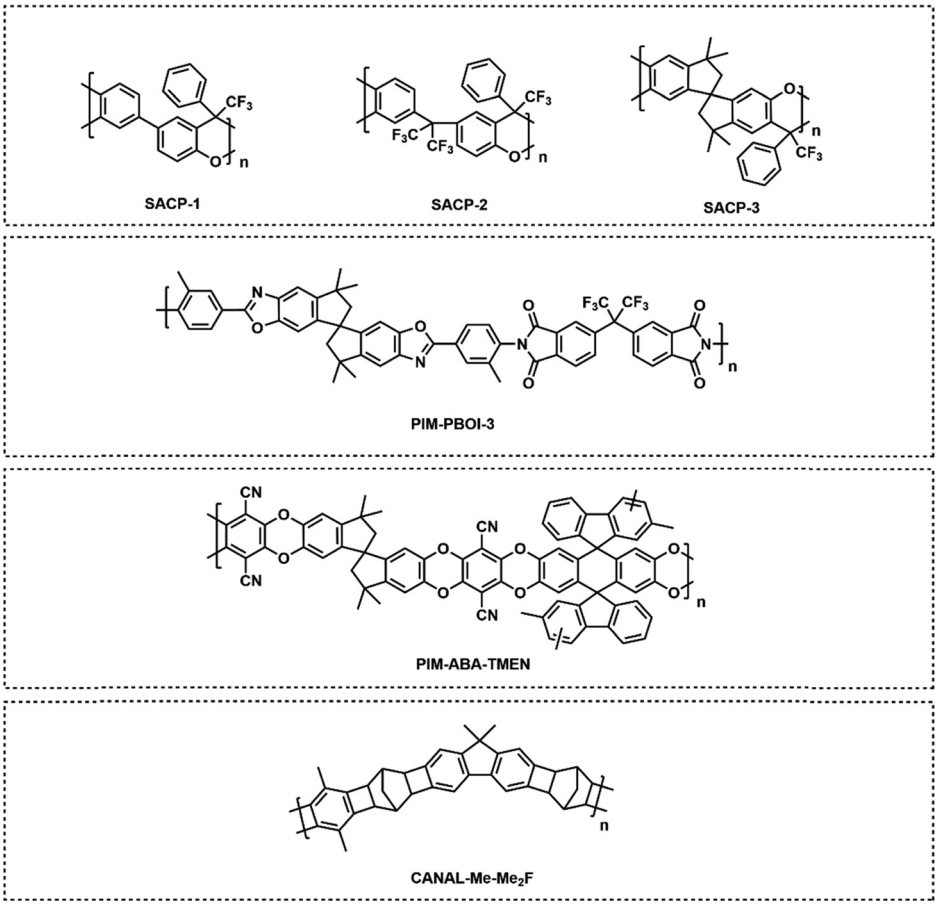

Fig. 30 Chemical structures of polymers of intrinsic microporosity containing other rigidifying backbone moieities for studies that reported pure-gas pressurization studies and/or mixed-gas permeation.[338–341]

et al. were also reported.[340] Mixed-gas (15 : 85 CO_2/N_2) data of PIM-ABA-TMEN (BET surface area = 952 $m^2\ g^{-1}$) (Fig. 30) at a total upstream feed pressure of 2 to 15 bar was collected. The mixed-gas CO_2 permeability of PIM-ABA-TMEN increased very slightly from 9191.50 barrer at a total feed pressure of 2 bar to 9242.50 barrer at a total feed pressure of 15 bar, indicating a less than 1% increase over the pressure range considered.[340] In addition, the mixed-gas CO_2/N_2 selectivity increased slightly from 19.63 to 21.20, representing an 8% increase over the pressure range considered.[340]

Polymers developed *via* catalytic arene–norbornene annulation (CANAL) polymerization have also shown promising plasticization resistance. Mixed-gas permeation for CO_2/CH_4 (50 : 50) of one such polymer developed in 2022, known as CANAL-Me-Me_2F (Fig. 30), was evaluated. It was found that the mixed-gas selectivity remained above 35 even at 14 bar of CO_2 partial pressure, significantly exceeding the 2018 CO_2/CH_4 mixed-gas upper bound. The authors attributed this high performance to the 3D backbone contortions of CANAL polymers contributing to high gas selectivity.[137,341]

4.1.2. Interchain rigidity involving hydrogen bonding groups. The idea that intrachain rigidity alone cannot be used to mitigate plasticization in polymer membranes has prompted researchers to investigate the effects of interchain rigidity on plasticization resistance. The incorporation of polar moieties that can hydrogen bond has shown some success in mitigating the effects of plasticization.[138,342–348] In this section, BET surface areas are reported, where applicable, to further illustrate the effects of hydrogen bonding groups on polymer packing. BET analysis is somewhat variable for microporous polymers, and oftentimes, different groups will report slightly different values for the same polymer composition, which can relate to testing conditions or polymer preparation. In addition, the use of BET surface area to assess the microporosity in polymers has been a subject of controversy.[349] However, in this review, we will indicate BET surface area reported for a specific study, even if those values differ from one paper to another for the same polymer.

Abdulhamid *et al.* demonstrated that a trimethyl-functional polyimide with substituted carboxylic acid (6FDA-TrMCA, BET surface area = 260 $m^2\ g^{-1}$) had higher CO_2/CH_4 selectivity (both in the pure- and equimolar mixed-gas cases) than the unsubstituted 6FDA-TrMPD analog (BET surface area = 450 $m^2\ g^{-1}$). While these polymers have classically been defined as non-porous,[350,351] we choose to include them in this review because of their reported BET surface areas. This unambiguous structure–property study suggests that the presence of –COOH functionality leads to interchain hydrogen bonding and charge transfer complex (CTC)

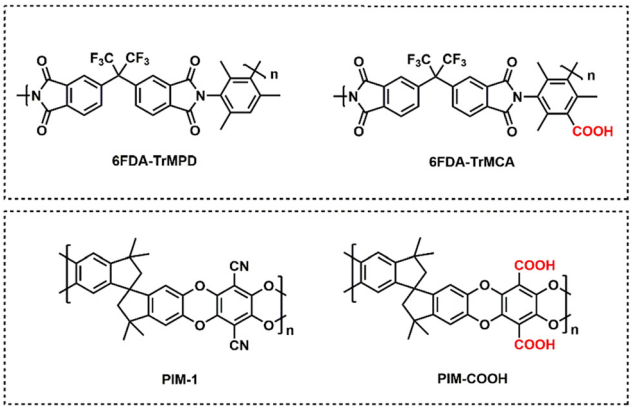

Fig. 31 Chemical structures of polymers of intrinsic microporosity containing carboxylic acid functionality (along with non-functionalized counterparts) that reported pure-gas pressurization studies and/or mixed-gas permeation.[138,342]

formation, two key features that correlate with increased interchain rigidity.[342] Note that TrMPD is also referred to as 2,4-diaminomesitylene (DAM) in the membrane literature.[342,352,353] Both structures, as presented in Fig. 31, have been investigated for plasticization.[342] At ~2 bar CO_2 partial pressure, the mixed-gas selectivity of 6FDA-TrMPD was almost 10% higher than its pure-gas selectivity, while the mixed-gas selectivity of 6FDA-TrMCA was about 7% higher than its pure-gas selectivity.[342] Similarly, at ~15 bar CO_2 partial pressure, the mixed-gas selectivity of 6FDA-TrMPD was about 15% higher than its pure-gas selectivity, while the mixed-gas selectivity of 6FDA-TrMCA was about 2% higher than its pure-gas selectivity.[342] Such effects are typically associated with competitive sorption[354–356] and also suggest plasticization resistance since selectivity was not compromised at higher feed pressures.[342] However, Mizrahi Rodriguez *et al.* found that the pure-gas CO_2 plasticization pressure of PIM-COOH (~5 bar) was lower than that of PIM-1 (~15 bar), despite the former being a carboxylic acid-functionalized version of the latter.[138] The structures of PIM-COOH (BET surface area = 373 m^2 g^{-1}) and PIM-1 (BET surface area = 886 m^2 g^{-1}) are shown in Fig. 31. The authors attributed this unexpected result to a potential disruption of secondary interactions when exposed to CO_2, which subsequently can lead to increased free volume and higher CO_2 diffusion at higher pressures.[138] In addition, mixed-gas (50 : 50 CO_2/CH_4) data was collected for PIM-COOH below and above the pure-gas plasticization pressure of ~5 bar (~1 bar and ~7 bar CO_2 partial pressure).[138] While the mixed-gas CO_2/CH_4 selectivity for PIM-COOH at ~1 bar CO_2 partial pressure was higher than that at ~7 bar CO_2 partial pressure, suggesting plasticization, PIM-COOH still displayed excellent transport properties that lied on the 2018 mixed-gas upper bound.[138,337]

A number of plasticization studies have also been performed on hydroxyl-functionalized PIMs, and these structures are presented in Fig. 32. When comparing the hydroxyl-functionalized TPDA-DAR to its non-functionalized analog (TPDA-*m*PDA), Alaslai *et al.* found that TPDA-DAR exhibited higher CO_2/CH_4 selectivity than TPDA-*m*PDA in both the pure- and mixed-gas (50 : 50 vol% CO_2/CH_4) scenarios up to a CO_2 partial pressure of ~20 bar.[343] For instance, at a CO_2 partial pressure of ~20 bar, both the pure- and mixed-gas selectivity of TPDA-DAR were about 65% higher than that of TPDA-*m*PDA.[343] This finding can be explained from the higher BET surface area found in TPDA-*m*PDA (565 m^2 g^{-1}) *versus* that of TPDA-DAR (308 m^2 g^{-1}), due to the presence of hydrogen bonds in the latter sample that increased CTC formation and tighter chain packing.[343] Both polymers displayed excellent plasticization resistance, as evident from the absence of an increase in either CO_2 or CH_4 permeability up to a CO_2 partial pressure of ~20 bar in both the pure- and mixed-gas cases.[343] Additionally, while the CO_2/CH_4 selectivity of both polymers decreased with increasing CO_2 partial pressure for both pure- and mixed-gas cases, the mixed-gas CO_2/CH_4 selectivity and CO_2 permeability of TPDA-DAR was 38 and 140 barrer, respectively, at a partial CO_2 pressure of ~10 bar. This result lies on the 2018 mixed-gas upper bound[337] and thus indicates promising gas separation properties.[343]

Alaslai *et al.* also compared 6FDA-DAT1-OH with its non-functionalized analog 6FDA-DAT1 (Fig. 32) and found that the former had a pure-gas CO_2 permeability of 70 barrer and a CO_2/CH_4 selectivity of 50, while the latter had a pure-gas CO_2 permeability and a CO_2/CH_4 selectivity of 120 barrer and 38, respectively.[344] The decrease in permeability and increase in selectivity with hydroxyl-functionalization can be attributed to the lower BET surface area of 6FDA-DAT1-OH (160 m^2 g^{-1}) compared to that of 6FDA-DAT1 (320 m^2 g^{-1}), which results from strong CTC formation that could occur because of hydrogen bonding tightening the polymer microstructure.[344] In addition, 6FDA-DAT1-OH did not exhibit a CO_2 plasticization pressure up to 20 bar CO_2 partial pressure in either the pure- or mixed-gas (1 : 1 molar ratio CO_2/CH_4) scenario while maintaining a mixed-gas CO_2 permeability of 50 barrer and a CO_2/CH_4 selectivity of 40 at a CO_2 partial pressure of 10 bar, indicating strong plasticization resistance.[344]

Alghunaimi *et al.* synthesized the hydroxyl-functionalized PIM-polyimide (PIM-PI) TDA1-APAF (BET surface area = 260 m^2 g^{-1}) (Fig. 32), which exhibited a pure-gas CO_2 permeability of 44 barrer and a CO_2/CH_4 selectivity of 55 at a feed pressure of 2 bar.[345] In both the pure- and mixed-gas (1 : 1 CO_2/CH_4 mixture) cases, TDA1-APAF did not show a CO_2 plasticization pressure up to 15 bar CO_2 partial pressure[345] and displayed a mixed-gas CO_2/CH_4 selectivity of ~45 at 15 bar CO_2 partial pressure,[345] which shows promise for plasticization resistance. Similarly, Ma *et al.* demonstrated that both PIM-6FDA-OH (BET surface area = 225 m^2 g^{-1}) and PIM-PMDA-OH (BET surface area = 190 m^2 g^{-1}) (Fig. 32) had high mixed-gas CO_2/CH_4 selectivity (>20) even at a high CO_2 partial pressure of 20 bar for a 1 : 1 molar ratio.[346] More recently, in 2022, Weng *et al.* synthesized HSBI-4-CF_3 (BET surface area = 318 m^2 g^{-1}) and HSBI-3-CF_3 (BET surface area = 287 m^2 g^{-1}) (Fig. 32), two hydroxyl-functionalized PIMs *via* a Friedel–Crafts polycondensation reaction.[357] Both the pure-gas CO_2 and CH_4 permeabilities of HSBI-4-CF_3 and HSBI-3-CF_3 continuously decreased with increasing feed pressure from 2 to 18 bar, indicating strong plasticization resistance that can be attributed to hydrogen bonding between the hydroxyl groups.[357]

Amidoxime functionalization of PIM-1 (listed as AO-PIM-1 (Fig. 33)) has also shown promising plasticization resistance, as

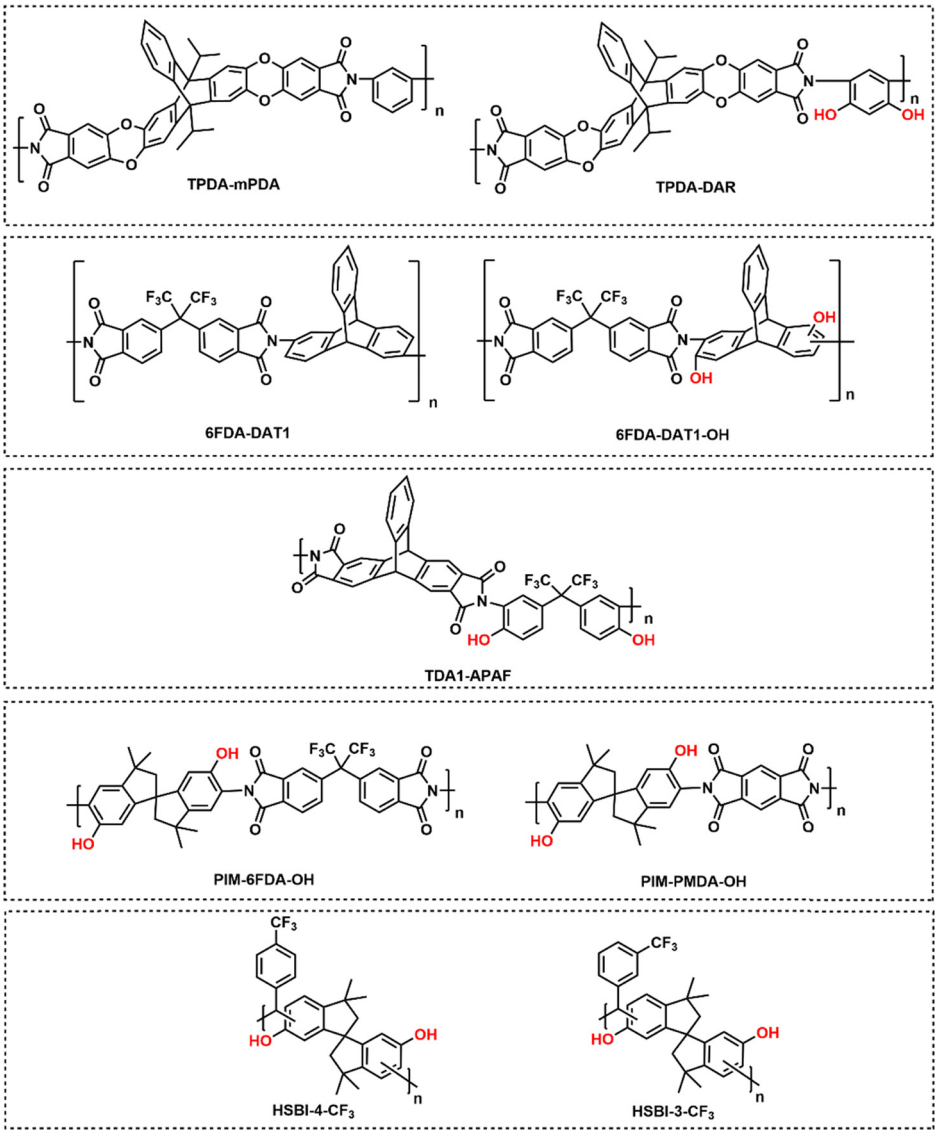

Fig. 32 Chemical structures of polymers of intrinsic microporosity containing hydroxyl functionality (along with non-functionalized counterparts), for studies that reported pure-gas pressurization studies and/or mixed-gas permeation.[343–346,357]

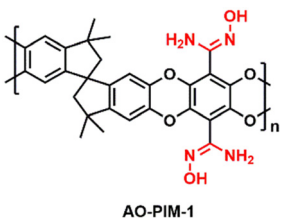

Fig. 33 Chemical structure of AO-PIM-1, a polymer of intrinsic microporosity containing amidoxime functionalization (highlighted in red).[347,348]

it can rigidify the polymer matrix and introduce more microporosity due to intermolecular hydrogen bonding.[347] Swaidan *et al.* found that AO-PIM-1 (BET surface area = 482 $m^2\ g^{-1}$) had a three-fold increase in pure-gas CO_2/CH_4 diffusivity selectivity over PIM-1 (BET surface area = 768 $m^2\ g^{-1}$) with comparable solubility selectivity.[347] In addition, the mixed-gas CO_2/CH_4 (50 : 50 CO_2/CH_4 mixture) selectivity of AO-PIM-1 decreased by about 13% from ~23.7 at a total feed pressure of 4 bar to ~21 at a total feed pressure of 20 bar.[347] For PIM-1, the mixed-gas selectivity decreased by about 60% under similar conditions to ~8 at a total feed pressure of 20 bar due to the significant increase in CH_4 diffusion coefficients from CO_2-induced swelling.[347] These results suggest that amidoxime functionalization can lead to plasticization resistance.[347] AO-PIM-1 was also examined for its efficacy in sour gas separations by Yi *et al.*, and it was found that when the polymer was exposed to a ternary feed mixture of 20% H_2S, 20% CO_2, and 60% CH_4 at 35 °C, the CO_2/CH_4 selectivity was relatively stable up to a total feed pressure of 80 bar, while H_2S/CH_4 selectivity increased from 50 at a total feed pressure of 10 bar to ~70 at a total feed pressure of 80 bar.[348] This suggests some degree of plasticization with H_2S.

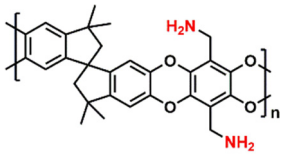

Amine-PIM-1

Fig. 34 Chemical structure of amine-PIM-1, a polymer of intrinsic microporosity containing amine functionalization (highlighted in red).[358]

Satilmis *et al.* synthesized an amine-functionalized version of PIM-1, named amine-PIM-1 (Fig. 34).[358] This structure is often referred to as PIM-NH_2.[38,142] Post-synthetic modification reactions reached 93% conversion from the cyano group in PIM-1 to an amine group. For gas permeation testing, increasing the feed pressure of CO_2 from 0.2 to 1 bar resulted in a decreased permeability from ~1400 to ~800 barrer, while—interestingly—CO_2 diffusivity increased by almost 60%.[358] This unusual transport behavior warrants further investigation to understand the role of amine functionality on CO_2 transport and plasticization resistance in these microporous polymers.

In addition to introducing hydroxyl groups to facilitate CTC formation, thermal annealing has been used to further supplement interchain hydrogen bonding with CTCs, allowing polymer chains to relax into a denser structure.[34,48,159] Swaidan *et al.* thermally annealed PIM-6FDA-OH (Fig. 35) at 250 °C for 24 h, which resulted in enhanced interchain hydrogen bonding with CTCs.[159] In the pure-gas case, no observable C_3H_6 plasticization pressure was found in the thermally-annealed PIM-6FDA-OH sample up to a feed pressure of 5.0 bar, while PIM-6FDA-OH without thermal annealing had a C_3H_6 plasticization pressure of ~3.0 bar.[159] In the mixed-gas case (50 : 50 C_3H_6/C_3H_8), thermally-annealed PIM-6FDA-OH did not exhibit a plasticization pressure up to a C_3H_6 partial feed pressure of 2.5 bar, while PIM-6FDA-OH without thermal annealing showed a C_3H_6 plasticization pressure of ~2.0 bar.[159] In addition, thermal annealing of PIM-6FDA-OH still resulted in a 50% increase in C_3H_6/C_3H_8 selectivity in both pure- and mixed-gas cases.[159] Yi *et al.* also thermally annealed PIM-6FDA-OH using the same procedure, but studied this polymer for sour gas separations.[48] They found that in pure-gas tests, the H_2S plasticization pressure was around 4.5 bar and the CO_2 plasticization pressure was greater than 28 bar for thermally-annealed PIM-6FDA-OH.[48] In addition, in mixed-gas tests (15% H_2S, 15% CO_2, 70% CH_4), thermally-annealed PIM-6FDA-OH maintained an excellent CO_2/CH_4 selectivity (~25) even at a total feed pressure of nearly 50 bar, while H_2S/CH_4 selectivity reached up to 30 at a total pressure of nearly 50 bar.[48]

In a study by Swaidan *et al.*, the effects of thermal annealing at 250 °C on the hydroxyl-functionalized TPDA-APAF and methyl-functionalized TPDA-ATAF (Fig. 35) were investigated.[34] Without thermal annealing, both TPDA-APAF and TPDA-ATAF experienced increases in CO_2 and CH_4 permeability in the mixed-gas (50 : 50 CO_2/CH_4) case, along with observable CO_2 plasticization pressures of 10 bar for both polymers in pure- and mixed-gas cases.[34] However, when the polymers were thermally annealed, CO_2 and CH_4 permeabilities, in both the pure- and mixed-gas cases, were relatively consistent up to a CO_2 partial pressure of 25 bar, with TPDA-APAF exhibiting lower CO_2 permeability but higher CO_2/CH_4 selectivity due to hydroxyl functionality.[34] Examples involving more intensive thermal treatments that lead to changes in chemical structure (such as thermal rearrangement, carbon molecular sieve formation, and crosslinking) will be discussed in Section 4.2.

4.1.3. Interchain rigidity involving other secondary interactions. While hydrogen bonding has shown promise in rigidifying PIM structures to mitigate plasticization, other secondary interactions have been shown to be effective as well. For example, the triptycene moiety is often used to increase intrachain rigidity and

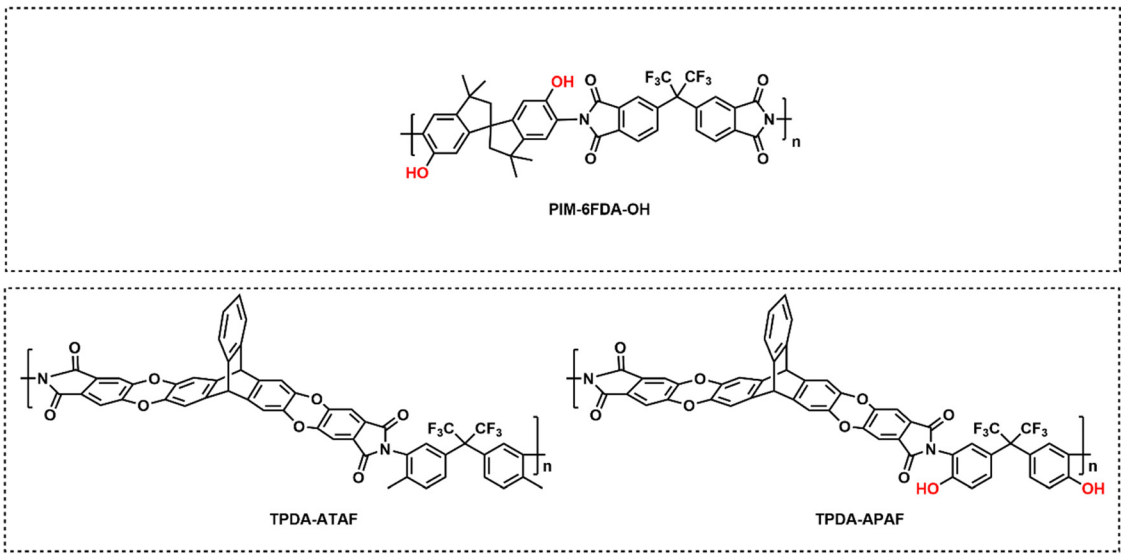

Fig. 35 Chemical structures of thermally-treated polymers of intrinsic microporosity containing hydrogen bonding functionality that reported pure-gas pressurization studies and/or mixed-gas permeation.

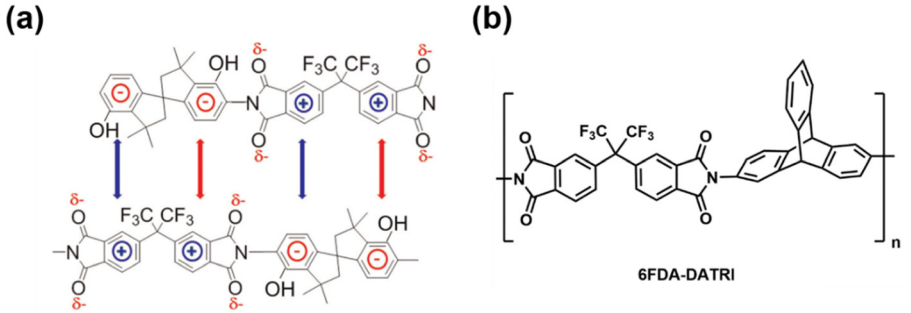

Fig. 36 (a) Example of π–π interactions found in electron-rich aromatic groups of PIM-6FDA-OH due to the formation of charge-transfer complexes (CTCs). Reprinted with permission from ref. 159 (Copyright Elsevier, 2015). (b) Chemical structure of the triptycene-containing 6FDA-DATRI, which is equivalent to 6FDA-DAT1 in Fig. 32.[365]

generate free volume in microporous polymers.[28,29,321,322,359–364] Aromatics can also introduce pseudophysical crosslinking by interlocking and π–π interactions between the π orbitals present in phenyl rings (Fig. 36a).[365–367] In 2011, Cho and Park demonstrated that, with a mixed-gas 50 : 50 CO_2/CH_4 feed at a CO_2 partial pressure of up to ~9 bar, the CO_2/CH_4 selectivity of the triptycene-containing 6FDA-DAT1 (referred to as "6FDA-DATRI" in the manuscript) (Fig. 36b) was maintained, while CO_2/CH_4 selectivity of 6FDA-mPDA and 6FDA-mTMPD decreased with increasing feed pressure.[365] This result suggests that the secondary interactions resulting from the triptycene moiety may help to mitigate plasticization.

In addition to the π–π interactions between phenyl rings in triptycene groups, it has also been found that different substituents that alter packing of polymer chains may likewise lead to plasticization resistance. In 2018, Bezzu *et al.* examined PIM-SBF-1 and PIM-SBF-5 (Fig. 37), which have a hydrogen and *tert*-butyl substituent, respectively.[368] When exposed to a CO_2/CH_4 mixture feed of 35 : 65 vol% from 1 to 6 bar, both the hydrogen-containing PIM-SBF-1 and the *t*-butyl-containing PIM-SBF-5 experienced a CO_2 permeability and CO_2/CH_4 selectivity decrease of about 20% as feed pressure increased.[368] However, when the feed pressure was kept constant at 3 bar, it was found that permeability and selectivity of PIM-SBF-5 was independent of gas composition ranging from 10–50% CO_2.[368] While this study focused on physical aging and found that PIM-SBF-5 had considerably slower aging than PIM-SBF-1 due to the bulkier *tert*-butyl groups, which resulted in more stable polymer chain spacing during aging,[368] these findings suggest that strategies to improve stability of polymer chain spacing could be applied to mitigate plasticization as well.

Introducing fluorine functionality to polymers can enhance interchain interactions,[39,369] which can improve plasticization resistance. A fluorine-functionalized PIM that has been analyzed for gas transport properties is PIM-2 (Fig. 38).[369] In this work, Fuoco *et al.* investigated mixed-gas tests for both CO_2/CH_4 (50 : 50 vol%) and CO_2/N_2 (15 : 85 vol%), and found that when the feed pressure was increased from 1 to 6 bar, both CO_2/CH_4 and CO_2/N_2 mixed-gas selectivities were slightly higher than the respective ideal selectivities, likely due to competitive sorption.[369] In addition, as the feed pressure was increased, mixed-gas CO_2 permeability decreased slightly due to saturation of Langmuir sorption sites, while both CH_4 and N_2 permeability were relatively constant.[369] This finding is indicative of plasticization resistance as CH_4 and N_2 permeability would otherwise increase if the polymer experienced dilation from CO_2-induced plasticization.

In 2019, a class of polymers generated *via* ring opening metathesis polymerization (ROMP) were studied for gas separation applications.[39] These polymers, CF_3-ROMP and OMe-ROMP (Fig. 39), contain rigid side chains and flexible poly(norbornene) backbones.[39] This new structural design may have promoted greater "physical interlocking" and interchain rigidity between side chains, ultimately leading to outstanding plasticization resistance in which no CO_2 plasticization pressure was observed up to a pure-gas CO_2 feed pressure of 51 bar.[39] In addition, preliminary mixed-gas experiments on CF_3-ROMP with a 50 : 50 vol% CO_2/CH_4 mixture at a feed pressure of 2 bar showed that the mixed-gas CO_2/CH_4 selectivity increased by 21.5% compared to the pure-gas case, potentially indicating an increase in solubility selectivity (due to competitive sorption).[39] In follow-up studies that investigated the role of side-chain length on plasticization

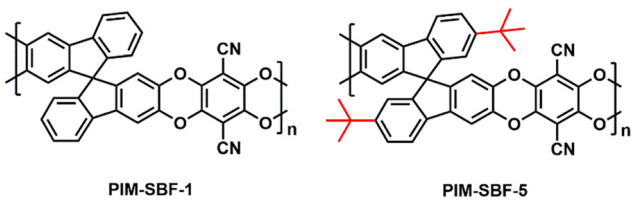

Fig. 37 Chemical structures of PIM-SBF-1 and PIM-SBF-5.[368] The *t*-butyl group in PIM-SBF-5 is highlighted in red.

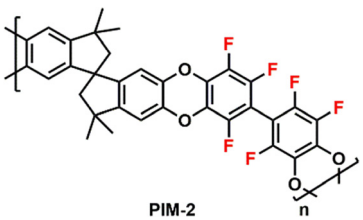

Fig. 38 Chemical structure of PIM-2.[369] Fluorines are highlighted in red.

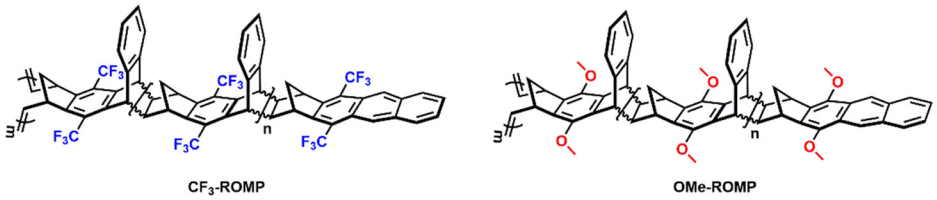

Fig. 39 Chemical structures of CF_3-ROMP and OMe-ROMP.[39] The CF_3 functional group is highlighted in blue, while the OMe functional group is highlighted in red.

resistance for OMe-ROMP, it was found that increasing side-chain length led to increased plasticization resistance. This was attributed to greater interchain rigidity from longer side chains.[370,371]

4.2. Post-synthetic packing structure modification

The following section addresses strategies related to post-synthetic packing structure modification (PPSM) to improve plasticization resistance. This section focuses on methods targeted towards altering the solid-state packing structure as opposed to the chemical structure described in detail in Section 4.1. PPSM strategies include structural rearrangement *via* thermal or UV methods as well as thermal and chemical crosslinking. Frequently, these strategies produce insoluble materials.

4.2.1. Structural transformation

4.2.1.1. Thermally rearranged polymers. The solid-state packing structure of certain polymers can be altered through a so-called thermal rearrangement reaction of a pre-cast film. As an aside, these polymers are more technically described as undergoing decarboxylation reactions since they do not follow classic rearrangement reactions found in organic chemistry. Nevertheless, thermally rearranged (TR) polymers have a corresponding conformational change to the angles of backbone connectivity from precursor to final form, and hence, they assume the descriptor of "rearrangement" to emphasize this structural change. First detailed by Park *et al.*, thermal rearrangement occurs when a polymer containing an *ortho*-functional hydroxy-imide is heated to approximately 400 °C. At this elevated temperature, the hydroxyl group reacts with the imide to form a benzoxazole *via* decarboxylation, causing a shift in the pore size distribution and generally improving transport properties.[311] A generalized reaction scheme is shown in Fig. 23. Originally demonstrated using polyimide homopolymers,[311] this strategy has been applied by a number of researchers for PIM-PI structures, shown below in Fig. 40.[372–377] The rearranged polymers containing benzoxazole groups have a more rigid and potentially crosslinked backbone structure compared to their polyimide precursor, indicated by the increase in glass transition temperature.[378]

Investigation of plasticization resistance for TR PIMs was first reported by Swaidan *et al.*, where they investigated the mixed-gas separation of CO_2/CH_4 and C_3H_6/C_3H_8 mixtures for TR polybenzoxazole (PBO) PIM-6FDA-OH (Fig. 40).[372,373] For a 50 : 50 CO_2/CH_4 mixture ranging from 4 to 20 bar total pressure, the base PIM-6FDA-OH polymer showed a decrease in selectivity from 34 to 22,[346] while the TR PBO displayed better plasticization resistance, showing a small decrease in selectivity from 18 to 15.[372] For a 50 : 50 C_3H_6/C_3H_8 mixture at 2 bar total pressure, the TR PBO showed a decrease from pure-gas selectivity of 15 to a mixed-gas selectivity of 11. However, in this case, the mixed-gas selectivity was stable with increasing feed pressure up to 5 bar, indicative of plasticization resistance.[373] Other researchers have investigated the plasticization benefits of the TR technique on other homopolymer backbones. Yerzhankyzy *et al.* reported the transport behavior of TR-6FDA-DAT1-OH (Fig. 40) for a 2 bar total pressure feed of 50 : 50 C_3H_6/C_3H_8, where the pure-gas to mixed-gas selectivity of a 28 day aged film decreased from 16 to 8, indicating significant effects of plasticization.[374] In contrast, Luo *et al.* reported no discernable plasticization pressure up to 15 bar CO_2 for TPHI-TR (Fig. 40).[375]

A variety of copolymer structures have been modified *via* the TR method to combine the transport and plasticization-resistance benefits of multiple structural groups. For example, Luo *et al.* synthesized TPBO, a copolymer based off of their previously reported TPHI structure, varying the relative amounts of each component (Fig. 40).[375,376] All copolymer films showed no CO_2 plasticization pressure up to 10 bar. However, the mixed-gas performance for only the homopolymer, possessing the same structure as TPHI-TR (Fig. 40), was reported. For 20 : 80 and 50 : 50 CO_2/CH_4 mixtures, the TPBO homopolymer showed decreasing selectivity from 68 to 59 and 63 to 55, respectively, with increasing CO_2 partial pressure from 1.5 to 3 bar for the 20 : 80 mixture and from 4 to 6.7 bar for the 50 : 50 mixture. The decrease in selectivity was driven by increased CH_4 permeability from 5.3 to 6.0 with respect to CO_2 partial pressure. The magnitude of these selectivities compare favorably against the stable CO_2/CH_4 pure-gas selectivity of 56 for pressures up to 10 bar.[376] More recently, Huang *et al.* developed a series of thermally rearranged pentiptyciene-based polybenzoxazoles (PPBO) polymers from a poly(*ortho*-hydroxyl imide) (PPHI) precursor.[379] PPBO films showed no plasticization pressure up to 16 bar in pure-gas permeation tests. The highest performing film (*i.e.*, a polymer treated using a heating rate of 50 °C min^{-1} for the intermediate heating step at 300 °C) showed no plasticization up to 6.6 bar in binary CO_2/CH_4 mixed-gas tests. Several variations of TR polymers with the Tröger's base structural group were recently reported by Hu *et al.*, whereby the 6F6FTB, 6FHABTB, and 6FTMTB copolymers were synthesized with varying amounts of the TR and Tröger's base repeat units (Fig. 40).[377] The mixed-gas behavior was investigated for the 6F6FTB-0.3 (n = 0.3) copolymer treated at 400 °C, 425 °C, and 450 °C for a 50 : 50 CO_2/CH_4 mixture for CO_2 partial pressures from 2 to 15 bar. The plasticization behavior for the three treatments were

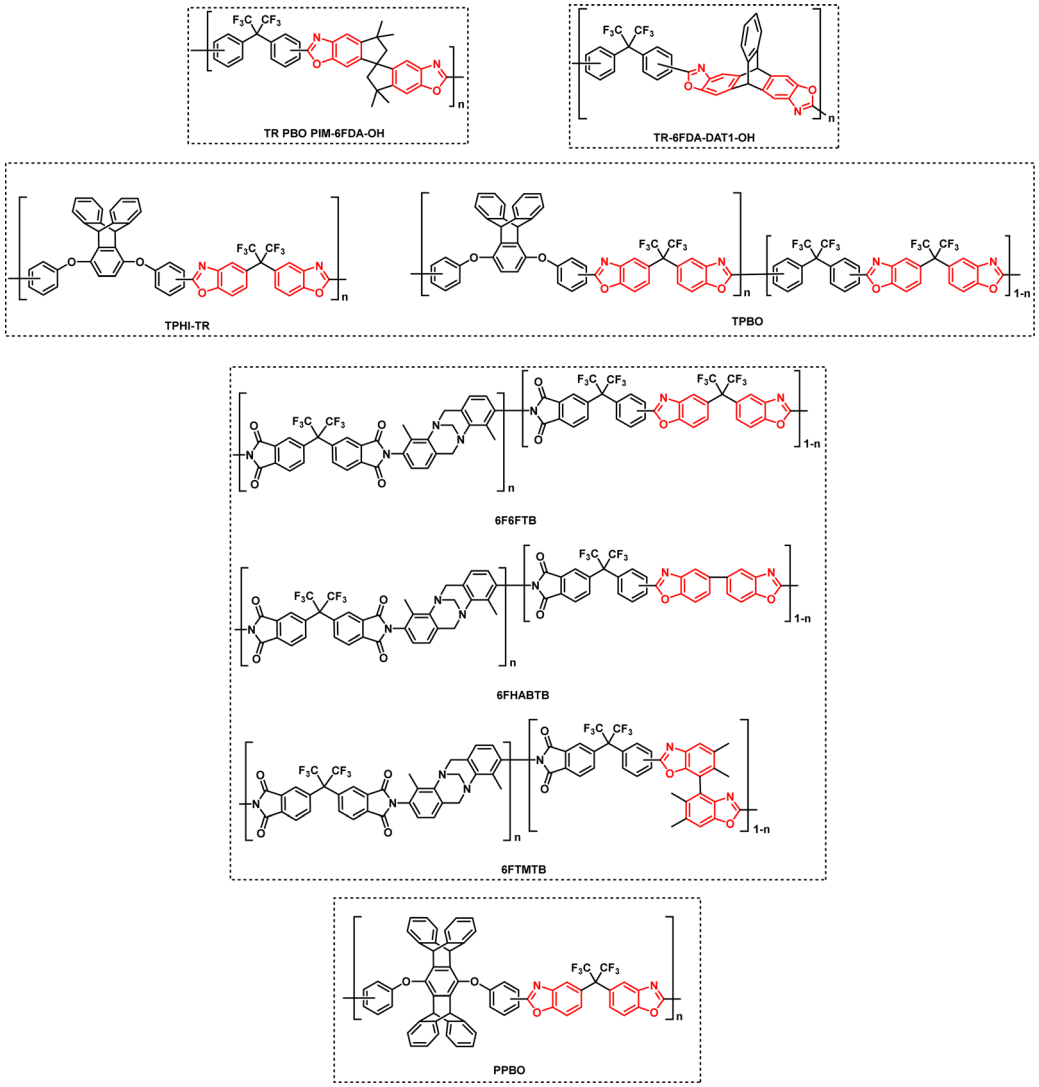

Fig. 40 Chemical structures of thermally rearranged polymers of intrinsic microporosity from studies that reported pure-gas pressurization studies or mixed-gas permeation. The benzoxazole functionality is highlighted in red.[372–377,379]

relatively similar, where the selectivity decreased as a function of increasing CO_2 partial pressure. More specifically, the selectivity decreased from 54 to 26, 40 to 25, and 30 to 20 for the 400 °C, 425 °C, and 450 °C treatments, respectively, showing a smaller percentage decrease in selectivity and improved plasticization resistance with increasing treatment temperature.[377]

4.2.1.2. Carbon molecular sieves. In addition to thermal rearrangement, higher temperature pyrolysis reactions can be used to create carbon molecular sieve (CMS) materials.[380] After pyrolysis in a controlled atmosphere at temperatures typically ranging from 500–800 °C, polymer precursors transform into chains of fused aromatic rings, significantly increasing both intrachain and interchain rigidity and resulting in improved plasticization resistance.[381] While there are a large number of studies regarding the transport behavior of CMS membranes derived from polyimides,[381–383] this section focuses explicitly on CMS membranes derived from microporous polymers.

Along with TR PBO and PIM-6FDA-OH discussed earlier, Swaidan *et al.* also investigated the formation of CMS membranes from PIM-6FDA-OH.[372] For 50 : 50 CO_2/CH_4 mixtures ranging from 4 to 30 bar total pressure, the CMS membranes formed from 600 °C and 630 °C cures showed roughly the same drop in selectivity from 40 to 20, while the CMS membrane formed from an 800 °C cure showed a larger drop in selectivity from 80 to 50 compared to the base PIM-6FDA-OH polymer.[346,372] While the significant decrease in selectivity with pressure is indicative of morphological changes, the mixed-gas selectivity values are very high for the tested pressures and may be suitable for natural gas sweetening applications. Separation of equimolar C_2H_4/C_2H_6 mixtures for PIM-6FDA-OH CMS membrane treated at 800 °C was also tested by Salinas *et al.*, where a decrease in selectivity from 14 to 8 was observed with increasing total feed pressure from 4 to 20 bar.[384] The decrease in selectivity was attributed to an increase in the C_2H_6 permeability originating from physical changes to the CMS structure.

Salinas *et al.* also investigated the mixed-gas C_2H_4/C_2H_6 transport performance for a CMS formed from PIM-6FDA.[385] The PIM-6FDA CMS membrane treated at 800 °C showed a smaller decrease in selectivity compared to PIM-6FDA-OH CMS, decreasing from 17.9 to 15.6 for an equimolar C_2H_4/C_2H_6 mixture with increasing total feed pressure from 4 to 20 bar. The improved stability was attributed to its tighter packed CMS structure compared to its PIM-6FDA-OH counterpart, as suggested by the XRD and Raman spectra. The authors note that the presence of hydroxyl functional groups appeared to negatively affect performance and hypothesized that "it is likely that the additional larger pores created during PBO transformation for PIM-6FDA-OH precursor CMS membranes during the pyrolysis process undermine or slow down the formation of more tightly sintered CMS structure".[385] Recently, thin-film composite CMS membranes were fabricated based on PIM-6FDA-OH[386] and had CO_2/CH_4 selectivities of 43. The authors found that the 3 μm and 100 nm films had accelerated microstructure collapse indicative of physical aging. In another study, Pinnau and colleagues prepared CMS membranes through the pyrolysis of a CANAL-Tröger's base ladder polymer of intrinsic microporosity precursor (CANAL-TB-1).[387] The membranes showed pure-gas selectivities of 39, 1952, and >8200 for H_2/CO_2, H_2/N_2, and H_2/CH_4 and mixed-gas selectivities of 174 for H_2/CO_2 at a 10 bar total feed pressure with a H_2 permeability of 8.2 barrer.

4.2.1.3. Polymers with UV transformations. Another method that has been considered to induce transformation of the polymer backbone is UV treatment, primarily focusing on PIM-1. Li *et al.* investigated the effect of UV irradiation on PIM-1 through exposure of dense membranes to a 254 nm wavelength lamp for periods ranging from 10 min to 4 h.[388] As shown in Fig. 41, the authors proposed a 1,2-migration reaction mechanism involving the destruction of the spirocenter catalyzed by radicals generated by UV exposure. The destruction of the spirocenter was confirmed through WAXS and PALS, where the elimination of the peak corresponding to the largest *d*-spacing in PIM-1 and a decrease in the average free volume radius supported the hypothesized mechanism. The authors tested the UV-rearranged PIM-1 polymer for a number of gas mixtures, including ternary mixtures with H_2S and water.[388,389] Comparing a binary mixed-gas feed of 50 : 50 CO_2/CH_4 to a ternary feed of 50 : 49.95 : 0.05 $CO_2/CH_4/H_2S$ at ~7 bar total pressure, the CO_2/CH_4 selectivity dropped from 25.4 to 9.1 for the 20 min treated sample, demonstrating the strong effect of H_2S as a plasticizing gas.[388] A similar test was conducted on a 4 h UV treated membrane with increasing water concentration in a 50 : 50 balance H_2/CO_2 feed at 2 bar total pressure. As the water concentration in the feed increased from 0 to 15.8 mol%, the selectivity dropped from 10.5 to 6.9, which the authors attributed to both water vapor induced plasticization and competitive sorption from water vapor and CO_2 that would decrease H_2 permeability.[389]

Song *et al.* also investigated the effect of UV irradiation on PIM-1 membranes through exposure to a 254 nm wavelength lamp for a period of 5 to 60 minutes.[390] Interestingly, a photo-oxidation mechanism was proposed, counter to the 1,2-migration reaction mechanism previously discussed. Specifically, Song proposed an oxidative chain scission mechanism in

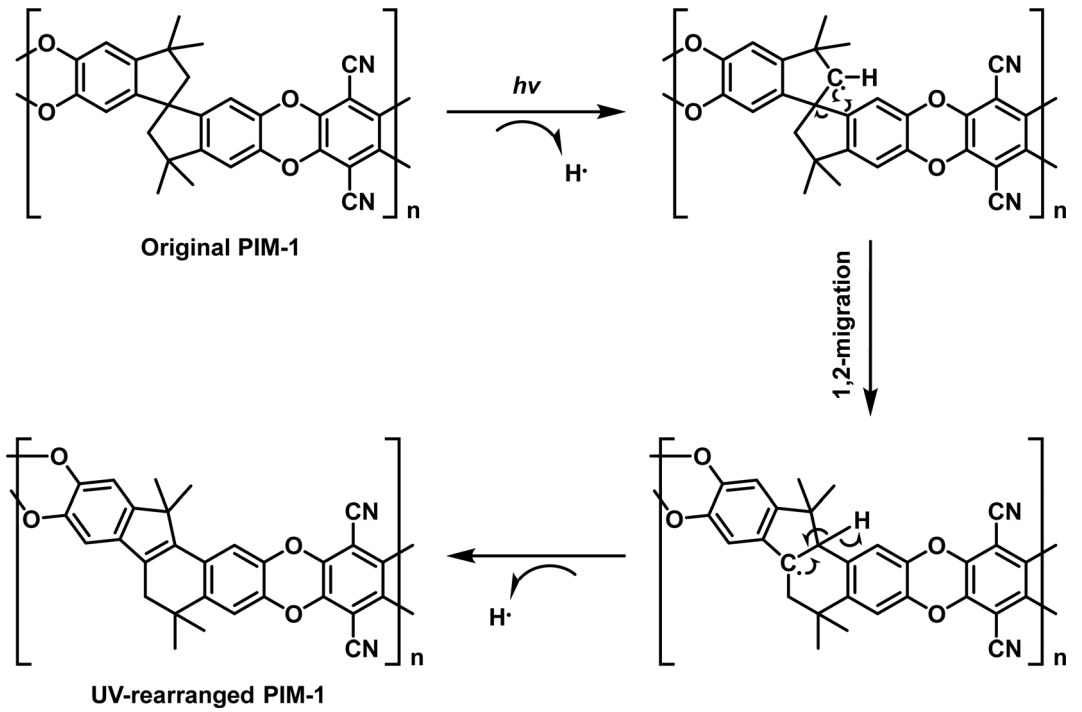

Fig. 41 Proposed 1,2-migration mechanism for UV-exposed PIM-1 proposed by Li *et al.*, resulting in the elimination of the spirocenter. Adapted with permission from ref. 388 (Copyright Wiley-VCH, 2012).

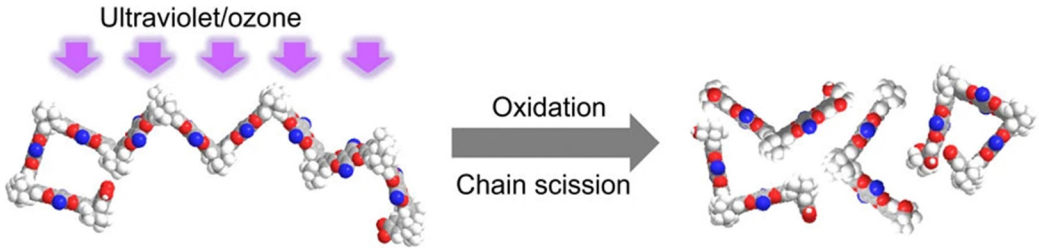

Fig. 42 Proposed chain scission mechanism for UV-exposed PIM-1 in the presence of oxygen, resulting in smaller, fragmented chains. These fragmented chains are hypothesized to pack closer together and effectively form a selective layer at the exposed surface of the film. Adapted with permission from ref. 390 (Copyright Springer Nature, 2013).

which the UV radiation generates singlet oxygen and ozone from atmospheric O_2, which then attack the polymer chains at the surface (Fig. 42). This hypothesis was supported by the presence of peaks corresponding to carbonyl and hydroxyl groups observed *via* FTIR for the UV-treated samples. The fragmented chains can pack more efficiently and reduce porosity, as explored *via* molecular dynamics simulations for PIM-1 and the fragmented polymer. The tighter packing of chains at the surface effectively formed a thin selective layer at the exposed surface, similar to an asymmetric membrane, resulting in decreased pure-gas CO_2 permeability and increased CO_2/CH_4 ideal selectivity as a function of UV exposure time. When tested in a 50 : 50 CO_2/CH_4 mixture ranging from 4 to 12.5 bar CO_2 partial pressure, UV-treated membranes displayed an almost identical percentage loss in selectivity from 23 to 12 (48%) to that of the PIM-1 control, which decreased from 13 to 7 (46%). These films were also tested using a 50 : 50 CO_2/N_2 gas mixture under the same partial pressure conditions, showing decreased selectivity with respect to CO_2 partial pressure from 32 to 20 for the UV-treated samples and from 25 to 17 for PIM-1.[390]

4.2.2. Crosslinking

4.2.2.1. Thermal crosslinking. Thermal crosslinking is a common method to mitigate the effects of plasticization by reducing interchain mobility. In terms of microporous polymers, the PIM subclass has been investigated rather extensively. Du *et al.* thermally treated carboxylic acid-functionalized PIMs (C-PIMs).[391] In their study, the authors prepared C-PIM through a post-synthetic base-catalyzed hydrolysis reaction to convert a percentage of the nitrile groups in PIM-1 to carboxylic acid.[391] They hypothesized a thermally-induced decarboxylation reaction could produce a stable phenyl radical site that would crosslink with other sites across chains, as shown in Fig. 43, resulting in crosslinked decarboxylated PIMs (DC-PIMs). High pressure pure-gas CO_2 tests revealed DC-PIM films formed from C-PIM films with higher degrees of conversion did not display a plasticization pressure up to ~56 bar CO_2. Additionally, mixed-gas tests for 90 : 10 CO_2/N_2 showed a smaller decrease in the relative mixed-gas CO_2/N_2 selectivity with respect to CO_2 partial pressure for all DC-PIMs compared to PIM-1.[391]

Li *et al.* investigated the thermal crosslinking of pristine PIM-1, where a 300 °C treatment of dense PIM-1 membranes under vacuum was proposed to cause the native nitrile groups to form stable, bulky triazine rings connecting separate chains, as shown in Fig. 44.[392] The crosslinked polymers showed excellent mixed-gas selectivity of 54 for a 50 : 50 CO_2/CH_4 mixture at ~7 bar and a mixed-gas selectivity of 38.9 for a 50 : 50 CO_2/N_2 mixture after crosslinking.[392]

Song *et al.* reported a different method for crosslinking PIM-1 *via* controlled thermal oxidation, where dense PIM-1 films were heated to 385 °C under a controlled atmosphere containing 0 to 200 ppm O_2.[393] The authors hypothesize that the high temperature treatment will cause oxidative crosslinking of polymer chains similar to vulcanization (Fig. 45), thus resulting in a crosslinked network. The mixed-gas separation performance for the thermally-oxidated films (TOX-PIM-1) was tested using 50 : 50 mixtures of CO_2/CH_4 and CO_2/N_2 for a CO_2 partial pressure range of 2 to 15 bar. For CO_2/CH_4, TOX-PIM-1 showed a decrease in mixed-gas selectivity from 60 to 20 while PIM-1 decreased from 12 to 6. For CO_2/N_2 mixtures, TOX-PIM-1 selectivity showed a decrease from 45 to 23 and PIM-1 selectivity decreased from 20 to 14 for the same CO_2 partial pressure range. Additionally, a CO_2 plasticization pressure was not observed for the TOX-PIM-1 films.[393]

Chen *et al.* reported a method for crosslinking of PIM-BM-*x*, a partially bromomethylated structure using a methyl-substituted PIM-1 (PIM-M, see Fig. 46) as the precursor.[394] After thermal treatment at temperatures ranging from 200 °C to 300 °C, the bromine groups are hypothesized to react with the aromatic hydrogens, showing a loss of HBr and forming a crosslinked network, as shown in Fig. 46. High pressure pure-gas CO_2 permeability tests indicated improved plasticization resistance for longer treatment times and at higher temperatures, where pristine PIM-BM-70 and PIM-BM-70 treated at 200 °C for 10 h samples displayed a plasticization pressure less than 3.4 bar while the samples treated for 250 °C for 10 h and 300 °C for 5 h did not display a plasticization pressure up to ~35 bar.[394]

Zhang *et al.* reported a thermal crosslinking method for a carboxylate PIM (CA-PIM) using a decarboxylation method similar to Du *et al.*[391,395] The authors synthesized copolymers consisting of 2,6-diaminotriptycene (DAT) and 2,6-diaminotriptycene-14-carboxylic acid (DATCA) using 9 : 1 and 8 : 2 monomer ratios. When heated to at least 325 °C, it was proposed that the carboxylic acid groups on adjacent chains reacted and formed radicals, resulting in a direct crosslinking of the triptycene groups across chains, as shown in Fig. 47. High pressure pure-gas CO_2 permeation tests on both copolymer compositions showed similar results, where a plasticization pressure of 7 bar

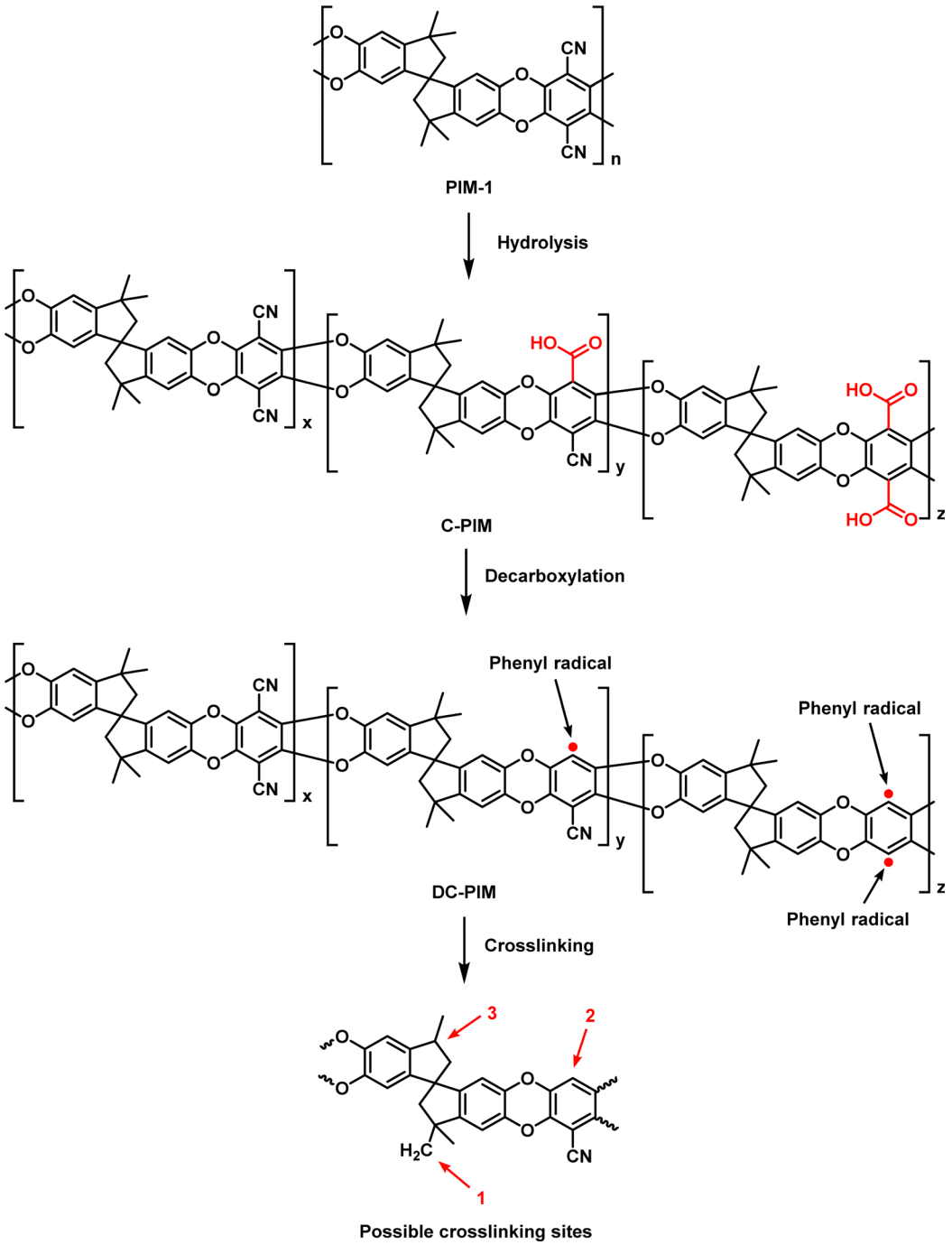

Fig. 43 Synthesis route from PIM-1 to DC-PIM and proposed crosslinking sites. Adapted with permission from ref. 391 (Copyright National Research Council of Canada, 2012).

and 17 bar was observed for copolymers heated to 300 °C and 325 °C, respectively, while a plasticization pressure was not observed up to 30 bar for the copolymer heated to 350 °C, suggesting that the crosslinking reaction had reached completion according to the authors.[395]

4.2.2.2. Chemical crosslinking. As opposed to thermal methods, chemical crosslinking takes advantage of multi-functional compounds to create crosslinked networks. One such method was reported by Du *et al.*, where 4-azido phenyl sulfone and 2,6-bis(4-azidobenzylidene)-4-methylcyclohexanone (Fig. 48) were used as chemical crosslinkers for PIM-1 *via* a nitrene reaction with the nitrile groups.[396] The crosslinked polymer films were tested for 50 : 50 and 80 : 20 CO_2/CH_4 feeds ranging from ~3 to ~17 bar total pressure. As pressure increased, the 4-azido phenyl sulfone-crosslinked film showed a decrease in selectivity from 19 to 17 and the 2,6-bis(4-azidobenzylidene)-4-methylcyclohexanone-crosslinked film showed a decrease in selectivity from 23 to 21.

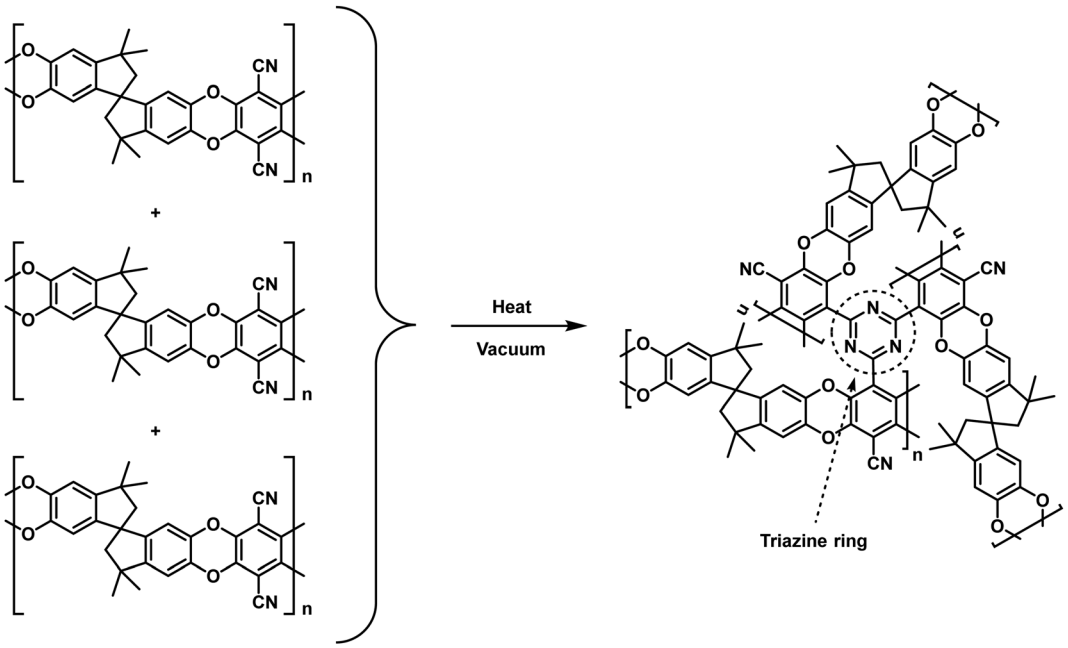

Fig. 44 Proposed crosslinking mechanism for three PIM-1 chains to form a triazine ring. Adapted with permission from ref. 392 (Copyright American Chemical Society, 2012).

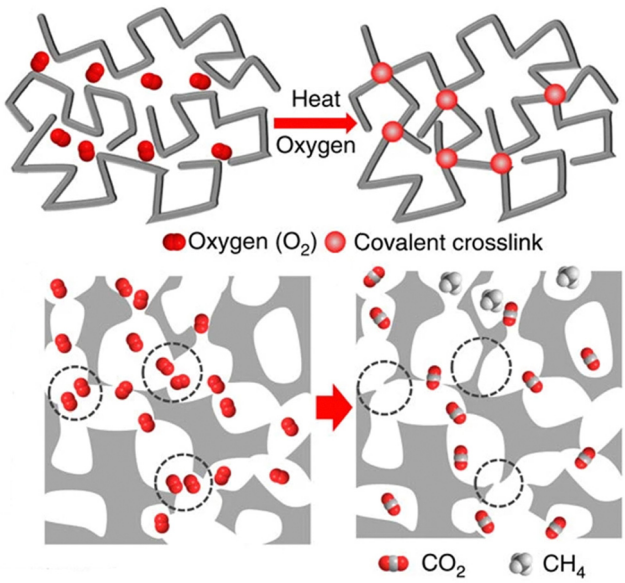

Fig. 45 Schematic for thermally-oxidated crosslinking of PIM-1 to form covalent crosslinks, effectively blocking off diffusion pathways. Adapted with permission from ref. 393 (Copyright Springer Nature, 2014).

Both films compared favorably to PIM-1, which showed a decrease in selectivity from 14 to 11. A plasticization pressure was not observed up to ~20 bar for pure-gas CO_2 tests for the crosslinked films.[396] A similar crosslinking reaction was investigated by Khan *et al.*, using a PEG-biazide (Fig. 48) to crosslink PIM-1.[397] In this case, high pressure pure-gas CO_2 tests up to ~30 bar did not show a plasticization pressure for samples with as little as 5 wt% of crosslinker.

Chemical crosslinking for polymers containing triptycene and Tröger's base structural units was investigated by Zhang *et al.*, where a triptycene-based diamine was functionalized with a carboxylic acid group and copolymerized with the triptycene-based diamine precursor to form a Tröger's base copolymer, CoPIM-TB.[398] The copolymers were crosslinked using a glycidol agent to react with carboxylic acid groups on different chains (Fig. 49). The crosslinked films were tested in a 50 : 50 CO_2/CH_4 mixture from ~2 to ~41 bar total pressure, showing a decrease in selectivity from 12 to 8 over this pressure range, primarily due to decreasing CO_2 permeability and stable CH_4 permeability. A plasticization pressure was not observed for pure-gas and mixed-gas CO_2 pressures up to ~20 bar.[398]

Liao *et al.* investigated the incorporation of divalent metal ions, such as Zn^{2+}, Mg^{2+}, and Ag^{+}, in hydrolyzed PIM-1 (C-PIM).[156] The authors hypothesized that the carboxylic acid groups of C-PIM would deprotonate in the presence of metal ions, after which the ions would then act as crosslinkers between polymer chains. The metal-crosslinked PIMs were tested for a 50 : 50 mixture of C_3H_6/C_3H_8 at total feed pressures up to ~9 bar. All three crosslinked systems showed improved plasticization resistance compared to PIM-1, with the Zn^{2+} crosslinked polymer showing the highest permeability due to its larger ionic radius, which results in higher internal free volume. Conversely, the Mg^{2+} crosslinked polymer showed the highest selectivity at high pressures, which the authors attributed to π-orbital interactions with C_3H_6.[156]

4.3. Composites, blends, and copolymers

The following section focuses on the use of composites, blends, and copolymers to improve plasticization resistance. The majority of strategies already discussed involve only one polymer backbone and its potential treatments and modifications.

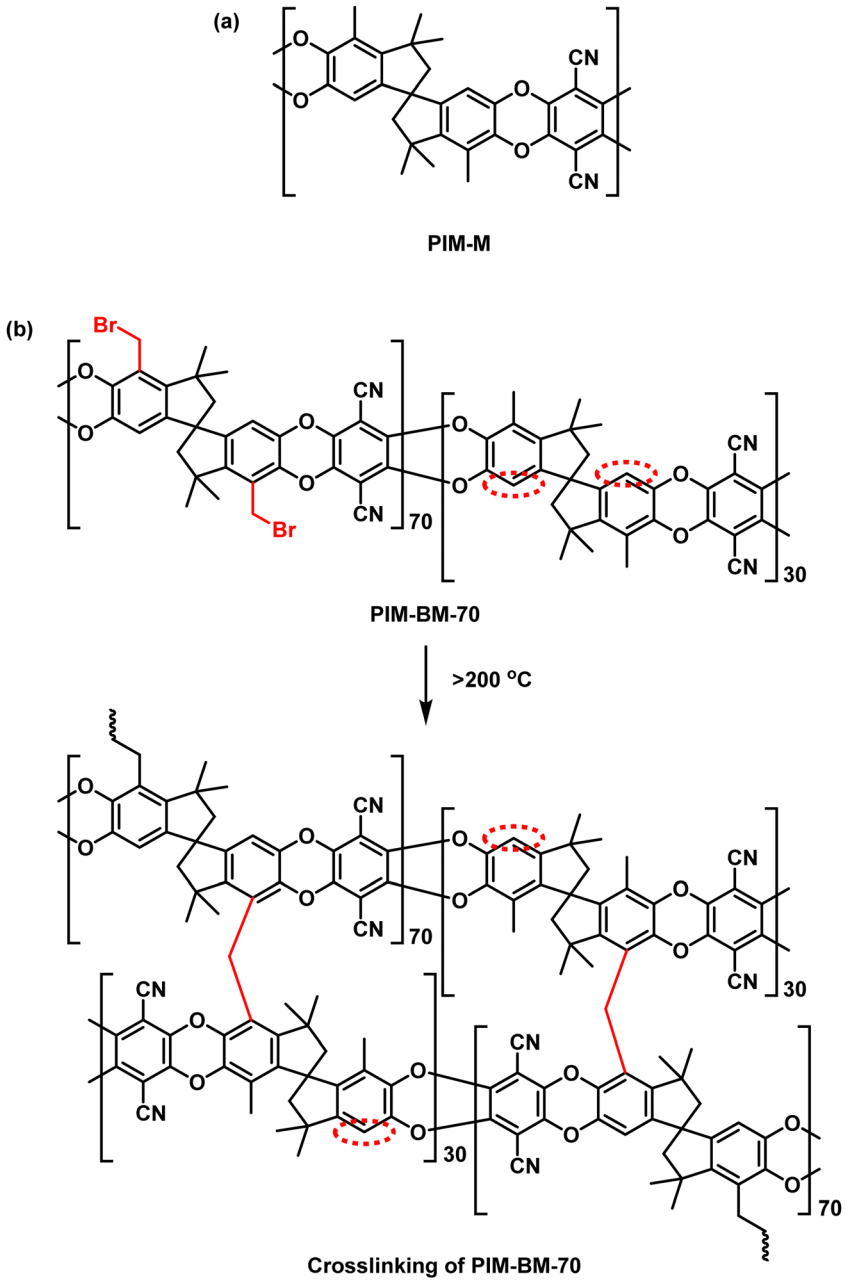

Fig. 46 (a) Structure for PIM-M. (b) Proposed crosslinking mechanism for heat-treated PIM-BM-70. Adapted with permission from ref. 394 (Copyright American Chemical Society, 2020).

Here, we expand the discussion to include systems with up to three unique components and their interactions that affect transport and plasticization resistance.

4.3.1. Polymer systems

4.3.1.1. Copolymers. Copolymerization has been previously investigated for conventional glassy polymers with the goal of combining the beneficial aspects of each component.[399–401] This section only focuses on reports detailing the plasticization resistance of copolymers that incorporate microporous structural units. It should be noted that many polymers discussed earlier in this section are copolymers as well (*e.g.*, 6F6FTB, CoPIM-TB, *etc.*) but are omitted from this section, since we intend to highlight approaches that are specifically designed to incorporate microporous subunits.

Wu *et al.* reported the copolymerization of 4-*tert*-butylcalix-[4]arene (CA) with the typical PIM-1 monomers to form a modified PIM-1 backbone structure, shown in Fig. 50.[402] The addition of small amounts of the CA unit was intended to force frustrated packing through both forced contortion and increased rigidity. The mixed-gas selectivity for a 50 : 50 CO_2/CH_4 mixture at ~7 bar total pressure was consistently lower than the pure-gas selectivity for each loading, with the 1.0% loading showing the best performance and plasticization resistance.[402]

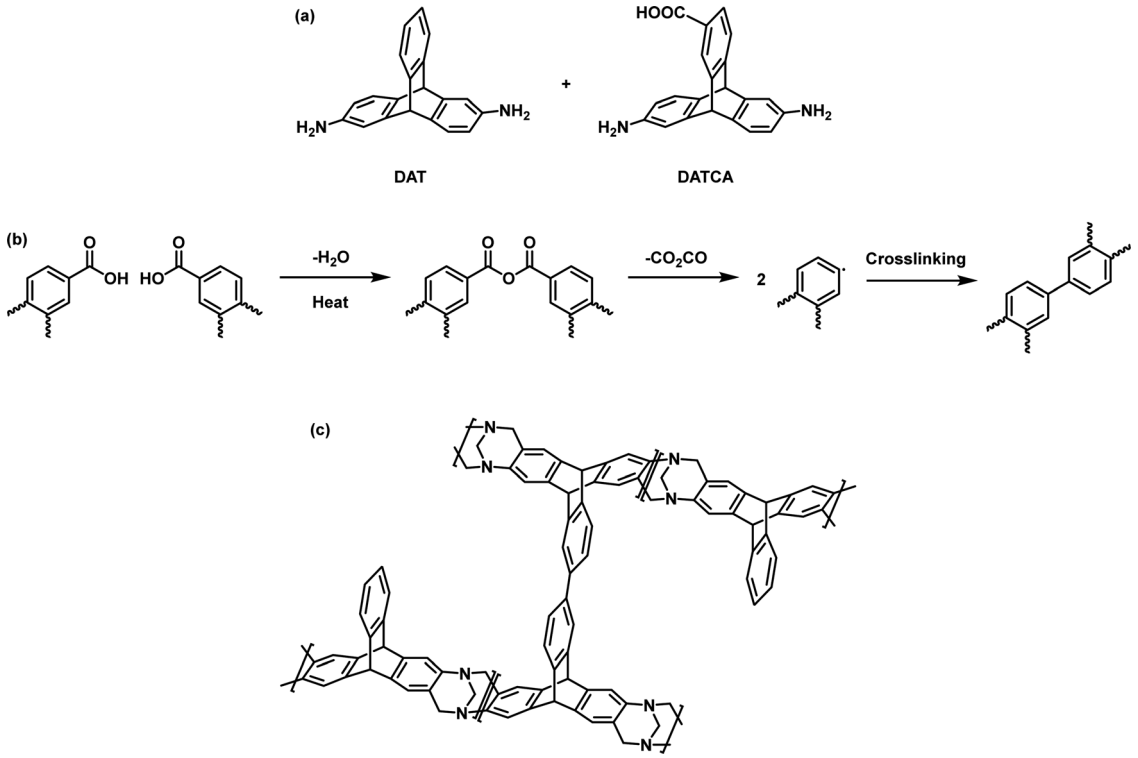

Fig. 47 (a) Monomers 2,6-diaminotriptycene (DAT) and 2,6-diaminotriptycene-14-carboxylic acid (DATCA). (b) Proposed crosslinking mechanism between two carboxylic acid groups when heated. (c) The final crosslinked structure, demonstrating the connection between two chains at the carboxylic acid groups of the DATCA monomer. Adapted with permission from ref. 395 (Copyright American Chemical Society, 2020).

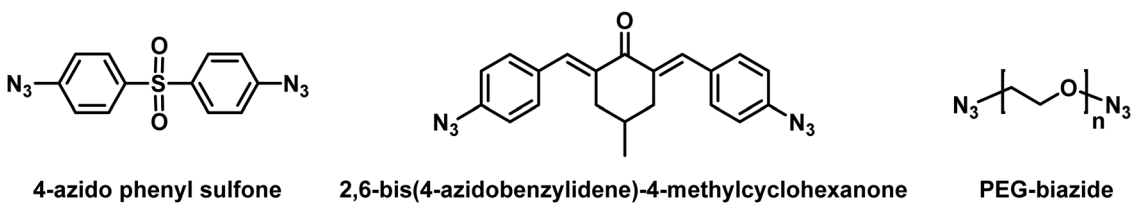

Fig. 48 Three azides investigated for the chemical crosslinking of PIM-1.[396,397]

A similar approach was reported by Liu *et al.*, where up to 2 wt% of beta-cyclodextrin (β-CD) monomer, possessing a hollow-bowl structure, was introduced to rigidify the backbone structure of PIM-1, shown in Fig. 51.[403] The polymers were tested under 50 : 50 CO_2/CH_4 mixed-gas conditions, where increasing amounts of β-CD resulted in more stable selectivity, with pure PIM-1 showing a 35% decrease in selectivity compared to a 13% decrease for 2% β-CD for CO_2 partial pressures from 2 to 10 bar.[403]

4.3.1.2. Miscible polymer–polymer blends. In a similar vein to copolymerization, the physical blending of polymers has also been investigated for a number of microporous polymers, with the same goal of combining the beneficial aspects of each component. Here, the focus is again on systems that incorporate at least one component that has microporous characteristics.

Yong *et al.* published a series of papers detailing the transport behavior of PIM-1/Matrimid® blended membranes.[224,404,405] First, the authors reported a simple physical blend of PIM-1 and Matrimid® and hypothesized that formation of CTCs between the two polymers could increase intrachain rigidity and thereby contribute to better performance and plasticization resistance. The mixed-gas selectivities of 34 and 30 for a 50 : 50 CO_2/CH_4 mixture at ~7 bar total pressure for 10 : 90 and 30 : 70 compositions of PIM-1/Matrimid® blends showed little change compared to the pure-gas selectivities of 35 and 30.[224] These polymer blends were then fabricated into hollow fibers, followed by heat treatment at 75 °C for 3 h and a subsequent silicon rubber coating procedure for 3 min to cure defects in the fibers. For a 50 : 50 CO_2/CH_4 mixture at ~2 bar total pressure, the 10 : 90 blend composition showed a decrease in selectivity to 23.1 compared to 26.2 for the pure-gas test, while the 15 : 85 blend composition showed a decrease in selectivity from 34.3 to 28.8, indicating low plasticization resistance with increasing amounts of PIM-1.[404] The authors then investigated the effects of a post-casting diamine crosslinking reaction.[405] In this work,

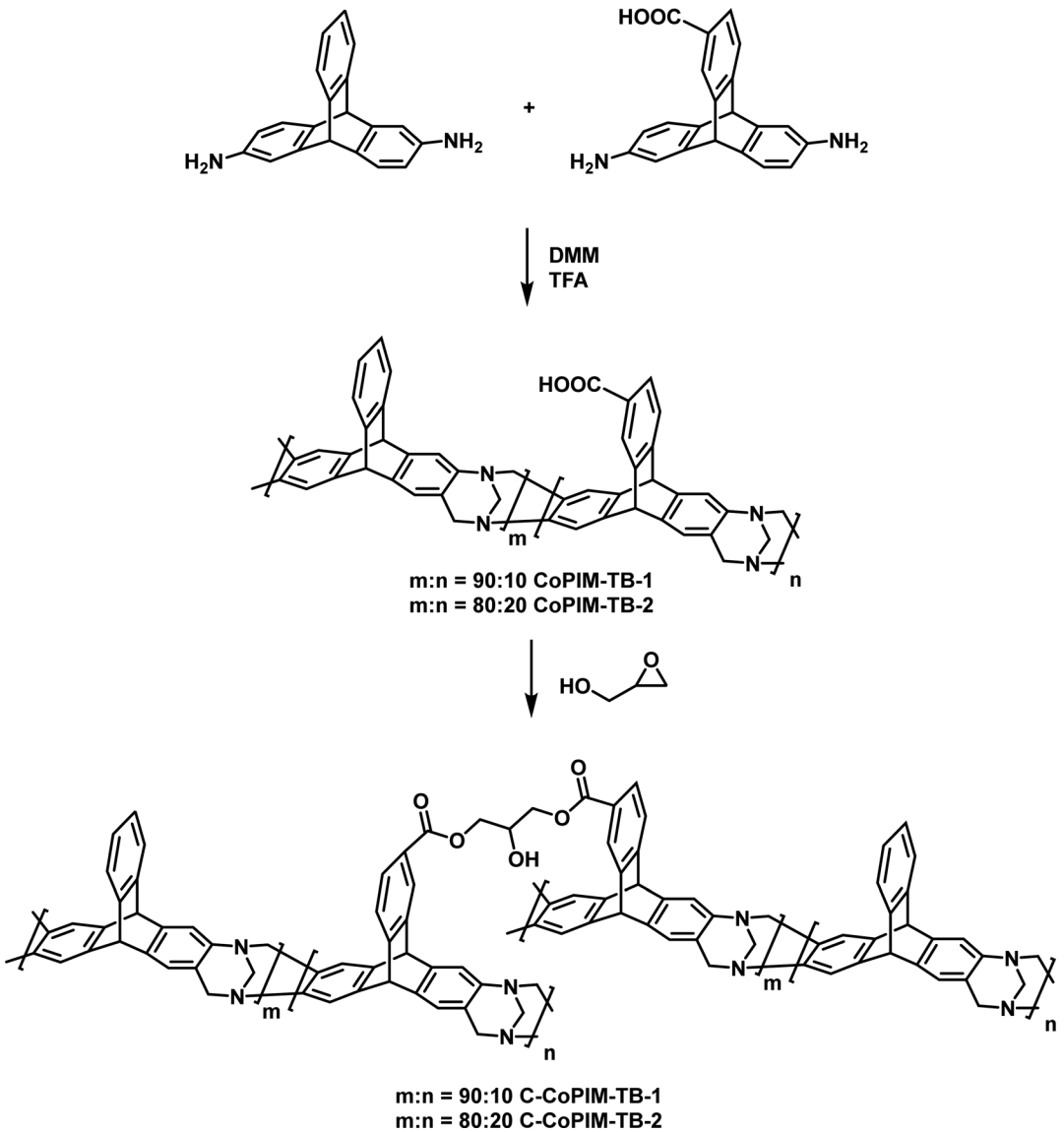

Fig. 49 Synthetic route for the synthesis of CoPIM-TB-1 and CoPIM-TB-2, followed by chemical crosslinking using a glycidol agent reacting with the carboxylic acid groups to form C-CoPIM-TB-1 and C-CoPIM-TB-2. Adapted with permission from ref. 398 (Copyright Elsevier, 2018).

as-cast PIM-1/Matrimid® films were immersed in a diamine solution (*e.g.*, trimethylenediamine (TMEDA), *p*-xylylenediamine (pXDA), triethylenetetramine (TETA), *etc.*). The diamine would then act as a crosslinker for the imide functionality on Matrimid® and form a Matrimid® crosslinked network within the PIM-1 polymer. The TETA-crosslinked membrane was tested in a 50 : 50 H_2/CO_2 gas mixture at ~7 bar total pressure and showed a decrease in pure-gas to mixed-gas selectivity from 9.6 to 5.3. It should be noted that both plasticization and competitive sorption could contribute to the decrease in selectivity for H_2/CO_2 mixtures, but requires further investigation.[405]

A similar strategy of blending PIM-1 with a commercial polymer was reported by Hao *et al.*, where the effect of adding PIM-1 to Ultem® was investigated.[406,407] For a 90 : 10 blend of Ultem®/PIM-1, 50 : 50 mixtures of CO_2/CH_4 and CO_2/N_2 at ~7 bar total pressure showed selectivities of 27.3 and 37.0, a slight increase compared to the pure-gas selectivities of 23.5 and 33.8, respectively, which was attributed to PIM-1 affinity to CO_2 and competitive sorption effects. Similar small increases were observed for the 80 : 20 blend as well.[406] The authors also formed hollow fibers of the 90 : 10 and 85 : 15 blended systems. Both fibers were tested for 50 : 50 CO_2/CH_4 with 3 bar CO_2 partial pressure and showed slight increases in permselectivity compared to the pure-gas permselectivities.[407]

A PIM-1 blend with sulfonated polyphenylenesulfone (sPPSU) was investigated by Yong *et al.*, where the secondary interactions caused by the sulfonic acid groups on sPPSU were hypothesized to increase interchain rigidity.[408] The blends were tested for a 50 : 50 CO_2/CH_4 gas mixture from ~5 to ~30 bar total pressure, where the 20 : 80 sPPSU/PIM-1 blend showed a slight decrease in mixed-gas selectivity from 26 to 23 over the pressure range.[408] PIM-1 was also blended with a Tröger's base polymer by Zhao

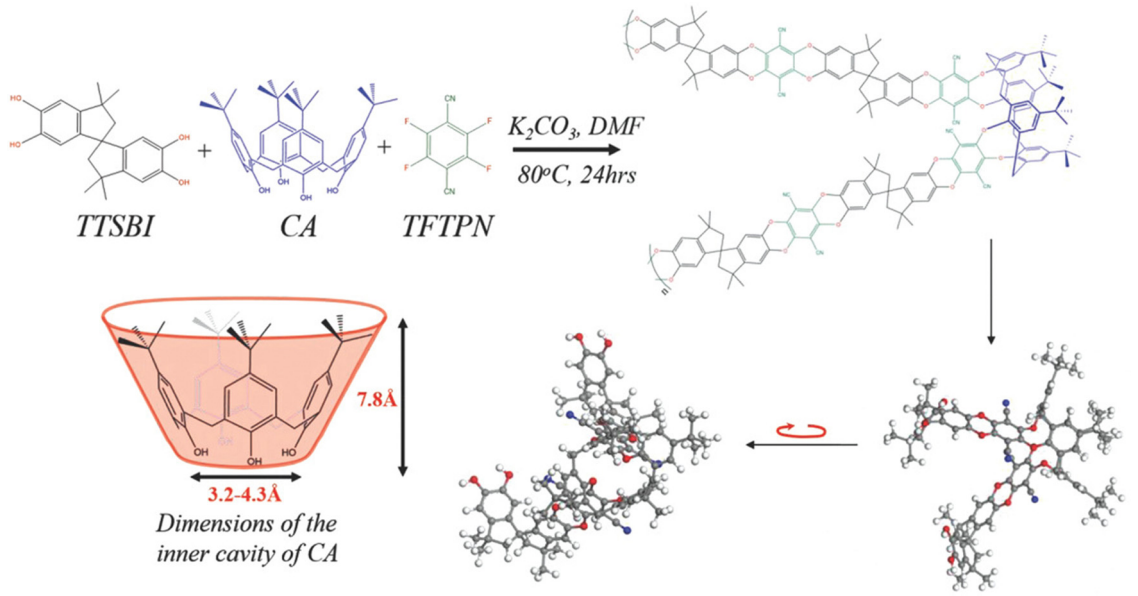

Fig. 50 Synthetic route for the incorporation of CA into the PIM-1 backbone. The CA dimensions and structure force contortion of the backbone. Reprinted with permission from ref. 402 (Copyright Wiley-VCH, 2018).

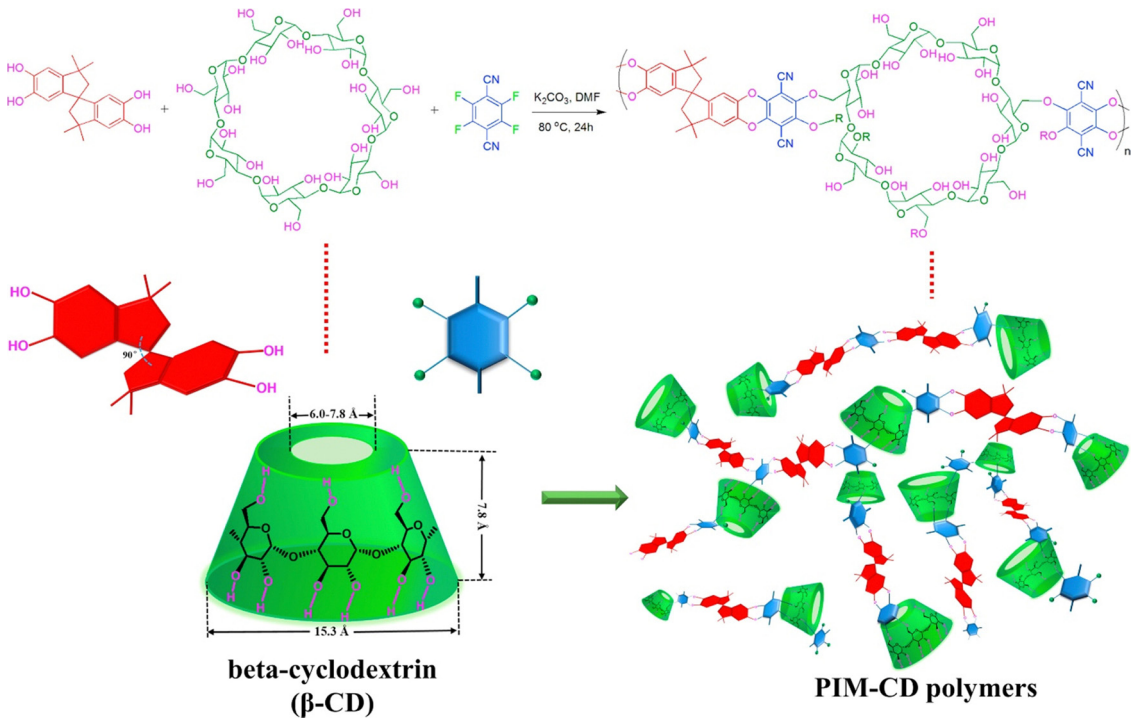

Fig. 51 Synthetic route for the incorporation of β-CD in the PIM-1 backbone. The inclusion of β-CD forces inefficient packing through its structure. Reprinted with permission from ref. 403 (Copyright Elsevier, 2017).

et al., chosen for its favorable nitrogen-nitrile interactions with PIM-1 and resulting in good miscibility and interchain rigidity.[223] The 8 : 2 and 6 : 4 PIM-1/TB blends did not show a plasticization pressure up to 40 bar, while PIM-1 displayed a plasticization pressure at 15 bar.[223]

Blends of PIM-1 and PEG of varying molecular weights (2k to 20k) and loadings (0 to 5 wt%) were investigated by Wu *et al.*[409] The authors hypothesized that the addition of the CO_2-philic PEG to the PIM-1 matrix would improve the separation performance for CO_2-based gas pairs, such as CO_2/CH_4 and CO_2/N_2. For pure-gas CO_2 tests ranging from 4 to 12 bar, plasticization pressures were not observed for PIM-1 or the blend containing 2.5 wt% of 20k PEG. In addition, similar decreases in permeability (77% for PIM-1 and 72% for the blend) were observed for

both membranes when comparing the permeability at 12 bar to that at 4 bar.[409]

C-PIMs have also been explored in blends with commercial polymers, such as Torlon® and Matrimid®, by Yong *et al.*[225,410] In both cases, it was hypothesized that the carboxylic acid functional group on C-PIM would allow for secondary hydrogen bond interactions with the other polymer in the blend, thereby increasing interchain rigidity. For the 90 : 10 C-PIM/Torlon® system, no plasticization pressure was observed up to ~30 bar, while pure C-PIM showed a plasticization pressure at ~20 bar. Additionally, the mixed-gas selectivity of 22.2 for a 50 : 50 CO_2/CH_4 mixture at ~7 bar total pressure was slightly lower than the pure-gas selectivity of 24.1.[410] Similarly, for the C-PIM/Matrimid® system, incorporation of 90 wt% C-PIM into Matrimid® increased the plasticization pressure to ~20 bar from ~4 bar for pure Matrimid®. The same mixed-gas conditions showed a small decrease in mixed-gas selectivity to 16.9 compared to the pure-gas selectivity of 17.2, showing comparable results to the C-PIM/Torlon® blend.[225]

In addition to the archetypal PIM-1 backbone, PIM-EA(H_2)-TB has also been blended with polybenzimidazole (PBI) and Matrimid® by Sánchez-Laínez *et al.* and Esposito *et al.*, respectively.[411,412] For the PIM-EA(H_2)-TB/PBI blend, the authors aimed to combine two structures that showed promising separation for H_2/CO_2 mixtures, arguing that PIM-EA(H_2)-TB is more appropriate for this separation than PIM-1 due to its higher intrachain rigidity. Asymmetric membranes were prepared for blends with 0 to 20 wt% of PIM-EA(H_2)-TB in PBI and tested for a 50 : 50 H_2/CO_2 mixture from 3 to 6 bar total pressure, showing increased mixed-gas selectivity from 10 to 21 with increasing pressure in the 20 wt% case due to dual-mode effects.[411] For the 50 : 50 PIM-EA(H_2)-TB/Matrimid® blend, a 35 : 65 CO_2/CH_4 mixture ranging from 1 to 6 bar total pressure resulted in a constant selectivity of 29 and showed little hysteresis. A constant selectivity of 43 was observed for a 15 : 85 CO_2/N_2 mixture for the same pressure range.[412]

4.3.2. Polymer–filler systems

4.3.2.1. Metal–organic frameworks. This section focuses on reports detailing the use of non-miscible fillers in a microporous polymer continuous phase to form what is generally considered to be a mixed-matrix membrane (MMM). In particular, significant research effort has been expended on the use of MOFs as a filler. A wide variety of MOFs, namely ZIFs and UiO-66, among others, and their various derivatives, have been investigated to improve transport performance and plasticization resistance of microporous polymers. Out of 34 studies resulting from our literature search related to the incorporation of MOFs in microporous polymers, MMMs fabricated with ZIF- and UiO-66-based MOFs were reported in 41% and 35% of the studies, respectively. Interestingly, 21% of the total studies reported an amine or nitrile functionalization of the ligand, indicating an emphasis on improved interfacial compatibility between the polymer and MOF. The unmodified structures for the most studied MOFs discussed in this section are shown in Fig. 52.[134] These structures do not include all varieties and variations of MOFs discussed below for the sake of brevity.

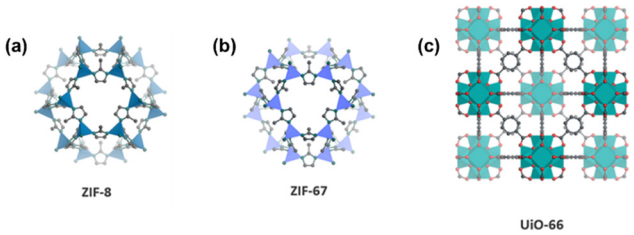

Fig. 52 MOF structures for (a) ZIF-8, (b) ZIF-67, and (c) UiO-66. Legend: gray, C; red, O, teal, N; dark blue, Zn; light blue, Co; light green, Zr. Reprinted with permission from ref. 134 (Copyright American Chemical Society, 2020).

There has been a significant research effort on incorporating the ZIF family of MOFs as a filler in microporous polymers primarily due to their excellent size-sieving properties, with the most well-known and most investigated being ZIF-8.[413] Ma *et al.* reported an MMM of PIM-6FDA-OH and ZIF-8 with filler loadings up to 65 wt%.[414] The authors investigated enhanced interfacial compatibility between the polymer and MOF based on hydrogen bonds between the –OH groups of the polymer and the nitrogen groups on ZIF-8. MMMs with 33 wt% and 65 wt% loading were tested for 50 : 50 C_3H_6/C_3H_8 mixed feed from 2 to 7 bar total pressure and showed only a small decrease in selectivity from 22 to 21 and 31 to 29 with increasing feed pressure, respectively, while pure PIM-6FDA-OH selectivity decreased from 21 to 12 from 2 to 6 bar total pressure.[414] ZIF-8 was also used as a filler in a blended PIM-1/6FDA-DAM polymer matrix by Sánchez-Laínez *et al.*[415] The authors observed that ZIF-8 exhibited better compatibility with 6FDA-DAM than with PIM-1, resulting in uniform dispersion throughout the polymer matrix. The MMMs were tested for 50 : 50 CO_2/CH_4 and 10 : 90 CO_2/N_2 mixtures at 3 bar total pressure, with MMMs containing 10 wt% ZIF-8 in PIM-1/6FDA-DAM showing the best combination of permeability and selectivity.[415] ZIF-8 and SiO_2 were also investigated as fillers in TOX-PIM-1 by Song *et al.*, where the authors first blended the filler with PIM-1 and the entire system was thermally oxidized as described previously.[393,416] For a 50 : 50 CO_2/CH_4 mixture for CO_2 partial pressure from 2 to 9 bar, the TOX-PIM-1/ZIF-8 and TOX-PIM-1/SiO_2 MMMs showed effectively the same mixed-gas selectivity change from 35 to 20, while the pure TOX-PIM-1 selectivity decreased from 60 to 30, indicating improved plasticization resistance due to the presence of the fillers.[416] More recently, Xiong *et al.* developed porous asymmetric composite membranes based from ZIF-8 and the amidoxime-functionalized polymer, AO-PIM-1.[417] The MOF was grown *in situ* using the amidoxime functionality as coordinate sites for Zn^{2+} ions. The membranes had H_2 permeabilities of 5688 barrer and H_2/CO_2 selectivities of 12.

A number of different ZIFs have been investigated as a filler for PIM-1. Hao *et al.* combined up to 30 wt% of ZIF-71 in PIM-1, followed by UV treatment to promote photo-oxidative scission that resulted in a dense selective layer as described by Song *et al.* earlier.[390,418] ZIF-71 was chosen for its large pore aperture of 4.2 Å to promote permeability. The UV-treated 30 wt%

ZIF-71/PIM-1 MMM showed a pure-gas CO_2/CH_4 selectivity of 35.6, which was greater than the demonstrated mixed-gas selectivity of 28.8 and 28.3 for a 50 : 50 and 30 : 70 CO_2/CH_4 gas mixtures at ~7 bar total pressure. Additionally, the mixed-gas CO_2 permeability for a 50 : 50 CO_2/CH_4 mixture increased from 2,224 to 3,020 barrer with increased loading from 20 wt% to 30 wt%.[418] Wu *et al.* investigated MMMs with up to 30 wt% of ZIF-67 in PIM-1. ZIF-67 is isostructural to ZIF-8, but contains Co instead of Zn, which results in slightly stiffer metal–ligand coordination, and hence improved size-sieving separations.[419] The MMMs were tested in a 30 : 70 CO_2/CH_4 mixture at 2 bar CO_2 partial pressure and showed a decrease in mixed-gas selectivity when compared to the pure-gas selectivity, with the smallest decrease from 12 to 11.2 observed for the 30 wt% loaded MMM.[419] The same group also reported the transport behavior of up to 36 wt% of ZIF-67 hollow nanoparticles (ZIF-HNPs) in a PIM-1 matrix.[420] The authors differentiate conventional solid nanoparticles (ZIF-SNPs) from ZIF-HNPs by the ability to regulate the cavity size of ZIF-HNPs and thereby control the permeability ratio of PIM-1 to the ZIF-HNPs.[420] Under the same testing conditions, similar changes in mixed-gas selectivity were observed with the highest loading MMMs showing the smallest decrease from 17 to 16.[420] Again from the same group, Wang *et al.* investigated the effect of up to 30 wt% of amino-functionalized ZIF-7 (NH_2-ZIF-7) in PIM-1.[421] The authors suggested that the addition of the $-NH_2$ promoted favorable interaction with the PIM-1 matrix and caused rigidification of the polymer chains at the interface and partial blockage of the MOF pores. Under the same 30 : 70 CO_2/CH_4 mixed-gas testing conditions, the highest loading MMM tested showed the smallest decrease in mixed-gas selectivity from 21 to 20.[421] Task-specific ionic liquids (TSILs) have also been used to modify ZIF-67 to form MMMs with PIM-1 by Han *et al.*[422] Specifically, the TSILs shown in Fig. 53, tetramethylgunidinium phenol (TMGHPhO) and tetramethylgunidinium imidazole (TMGHIM), were coated on the ZIF-67 particles and were hypothesized to improve CO_2 solubility as well as improve the interfacial compatibility between the MOF and the PIM-1 matrix. For a 50 : 50 CO_2/CH_4 mixture at 2 bar total pressure, the 10 wt% TMGHIM@ZIF-67/PIM-1 MMM showed a mixed-gas selectivity of 9.3, lower than the ideal selectivity of 10.5 and suggesting limited sorption enhancement effects.[422]

Significant research efforts have focused on the addition of UiO-66 derivatives in microporous matrices. Tien-Binh *et al.* explored the incorporation of UiO-66-NH_2 in PIM-1 through an *in situ* cross-interfacial nucleophilic aromatic substitution reaction during polymer synthesis shown in Fig. 54a.[423] By introducing the UiO-66-NH_2 particle as a starting polymerization reagent, the MOF effectively acts as a chain terminator for PIM-1 polymer chains, thus introducing a covalent bond between the polymer and the filler. This system was tested for a 50 : 50 CO_2/CH_4 mixture from 2 to 10 bar CO_2 partial pressure and showed a constant selectivity of 19 across the entire pressure range, while the control UiO-66-NH_2/PIM-1 MMM showed a decrease in selectivity from 13 to 10.[423] UiO-66-NH_2 was also used as a filler in partially converted amidoxime-modified PIM-1 (PAO-PIM-1) by Wang *et al.*[424] The authors hypothesized that a hydrogen bonding network between the $-NH_2$ groups on the MOFs and the amidoxime groups on the PAO-PIM-1 backbone would result in improved interfacial compatibility as shown in Fig. 54b. An MMM containing 30 wt% UiO-66-NH_2 was tested under a mixed CO_2/CH_4 and CO_2/N_2 feed at 1 bar total pressure with varying volumetric compositions (3 : 7, 1 : 1, and 7 : 3). For both gas mixtures, the mixed-gas selectivity increased with CO_2 partial pressure, indicating beneficial competitive sorption and minimal plasticization for the tested pressure range.[424] Another UiO-66 derivative, UiO-66-CN, was investigated by Yu *et al.* for incorporation into PIM-1, followed by a high temperature cure to form bulky triazine rings between two nitrile groups of separate PIM-1 chains and the nitrile group of UiO-66-CN, using a thermal crosslinking reaction as described earlier in this section. The process is shown in Fig. 54c.[392,425] The 20 wt% MMM showed hysteresis resistance *via* high pressure CO_2 cycling tests, where consistent CO_2 permeability was observed for a 50 : 50 CO_2/N_2 feed cycled three times between 1.4 to 4 bar.[425] UiO-66 was once again modified by Prasetya *et al.* through a mixed-ligand approach by loading azobenzene linkers inside of the framework.[426] The MMMs were tested for a 15 : 85 CO_2/N_2 mixed feed at 1.4 bar total pressure, and it was found that higher loadings of azobenzene linkers displayed a smaller difference between pure-gas and mixed-gas selectivity, with the 100% azobenzene linker MOF showing a decrease in selectivity from 19 to 18. The change in performance with respect to increasing azobenzene linker percentage was attributed to the bulky azobenzene structure causing decreased CO_2 sorption, resulting in improving plasticization resistance.[426] UiO-66-NH_2 was also investigated as a filler in a blended PIM-1/MEEP80 system by Muldoon *et al.*, where the $-NH_2$ functionality was hypothesized to promote favorable polymer–filler interactions and thereby improve plasticization resistance.[427] The MMM with 10 wt% loading of UiO-66-NH_2 in a 75 : 25 PIM-1/MEEP80 blend was tested in a 14 : 86 CO_2/N_2 mixed-gas feed from 1.5 to 3.5 bar total pressure, showing a small decrease in mixed-gas selectivity from 27.1 to 26.7.[427] Work by Geng *et al.* has also implemented defect-engineered UiO-66 nanoparticles as pillars to prevent the collapse of the PIM-1 structure and reduce physical aging.[428] In another recent study, Husna *et al.* grafted UiO-66-NH_2 particles with PIM-1 to increase the overall compatibility of the filler into a PEBAX matrix.[429] The surface-modified MOF provided additional molecular transport channels for the MMM, yielding a CO_2 permeability of 247 with a CO_2/N_2 selectivity of 56, improved mechanical properties and excellent aging resistance.

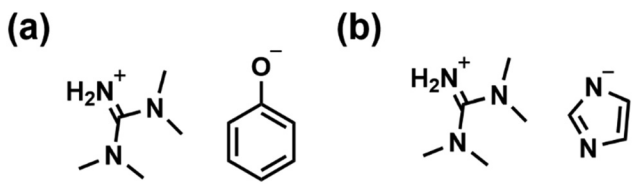

Fig. 53 Chemical structures for (a) TMGHPhO and (b) TMGHIM used to modify ZIF-67.[422]

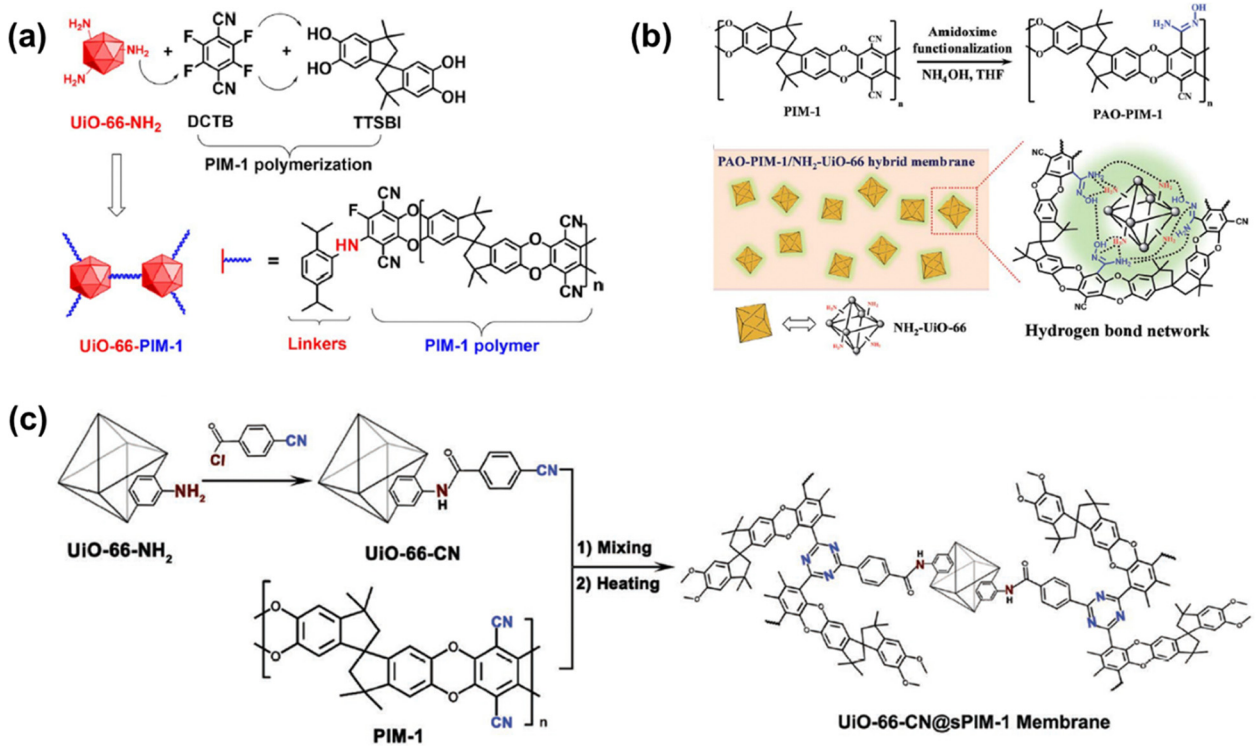

Fig. 54 Conceptualization for the integration of UiO-66-based MOFs in polymers of intrinsic microporosity *via* (a) direct nucleophilic aromatic substitution during synthesis,[423] (b) hydrogen bonding,[424] and (c) post-synthesis crosslinking.[425] Reprinted with permission from ref. 423–425 (Copyright Elsevier, 2018; Royal Society of Chemistry, 2017; and Wiley-VCH, 2019).

Another class of widely investigated MOFs are MIL-type MOFs. For simplicity, MIL-101 refers to MIL-101(Cr) MOF unless stated otherwise. Khdhayyer *et al.* investigated the effect of MIL-101 MOFs and their derivatives in PIM-1.[430] The authors found that MIL-101 showed the best performance among those tested. The 47 vol% MIL-101/PIM-1 MMM was tested for 15 : 85 CO_2/N_2 and 35 : 65 CO_2/CH_4 mixtures from 1 to 6 bar total pressure, showing small decreases in mixed-gas selectivity of 27 to 25 and 24 to 20, respectively.[430] Sabetghadam *et al.* reported the incorporation of NH_2-MIL-53(Al) with Matrimid® in a PIM-1 matrix.[431] The authors hypothesized that a small loading of Matrimid® would promote enhanced phase compatibility between the MOF and PIM-1. For an MMM containing 25 wt% loading of MOF in a 9.1 : 90.9 Matrimid®/PIM-1 blend, mixed-gas selectivity for a 15 : 85 CO_2/N_2 feed compared to a feed with 2.3 mol% water increased from 23 to 28, demonstrating beneficial competitive sorption effects resulting from a plasticization-resistant MMM.[431] Similarly, Fan *et al.* fabricated MMMs with loadings up to 30 wt% using NH_2-MIL-53(Al) in Tröger's base polymers to take advantage of beneficial interaction between the MOF $-NH_2$ and the Tröger's base functionality.[432] For 10 : 90 CO_2/N_2 and 50 : 50 CO_2/CH_4 mixtures ranging from 4 to 15 bar total feed pressure, the 20% loading MMM showed a constant mixed-gas selectivity for both mixtures of 26 and 24, respectively, while the mixed-gas selectivity for the pure polymer decreased from 26 to 22 for the CO_2/CH_4 mixture.[432]

Prasetya *et al.* also investigated the use of Azo-DMOF-1 as a filler in PIM-1, shown in Fig. 55a.[433] The authors hypothesized that the azobenzene functionalities would improve CO_2 sorption. When tested for a 50 : 50 CO_2/N_2 mixed feed at 1.5 bar total pressure, the 10 wt% Azo-DMOF-1/PIM-1 MMM showed a decrease in pure- to mixed-gas selectivity from 20 to 11, indicating limited sorption enhancement effects.[433] Mg-MOF-74 was also used to form MMMs with PIM-1 by Tien-Binh *et al.*[434] The authors hypothesized that the hydroxyl groups of the Mg-MOF-74 fillers could undergo a chemical crosslinking reaction with the fluoride chain ends of PIM-1 and improve interfacial compatibility while constructing channels for gas transport, shown in Fig. 55b. PIM-1 and MMMs containing 10 and 20 wt% MOF in PIM-1 were tested using 50 : 50 CO_2/CH_4 mixed-gas feeds ranging from 4 to 20 bar total pressure. PIM-1 showed a drop in mixed-gas selectivity from 13 to 6 as a result of increasing CH_4 permeability with pressure. Meanwhile, the 10 and 20 wt% MMMs showed stable CH_4 permeability and consistent mixed-gas selectivity of 13.1 and 19.2, respectively, indicating effective plasticization resistance.[434] In 2022, Pu *et al.* incorporated amino-functionalized NUS-8-MOF nanosheets into PIM-1[435] to increase interfacial compatibility and improve overall CO_2 transport in MMMs. At a 10 wt% filler loading, the MMMs had a CO_2 permeability of 14 000 barrer and a CO_2/N_2 selectivity of 30. The effect of plasticization on the MMMs was tested using mixed-gas high-pressure permeation tests up to 50 bar for CO_2/N_2 and CO_2/CH_4 mixtures at 20 vol% and 30 vol% of CO_2, respectively. No plasticization was observed for CO_2/N_2 tests up to 50 bar. In CO_2/CH_4 tests, CH_4 permeability increased slightly after approximately 5 bar for PIM-1. The plasticization pressure

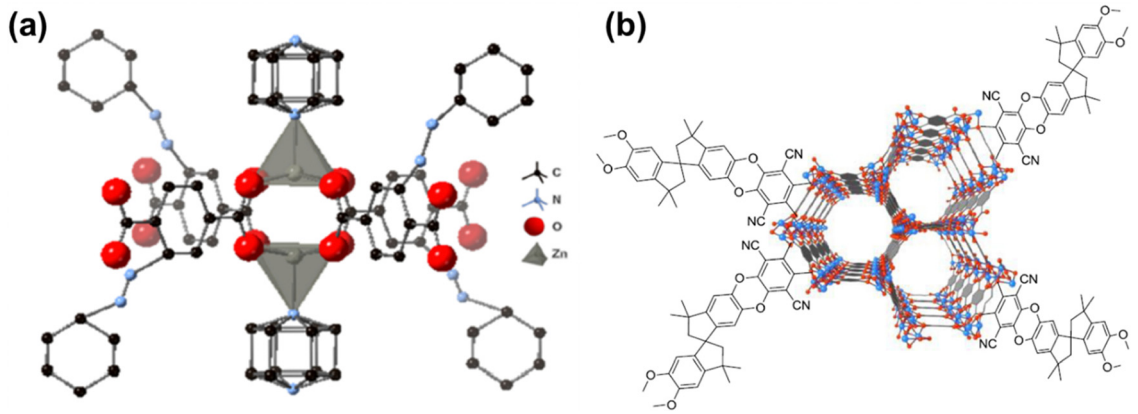

Fig. 55 (a) Structure for Azo-DMOF-1[433] and (b) conceptualization of transport channels created by Mg-MOF-74 in PIM-1.[434] Reprinted with permission from ref. 433 and 434 (Copyright American Chemical Society, 2018 and Elsevier, 2016).

for CH_4 decreased as a function of MOF addition, where at 13.2% MOF loading, no increase in CH_4 permeability was observed up to 50 bar.

4.3.2.2. Other fillers. While MOFs occupy a large portion of the research space for fillers in polymer membranes, several other fillers have also been investigated such as silica-based particles, carbon nanotubes, graphene oxide, and porous organic frameworks.

Polyhedral oligomeric silsesquioxane (POSS) nanoparticles have been investigated as a filler in PIM-1 due to their potential to improve gas diffusion by increasing porosity as well as for their tunable functional groups to improve compatibility and dispersibility.[436] For example, Yong *et al.* created MMMs using up to 20 wt% of DiSilanolIsobutyl POSS nanoparticles (SO1440) in PIM-1 to study changes in plasticization behavior with filler content.[436] DiSilanolIsobutyl POSS, shown in Fig. 56a, was chosen for its high solubility in a dichloromethane casting solvent. MMMs containing 2 and 10 wt% of POSS were tested using a 50 : 50 CO_2/CH_4 mixed feed from ~5 to ~30 bar total pressure and showed a similar decrease in mixed-gas selectivity from 12.5 to 9 with increasing pressure.[436] Kinoshita *et al.* investigated the effect of up to 20 wt% of nitro- and amine-modified POSS particles in PIM-1, hypothesizing that the modified groups could promote improved interfacial compatibility between the filler and the polymer matrix. The structure of the amine-modified POSS (OAPS) is shown in Fig. 56b.[437] The 5 wt% amine-modified POSS MMM was tested for 50 : 50 CO_2/CH_4 and 50 : 50 CO_2/N_2 mixtures from 2 to 10 bar CO_2 partial pressure. For the CO_2/CH_4 mixture, the mixed-gas selectivity decreased from 12 to 9, while CO_2/N_2 mixed-gas selectivity decreased from 17.5 to 15 with increasing pressure.[437]

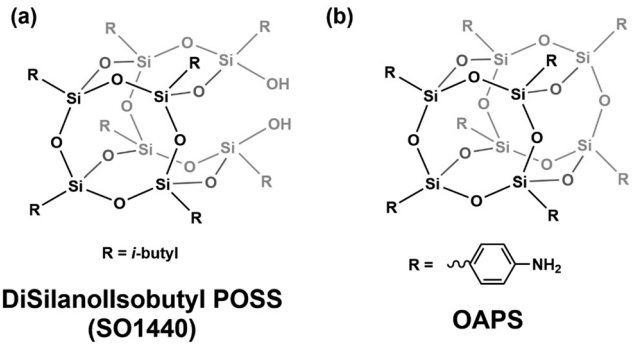

Fig. 56 Chemical structures for (a) DiSilanolIsobutyl POSS[436] and (b) octa aminophenyl POSS (OAPS).[437]

Carbon nanotubes have received interest as a filler in polymer membranes for their beneficial mechanical properties and fast diffusion due to their inherent inner-wall smoothness. Khan *et al.* synthesized functionalized multi-walled carbon nanotubes (f-MWCNTs) as a filler in PIM-1.[438] The authors modified the MWCNTs with poly(ethylene glycol) (PEG) to aid in matrix dispersion and created MMMs with up to 3% f-MWCNT loading. Addition of just 0.5 wt% of f-MWCNTs resulted in the elimination of a plasticization pressure for high pressure CO_2 tests up to ~30 bar, which was attributed to the strong interaction between the PEG functionality and the polymer matrix.[438] Along a similar line, Sun *et al.* synthesized pristine, acid-, and amine-functionalized MWCNTs as a filler in Cardo-PIM-1.[439] The MMMs were tested for a 50 : 50 CO_2/N_2 mixture at ~1 bar, showing the highest selectivity for the amine-functionalized MWCNTs.[439]

In addition to the 1-D nature of carbon nanotubes, 2-D sheet-like materials have been used as fillers as well. For example, Kim *et al.* formed 2-D scaffolds of graphene oxide nanosheets inside of a TR polymer.[440] Graphene oxide (GO) was expected to improve size selectivity and mechanical properties of the material. MMMs with 1.0 wt% loading of GO showed a CO_2/CH_4 pure-gas selectivity of 32.4 and a mixed-gas selectivity of 35.1 for a 50 : 50 mixture at ~1 bar total feed pressure. A slight increase in selectivity was observed for CO_2/N_2 as well, from 17.7 to 18.2.[440]

In contrast to MOFs, another category of fillers that have been incorporated into microporous polymers are porous organic frameworks (POFs). These materials are similar to MOFs in that the porous structure is meant to improve diffusion and potentially diffusion selectivity, but they do not contain metal–ligand coordinative bonds. As such, the porous structure is

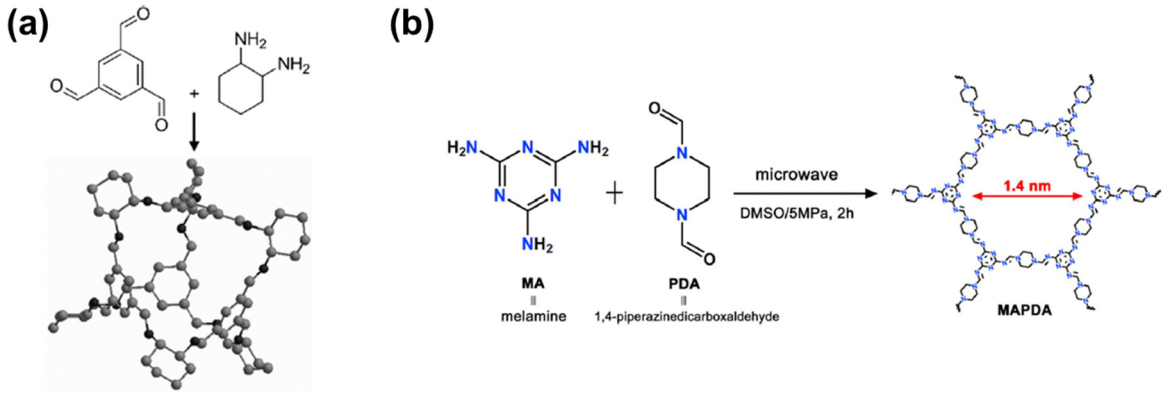

Fig. 57 Synthesis route and chemical structures for (a) CC3[441] and (b) MAPDA.[442] Reprinted with permission from ref. 441 and 442 (Copyright Wiley-VCH, 2013 and Elsevier, 2019).

entirely organic, and thus, it is expected to have better dispersion in the continuous organic polymer phase.[441] Bushell *et al.* synthesized a porous imine cage (CC3) as a filler for PIM-1 (Fig. 57a).[441] CC3 was synthesized from 1,3,5-triformylbenzene and (*R*,*R*)-1,2-diaminocyclohexane to form a cage-like structure. MMMs with 30 wt% loading were tested in a ternary 35 : 10 : 55 $CO_2/O_2/N_2$ mixture for a total pressure up to 6.5 bar and showed an increase in selectivity from 13 to 15 due to a combination of suppressed plasticization and competitive sorption effects.[441] Similarly, Yu *et al.* synthesized MAPDA, a POF made from melamine and 1,4-piperazinedicarboxaldehyde, as a filler in PIM-1 (Fig. 57b).[442] MMMs with loadings up to 20 wt% MAPDA were fabricated. The incorporation 15 wt% of the POF showed a decrease in mixed-gas selectivity for a 50 : 50 CO_2/N_2 mixture from 40 to 30 with increasing pressure from 2 to 4 bar total pressure. However, a stable CO_2/N_2 mixed-gas selectivity was observed for up to 70 h of continuous testing at 3 bar feed pressure.[442] There have also been significant research efforts into the application of porous aromatic frameworks (PAFs) in microporous polymers, but these materials have primarily been studied for aging resistance.[443–446]

5. Overview of plasticization performance of microporous polymers

This section summarizes published work on the plasticization behavior of microporous polymers that have been evaluated through high-pressure permeation and/or mixed-gas tests. In addition, studies on long-term performance and stability of membranes are summarized. A list of recent reports on microporous materials was compiled using the SciFinder search engine, where the keywords "PIM", "polymers of intrinsic microporosity", "gas separations", "membranes", and "plasticization" were used to identify research papers that reported gas separation performance on microporous polymers until the end of 2022. When not tabulated in the studies, permeability and selectivity data points were digitally extracted using WebPlotDigitizer.[447]

5.1. High-pressure permeation performance

One of the most common methods to evaluate the susceptibility of a membrane to plasticization is a high-pressure permeation test. This test involves increasing the feed pressure of polarizable or condensable gases (*e.g.*, CO_2, C_3H_6, H_2S, *etc.*) while monitoring pure- or mixed-gas permeability. During high-pressure tests, the pressure at which the permeability begins to increase is commonly referred to as the "plasticization pressure". As discussed in Sections 2 and 3, the plasticization pressure is the point at which increasing diffusion coefficients overtake decreasing sorption coefficients, resulting in an overall increase in permeability.[42,72] While the plasticization pressure of the condensable gas can be an initial indication of plasticization in a polymer film, it does not evaluate co-permeating species, and thus reveals no information on changes in selectivity for a real binary separation. Therefore, other more direct indications of plasticization are also discussed in this section. The following sections summarize the performance of a variety of microporous polymers that have been evaluated with high-pressure permeation tests, including polymers with post-synthetic modifications (PSM) and multi-component systems, such as blends and mixed-matrix membranes (MMMs).

5.1.1. Pure microporous polymers. This section will consider films formed solely from microporous polymers developed for gas separations. Fig. 58 showcases high-pressure permeation data of CO_2 and CH_4 for polymers containing hydrogen bonding groups (such as –OH, –COOH, $–NH_2$, among others) and polymers without hydrogen bonding groups (such as those containing –CN functionality). Fig. 58a and b represent data collected from pure-gas tests, while Fig. 58c–f represent data collected mixed-gas tests (CO_2/CH_4). To allow for direct comparisons across different manuscripts, high-pressure permeation tests were normalized using permeability values for tests at the lowest pressure, usually 1 bar. Additionally, graphs were truncated at 17 bar CO_2 partial pressure for ease of comparison among datasets, which were most commonly limited to pressures below 20 bar. It is important to note, however, that plasticization pressures above 20 bar have been reported. For example, He *et al.* reported a pure-gas CO_2 plasticization pressure of ~27 bar

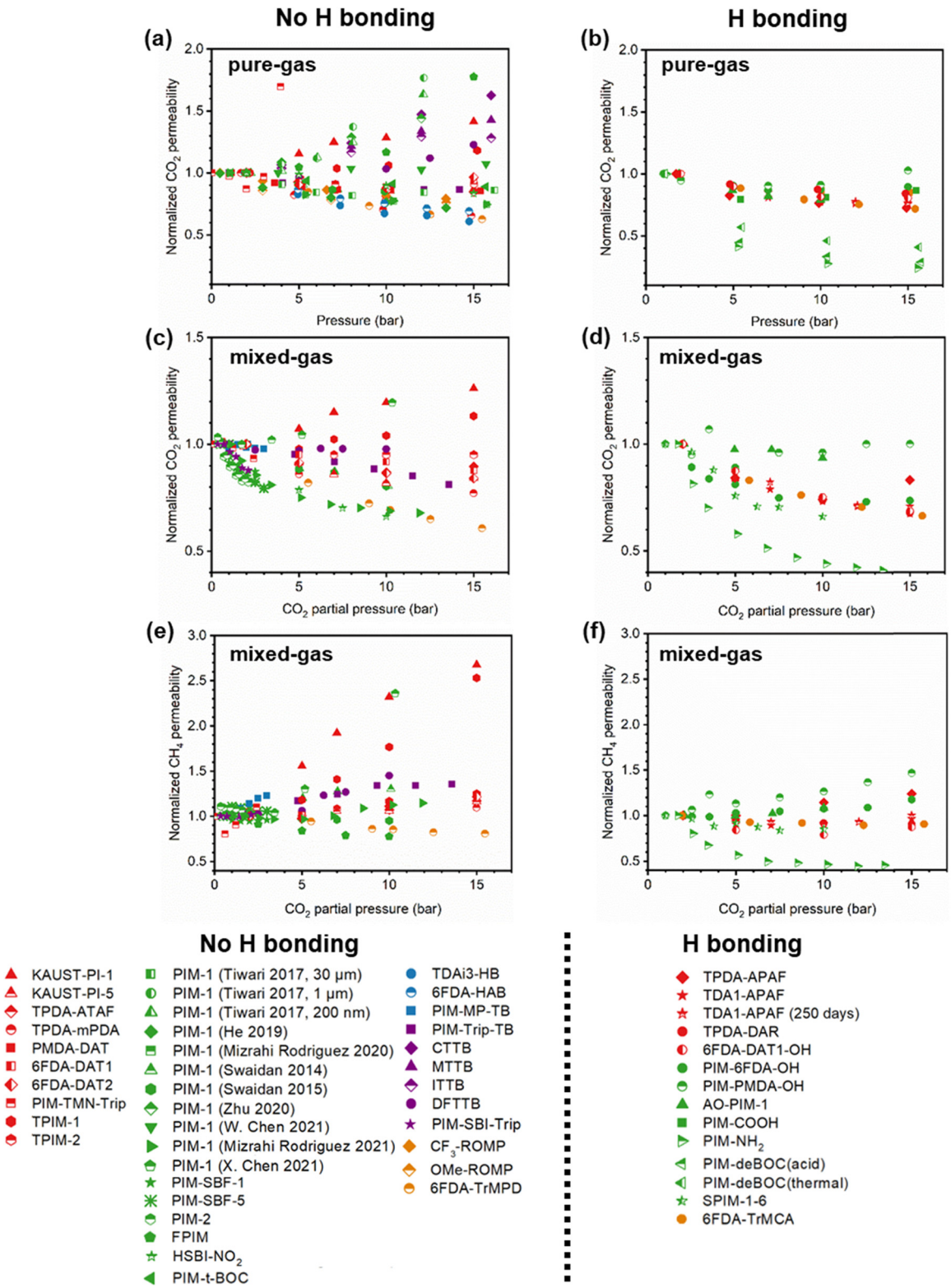

Fig. 58 Normalized CO_2 permeability (a)–(d) or normalized CH_4 permeability (e) and (f) *vs.* CO_2 partial pressure for pure polymers. (a) and (b) represent data from pure-gas measurements, while (c)–(f) represent data from mixed-gas measurements. Red points represent polymers containing triptycene units, green points represent polymers containing SBI/SBF units, blue points represent polymers containing TB (or TB-like units), purple points represent polymers containing both triptycene and TB units, and orange points represent all other polymers.

for PIM-1,[39] which would not appear in Fig. 58. Evaluating plasticization performance beyond 20 bar is of importance when considering applications such as natural gas sweetening, where wellhead pressures can reach well over 50 bar.[348]

In general, polymers containing hydrogen bonding groups exhibit less significant increases in CO_2 permeability, in both pure- and mixed-gas cases, compared to polymers without hydrogen bonding groups. This finding can be attributed to secondary forces that help facilitate the formation of charge transfer complexes (CTCs) and a reduction in cooperative polymer chain mobility, which is often described in the literature as "rigidifying" polymer chains.[34,342–348,448] A more rigorous method to identify plasticization effects involves evaluating the permeability of the weaker sorbing gas at high pressures during mixed-gas tests.[34] CH_4 is typically not a plasticizing gas due to its lower critical temperature (T_c = 190.55 K) than common plasticizing gases such as CO_2 (T_c = 304.13 K). As a result, in a pure-gas scenario, CH_4 permeability would not be expected to increase significantly with increasing feed pressure. However, when CO_2/CH_4 mixtures are considered, polymer chain mobility due to the presence of CO_2 can cause CH_4 permeability to increase, also known as "CH_4-creep," a phenomena that can more directly identify plasticization effects, especially in cases where CO_2 permeability appears constant.[34] Notably, when considering CH_4 permeability for high-pressure mixed-gas tests, polymers with hydrogen bonding groups generally show smaller increases in CH_4 permeability than polymers without hydrogen bonding groups. Secondary forces offer a clear means to mitigate plasticization effects.

Fig. 59 presents normalized CO_2/CH_4 permselectivity as feed pressure increases. Fig. 59a and b distinguish between polymers with hydrogen bonding groups and polymers without hydrogen bonding groups. Both pure- and mixed-gas permselectivities are reported. In general, mixed-gas permselectivities are lower than pure-gas permselectivities regardless of whether the polymer contains hydrogen bonding groups. This general trend can be attributed to the increase in CH_4 permeability in the presence of CO_2. Moreover, the decrease in CO_2/CH_4 selectivity from the pure- to mixed-gas case for polymers without hydrogen bonding groups is much more significant than that for polymers with hydrogen bonding groups, consistent with previous trends suggesting that hydrogen bonding moieties can suppress plasticization.

5.1.2. Post-synthetic modification. In this section, trends for high-pressure permeation tests on post-synthetically modified samples are discussed. Fig. 60a and c showcase the effects of thermal annealing on CO_2 and CH_4 permeability with increasing pressure in a 50 : 50 CO_2/CH_4 mixture for TPDA-APAF and TPDA-ATAF. In this work, Swaidan *et al.* showed that thermally annealing TPDA-ATAF and TPDA-APAF at 250 °C for 24 h led to more stable CH_4 permeabilities up to a CO_2 partial pressure of 25 bar.[34] While TPDA-ATAF and TPDA-APAF showed mixed-gas CO_2 plasticization pressures at ~10 bar before annealing at 250 °C, no detectable

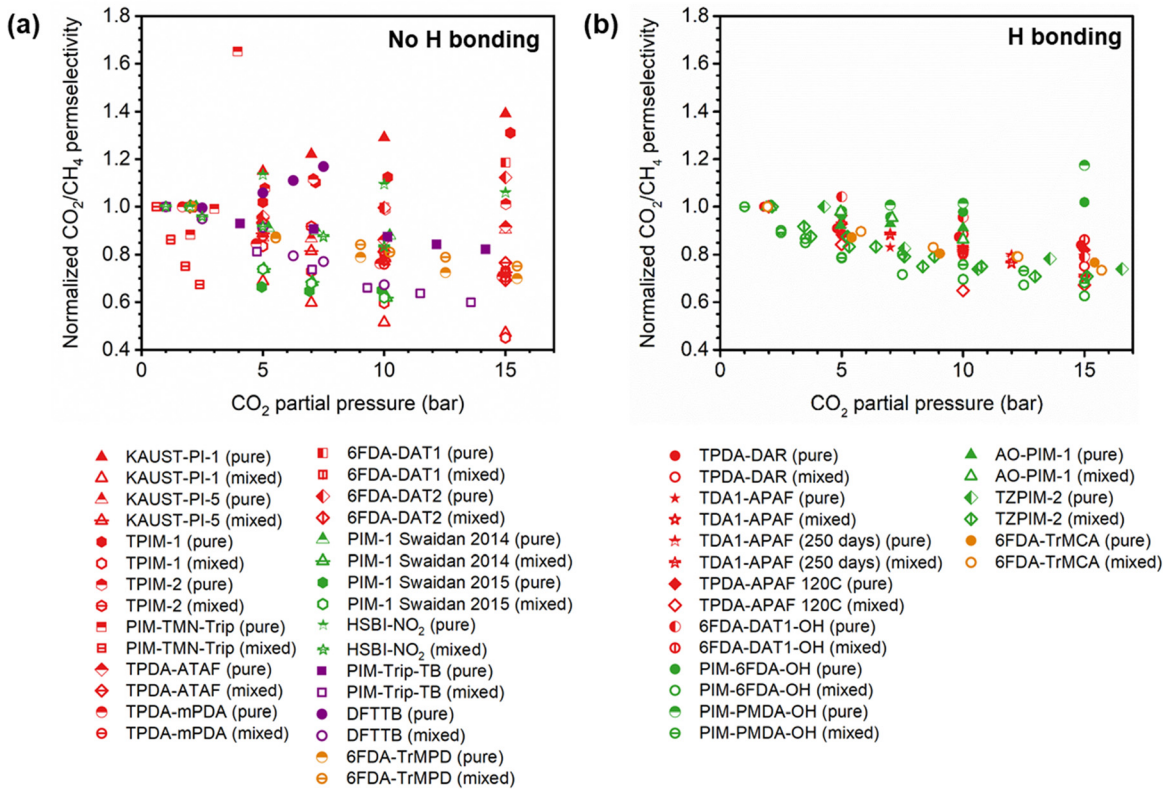

Fig. 59 Normalized CO_2/CH_4 permselectivity *vs.* CO_2 pressure for pure polymers with (a) hydrogen bonding groups, and (b) no hydrogen bonding groups. Red points represent polymers containing triptycene units, green points represent polymers containing SBI/SBF units, purple points represent polymers containing both triptycene and TB units, and orange points represent all other types of polymers.

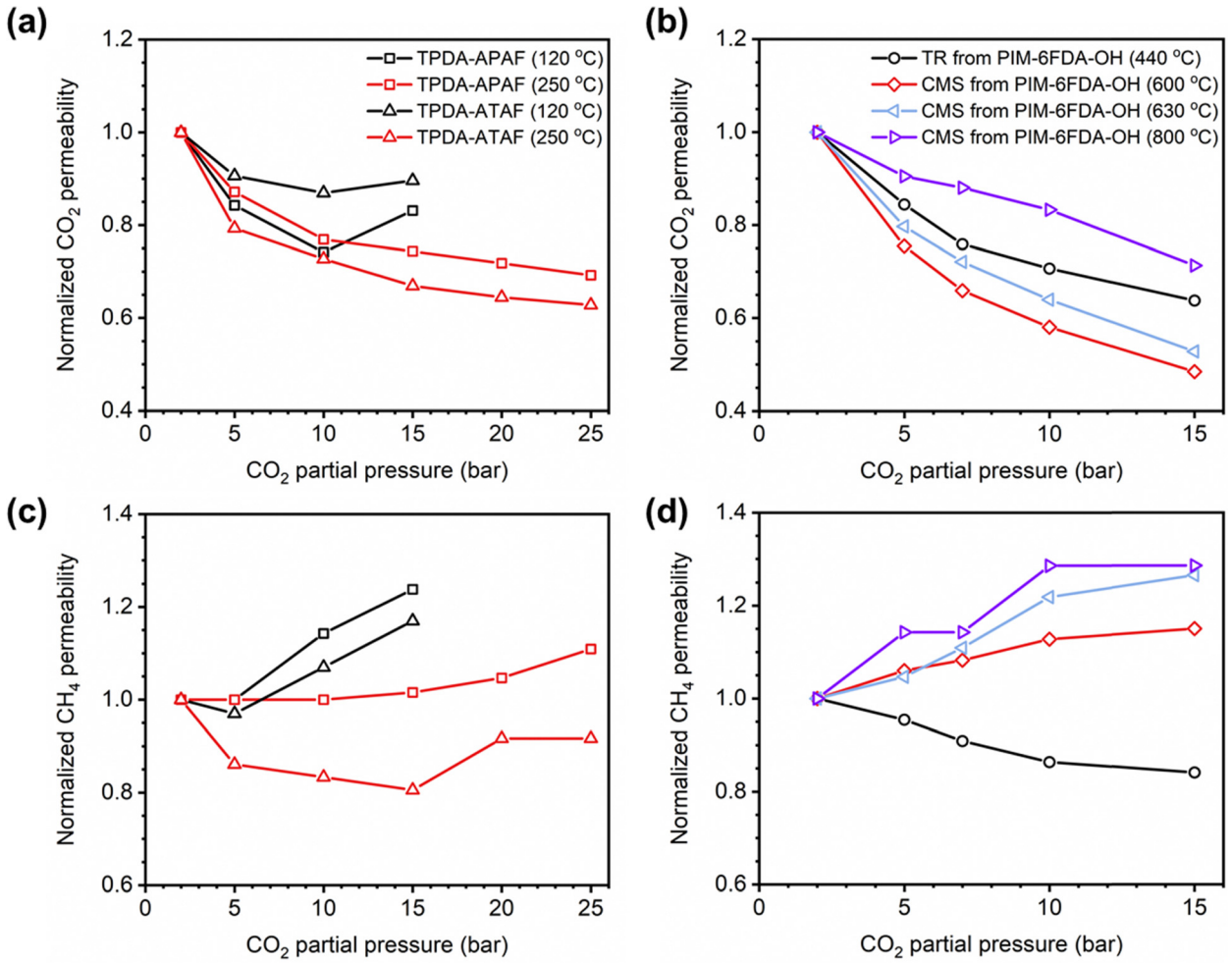

Fig. 60 Normalized CO_2 permeability *vs.* CO_2 partial pressure for (a) thermally annealed polymers[34] and (b) carbon molecular sieves or thermally rearranged polymers.[372] Normalized CH_4 permeability *vs.* CO_2 partial pressure for (c) thermally annealed polymers[34] and (d) carbon molecular sieves or thermally rearranged polymers.[372]

mixed-gas CO_2 plasticization pressure up to 25 bar CO_2 partial pressure was found after annealing.[34] The authors concluded that thermal annealing helped to decrease polymer chain mobility and facilitate CTC formation in both TPDA-ATAF and TPDA-APAF, which improved resistance to CO_2-induced swelling.[34]

In a separate study, Swaidan *et al.* examined how high-pressure mixed-gas (50 : 50 CO_2/CH_4) permeation changed between PIM-6FDA-OH and its thermally-rearranged (TR) and carbon molecular sieve (CMS) analogues.[372] Fig. 60b and d depict the CO_2 and CH_4 permeabilities as functions of CO_2 partial pressure, respectively, of the TR and CMS analogs of PIM-6FDA-OH.[372] While the CO_2 permeability of the TR analog decreased more than that of the CMS analog treated at 800 °C, the CH_4 permeability of the TR analog was more stable than that of the three CMS analogs up to a CO_2 partial pressure of 15 bar.[372] Swaidan *et al.* concluded that sorption of CO_2 increased due to an increase in the number of ultramicropores formed when transforming the TR polymer to a CMS material.[449] The resulting dilation from enhanced CO_2 sorption thus increased CH_4 permeability.[372] However, when treated at 800 °C, pore collapse from heat treatment was significant enough to reduce CO_2 sorption and also reduce corresponding effects from dilation.[372]

Besides thermal annealing and TR/CMS formation, thermal and chemical crosslinking have been used to suppress plasticization in microporous polymers. Fig. 61 displays high-pressure CO_2 permeation data for three examples of thermal crosslinking on microporous polymers. Specifically, Fig. 61a shows a comparison between PIM-1 and its thermally-oxidated crosslinked version (TOX-PIM-1).[393] PIM-1 and TOX-PIM-1 (treated for 24 h) exhibit similar decreases in mixed-gas (50 : 50 vol% CO_2/CH_4) CO_2 permeability up to a CO_2 partial pressure of ~15 bar.[393] When comparing the mixed-gas CO_2/CH_4 selectivity (Fig. 61d), both samples showed similar decreases over the pressure range considered.[393]

In Fig. 61b, pure-gas high-pressure CO_2 permeation data is shown for PIM-1, as well as two thermally crosslinked decarboxylated PIMs, denoted as "DC-PIM-1" and "DC-PIM-2".[391] Before thermal crosslinking, PIM-1 underwent a controlled base hydrolysis reaction to convert the nitrile groups into

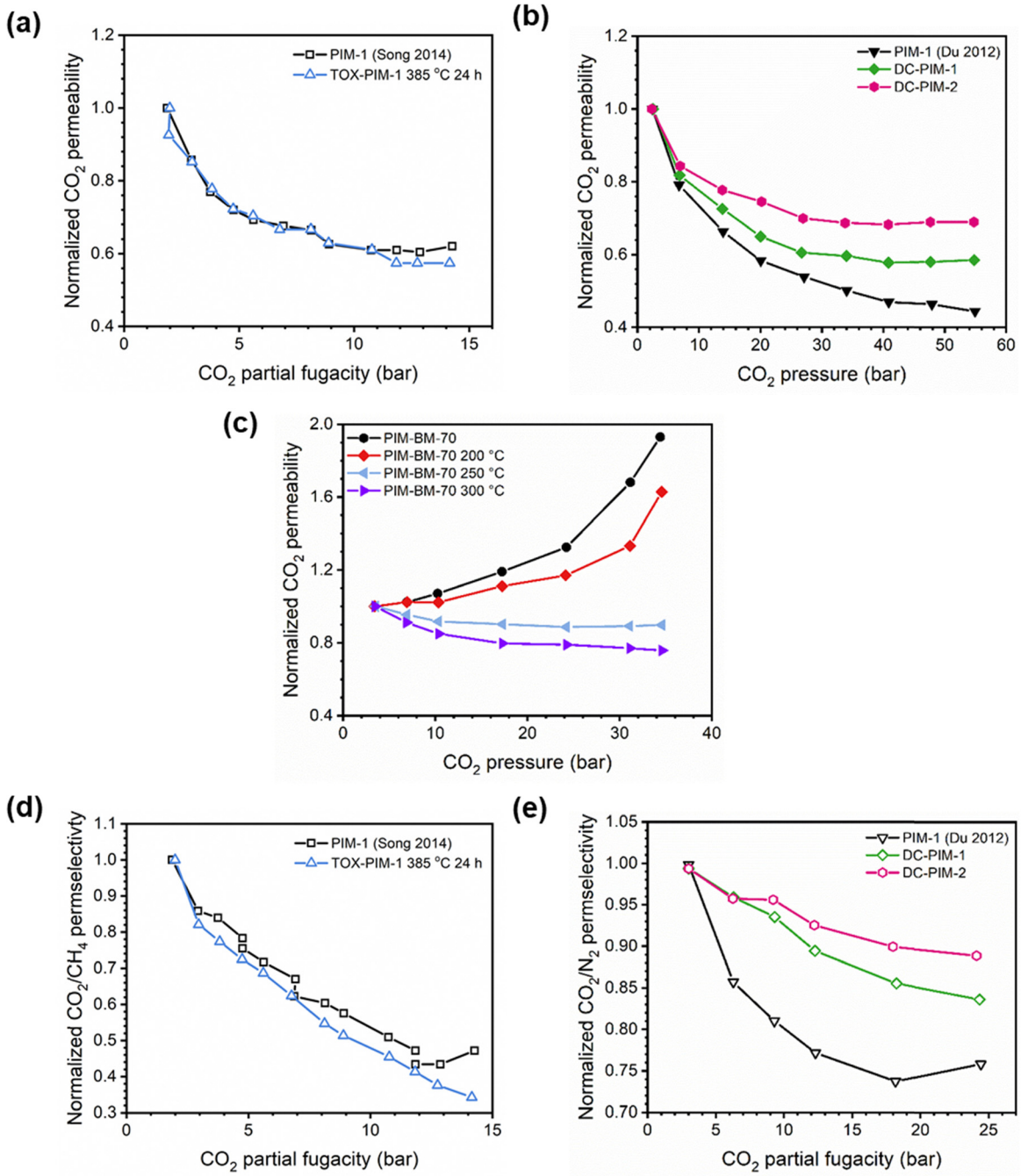

Fig. 61 Normalized CO_2 permeability *vs.* CO_2 pressure/fugacity for thermally crosslinked samples including (a) TOX-PIM-1,[393] (b) decarboxylated PIM-1,[391] and (c) PIM-BM-70.[394] (d) normalized CO_2/CH_4 permselectivity for TOX-PIM-1,[393] and (e) normalized CO_2/N_2 permselectivity for decarboxylated PIM-1[391] *vs.* CO_2 fugacity.

carboxyl groups.[391] C-PIM-1 (degree of hydrolysis = ~22%) and C-PIM-2 (degree of hydrolysis = ~41%) were then thermally crosslinked to form DC-PIM-1 and DC-PIM-2.[391] While PIM-1, DC-PIM-1, and DC-PIM-2 do not show signs of CO_2-induced plasticization pressure points up to a feed pressure of 55 bar, PIM-1 is severely affected by strongly sorbing CO_2 (as evident by the large decrease in CO_2 permeability as pressure increases).[391] However, with increased degrees of hydrolysis and crosslinking, DC-PIM-1 and DC-PIM-2 experience a smaller change in permeability.[391] This relative change in normalized CO_2 permeability with increasing pressure does not indicate plasticization resistance, but is likely a result of decreased CO_2 sorption capacity.[450] Fig. 61e presents the normalized mixed-gas selectivity for CO_2/N_2 (90 : 10) for PIM-1, DC-PIM-1, and DC-PIM-2. Notably, the change in selectivity over the fugacity range tested for DC-PIM-1 and DC-PIM-2 is less than that for PIM-1, which the authors attributed to the presence of crosslinks rigidifying the polymer chains and suppressing plasticization.[391] This example

showcases the importance of mixed-gas testing to elucidate the effects of plasticization. Fig. 61c shows the effects of increasing levels of thermal crosslinking (with increasing temperatures and hold times) on the pure-gas high-pressure CO_2 permeation of PIM-BM-70.[394] As the degree of crosslinking of PIM-BM-70 increases, the film becomes more plasticization-resistant as evident by the stabilization of CO_2 permeability with increasing feed pressure.[394]

Fig. 62 displays two examples of chemical crosslinking on microporous polymers for high-pressure permeation tests.[396,397] As seen in Fig. 62a, Du *et al.* found that crosslinking PIM-1 with either 4-azido phenyl sulfone (azide1) or 2,6-bis(4-azidobenzylidene)-4-methylcyclohexanone (azide2) (PIM-1/azide mol ratio = 80/20) led to more stable pure-gas CO_2 permeabilities up to a feed pressure of ~20 bar.[396] Pure- and mixed-gas CO_2/CH_4 high-pressure tests for PIM-1/azide1 and PIM-1/azide2 are shown in Fig. 62c.[396] In the pure- and mixed-gas (80 : 20 or 50 : 50 mol% CO_2/CH_4) scenarios, crosslinking led to more stable permselectivities across all pressures tested, suggesting that chemical crosslinking can increase plasticization resistance.[396] In Fig. 62b, Khan *et al.* found that crosslinking PIM-1 with 5 wt% PEG-biazide led to increased stability of pure-gas CO_2 permeability up to a feed pressure of ~30 bar, but further increasing the amount of PEG-biazide up to 20 wt% led to minimal improvements.[397] The normalized high-pressure pure-gas CO_2/CH_4 selectivity as a function of pressure for PIM-1/PEG-biazide is shown in Fig. 62d, where the addition of PEG-biazide led to more stable selectivity.[397] Of course, these pure-component tests may not fully capture plasticization effects that would be more apparent in mixed-gas tests.

5.1.3. Composites, blends, and copolymers. As discussed in Section 4, multi-component systems such as MMMs, polymer blends, and copolymers have been considered for plasticization resistance in microporous polymers. To show a few examples, Fig. 63a–d present high-pressure CO_2 permeation tests for a few select MOF-based MMMs formed with microporous polymers. Fig. 63a depicts pure-gas high-pressure CO_2 permeation data of PIM-1, as well as ZIF-7/PIM-1 and NH_2-ZIF-7/PIM-1. Interestingly, the addition of ZIF-7 resulted in CO_2 permeabilities that changed less with pressure than PIM-1. Even smaller changes in

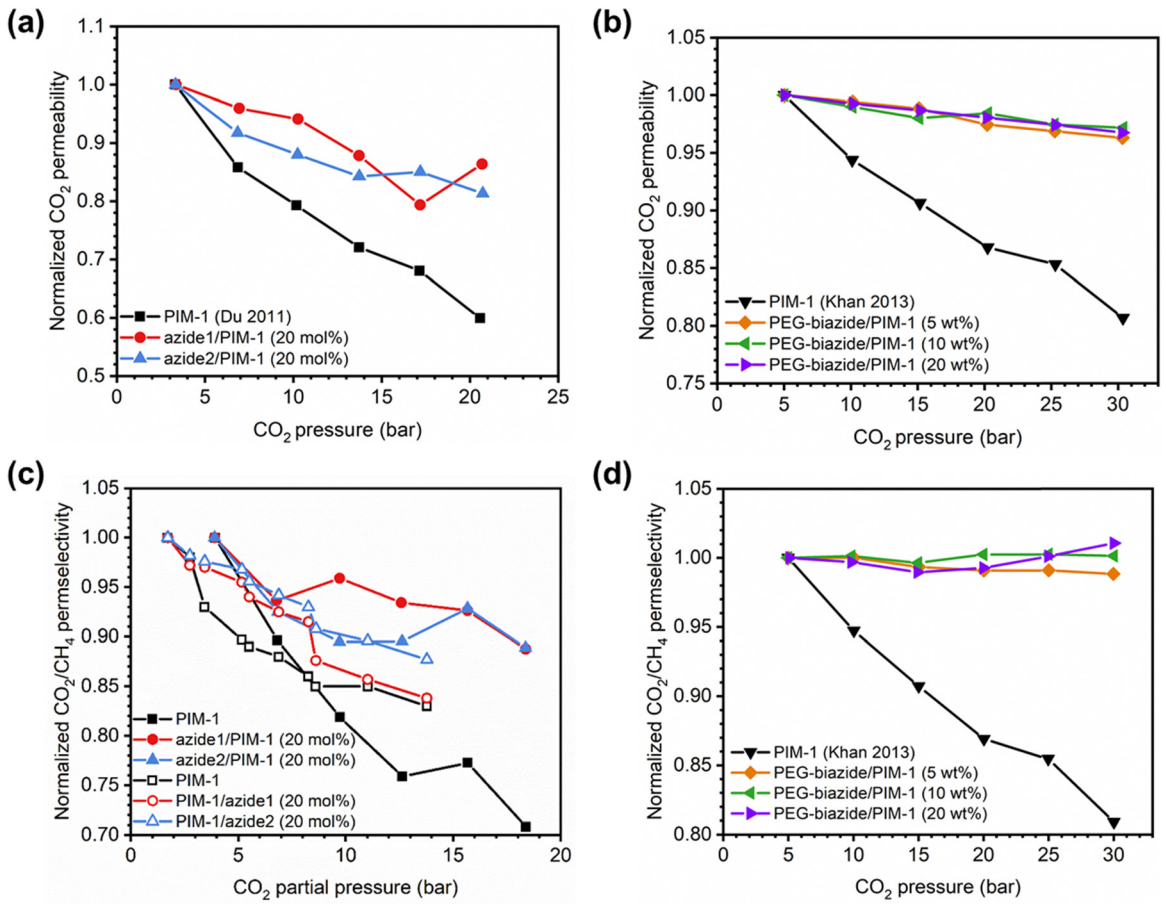

Fig. 62 Normalized CO_2 permeability *vs.* CO_2 pressure for PIM-1 samples chemically crosslinked with (a) azides[396] and (b) PEG-biazide.[397] CO_2 pressure *vs.* normalized CO_2/CH_4 permselectivity for PIM-1 samples crosslinked with (c) azides[396] and (d) PEG-biazide.[397] Filled symbols represent pure-gas measurements, while unfilled symbols represent mixed-gas measurements. For (c), mixed-gas CO_2/CH_4 compositions tested were 50 : 50 or 80 : 20 mol%. Total feed pressures tested were 3.4, 6.9, 10.3, 13.8, and 17.2 bar, which correspond to 1.7, 3.4, 5.2, 6.9, and 8.6 bar CO_2 partial pressures (50 : 50 mol%) and 2.76, 5.51, 8.26, 11.02, and 13.8 bar CO_2 partial pressures (80 : 20 mol%). Note that (d) presents ideal selectivities calculated from pure-gas tests.

CO_2 permeability were recorded with the addition of NH_2-ZIF-7.[421] Similar results were reported for UiO-66/PIM-1 MMMs, where UiO-66-NH_2 in PIM-1 resulted in smaller changes in mixed-gas CO_2 permeability compared to UiO-66 fillers. An *in situ* crosslinked MMM (PIM-*co*-UiO-66) experienced very small changes in normalized CO_2 permeability over the pressure range tested, and the authors suggested that this finding was due to crosslinks that enabled less polymer chain movement (Fig. 63b).[423] The addition of ZIF-8 to both PIM-1 and TOX-PIM-1[416] and the crosslinking of MOF-74 to PIM-1[434] similarly result in smaller changes in normalized CO_2 permeability over the tested pressure range in mixed-gas conditions (50 : 50 vol% CO_2/CH_4), as highlighted in Fig. 63c and d. These findings contrast those of polyimide/MOF MMMs, where normalized CO_2 permeaility, while more stable, often decreases with MOF addition.[451–455] Thus, an additional figure of merit needs to be considered to better understand the role of plasticization for MOF-based MMMs formed with microporous polymers.

As previously highlighted, high-pressure CO_2 permeability is often insufficient for determining the degree of plasticization resistance for a sample, especially when plasticization pressures (as often indicated by an increase in CO_2 diffusivity) are not observed within the pressure range considered. This effect is demonstrated in Fig. 63e, which presents high-pressure mixed-gas CH_4 permeabilities for select MMMs as a function of CO_2 partial pressure. While previously discussed CO_2 data showed an apparent stabilization of permeability with MOF incorporation, MOF addition does not always result in stable CH_4 permeabilities as feed pressure increases, indicating susceptibility to plasticization. For instance, over the pressure range tested, the addition of UiO-66 to PIM-1 resulted in a slight increase in normalized CH_4 permeability while addition of UiO-66-NH_2 to PIM-1 led to more stabilized CH_4 permeabilities, due to increased interfacial compatibility from the amine.[421] It was also found that the addition of ZIF-8 to either PIM-1 or TOX-PIM-1 led to slightly increased normalized CH_4 permeability over the pressure ranges tested.[416]

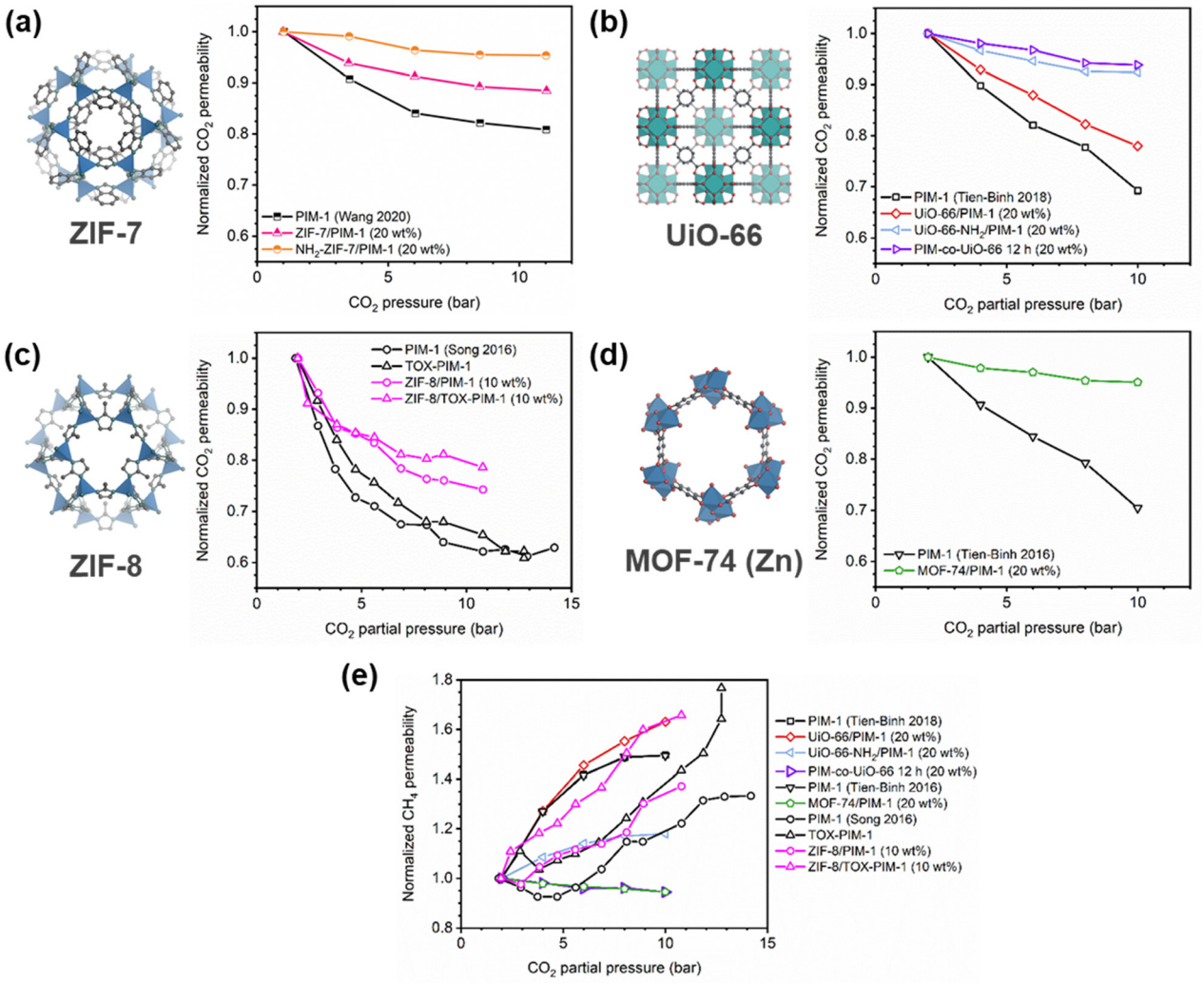

Fig. 63 (a)–(d) Normalized CO_2 permeability *vs.* CO_2 pressure for select MMMs.[416,421,423,434] (a) represents data for pure-gas measurements, while (b)–(d) represents data for mixed-gas measurements. (e) Normalized CH_4 permeability *versus* CO_2 partial pressure for mixed-gas tests for select MMMs. For ease of comparison, crystal structures of unfunctionalized MOFs are presented next to corresponding figures.

Compared to physical mixing of MOFs and polymers, one approach that shows consistent improvements in plasticization resistance is using MOF–polymer crosslinking. For instance, by chemically crosslinking PIM-1 and UiO-66 (PIM-*co*-UiO-66), the normalized CH_4 permeability over the pressure range tested was stable, suggesting plasticization resistance.[421] Similarly, crosslinking MOF-74 to PIM-1 resulted in a very stable normalized CH_4 permeability over the pressure range tested.[434]

High-pressure permeation tests have also been conducted on polymer blends as shown in Fig. 64. It was found that the integration of Torlon® into cPIM-1 improved plasticization resistance by forming hydrogen bonds and also reducing the intersegmental mobility in cPIM-1 (Fig. 64a).[410] Blends of Matrimid® and cPIM-1 were also studied. While Matrimid® had a pure-gas CO_2 plasticization pressure of ~5 bar, the addition of cPIM-1, even at a small loading of 5 wt%, increased the plasticization pressure up to ~10 bar (Fig. 64b).[225] The suppression of plasticization in Matrimid® by the addition of cPIM-1 was attributed to newly-formed hydrogen bonds between the polymers, as well as the inclusion of the rigid backbone of cPIM-1.[225]

5.1.4. High-pressure permeation considering gas mixtures in addition to CO_2. While CO_2 high-pressure permeation tests in pure- and mixed-gas cases are the most commonly used to study plasticization, C_3H_6/C_3H_8 and $CO_2/CH_4/H_2S$ mixtures have also been reported. Fig. 65a and b show normalized high-pressure permeation tests in select microporous polymer samples for C_3H_6 and C_3H_8, respectively. Although KAUST-PI-1 displays stronger intrachain rigidity than PIM-PI-1, its C_3H_6 and C_3H_8 permeabilities increased more rapidly for the pressure range tested, again bolstering the claim that intrachain rigidity alone cannot suppress plasticization.[90,329,334] When considering the sorption isotherms (Fig. 65c), which were fit using the dual-mode sorption model, KAUST-PI-1 possessed higher C'_H values for C_3H_6 and C_3H_8 (72 and 70 $cm_{STP}^3\ cm_{pol}^{-3}$, respectively) than PIM-PI-1 (69 and 63 $cm_{STP}^3\ cm_{pol}^{-3}$, respectively), which is consistent with the more microporous structure of KAUST-PI-1.[329] However, the k_d values for KAUST-PI-1 for C_3H_6 and C_3H_8 (7.9 and 6.1 $cm_{STP}^3\ cm_{pol}^{-3}\ bar^{-1}$, respectively) are lower than those for PIM-PI-1 (9.9 and 9.0 $cm_{STP}^3\ cm_{pol}^{-3}\ bar^{-1}$, respectively), which the authors attributed to the spirobisindane unit of PIM-PI-1 facilitating slightly higher chain mobility than the triptycene unit in KAUST-PI-1 and increasing gas uptake in the equilibrium sorption mode.[329] KAUST-PI-1 has a strongly sieving microstructure with narrower ultramicropores (promoted by intrachain rigidity) than PIM-PI-1 and was also found to be more susceptible to plasticization.[90,329] PIM-6FDA-OH, on the other hand, sorbs less gas than both KAUST-PI-1 and PIM-PI-1.[159] The normalized C_3H_6 and C_3H_8 permeability profiles of PIM-6FDA-OH (Fig. 65a and b) are also considerably more stable with increasing pressure than those of KAUST-PI-1 and PIM-PI-1.[159] The presence of the hydrogen bonding –OH group in PIM-6FDA-OH creates a denser polymer structure through secondary forces and facilitates CTC formation,[159] which help to decrease polymer chain translational motion and mitigate plasticization effects. The lower sorption capacity of PIM-6FDA-OH compared to KAUST-PI-1 and PIM-PI-1 (Fig. 65c) can be attributed to the tighter packing in PIM-6FDA-OH, restricting gas sorption.[159,373]

Both thermal annealing[159] and addition of nitrogen-containing ZIF-8[414] to PIM-6FDA-OH also led to a more stable C_3H_6 permeability and a lower normalized C_3H_8 permeability (Fig. 65a and b). Thermal annealing facilitated CTC formation and improved plasticization resistance,[159] similar to earlier results for TPDA-ATAF and TPDA-APAF discussed in Section 5.1.2.[34] The strong molecular interactions between the hydroxyl groups in PIM-6FDA-OH and the nitrogen in ZIF-8 also restricted polymer chain mobility, improving plasticization resistance.[414] In addition, TR and CMS analogues of PIM-6FDA-OH were tested (Fig. 65a and b), and it was found that, while both analogues did not show signs of plasticization over the pressure range tested, the mixed-gas permeabilities of C_3H_6 and C_3H_8 for the CMS film decreased more with increasing pressure than those for the TR film.[373] This result is consistent with earlier examples of CO_2/CH_4 mixed-gas tests for CMS and TR PIM-6FDA-OH and indicative of how such thermal treatments can induce plasticization resistance when considering different mixtures.[372]

Mixtures involving H_2S have also been considered for plasticization studies in microporous polymers particularly since

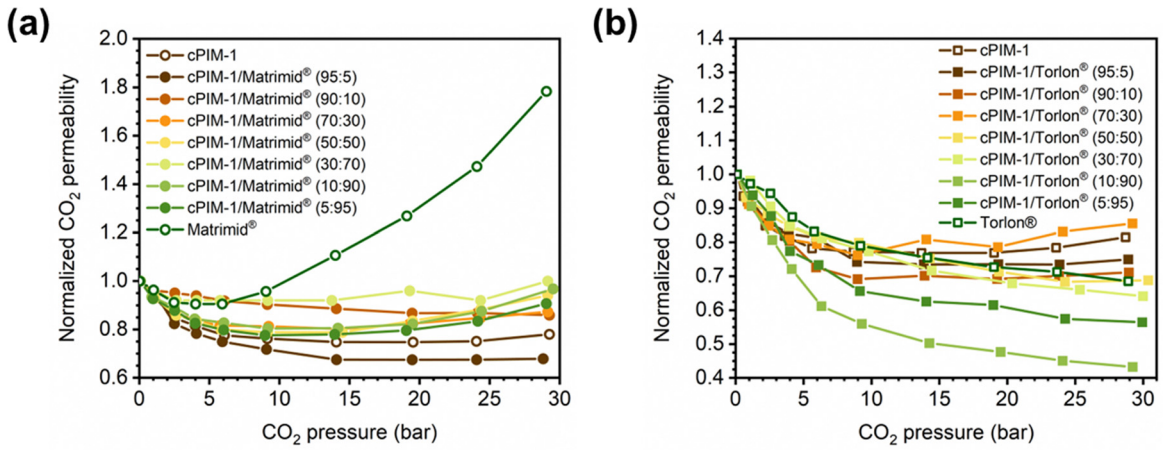

Fig. 64 Normalized CO_2 permeability *vs.* CO_2 pressure for (a) a set of cPIM and Matrimid® blends,[225] and (b) a set of cPIM and Torlon® blends.[410]

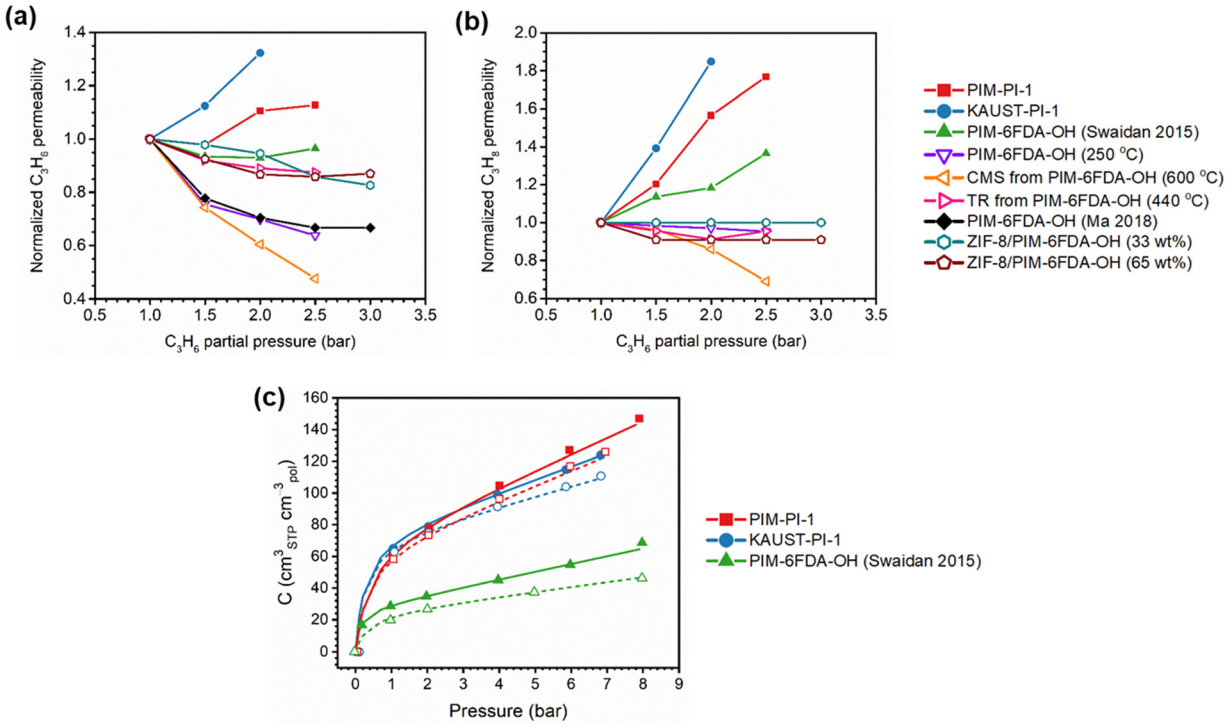

Fig. 65 Normalized (a) C_3H_6 and (b) C_3H_8 permeabilities *vs.* C_3H_6 pressure for select polymers tested in the literature.[159,329,373,414] Filled symbols represent untreated samples, while unfilled symbols represent samples that either contain fillers or are treated. (c) Reported C_3H_6 (solid lines, filled symbols) and C_3H_8 (dashed lines, unfilled symbols) sorption isotherms that were fit using the dual-mode sorption model for PIM-6FDA-OH, KAUST-PI-1, and PIM-PI-1.[159,329]

H_2S is a highly condensable contaminant commonly found in natural gas and biogas.[48,348,456] Due to its high condensability and critical temperature (T_c = 373.1 K) that result in increased sorption, the presence of H_2S in a mixture can lead to significant dilation and plasticization. The relative sorption capacity for H_2S compared to less condensable gases found in natural gas (*i.e.*, CO_2 and CH_4) is shown in Fig. 66a–c for several samples, where H_2S sorption for PIM-1, PIM-6FDA-OH, and AO-PIM-1 is significantly higher than that of CO_2 (T_c = 304.13 K), and CH_4 (T_c = 190.55 K).[48,348] Consequently, H_2S will typically result in significantly increased normalized permeabilities in high-pressure pure-gas tests. Yi *et al.* demonstrated this effect in PIM-6FDA-OH, where in a 15 : 15 : 70 $H_2S/CO_2/CH_4$ mixture tested from 7 to 48 bar total pressure, the normalized mixed-gas H_2S permeability increased by almost three-fold at the highest pressure, while that of CO_2 decreased to about 60% of its original value at 7 bar total pressure and CH_4 permeability remained nearly constant (Fig. 66d–f).[48] Interestingly, while the mixed-gas CO_2/CH_4 selectivity decreased with increasing pressure, the H_2S/CH_4 selectivity increased (Fig. 66g–h). This result is indicative of competitive sorption effects, where CO_2 and H_2S compete for the Langmuir sorption modes, and the more condensable gas (H_2S) will outcompete other gases in the mixture and result in decreased CO_2 permeability and increased H_2S/CH_4 sorption selectivity in the mixed-gas case.[48] While CO_2/CH_4 selectivity is controlled by both diffusion and sorption selectivity, H_2S/CH_4 selectivity is dominated by sorption selectivity.[100,348] Competitive sorption effects will be discussed in more detail in Section 5.2. Similar trends in CO_2/CH_4 and H_2S/CH_4 selectivity were found for PIM-1, AO-PIM-1 (fresh), and AO-PIM-1 (rejuvenated) tested in a 20 : 20 : 60 mol% $H_2S/CO_2/CH_4$ mixture.[348] Examples of this phenomenon have been reported for polyimide films as well.[100,318,457–459] Recently, Liu *et al.* found that 6FDA-DAM displayed increasing H_2S/CH_4 selectivity up to ~31 when exposed to a 20 : 20 : 60 $H_2S/CO_2/CH_4$ ternary gas mixture at a total feed pressure of 46 bar, even with a decrease in CO_2/CH_4 selectivity from ~30 to ~18 and a plasticization pressure for CO_2 at around 28 bar.[100]

5.1.5. Summary of high-pressure permeation data in literature. Table 4 reports the pure-gas CO_2 plasticization pressures of microporous polymers in literature, as well as thickness, Young's Modulus, T_g, permeability, and treatment and test conditions, where available. Tables 5 and 6 display analogous tables for C_3H_6 and H_2S plasticization pressure points, respectively, along with mixture composition if applicable. Many polymers listed in Tables 4–6 are reported to have thicknesses on the micron scale (*i.e.*, >1 μm). However, one notable example of thinner membranes (*i.e.*, <1 μm) was reported by Tiwari *et al.*, in which three different thicknesses of PIM-1 were tested (30 μm, 1 μm, and 200 nm).[460] While the thick PIM-1 film (30 μm) displayed a CO_2 plasticization pressure of ~8 atm, both of the thinner PIM-1 films (1 μm and 200 nm) showed immediate increase in CO_2 permeability with increasing CO_2 pressure.[460] This result indicates that thin films (*i.e.*, <1 μm) are affected by plasticization more than thick films (*i.e.*, >1 μm). Given that thinner membranes are more ideal in an industrial setting in order to

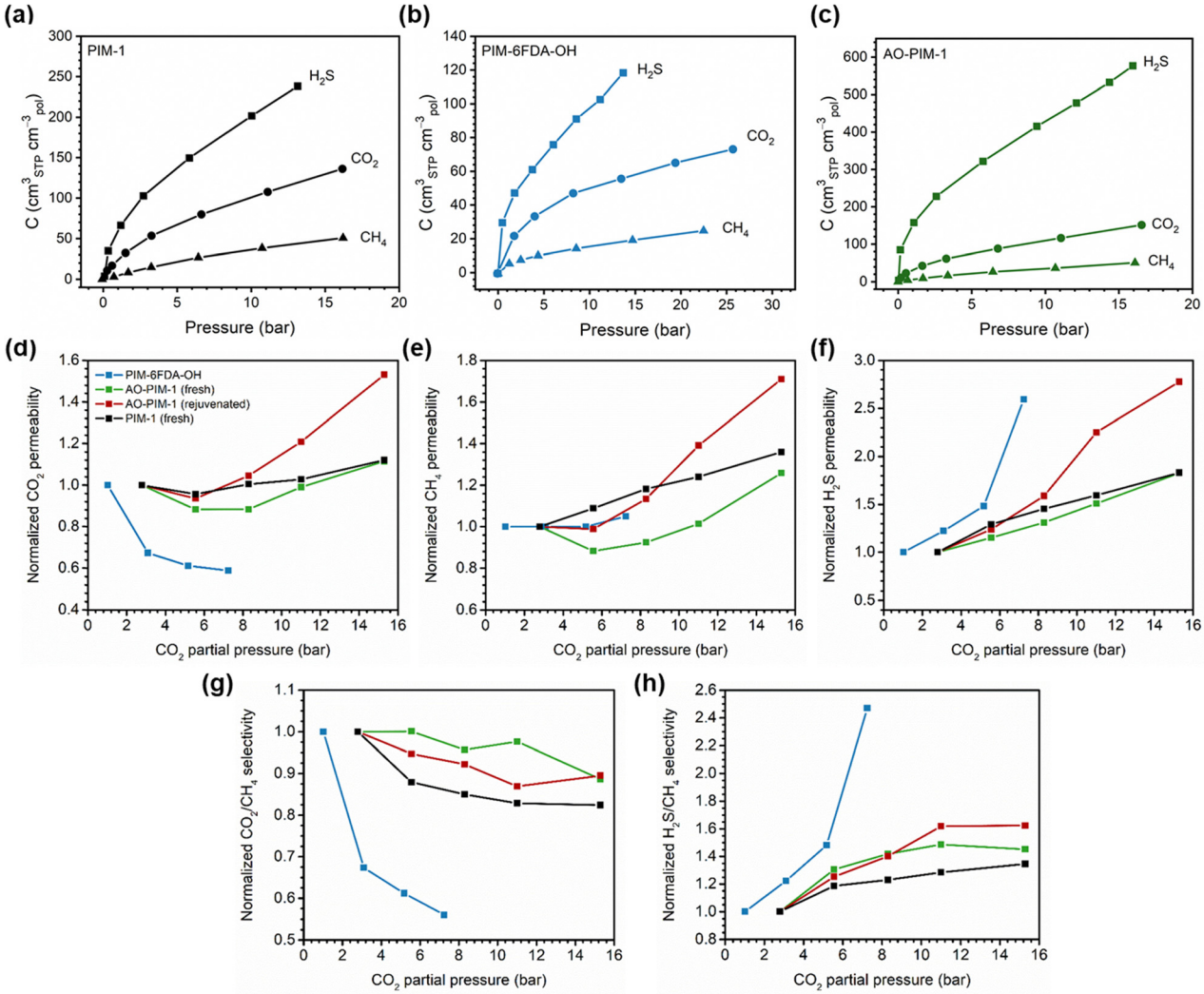

Fig. 66 H_2S, CO_2, and CH_4 pure-gas sorption isotherms for (a) PIM-1,[348] (b) PIM-6FDA-OH,[48] and (c) AO-PIM-1.[348] Normalized (d) CO_2, (e) CH_4, and (f) H_2S permeabilities and (g) CO_2/CH_4 and (h) H_2S/CH_4 selectivities in a $CO_2/CH_4/H_2S$ ternary mixture *versus* CO_2 partial pressure for PIM-1,[348] AO-PIM-1,[348] and PIM-6FDA-OH.[48] Data was collected at 35 °C.

maximize productivity, comparing the performance of thick *versus* thin membranes should be considered when evaluating the performance of promising polymers.

As mentioned in Section 3, T_g and mechanical properties correlate with chain mobility and plasticization resistance. For many of the samples tabulated, no T_g was detected due to polymer degradation before T_g. In general, the glass transition temperatures of microporous polymers are higher than those of other polymers, which is consistent with their ultrahigh backbone stiffness and limited chain mobility. However, because most microporous polymers considered in Tables 4–6 do not detect a T_g within the testing temperatures, a direct correlation between T_g and plasticization pressure is not possible. Specialized methods such as molecular dynamics simulation and ultrafast DSC, as mentioned in Section 3, can be used to extract information on the T_g and should be taken into consideration to establish relationships between T_g and plasticization pressure in the future.

Furthermore, for the samples considered in Tables 4–6, the Young's Modulus ranged from 0.39 to 2.80 GPa, which is similar to results found for traditional glassy polymers.[461] However, no clear relationships were found between the Young's Modulus and the plasticization pressure, indicating that mechanical properties alone cannot be used to predict a polymer's susceptibility to plasticization.

5.1.6. CO_2 concentration at the plasticization pressure. As discussed in Section 2, studying permeation with increasing pressure can result in a minimum permeability value, where increases in diffusion can be offset by decreases in sorption. In 1999, Bos *et al.* proposed that a polymer would undergo plasticization upon reaching a CO_2 concentration of 38 ± 7 cm_{STP}^3 cm_{pol}^{-3}.[42] Since that initial report, a variety of new microporous polymers have been synthesized with ultrahigh sorption, allowing for a comparison between plasticization pressures and sorption for many new materials.[80] Here, we evaluate the relationship between the concentration of the plasticizing penetrant (CO_2) and the

Table 4 Reported pure-gas CO_2 plasticization pressures of microporous polymers in literature. Permeabilities are reported for the given test temperature and test pressure

Polymer name	Membrane treatment conditions	Thickness (μm)	Young's modulus (GPa)	T_g (°C)	Test temperature (°C)	Test pressure (bar)	CO_2 permeability (barrer)	CO_2 plasticization pressure (bar)	Ref.
cPIM-1/Torlon® (5 : 95)	40 °C vacuum 12 h; 75 °C vacuum 24 h; 250 °C vacuum 12 h	50 ± 5	n/a	278	35	~3.5	0.68	>30	410
cPIM-1/Torlon® (10 : 90)	40 °C vacuum 12 h; 75 °C vacuum 24 h; 250 °C vacuum 12 h	50 ± 5	n/a	285	35	~3.5	1.23	>30	
cPIM-1/Torlon® (30 : 70)	40 °C vacuum 12 h; 75 °C vacuum 24 h; 250 °C vacuum 12 h	50 ± 5	n/a	286, 415	35	~3.5	4.82	>30	
cPIM-1/Torlon® (50 : 50)	40 °C vacuum 12 h; 75 °C vacuum 24 h; 250 °C vacuum 12 h	50 ± 5	n/a	297, 403	35	~3.5	21.4	>30	
cPIM-1/Torlon® (70 : 30)	40 °C vacuum 12 h; 75 °C vacuum 24 h; 250 °C vacuum 12 h	50 ± 5	n/a	319, 399	35	~3.5	440	>30	
cPIM-1/Torlon® (90 : 10)	40 °C vacuum 12 h; 75 °C vacuum 24 h; 250 °C vacuum 12 h	50 ± 5	n/a	360, 399	35	~3.5	1013	>30	
cPIM-1/Torlon® (95 : 5)	40 °C vacuum 12 h; 75 °C vacuum 24 h; 250 °C vacuum 12 h	50 ± 5	n/a	n/a	35	~3.5	1382	>30	
cPIM-1	40 °C vacuum 12 h; 75 °C vacuum 24 h; 250 °C vacuum 12 h	50 ± 5	n/a	n/a	35	~3.5	2654	20	
KAUST-PI-1	120 °C vacuum 24 h; MeOH 24 h; 120 °C vacuum 24 h	70	n/a	>350	35	2	2329	<2	90
KAUST-PI-5	120 °C vacuum 24 h; MeOH 24 h; 120 °C vacuum 24 h	70	n/a	>350	35	2	1560	10	
cPIM-1/Matrimid® (5 : 95)	25 °C min^{-1} to 250 °C then hold in vacuum 12 h	50 ± 5	2.60 ± 0.34	325	35	~3.5	13.6	9	225
cPIM-1/Matrimid® (10 : 90)	25 °C min^{-1} to 250 °C then hold in vacuum 12 h	50 ± 5	2.71 ± 0.11	332	35	~3.5	17.9	9	
cPIM-1/Matrimid® (30 : 70)	25 °C min^{-1} to 250 °C then hold in vacuum 12 h	50 ± 5	2.05 ± 0.99	352	35	~3.5	48.7	9	
cPIM-1/Matrimid® (50 : 50)	25 °C min^{-1} to 250 °C then hold in vacuum 12 h	50 ± 5	1.84 ± 0.94	361	35	~3.5	145	9	
cPIM-1/Matrimid® (70 : 30)	25 °C min^{-1} to 250 °C then hold in vacuum 12 h	50 ± 5	1.95 ± 0.79	370	35	~3.5	486	14	
cPIM-1/Matrimid® (90 : 10)	25 °C min^{-1} to 250 °C then hold in vacuum 12 h	50 ± 5	n/a	>450	35	~3.5	982	9	
cPIM-1/Matrimid® (95 : 5)	25 °C min^{-1} to 250 °C then hold in vacuum 12 h	50 ± 5	n/a	>450	35	~3.5	2268	14	
cPIM-1	25 °C min^{-1} to 250 °C then hold in vacuum 12 h	50 ± 5	n/a	>450	35	~3.5	2654	14	
(PIM-PI)-(6FDA-durene-PI)(1 : 4)	70 °C for 24 h once, then peeled membrane off, then 70 °C for 24 h again	45–55	n/a	n/a	30	2	1265	>2	462
TPDA-APAF	120 °C vacuum 24 h; 250 °C vacuum 24 h	45–60	1.13	>350	35	2	46	>25	34
TPDA-ATAF	120 °C vacuum 24 h; 250 °C vacuum 24 h	45–60	1.99	>350	35	2	125	>25	
TPDA-APAF	120 °C vacuum 24 h	45–60	1.13	>350	35	2	99	10	
TPDA-ATAF	120 °C vacuum 24 h	45–60	1.99	>350	35	2	325	10	
6FDA-TrMPD	200 °C vacuum 24 h	85	1.2 ± 0.1	397	35	2	498	>16	342
6FDA-TrMCA	200 °C vacuum 24 h	85	1.1 ± 0.1	>360	35	2	144	>16	
PIM-6FDA-OH	*n*-Hexane/DCM (90/10) 24 h; air-dried; 120 °C vacuum 24 h	80–100	n/a	>330	35	1	263	7	346
PIM-PMDA-OH	*n*-Hexane/DCM (90/10) 24 h; air-dried; 120 °C vacuum 24 h	80–100	n/a	>330	35	1	198	5	
AO-PIM-1	MeOH 24 h; 120 °C vacuum 24 h	80–100	n/a	n/a	35	2	1153	>10	347
PIM-1	MeOH 24 h; 120 °C vacuum 24 h	80–100	n/a	n/a	35	2	5919	>10	
TPDA-mPDA	MeOH 24 h; air-dried; 120 °C vacuum (24 h)	40 ± 5	n/a	n/a	35	2	349	>20	343
TDA-DAR	MeOH 24 h; air-dried; 120 °C vacuum 24 h	40 ± 5	n/a	n/a	35	2	215	>20	
PMDA-DAT	200 °C vacuum 24 h	70–80	n/a	>450	35	1	51.4	15.2	331
CF_3-ROMP	EtOH 48 h; air-dried 24 h; 35 °C vacuum 8 h	119	n/a	>350	35	1	18 490	>51	39
OMe-ROMP	EtOH 48 h; air-dried 24 h; 35 °C vacuum 8 h	160	n/a	>300	35	1	2900	>51	
PIM-1	EtOH 48 h; air-dried 24 h; 35 °C vacuum 8 h	119	n/a	n/a	35	1	12 318	27	
CTTB	MeOH 12 h; RT 3 d	54	0.42	>380	35	2	3087	<2	335
MTTB	MeOH 12 h; RT 3 d	60	0.44	>380	35	2	3155	<2	
ITTB	MeOH 12 h; RT 3 d	54	0.50	>380	35	2	3901	<2	
6FDA-HB	120 °C vacuum overnight; MeOH 12 h; 120 °C vacuum 24 h	70 ± 5	0.72	n/a	35	2	286	>15	328
TDAi3-HB	120 °C vacuum overnight; MeOH 12 h; 120 °C vacuum 24 h	70 ± 5	2.12	n/a	35	2	998	>15	
PIM-1	120 °C vacuum 12 h; MeOH 12 h; 120 °C vacuum 24 h	102	n/a	n/a	35	2	5921	>10	28
TPIM-1	120 °C vacuum 12 h; MeOH 12 h; 120 °C vacuum 24 h	103	n/a	n/a	35	2	1551	<2	
TPIM-2	120 °C vacuum 12 h; MeOH 12 h; 120 °C vacuum 24 h	46	n/a	n/a	35	2	412	>15	
PIM-Trip-TB	MeOH 24 h; 120 °C vacuum 20 h	105	n/a	n/a	n/a	1	4109	14.2	334
TDA1-APAF	MeOH 10 h; air-dried; 250 °C vacuum 12 h	70 ± 5	n/a	n/a	35	2	40	>15	345
TDA1-APAF	MeOH 10 h; air-dried; 250 °C vacuum 12 h; aged 250 d	70 ± 5	n/a	n/a	35	2	30	>15	
PIM-TMN-Trip	MeOH 24 h	161	n/a	n/a	25	1	10 910	3	463
PIM-TMN-Trip	MeOH 24 h; 25 °C at 500 kPa for 2 weeks	161	n/a	n/a	25	1	9480	1.7	
PIM-1	130 °C 12 h	40–60	n/a	n/a	35	1	2800	15	138
PIM-COOH	130 °C 12 h	40–60	n/a	n/a	35	1	290	5	

Table 4 (*continued*)

Polymer name	Membrane treatment conditions	Thickness (μm)	Young's modulus (GPa)	T_g (°C)	Test temperature (°C)	Test pressure (bar)	CO_2 permeability (barrer)	CO_2 plasticization pressure (bar)	Ref.
TZPIM-2	Washed in water (pH = 4–5) several times; soaked in MeOH; 120 °C vacuum 12 h	70–90	n/a	>350	22	1	3083	>17	37
PIM-1	80 °C vacuum 12 h	30	n/a	n/a	30	4	3799	>12	409
PIM-1/PEG 20k kDA (2.5 wt%)	80 °C vacuum 12 h	30	n/a	n/a	30	4	2278	>12	
AM_93a	MeOH overnight; RT 24 h	76	n/a	n/a	25	1	1740	>1	358
PIM-6FDA-OH	120 °C vacuum 12 h; 250 °C vacuum 24 h	n/a	n/a	>380	35	~2.2	143	19	48
(PIM-PI)x-*b*-(PI)y (x : y= 9 : 36 or 1 : 4)	70 °C 24 h	40–50	2.25	390	30	2	3011	>2	464
DFTTB	MeOH 12 h; RT 24 h	65	0.39	>350	30	2	3146	5	336
PIM-1	Cast from chloroform; 80 °C vacuum 24 h; 110 °C vacuum 48 h	30	n/a	n/a	35	2	10 675	8	460
PIM-1	Cast from chloroform; 80 °C vacuum 24 h; 110 °C vacuum 48 h	1	n/a	n/a	35	2	551	<2	
PIM-1	Cast from o-DCB; 80 °C vacuum 24 h; 110 °C vacuum 48 h	0.2	n/a	n/a	35	2	412	<2	
6FDA-DAT1-OH	120 °C vacuum 24 h; 200 °C vacuum 24 h	75 ± 5	n/a	n/a	35	2	70	>20	344
6FDA-DAT1	MeOH 10 h; air-dried; 120 °C vacuum 12 h	65 ± 5	n/a	n/a	35	2	120	8	333
6FDA-DAT2	MeOH 10 h; air-dried; 120 °C vacuum 12 h	65 ± 5	n/a	n/a	35	2	210	8	
FPIM-5	MeOH 12 h; 120 °C vacuum 12 h; soaked with 5 : 95 F_2/N_2 gas at 4 bar 5 min	45	1	n/a	35	2	22.3	<2	465
HSBI-NO_2	RT 24 h; dried in 180 °C tube furnace under N_2 2 h	70	1.94	n/a	35	2	144	>15	466
PIM-1	130 °C vacuum 12 h	58.0 ± 0.9	n/a	n/a	35	~1.2	9000	~14	142
PIM-NH_2	MeOH 24 h; 130 °C vacuum 12 h	49 ± 2	n/a	n/a	35	~1.2	1070	>29	
PIM-t-BOC	MeOH 24 h; 130 °C vacuum 12 h	70 ± 9	n/a	n/a	35	~1.2	110	~10	
PIM-deBOC(acid)	MeOH 24 h; 130 °C vacuum 12 h	65.0 ± 0.6	n/a	n/a	35	~1.2	460	>29	
PIM-deBOC(thermal)	MeOH 24 h; 130 °C vacuum 12 h	83 ± 2	n/a	n/a	35	~1.2	630	>29	
UiO-66-CN@sPIM-1 (20 wt%)	Heated in N_2 flow (25 ml min^{-1}) from 30 to 250 °C (1 °C min^{-1}), then held for 24 h	26	1.30	n/a	25	1.4	16 121	<1.4	425
PIM-1	MeOH 4 h; 120 °C 16 h	109.4 ± 4.2	0.530 ± 0.152	n/a	30	2	6211	>30	438
f-MWCNTs/PIM-1 (0.5 wt%)	MeOH 4 h; 120 °C 16 h	121.7 ± 3.9	0.626 ± 0.122	n/a	30	2	7535	>30	
f-MWCNTs/PIM-1 (1 wt%)	MeOH 4 h; 120 °C 16 h	113.4 ± 4.7	0.666 ± 0.153	n/a	30	2	7813	20	
f-MWCNTs/PIM-1 (2 wt%)	MeOH 4 h; 120 °C 16 h	117.5 ± 4.8	0.685 ± 0.175	n/a	30	2	12 274	25	
f-MWCNTs/PIM-1 (3 wt%)	MeOH 4 h; 120 °C 16 h	115.1 ± 5.1	0.640 ± 0.170	n/a	30	2	4816	<5	
PIM-1	MeOH 24 h; 120 °C vacuum 24 h	85 ± 5	1.01 ± 0.06	n/a	30	2	4533	>11	421
ZIF-7/PIM-1 (20 wt%)	MeOH 24 h; 120 °C vacuum 24 h	85 ± 5	1.16 ± 0.03	n/a	30	2	2663	>11	
NH_2-ZIF-7/PIM-1 (20 wt%)	MeOH 24 h; 120 °C vacuum 24 h	85 ± 5	1.23 ± 0.06	n/a	30	2	2953	>11	
OAPS/PIM-1 (5 wt%)	110 °C vacuum 24 h	70	2.80	n/a	25	4	3266	>10	437
PIM-EA(Me_2)-TB	n/a	100	n/a	n/a	25	2	8200	<2	467
PAF-1/PIM-EA(Me_2)-TB (10 wt%)	n/a	100	n/a	n/a	25	2	9780	<2	
PIM-EA(H_2)-TB	n/a	100	n/a	n/a	25	2	6660	<2	
PAF-1/PIM-EA(H_2)-TB (10 wt%)	n/a	100	n/a	n/a	25	2	14 120	<2	
PIM-1	Stirred at 25 °C (24 h) with 3-aminopropyl trimethoxysilane (5 wt%) and 0.1 M hydrochloric acid, washed three times with water	n/a	n/a	n/a	25	1	744	<1	468
PIM-*co*-MOF (23 wt%)	Stirred at 25 °C (24 h) with 3-aminopropyl trimethoxysilane (5 wt%) and 0.1 M hydrochloric acid, washed three times with water	n/a	n/a	n/a	25	1	639	<1	
MAPDA/PIM-1 (15 wt%)	RT 12 h	n/a	1.16	n/a	25	3	7862	<2	442
PPM-10@MMM	40 °C 48 h	40–50	n/a	n/a	30	1	3827	20	469
PIM-1	60 °C vacuum overnight	25	n/a	n/a	35	4	4110	<4	470
IL@MOF/PIM-1 (5 wt%)	60 °C vacuum overnight	25	n/a	n/a	35	4	9420	~16	
PIM-[durene(m)-*co*-PEG/PPG(n)]-PI (1 : 0.05)	70 °C vacuum 24 h; peeled from casting dish; 70 °C vacuum 24 h	40–50	1.67	n/a	30	~1	669	~10	471

Table 4 (*continued*)

Polymer name	Membrane treatment conditions	Thickness (μm)	Young's modulus (GPa)	T_g (°C)	Test temperature (°C)	Test pressure (bar)	CO_2 permeability (barrer)	CO_2 plasticization pressure (bar)	Ref.
PIM-[durene(m)-*co*-PEG/PPG(n)]-PI (1 : 0.10)	70 °C vacuum 24 h; peeled from casting dish; 70 °C vacuum 24 h	40–50	1.33	n/a	30	~1	349	~15	
PIM-1	120 °C vacuum 16 h	100–120	n/a	>400	30	1	8919	>30	397
Crosslinked PEG-biazide/PIM-1 (5 wt%)	120 °C vacuum 16 h	100–120	n/a	>400	30	1	2711	>30	
Crosslinked PEG-biazide/PIM-1 (10 wt%)	120 °C vacuum 16 h	100–120	n/a	>400	30	1	1565	>30	
Crosslinked PEG-biazide/PIM-1 (20 wt%)	120 °C vacuum 16 h	100–120	n/a	>400	30	1	433	>30	
PIM-1	175 °C vacuum 7.5 h	50–70	n/a	>350	25	3.4	3702	>20	396
Cross-linked azide1/PIM-1 (20 mol%)	175 °C vacuum 7.5 h	50–70	n/a	>350	25	3.4	80	>20	
Cross-linked azide2/PIM-1 (20 mol%)	175 °C vacuum 7.5 h	50–70	n/a	>350	25	3.4	219	>20	
PIM-Br	MeOH overnight; 80 °C vacuum	60 ± 10	0.0108 ± 0.0023	n/a	35	6.89	1853	<3.5	472
PIM-Br/PBI-95 : 5	MeOH overnight; 80 °C vacuum	60 ± 10	0.0229 ± 0.0030	n/a	35	6.89	1645	<3.5	
PIM-Br/PBI-85 : 15	MeOH overnight; 80 °C vacuum	60 ± 10	0.0405 ± 0.0036	n/a	35	6.89	1356	<3.5	
PIM-Br/PBI-95 : 5–150	MeOH overnight; 80 °C vacuum	60 ± 10	0.0260 ± 0.0046	n/a	35	6.89	1850	<3.5	
PIM-Br/PBI-95 : 5–250	MeOH overnight; 80 °C vacuum	60 ± 10	0.0348 ± 0.0060	n/a	35	6.89	2264	~21	
PIM-Br/PBI-95 : 5–300	MeOH overnight; 80 °C vacuum	60 ± 10	0.0376 ± 0.0031	n/a	35	6.89	3313	>41	
PIM-BM-70	Dipped in MeOH; 70 °C vacuum 24 h	n/a	n/a	n/a	25	3.4	1689	<3.4	394
PIM-BM-70 200 °C-10 h	Dipped in MeOH; 70 °C vacuum 24 h	n/a	n/a	n/a	25	3.4	508	<3.4	
PIM-BM-70–250 °C-10 h	Dipped in MeOH; 70 °C vacuum 24 h	n/a	n/a	n/a	25	3.4	142	>35	
PIM-BM-70–300 °C-5 h	Dipped in MeOH; 70 °C vacuum 24 h	n/a	n/a	n/a	25	3.4	48.3	>35	
PIM-1	Washed in acidified water, MeOH 1 h; air-dried; 200 °C 0.5 h; 375 °C 40 min	70–90	n/a	n/a	25	3.4	5093	>55	391
DC-PIM-1	Washed in acidified water, MeOH 1 h; air-dried; 200 °C 0.5 h; 375 °C 40 min	70–90	n/a	n/a	25	3.4	2345	>55	
DC-PIM-2	Washed in acidified water, MeOH 1 h; air-dried; 200 °C 0.5 h; 375 °C 40 min	70–90	n/a	n/a	25	3.4	1987	>55	
PIM-Trip-TB	100 °C 24 h	100	n/a	n/a	25	1	8616	>20	398
CoPIM-TB-1	100 °C 24 h	100	n/a	n/a	25	1	7835	>20	
CoPIM-TB-2	100 °C 24 h	100	n/a	n/a	25	1	6767	>20	
C-CoPIM-TB-1	100 °C 24 h	100	n/a	n/a	25	1	5437	>20	
C-CoPIM-TB-2	100 °C 24 h	100	n/a	n/a	25	1	4251	>20	
TR from PIM-6FDA-OH (440 °C)	*n*-Hexane/DCM (90/10) 24 h; air-dried; 120 °C vacuum 24 h	80–100	n/a	n/a	35	2	816	>15	372
CMS from PIM-6FDA-OH (600 °C)	*n*-Hexane/DCM (90/10) 24 h; air-dried; 120 °C vacuum 24 h	80–100	n/a	n/a	35	2	5028	>15	
CMS from PIM-6FDA-OH (630 °C)	*n*-Hexane/DCM (90/10) 24 h; air-dried; 120 °C vacuum 24 h	80–100	n/a	n/a	35	2	2880	>15	
CMS from PIM-6FDA-OH (800 °C)	*n*-Hexane/DCM (90/10) 24 h; air-dried; 120 °C vacuum 24 h	80–100	n/a	n/a	35	2	552	>15	
PIM-BM/TB	MeOH overnight; 70 °C vacuum 24 h	50	1.24	n/a	35	3.45	2007	>35	473
PIM-BM/TB-80C-20 h	MeOH overnight; 70 °C vacuum 24 h; 80 °C 200 ppm O_2/balance N_2 20 h	50	1.20	n/a	35	3.45	987	24.1	
PIM-BM/TB-200C-20 h	MeOH overnight; 70 °C vacuum 24 h; 200 °C 200 ppm O_2/balance N_2 20 h	50	1.05	n/a	35	3.45	391	>35	
PIM-BM/TB-250C-10 h	MeOH overnight; 70 °C vacuum 24 h; 250 °C 200 ppm O_2/balance N_2 10 h	50	n/a	n/a	35	3.45	197	>35	
PIM-BM/TB-300C-2 h	MeOH overnight; 70 °C vacuum 24 h; 300 °C 200 ppm O_2/balance N_2 2 h	50	n/a	n/a	35	3.45	218	>35	
PIM-BM/TB-300C-5 h	MeOH overnight; 70 °C vacuum 24 h; 300 °C 200 ppm O_2/balance N_2 5 h	50	1.01	n/a	35	3.45	79	>35	

Table 5 Reported C_3H_6 plasticization pressures of microporous polymers in literature. Permeabilities are reported for the given test temperature and test pressure

Polymer name	Membrane treatment conditions	Thickness (μm)	Young's Modulus (GPa)	T_g (°C)	Test temperature (°C)	Total test pressure (bar)	Mixture composition (mol%)	C_3H_6 permeability (barrer)	C_3H_6 plasticization pressure (bar)	Ref.
PIM-6FDA-OH	*n*-Hexane/DCM (90/10) 24 h; air-dried; 120 °C vacuum 24 h	n/a	n/a	n/a	35	2	Pure-gas	5.1	3	159
PIM-6FDA-OH	*n*-Hexane/DCM (90/10) 24 h; air-dried; 120 °C vacuum 24 h; 250 °C vacuum 24 h	n/a	n/a	n/a	35	2	Pure-gas	3.5	>5	
PIM-6FDA-OH	*n*-Hexane/DCM (90/10) 24 h; air-dried; 120 °C vacuum 24 h	n/a	n/a	n/a	35	2	50 : 50 C_3H_6/C_3H_8	4.0	2	
PIM-6FDA-OH	*n*-Hexane/DCM (90/10) 24 h; air-dried; 120 °C vacuum 24 h; 250 °C vacuum 24 h	n/a	n/a	n/a	35	2	50 : 50 C_3H_6/C_3H_8	3.3	>2.5	
PIM-PI-1	120 °C vacuum 24 h; MeOH 24 h; 120 °C vacuum 24 h	~130	n/a	n/a	35	2	50 : 50 C_3H_6/C_3H_8	235	1.5	329
KAUST-PI-1	120 °C vacuum 24 h; MeOH 24 h; 120 °C vacuum 24 h	~100	n/a	n/a	35	2	50 : 50 C_3H_6/C_3H_8	511	<1	
TR from PIM-6FDA-OH (440 °C)	120 °C vacuum 24 h; *n*-hexane/DCM (90/10) 24 h; 120 °C vacuum 24 h	n/a	n/a	n/a	35	2	50 : 50 C_3H_6/C_3H_8	11.9	>5	373
CMS from PIM-6FDA-OH (600 °C)	120 °C vacuum 24 h; *n*-hexane/DCM (90/10) 24 h; 120 °C vacuum 24 h	n/a	n/a	n/a	35	2	50 : 50 C_3H_6/C_3H_8	50.6	>5	
PIM-6FDA-OH	250 °C vacuum 24 h	40–60	0.51 ± 0.02	n/a	35	2	50 : 50 mol% C_3H_6/C_3H_8	2.7	>6	414
ZIF-8/PIM-6FDA-OH (33 wt%)	250 °C vacuum 24 h	40–60	0.92 ± 0.04	n/a	35	2	50 : 50 mol% C_3H_6/C_3H_8	9.2	>7	
ZIF-8/PIM-6FDA-OH (65 wt%)	250 °C vacuum 24 h	40–60	0.47 ± 0.06	n/a	35	2	50 : 50 mol% C_3H_6/C_3H_8	34.6	~5	

Table 6 Reported H_2S plasticization pressures of microporous polymers in literature. Permeabilities are reported for the given test temperature and test pressure

Polymer name	Membrane treatment conditions	Thickness (μm)	Young's Modulus (GPa)	T_g (°C)	Test temperature (°C)	Total test pressure (bar)	Mixture composition (mol%)	H_2S permeability (barrer)	H_2S plasticization pressure (bar)	Ref.
PIM-6FDA-OH	120 °C vacuum 12 h; 250 °C vacuum 24 h	n/a	n/a	>380	35	1	Pure-gas	30	4.5	48
PIM-6FDA-OH	120 °C vacuum 12 h; 250 °C vacuum 24 h;	n/a	n/a	>380	35	5	15 : 15 : 70 CO_2/H_2S/CH_4	24	<0.75	
PIM-1	MeOH; air-dried; 120 °C vacuum	50–60	n/a	n/a	35	1	Pure-gas	4808	<1	348
PIM-1	MeOH; air-dried; 120 °C vacuum	50–60	n/a	n/a	35	~14	20 : 20 : 60 (mol%) CO_2/H_2S/CH_4	10 750	<2.8	
AO-PIM-1	MeOH; air-dried; 120 °C vacuum	50–60	n/a	n/a	35	1	Pure-gas	1124	<1	
AO-PIM-1	MeOH; air-dried; 120 °C vacuum	50–60	n/a	n/a	35	~14	20 : 20 : 60 (mol%) CO_2/H_2S/CH_4	2385	<2.8	
AO-PIM-1	6 months aged; 120 °C 12 h; MeOH 24 h; *n*-hexane 24 h; air-dried; 120 °C vacuum 24 h	50–60	n/a	n/a	35	1	Pure-gas	880	<1	
AO-PIM-1	6 months aged; 120 °C 12 h; MeOH 24 h; *n*-hexane 24 h; air-dried; 120 °C vacuum 24 h	50–60	n/a	n/a	35	~14	20 : 20 : 60 (mol%) CO_2/H_2S/CH_4	1445	<2.8	

reported plasticization pressure of both CO_2 and CH_4 for microporous polymers. The CO_2 concentration at the pure-gas CO_2 plasticization pressure, the mixed-gas CO_2 plasticization pressure (CO_2/CH_4 mixture), or the mixed-gas CH_4 plasticization pressure (CO_2/CH_4 mixture) for select samples are discussed. To allow for a more direct comparison between studies, only manuscripts including both high-pressure permeation and sorption studies were included in this analysis. Similar analyses for other plasticizing penetrants (C_3H_6, C_3H_8, H_2S) were not considered due to lack of available data.

Fig. 67a–c depict the CO_2 concentration at the plasticization pressure for each sample. Interestingly, the CO_2 concentration is independent of the plasticization pressure. From these findings, it appears that a concentration of 38 ± 7 cm_{STP}^3 cm_{pol}^{-3}, which was previously reported for non-microporous polymers, does not correlate with plasticization pressures for

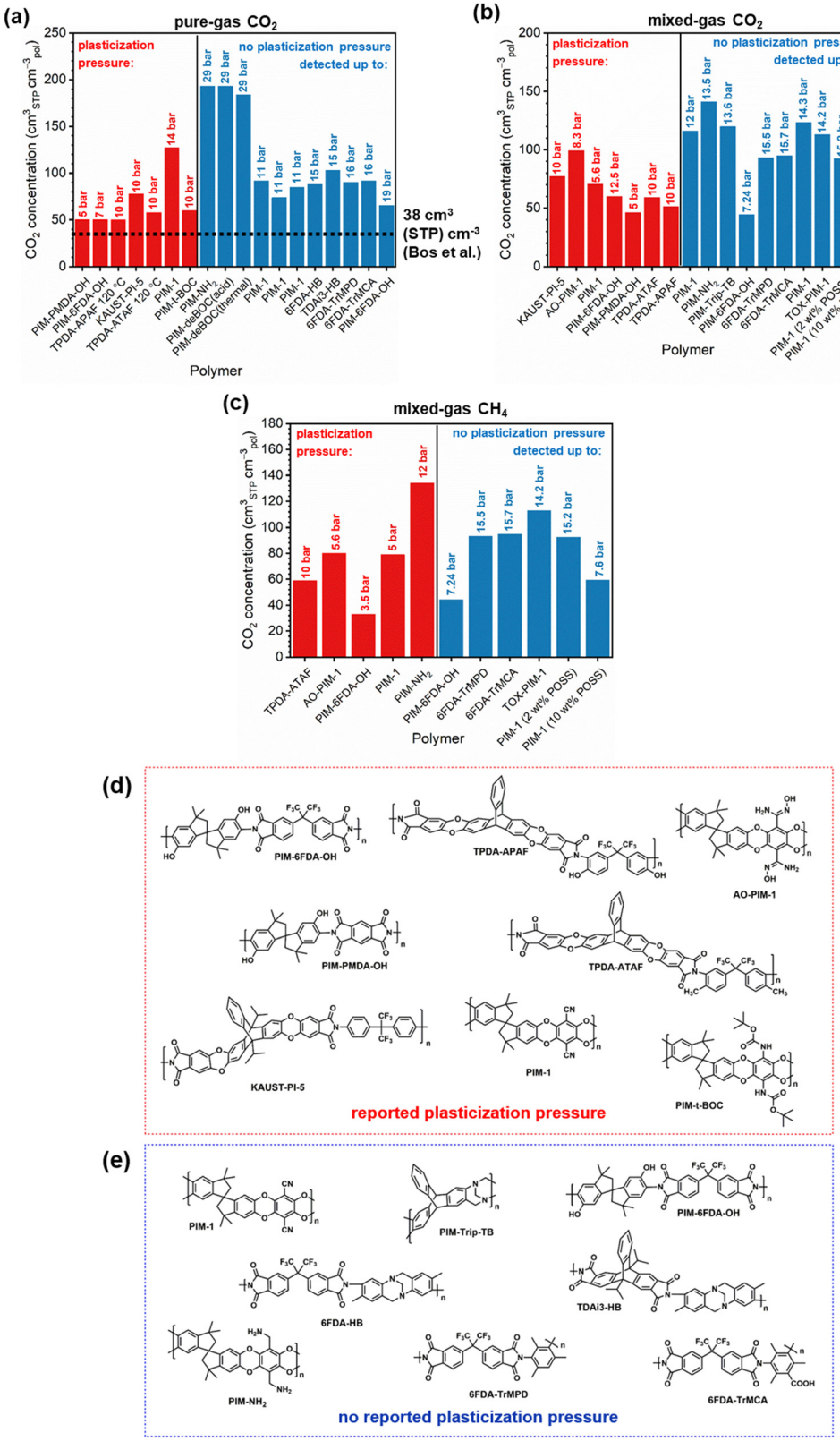

Fig. 67 CO_2 concentration at the plasticization pressure (red) or maximum CO_2 pressure tested (blue) in a (a) pure-gas CO_2 test, (b) mixed-gas CO_2 test (with CH_4), and (c) mixed-gas CH_4 test (with CO_2). For (c), the CO_2 concentration at the CH_4 plasticization pressure was used. Polymer structures that (d) exhibited a pure-gas CO_2 plasticization pressure, and (e) did not exhibit a pure-gas CO_2 plasticization pressure up to the maximum pressure tested. Note that PIM-1 is included in both (d) and (e) due to multiple published studies.

microporous polymers.[42] In fact, all microporous polymers considered sorb more CO_2 before the onset of plasticization than Bos *et al.* originally observed. Besides a "critical concentration", other correlating variables have been suggested too.[80,87] While out of scope for this review, further analyses on the relationship between these parameters and the onset of plasticization in polymer membranes would be useful. Our findings suggest that identifying simple correlating variables to predict plasticization pressure is difficult and that the interplay of equilibrium sorption and non-equilibrium polymer chain dynamics is challenging to de-couple when investigating plasticization. Further development of theory is needed to accurately predict the onset of plasticization and how to mitigate these effects in polymer membranes.

The structures of samples that either reached a pure-gas CO_2 plasticization pressure or did not reach a pure-gas CO_2 plasticization pressure at the pressure range tested are also displayed in Fig. 67d and e. It is interesting to note that two structures listed (PIM-1 and PIM-6FDA-OH) can either show a pure-gas CO_2 plasticization pressure or not, which underscores the fact that the plasticization pressure can change depending on a number of additional factors including thickness, treatment conditions, pressure range of the measurement, and gas composition.[460]

5.2. Mixed-gas permeation performance

As shown in Section 5.1, pure- and mixed-gas high pressure permeation data are useful for evaluating plasticization phenomena in polymers. In particular, high-pressure permeation trends in gas mixtures can unambiguously determine when plasticization is occurring in a given sample. As an extension of the discussion in Section 5.1, this section reviews: (1) pure- and mixed-gas permeation data for microporous materials and commonly tested conditions, (2) research progress on competitive sorption for gas mixtures, and (3) a summary of literature trends in plasticization for gas mixtures and mitigation techniques reviewed in Sections 4 and 5.1 (*i.e.*, hydrogen bonding, post-synthetic modification, and multi-component systems).

5.2.1. Mixed-gas permeation data. Mixed-gas permeation in microporous polymers has been evaluated for various industrially relevant mixtures. Some examples include application targets of natural gas purification and biogas upgrading (*e.g.*, CO_2/CH_4), sour gas separations (*e.g.*, $H_2S/CO_2/CH_4$), post-combustion carbon capture (*e.g.*, CO_2/N_2), olefin/paraffin separations (*e.g.*, C_3H_6/C_3H_8), pre-combustion carbon capture (*e.g.*, H_2/CO_2), nitrogen generation from air (*e.g.*, O_2/N_2), and hydrogen recovery (*i.e.*, H_2/N_2 and H_2/CH_4).[10,337] Table 7 provides an overview of commonly tested conditions reported in the literature up until the end of 2022 for some of these gas mixtures, the number of studies that tested similar conditions, and the primary industrial application for the separation. As shown in Table 7, certain separations such as binary CO_2/CH_4 separation for applications in natural gas and biogas purification, have been widely studied for a narrow range of feed compositions and temperatures, including many studies with testing conditions that essentially overlap. However, mixed-gas permeation involving other highly condensable and plasticizing impurities commonly found in these streams (*e.g.*, H_2S, N_2, C_{3+} hydrocarbons, aromatics including benzene, toluene, and xylene isomers (BTX), and water vapor) are underexplored.[474,475] Many reports have investigated the effects of contaminants on the separation capabilities of polymer membranes in industrial and lab-scale settings. Examples include commercial polyimides,[476] polynorbornene,[477] thermally-rearranged HAB-6FDA,[478] a blend of polyethersulfone and DSDA-TMMDA,[479] and Pebax®.[480] Some polymers, including cellulose acetate and derivatives, have even been deployed in industrial natural gas separations.[481] However, only few reports have tested sour gas mixtures ($H_2S/CO_2/CH_4$) in microporous polymers. In these cases, H_2S compositions ranged from 0.05 mol% to 20 mol%.[48,348,388,463] These values resemble typical gas well compositions found globally, which frequently range from ppm concentrations to 30 vol%[337,481] As a result of plasticization and permeability–selectivity trade-offs, membrane-based natural gas purification comprises only 10% of the natural gas separation market compared to other processes such as amine absorption.[10] Developing a more robust understanding of structure–property relationships for plasticization under relevant conditions could help to advance membrane technology into the remaining 90% of the market.[3,10] In addition to natural gas, upgrading biogas, a renewable energy resource produced during anaerobic digestion of biomass in landfills, has also become an attractive market for membranes.[482,483] Biogas upgrading involves lower gas inlet pressures and higher initial CO_2 concentrations, somewhat mitigating issues of plasticization,[482,483] although H_2S composition can be somewhat concentrated for these applications as well. As shown in Table 7, studies investigating hydrogen-based gas pairs covered a larger range of testing temperatures and compositions for H_2/CO_2 and H_2/N_2 separations, respectively, which is consistent with industrial conditions that are relevant for each application. When considering other emerging applications, studies involving olefin/paraffin separations (*e.g.*, C_3H_6/C_3H_8) have focused on more generalized binary mixtures, while those for carbon capture (*i.e.*, CO_2/N_2) have also evaluated the effects of ternary mixtures, including humid conditions.

Membrane performance is typically evaluated in the context of upper bound plots, which were first proposed by Robeson in 1991[17] and later revisited in 2008.[18] These upper bound plots were empirically derived using a database of pure-gas permeation data evaluated at pressures of approximately 1 to 10 bar. These plots are thus useful for comparing performance in relatively low-pressure pure-gas conditions but are insufficient to benchmark performance for more industrially relevant mixtures. For CO_2/CH_4 mixtures, Wang *et al.* proposed a new mixed-gas upper bound in 2018 using literature data for 70 microporous polymers tested using a 50 : 50 CO_2/CH_4 mixture at a CO_2 partial pressure of 10 bar.[337] This upper bound is highlighted throughout this section for comparison of mixed-gas data. However, comparing mixed-gas tests performed at different pressures and temperatures can lead to challenges with accurately interpreting data, so the discussion here will be limited only to measurements taken at a CO_2 partial pressures of 1 to 2 bar or up to 12 bar and temperatures ~25 to 35 °C. For

Table 7 Testing conditions for literature involving gas mixtures and microporous polymers

Gas mixture	# of papers	Testing conditions: Composition[b]	Testing conditions: Temperature (°C)	Testing conditions: Contaminants	Relevant industrial application
CO_2/CH_4	31	50 : 50	30–35	—	Biogas upgrading and natural gas purification[482]
	3	50 : 50	N/A	—	Organic waste: (60–70% CH_4; 30–40% CO_2; 0–5000 ppm H_2S)
	25	50 : 50	22–25	—	Landfill waste: (35–65% CH_4; 15–50% CO_2; 5–40% N_2; 0–100 ppm H_2S)
	5	35 : 65	N/A	—	Natural gas: (75–95% CH_4; 1–10% CO_2; 4–10 000 ppm H_2S)
	3	30 : 70	30	—	
	3	20 : 80	30–35	—	
	1	40 : 60	25	—	
$H_2S/CO_2/CH_4$ ternary	1	15 : 15 : 70	35	H_2S	
	1	20 : 20 : 60	35	H_2S	
	1	0.05 : 50 : 49.95	35	H_2S	
	1	33.6 : 64 : 2.4 $CO_2/CH_4/N_2$	25	ppm H_2S	
CO_2/N_2	5	50 : 50	35–37	—	Carbon capture from point sources[24,484]
	6	15 : 85	35	—	Post-combustion flue gas from coal or natural-gas fired power plants, and cement/steel production:
	2	9 : 91	35	—	(4–30% CO_2 at atmospheric pressure with contaminants such as SO_X, NO_X, water, and trace metals)
	1	10 : 90	25	—	
	9	50 : 50	22–25	—	
	3	15 : 85	N/A	—	
	4	15 : 85	22–25	—	
	1	20 : 80	30	—	
	1	30 : 70 & 70 : 30	25	—	
	1	40 : 60	25	—	
	1	20 : 80 & 80 : 20	25	—	
CO_2/N_2 ternary	1	15 : 85	30	2.5, 25, 41.5 RH[a]	
	1	9 : 91	30	7 & 26 RH	
	1	20 : 20	40	61% Ar	
	2	20 : 20	22	60% Ar	
	1	5% flue gas (14 : 86)	22	95% H_2O vapor	
	1	15 : 80	25	5% O_2	
C_3H_6/C_3H_8	8	50 : 50	35	—	Alkene/alkane or olefin/paraffin separations[134]
H_2/N_2	3	50 : 50	25	—	H_2 recovery from ammonia synthesis plants[11,106] (30–80% H_2)
	1	20 : 80	22	—	
	1	30 : 70	25	—	
	1	70 : 30	25	—	
H_2/CH_4	4	50 : 50	35	—	
	1	50 : 50	25	—	
H_2/CO_2	3	50 : 50	35	—	Carbon capture[10,52]
	1	50 : 50	35, 60, 90, 120	—	Pre-combustion/syngas: (30% CO_2, 20% CO, 45% H_2, and other inert gases at 100–150 °C)
	1	50 : 50	180	—	
	1	12 to 39% RH in CO_2	30	H_2O	
	1	50 : 49	35, 60, 90	1% CO	
	1	Equimolar	120	H_2O: 1.51–15.8%	

[a] Relative humidity is indicated as RH. [b] Composition ratios are listed in the same order as the gas pair, *e.g.*, a CO_2/CH_4 mixture with a 30 : 70 composition has 30% CO_2 and 70% CH_4.

C_3H_6/C_3H_8 mixtures, Burns and Koros developed a pure-gas upper bound in 2003[330] and, in 2012, Zhang *et al.* reported a mixed-gas upper bound using permeation data measured at temperatures from 35 to 50 °C and at pressures between 1 to 4 bar.[485] Other pure-gas upper bounds for CO_2- and H_2-based gas pairs have been recently proposed.[326,337,486] Finally, upper bounds for ternary mixtures have yet to be defined in part due to the limited size of datasets and variability in reported findings. For comparisons of transport performance in $H_2S/CO_2/CH_4$ mixtures, the combined acid gas selectivity (CAG) (*i.e.*, the summed CO_2 and H_2S permeabilities divided by the CH_4 permeability) proposed by Krafschik *et al.* has been commonly used.[48,348,457] The rest of this section will primarily focus on gas pairs containing condensable penetrants such as CO_2, H_2S, and C_3H_8 and several performance trends will be discussed in the context of upper bound benchmark plots.

Microporous polymers are frequently considered for CO_2-based separations because these separations often benefit from both sorption and diffusion selectivity. As a result, a large majority of mixed-gas studies for microporous polymers involve mixtures containing CO_2/CH_4 and CO_2/N_2. A collection of mixed-gas upper bound data from these studies is shown in

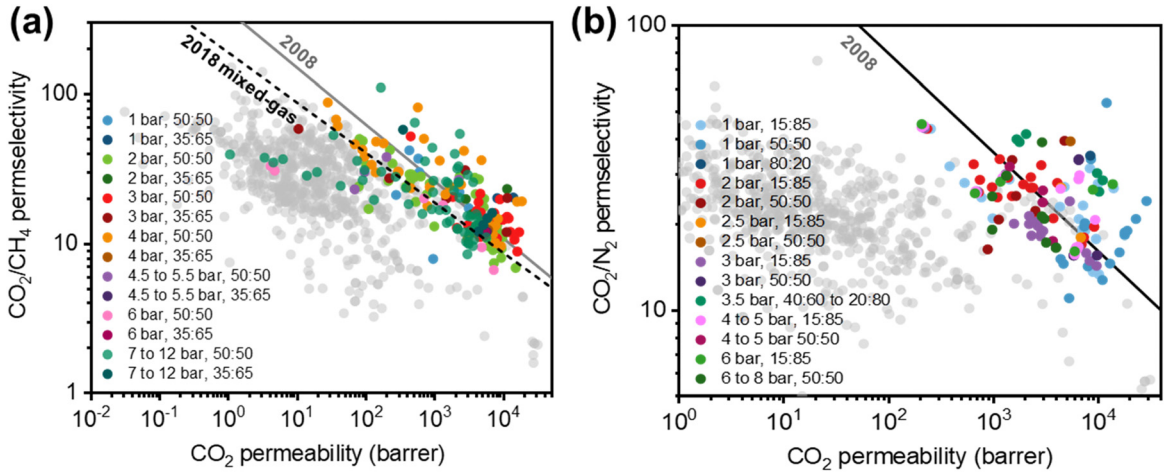

Fig. 68 (a) 2008 pure-gas[18] and 2018 mixed-gas[337] CO_2/CH_4 upper bound front and (b) 2008 pure-gas[18] CO_2/N_2 upper bound front. Also included are mixed-gas tests of microporous polymers in the literature, highlighted in colored symbols. Gray symbols denote Robeson database points for pure-gas tests in predominantly non-microporous polymers.[17,18] The legends show the gas feed mixture compositions and the mixed-gas total pressures for testing. At 3.5 bar, the CO_2/N_2 compositions tested include 40 : 60, 30 : 70, and 20 : 80.

Fig. 68 and compared to a larger set of upper bound data considered in the 2008 Robeson upper bound, which includes data from other non-microporous polymer backbones. Considering CO_2/CH_4 and CO_2/N_2 tests performed at total pressures below 12 bar and varying CO_2 compositions, the mixed-gas performance for microporous polymers (colored symbols) generally outperforms that of the pure-gas companion studies for polymers included in the 2008 upper bound (gray symbols). This trend highlights the promise of leveraging competition in microporous polymer backbones for gas separation applications when plasticization effects are limited. Subsequent subsections will further investigate these trends and discuss the effects of competition and plasticization in relation to upper bound performance of microporous polymers.

5.2.2. Competitive sorption. Competitive sorption in glassy polymers is the exclusion of one or more gases in a polymer matrix due to the presence of more strongly co-sorbing species in a mixture. Under the framework of the dual-mode sorption model, competitive sorption is characterized by preferential sorption into the Langmuir mode for one gas over others, resulting in reduced sorption capacity for the less condensable gases in a mixture. When sufficiently strong, competitive sorption can result in increased mixed-gas sorption selectivity in favor of the more condensable gas. For instance, in binary mixtures of CO_2/N_2 and CO_2/CH_4, competition effects can raise CO_2-based sorption selectivity because CO_2 sorbs significantly more strongly than the co-permeating species. This effect results in an overall increase in permselectivity, which is the opposite trend from plasticization. In this way, competition and plasticization can compete with each other and can influence permeability and permselectivity in complex and sometimes unexpected ways.

By contrast, in H_2-based mixtures such as H_2/CH_4 and H_2/CO_2, competitive effects can reduce transport performance by biasing sorption selectivity toward the more condensable penetrant (*i.e.*, CO_2 or CH_4), which leads to a decrease in overall permselectivity. Because the extent of competition is dependent on the relative sorption affinity of the gases in the mixture, the reader is referred to the tabulated critical temperatures (T_c) in Section 2, Table 2 for gases discussed throughout this section. Sorption correlates exponentially with T_c, which makes this parameter an excellent correlating variable for estimating competitive sorption effects. In ternary mixtures of $H_2S/CO_2/CH_4$, which were briefly discussed in Section 5.1.4, the relative condensability of the gases (H_2S (T_c = 373.3 °C) > CO_2 (T_c = 304.2 °C) > CH_4 (T_c = 190.6 °C)) results in complex competition phenomena. H_2S will preferentially sorb into the polymer due to its higher T_c, increasing its permeability. However, both CO_2 and CH_4 permeability decrease, resulting in an increase in H_2S/CH_4 sorption selectivity and permselectivity.[100,487]

Competitive sorption effects are inherently linked to the sorption characteristics of the polymer and gas mixture investigated. As a result, performance changes due to competition will vary depending on the gases considered, the gas mixture composition, and the sorption affinity of the polymer. In a laboratory setting, typical experiments used to evaluate competitive sorption include mixed-gas permeation and mixed-gas sorption tests.

For mixed-gas permeation tests that involve separating a more condensable gas from a less condensable gas (*i.e.*, CO_2/N_2, CO_2/CH_4, H_2S/CO_2, *etc.*), an increase in mixed-gas permselectivity compared to pure-gas permselectivity indicates a rise in sorption selectivity. This rise is due to competitive effects in which the less condensable penetrant will experience a decrease in sorption, and, thus, a decrease in permeability. The opposite trend (*i.e.*, when the mixed-gas permselectivity decreases compared to the pure-gas permselectivity) indicates plasticization, where diffusion and permeation of the less condensable penetrant increases due to enhanced chain mobility. Since plasticization and competitive sorption counterbalance each other, it is

possible to simultaneously observe an increase in permselectivity at low pressures (due to competition) with a decrease in permselectivity at high pressures (due to detrimental plasticization effects).

A direct indicator of competition phenomena is the mixed-gas sorption test. In these tests, the experimental mixed-gas sorption selectivity can be compared to the experimental pure-gas sorption selectivity to evaluate competition. Unfortunately, because mixed-gas sorption tests are highly specialized, very few of these custom-built systems exist in the world, limiting access to experimental data.[488–491] When not available, researchers have also applied models such as the dual-mode sorption (DMS) model[141,492] and the NELF model[104] to predict mixed-gas sorption data in polymers of interest using experimental pure-gas sorption isotherms. Generally, the mixed-gas DMS model provides a good qualitative prediction of mixed-gas sorption, but thermodynamically rigorous models such as NELF are required for quantitative mixed-gas sorption predictions.[143,493] When using the DMS and NELF models, pure-gas sorption isotherms are required, and for the NELF model, lattice fluid parameters must be known or estimated for a given polymer. These parameters can be collected through pressure–volume–temperature (PVT) experiments for polymers above their glass transition temperature.[494] However, when such measurements are not accessible, which is frequently the case for microporous polymers that do not exhibit measurable glass transition temperatures, additional sorption fitting of infinite dilution sorption coefficients[495,496] or molecular simulations,[497] are required.

5.2.2.1. Mixed-gas sorption and competition. Despite challenges associated with testing mixed-gas sorption, direct measurements of CO_2/CH_4 mixed-gas sorption have been collected in many glassy polymers such as cellulose triacetate (CTA),[160] 6FDA-TADPO,[498] 6FDA-HAB and its thermally rearranged analogue,[143] TZ-PIM,[356] PIM-1,[356] PTMSP,[356] 6FDA-mPDA,[355] PIM-Trip-TB,[334] and AO-PIM,[499] and some rubbery polymers such as polydimethylsiloxane (PDMS).[491,500] Other gas mixtures such as CO_2/C_2H_4, CO_2/N_2O, CO_2/C_2H_6, and $C_2H_6/CO_2/CH_4$ have also been tested for PMMA,[490,501] crosslinked PEO,[502] and PIM-1,[503] respectively. For CO_2 and CH_4 in glassy polymers, mixed-gas CO_2 sorption decreases slightly compared to the pure-gas case, whereas mixed-gas CH_4 sorption is significantly lower than the pure-gas case due to competitive sorption. In this way, CO_2/CH_4 selectivity can increase for mixtures compared to pure gases, providing there are limited plasticization effects at the testing conditions. Similar mixed-gas sorption trends are also observed when considering other gas mixtures in glassy polymers. The less condensable gas will always experience a larger depression in sorption from the pure- to mixed-gas case. Readers are directed to the above references for information on mixed-gas sorption of non-microporous glassy polymers.

Recently, a particularly important study considered mixed-gas sorption in cellulose triacetate (CTA), which is a commercial membrane material currently used for natural gas purification in industry. Genduso *et al.* evaluated mixed-gas sorption for CTA in mixtures containing 26, 51, and 75 mol% of CO_2 in CH_4 at 35 °C up to a partial CO_2 fugacity of ~10 bar.[160] In accordance with expected mixed-gas sorption trends, CO_2 uptake exhibited almost no change with increasing pressure relative to the pure-gas case, while CH_4 sorption decreased significantly. The concentration-averaged diffusion coefficients were also calculated, and the CH_4 diffusion coefficients increased with increasing CO_2 pressure. Moreover, the CH_4 diffusion coefficients were found to be higher in the mixed-gas case compared to the pure-gas case (*i.e.*, a 2.9-fold increase in diffusion coefficient for CH_4 at CO_2 partial pressure of 10 bar), unambiguously indicating plasticization. In the case of CO_2, mixed-gas diffusion coefficients remained within error of the pure-gas diffusion coefficients. Interestingly, CTA had a high CO_2/CH_4 sorption selectivity of 12.6 ± 2.8 at infinite dilution, surpassing that of PIM-1 and 6FDA-mPDA and nearly reaching the CO_2/CH_4 sorption upper bound.[504] However, compared to 6FDA-mPDA, PIM-1, and PIM-Trip-TB, CTA had CO_2/CH_4 diffusion selectivities and CO_2 diffusivities below the proposed mixed-gas and pure-gas diffusion upper bounds.[15]

Due to their high free volume structure and backbone functionality, microporous polymers have potential to concurrently display sorption-selective and size-sieving characteristics. Ricci *et al.* investigated mixed-gas sorption in CO_2/CH_4 for poly(trimethylsilyl propyne) (PTMSP), PIM-1, and tetrazole-functionalized PIM-1 (TZ-PIM) for mixtures at 10, 30, and 50 mol% of CO_2 at 25 °C, 35 °C, and 50 °C.[356] As shown in Fig. 69, in mixed-gas scenarios, CH_4 sorption decreased much more significantly than CO_2. As a result, CO_2/CH_4 mixed-gas sorption selectivity increased compared to the pure-gas case for all pressures considered. For instance, at a total pressure of 30 bar, the CO_2/CH_4 mixed-gas sorption selectivity of TZ-PIM was approximately 7.8 while the pure-gas sorption selectivity was approximately 2.5. Additionally, NELF predictions of mixed-gas sorption data for all gas mixture compositions showed excellent agreement with experiments. Finally, diffusion coefficients were calculated from the sorption–diffusion model using NELF sorption predictions and mixed-gas permeation. When considering a 50 : 50 CO_2/CH_4 mixture at a total pressure of 20 bar, the predicted CO_2/CH_4 sorption selectivity (6.8) for TZ-PIM had a much larger contribution to CO_2/CH_4 permselectivity (17.9) than the CO_2/CH_4 diffusion selectivity (2.6), indicating the stronger relative influence of sorption in membrane performance under more realistic conditions. This effect can be more pronounced in microporous polymers, which typically have higher gas sorption than traditional polyimides.[505] An extension of this work was recently published, where complex ternary mixtures of $C_2H_6/CO_2/CH_4$ were investigated for PIM-1.[503] Despite having a similar T_c to CO_2 (T_c = 304.2 K), the presence of C_2H_6 (T_c = 305.3 K) reduced the sorption capacity of CO_2 and CH_4 in the mixture, reducing overall separation performance metrics and demonstrating the importance of competition and exclusion in mixtures.

Binary mixed-gas CO_2/CH_4 sorption was also recently investigated in an HAB-6FDA polyimide (HAB = 3,3′-dihydroxy-4,4′-diamino-biphenyl, 6FDA = 2,2′-bis-(3,4-dicarboxyphenyl) hexafluoropropane dianhydride) and its thermally rearranged polymer analogue (TR450).[143] Similar trends to those found in CTA and the PIMs discussed earlier were observed here. In short,

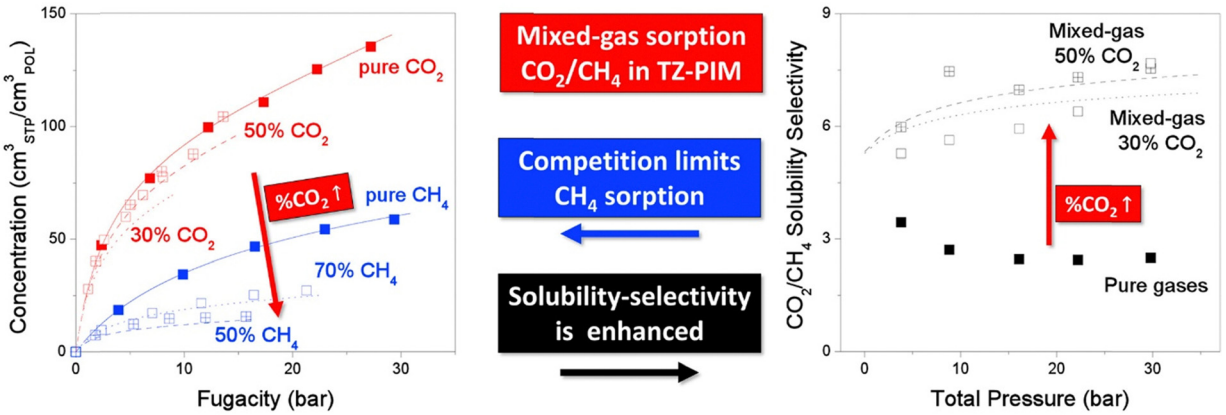

Fig. 69 (a) Pure- and mixed-gas sorption isotherms for TZ-PIM. Unfilled and filled data points denote experimental data collected for mixed-gas and pure-gas sorption tests, respectively. (b) pure- and mixed-gas solubility selectivity *versus* pressure plots for TZ-PIM. Dashed lines represent NELF predictions of the sorption and sorption selectivity data. Reprinted with permission from ref. 356 (Copyright Elsevier, 2019).

the CO_2 mixed-gas sorption was much less affected by the presence of CH_4, while the mixed-gas CH_4 sorption significantly decreased due to the presence of CO_2. As shown in Fig. 70, CO_2/CH_4 diffusion and sorption selectivities were calculated at various increasing pressures for the ideal and multi-component case. In pure-gas scenarios, diffusion selectivity contributed more than sorption selectivity to permselectivity (Fig. 70a). In mixed-gas scenarios, the presence of a highly sorbing penetrant (CO_2) had a detrimental effect on diffusion selectivity, while sorption selectivity increased and then remained relatively constant for the pressures considered (Fig. 70b). This same sorption–diffusion analysis was extended to a broader database of mixed-gas sorption studies in glassy polymers, where it was shown that permselectivity can be driven by sorption in multi-component scenarios (Fig. 70c).

5.2.2.2. Mixed-gas permeation and competition. In the absence of mixed-gas sorption experiments, applying models to pure-gas sorption tests and comparing experimental mixed-gas permeation tests can elucidate trends associated with competition and gas–polymer interactions. Using this approach, structure–property relationships were recently investigated for a family of functionalized and aged PIM-1 analogues with distinct CO_2 sorption affinities, as shown in Fig. 71a.[142] In this study, the CO_2/CH_4 sorption selectivity for the functionalized PIMs were compared against the 2014 pure-gas sorption upper bound developed by Lipscomb *et al.*[504] The PIM-1 sample functionalized with the primary amine group (PIM-NH_2) showed a remarkably high sorption selectivity of 12.6, which is close to the theoretically derived 2014 sorption upper bound. The six PIM-1 analogues were also evaluated under binary CO_2/CH_4 mixed-gas conditions at a total mixed-gas pressure of 2 bar, where increases in mixed-gas permselectivity (Fig. 71b) aligned directly with the predicted CO_2/CH_4 sorption selectivity enhancements of each PIM (Fig. 71a). Furthermore, because of its high CO_2 affinity and ability of forming hydrogen bonding through secondary interactions, PIM-NH_2 showed a 150% increase in CO_2/CH_4 permselectivity from the pure-gas case to the mixed-gas case while simultaneously maintaining a CO_2/CH_4 selectivity over 20 up to a total feed pressure of ~26 bar. Of note, the mixed-gas performance for this polymer sample was significantly higher than that in pure-gas tests due to the large increase in selectivity. This finding highlights the importance of evaluating films under realistic feed conditions, as the presence of condensable gases can drastically alter the transport properties.

In sour gas ternary mixtures, larger deviations between mixed- and pure-gas performance are observed due to the co-sorption of additional condensable penetrants (*i.e.*, H_2S) and the onset of beneficial plasticization effects. As discussed in Section 5.1, H_2S/CH_4 separation is dictated by sorption selectivity since H_2S (d_k = 3.6 Å) and CH_4 (d_k = 3.8 Å) have similar kinetic diameters. As a result, when the polymer is plasticized, H_2S diffusion can be significantly increased and CH_4 will be prevented from permeating due to competition, which leads to an increase in H_2S/CH_4 permselectivity. However, CO_2/CH_4 selectivity often decreases in these mixtures due to the plasticization effects incurred by both H_2S and CO_2, increasing CH_4 diffusivity, as well as competition between H_2S and CO_2, which leads to decreased CO_2 permeability. These trends have been investigated for a few microporous polymer systems discussed in Section 5.1, including PIM-6FDA-OH[48] and AO-PIM-1.[348] Other systems such as polyazole-based membranes[459] and 6FDA-based polyimides, and co-polyimides including 6FDA-DAM,[100] 6FDA-Durene/6FpDA,[506] and 6FDA-DAM/DABA copolymers[458] have also been investigated with ternary feeds. In such cases, co-polymer composition has been used to molecularly tailor sour gas transport for various gas compositions. In addition to polymer systems, Koros and Eddaoudi have reported successful design of MOF–polymer MMMs for simultaneous removal of CO_2 and H_2S from sour gas including incorporation of fluorinated NbOFFIVE-1-Ni, AlFFIVE-1-Ni, and (RE)-fcu-MOF (fcu = face centered cubic) fillers.[507,508] Addition of MOF into the polymer matrix helps to significantly increase permeabilities compared to conventional polyimides and to tune diffusion selectivity for CO_2/CH_4 and H_2S/CH_4 separations. More recently, the same groups reported on the design of highly tailorable and stable M-fcu-MOFs (M = metal) and incorporation of these MOFs into 6FDA-based polyimides.[509] Careful selection of molecular building blocks

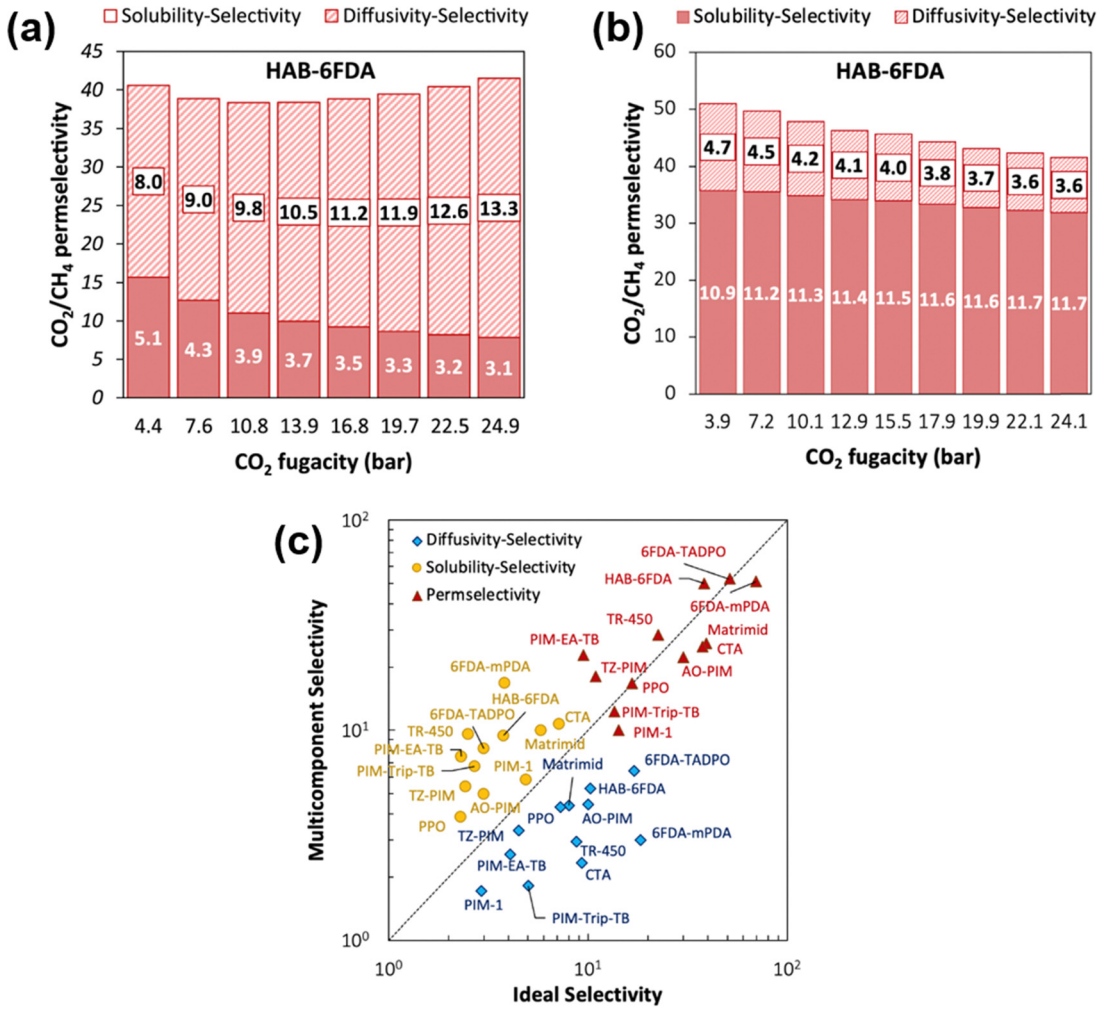

Fig. 70 (a) pure-gas and (b) mixed-gas CO_2/CH_4 permselectivity split into the sorption selectivity (predicted from NELF model analysis) and diffusivity selectivity (calculated from applying the sorption–diffusion model to experimentally determined permeabilities). (c) Comparison of CO_2/CH_4 ideal and mixed-gas permselectivity, diffusion selectivity, and sorption selectivity for reference polymers reported in ref. 143. Reprinted with permission from ref. 143 (Copyright Elsevier, 2020).

allowed for tailored pore apertures and chemical functionalities in MOFs for enhanced sour gas performance. Transport properties were additionally tuned through appropriate selection of a compatible polymer matrix. Finally, in certain cases, the addition of MOF helps to mitigate plasticization, which is further complimented by competitive sorption effects between H_2S, CO_2, and CH_4.

5.2.3. Robeson upper bound performance at low pressures. Changes in mixed-gas *versus* pure-gas performance can vary widely due to differences in polymer–gas interactions and the relative condensabilities of the gases considered. This subsection evaluates these trends using a database of mixed-gas literature results for microporous materials including low-pressure pure- and mixed-gas permeation data for CO_2/CH_4 and CO_2/N_2 gas pairs (Fig. 72), and H_2/CH_4 and C_3H_6/C_3H_8 gas pairs (Fig. 73). Select CMS membranes were considered because they were derived from microporous polymers. For these analyses, only polymers tested at a pure-gas total pressure identical to the partial pressure of either CO_2, H_2, or C_3H_6 in their respective mixtures were considered. For the plots considered in Fig. 72 and 73, pure-gas and mixed-gas data are denoted using filled/half-filled and unfilled symbols, respectively. Directly comparable data are connected by an arrow indicating the direction of the change in upper bound performance from pure-gas to mixed-gas. To more quantitatively evaluate differences in performance, the upper bound scoring metric reported by Qian and Asinger *et al.* was applied to the database.[134] This scoring metric evaluates the distance of the data point from the 2008 upper bound, where positive and negative values indicate performance above and below the upper bound, respectively. Data of samples, including casting solvent used, treatment conditions, thickness (l), gas composition, permeability, permselectivity, and score, for each of the gas pairs considered are tabulated in Tables 8–11.

Upper bound data for CO_2-based mixtures measured at total pressures of both 2 bar and 4 bar are shown in Fig. 72. In binary CO_2/CH_4 and CO_2/N_2 mixtures, the CO_2-based permselectivity either increases or decreases depending on the sample considered, highlighting the significance of functional chemistry

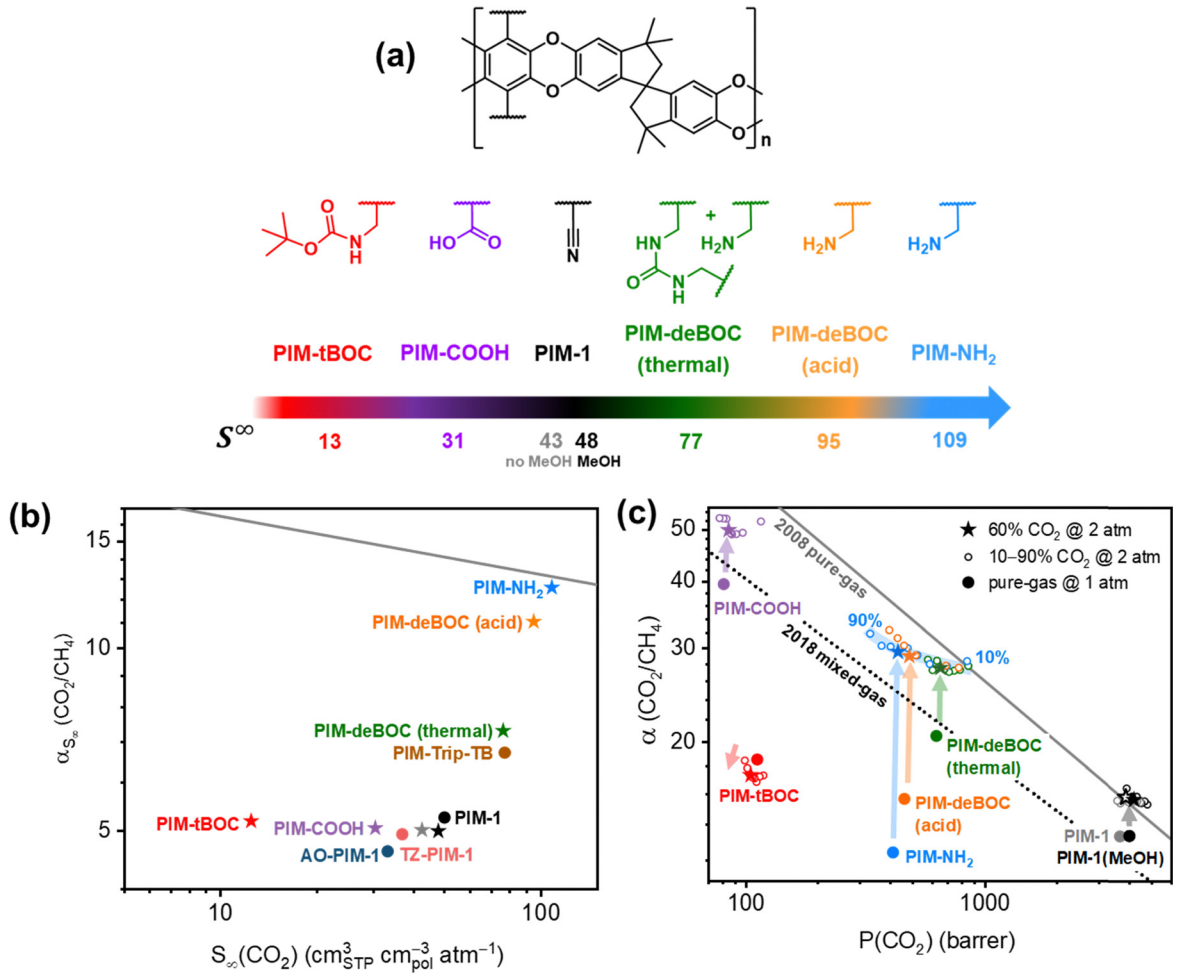

Fig. 71 (a) Chemical structures of PIM-1 functionalized analogues considered in the study and their pure-gas CO_2 sorption at infinite dilution. From left to right, the samples include the *tert*-butoxycarbonyl (–$CH_2NHCOOC(CH_3)_3$, PIM-*t*-BOC), carboxylic acid (–COOH, PIM-COOH), nitrile (–CN, PIM-1), partial urea (–NHCONH–, PIM-deBOC(thermal)) and primary amine (–CH_2NH_2, PIM-deBOC (acid) and PIM-NH_2) functionalized PIM-1 analogues. Grey and black stars indicate untreated and MeOH treated PIM-1 samples, respectively. (b) pure-gas CO_2/CH_4 sorption selectivity at infinite dilution *versus* CO_2 sorption at infinite dilution for PIM-1 analogues and literature references including AO-PIM-1[499] (dark blue circle), TZ-PIM-1[499] (pink circle), PIM-1[488] (black circle), PIM-Trip-TB[334] (brown circle). The gray line represents the 2014 CO_2/CH_4 sorption upper bound.[504] (c) CO_2/CH_4 2008 pure-gas[18] and 2018 mixed-gas[337] upper bounds for the PIM-1 analogues. Filled circles indicate pure-gas permeation tests performed at a total pressure of 1 bar, stars indicate CO_2/CH_4 mixed-gas tests with 60% CO_2 at a total pressure of ~2 bar, and unfilled circles denote CO_2/CH_4 mixed-gas permeation tests performed at CO_2 compositions ranging from 10% to 90% at a total pressure of ~2 bar. Reproduced from ref. 142 with permission from the Royal Society of Chemistry.

and gas composition in dictating competitive effects in CO_2-based mixtures. For the two studies considering gas feeds of 15 : 85 CO_2/N_2, the permselectivity increases in the mixed gas case. Deployment of CO_2/N_2 separations for carbon capture applications would likely involve low total feed pressures, where competitive sorption could be leveraged. When considering binary CO_2/CH_4 separations for natural gas purification, enhanced competitive effects are of most value when plasticization can be simultaneously mitigated. Plasticization trends observed for CO_2/CH_4 binary mixed-gas tests at higher pressures of 10 bar are further evaluated in Section 5.2.4.

Pure- and mixed-gas upper bound data for binary H_2/CH_4 and C_3H_6/C_3H_8 gas mixtures are summarized in Fig. 73. In the case of H_2/CH_4, there is very limited data in the literature, so we report on three studies by Mizrahi Rodriguez and Benedetti *et al.*,[142] Wu *et al.*,[514] and Huang *et al.*,[515] which show the expected reduction in permselectivity and H_2 permeability for the mixed-gas case. This result is consistent with the relative critical temperatures of the gases (CH_4 (T_c = 190.6 °C) > H_2 (T_c = 33.2 °C)), where CH_4 will sorb more strongly than H_2. As such, competitive sorption will bias sorption selectivity toward CH_4, reducing overall H_2 permeability and resulting in lower H_2/CH_4 mixed-gas permselectivity. Similar results have been observed for microporous polymers tested in gas mixtures including H_2/N_2[142,444] and H_2/CO_2.[388,389,405] In each of these cases, the critical temperatures of CO_2 and N_2, are much higher than that of H_2, resulting in a decrease of H_2 permeability and H_2-based selectivity when tested in gas mixtures.

An emerging membrane-based separation is the separation of alkenes from alkanes, commonly referred to as olefin/paraffin

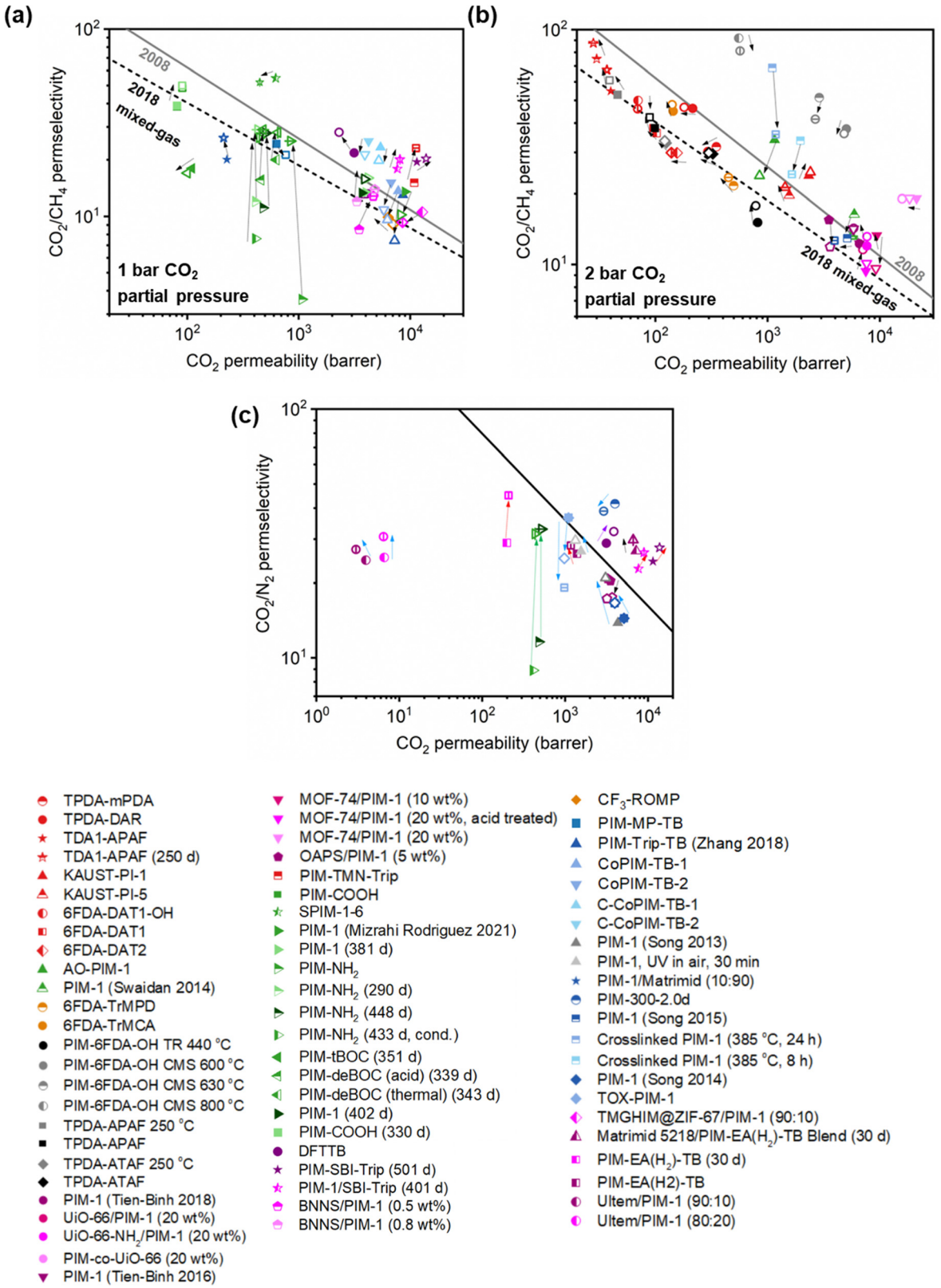

Fig. 72 (a) CO_2/CH_4 Robeson plot containing data for pure-gas measurements at 1 bar (filled/half-filled points) and 50 : 50 CO_2/CH_4 mixed-gas measurements at a total pressure of 2 bar (unfilled points). Arrows point from pure-gas data to corresponding mixed-gas data. (b) CO_2/CH_4 Robeson plot containing data for pure-gas measurements at 2 bar (filled/half-filled points) and 50 : 50 CO_2/CH_4 mixed-gas measurements at a total pressure of 4 bar (unfilled points). Arrows point from pure-gas data to corresponding mixed-gas data. (c) CO_2/N_2 Robeson plot containing data for pure-gas measurements (filled/half-filled points) and CO_2/N_2 mixed-gas measurements (open points). Black arrows point from pure-gas data at 2 bar to mixed-gas data (50 : 50 CO_2/N_2) at 4 bar total pressure, red arrows point from pure-gas data at 1 bar to mixed-gas data (15 : 85 CO_2/N_2) at 6 bar total pressure, blue arrows point from pure-gas data at 3.4–4 bar to mixed-gas data (50 : 50 CO_2/N_2) at 6.9 bar total pressure, green arrows point from pure-gas data at 1 bar to mixed-gas data (50 : 50 CO_2/N_2) at 2 bar total pressure, and purple arrows point from pure-gas data at 1 bar to mixed-gas data (15 : 85 CO_2/N_2) at 2 bar total pressure.

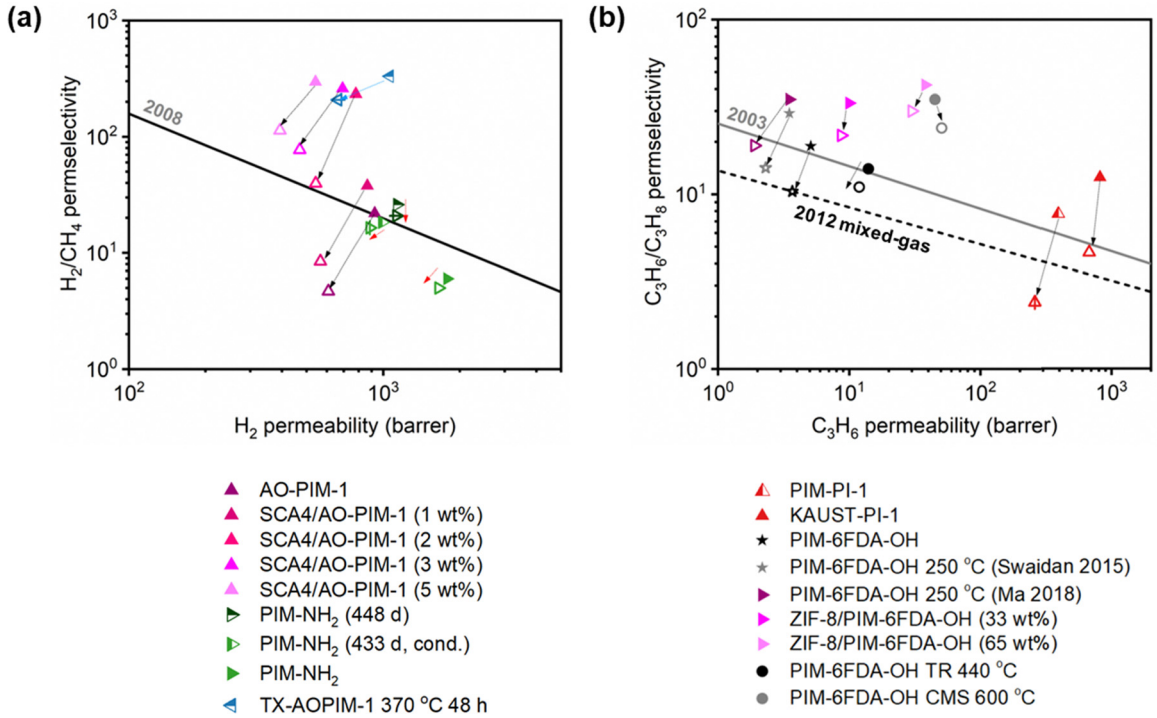

Fig. 73 (a) H_2/CH_4 Robeson plot containing data for pure-gas measurements at 3.4 bar (filled/half-filled points) and 50 : 50 H_2/CH_4 mixed-gas measurements at a total pressure of 6.9 bar (unfilled points). H_2/CH_4 Robeson plot containing data for pure-gas measurements (filled/half-filled points) and H_2/CH_4 mixed-gas measurements (unfilled points). Black arrows point from pure-gas data at 3.4 bar to mixed-gas data (50 : 50 H_2/CH_4) at 6.9 bar total pressure, red arrows point from pure-gas data at 1 bar to mixed-gas data (50 : 50 H_2/CH_4) at 2 bar total pressure, and blue arrows point from pure-gas data at 2 bar to mixed-gas data (50 : 50 CO_2/N_2) at 6 bar total pressure. (b) C_3H_6/C_3H_8 Robeson plot containing data for pure-gas measurements at 2 bar (filled/half-filled points) and 50 : 50 C_3H_6/C_3H_8 mixed-gas measurements at a total pressure of 4 bar (open points). Arrows point from pure-gas data to corresponding mixed-gas data.

separations. Ethylene and propylene are required in enormous volumes for the synthesis of commodity plastics (*e.g.*, polyethylene and polypropylene),[134] but because of their similar sizes and boiling points, olefin/paraffin separations often require energy-intensive cryogenic distillation. Membranes are highly desired for this separation, but the high polarizability of olefins and paraffins results in strong plasticization effects, precluding the use of many state-of-the-art commercial membranes. In addition to these industrial challenges, there are limited literature data on olefin/paraffin separation performance of emerging polymers such as PIMs.

Some limited low-pressure results are presented in Fig. 73b for C_3H_6/C_3H_8 separation in microporous materials. To the best of our knowledge, the only report of C_2H_4/C_2H_6 separation in microporous polymers has been performed for a CMS derived from PIM-6FDA-OH.[384] Because C_3H_8 (T_c = 369.9 °C) and C_3H_6 (T_c = 365.2 °C) have higher critical temperatures than CO_2 (T_c = 304.2 °C), they often interact more strongly with polymers and lead to plasticization, as highlighted in Section 5.1. For a C_3H_6/C_3H_8 mixture, the sorption affinity for C_3H_8 is slightly higher than that of C_3H_6 and, thus, competitive sorption effects should be unfavorable towards C_3H_6. Additionally, because the sorption of both C_3H_6 and C_3H_8 is high and their condensabilities are so similar, polymers are often plasticized by both of these gases, resulting in decreased mixed-gas permselectivity. Even when plasticization plays a role, mixed-gas C_3H_6 permeability decreases slightly, indicating some competitive sorption with C_3H_8, which will slightly reduce the permeability of both gases in the mixture. In short, these findings highlight the challenges of making stable and high-performance polymers for C_3H_6/C_3H_8 separation. In fact, many of the top performing samples in Fig. 73b are for MMMs and CMS membranes.

Fig. 74 summarizes the differences in score between the mixed-gas case and the corresponding pure-gas case for H_2/CH_4, C_3H_6/C_3H_8, CO_2/CH_4, and CO_2/N_2 mixtures for all microporous polymers represented in Tables 8–11. In this analysis, the upper bound score for a pure-gas test was subtracted from that for the mixed-gas test to provide an indication of magnitude and direction of the performance change. Therefore, a positive score indicates that the mixed-gas performance exceeded the pure-gas performance, while a negative score indicates the opposite trend. For CO_2-based mixtures, the scoring metric oscillates around zero, indicating that competitive benefits could outweigh plasticization effects for these separations. For H_2/CH_4, competition will reduce performance metrics (*i.e.*, H_2/CH_4 selectivity and H_2 permeability are both reduced in all mixtures), which can be generally applied to other H_2-based separations. For very condensable alkene/alkane gas pairs, plasticization effects outcompete competitive sorption at low pressures, often resulting in decreased performance (*i.e.*, decreased permeability and permselectivity). While competitive

Table 8 CO_2/CH_4 performance and upper-bound score for reported microporous polymers

Polymer	Casting solvent	Treatment and drying conditions	Thickness (μm)	Comp. (mol%)	P(CH_4) (barrer)	P(CO_2) (barrer)	α(CO_2/CH_4)	Score	Ref.
23–35 °C, P_{total} = 2 bar									
PIM-Trip-TB	$CHCl_3$	MeOH 24 h; 120 °C vacuum 20 h	105	Pure	310	4109	13	−0.130	334
				50 : 50	299	3914	13	−0.159	
CF_3-ROMP	$CHCl_3$	120 °C vacuum 24 h	119	Pure	644	6377	10	−0.245	39
				50 : 50	779	7063	9	−0.292	
PIM-MP-TB (118 d)	$CHCl_3$	MeOH 24 h; RT 24 h	94	Pure	26	633	24	−0.224	327
PIM-MP-TB (110 d)				52 : 48	36	766	21	−0.282	
PIM-Trip-TB	NMP	100 °C vacuum 24 h	—	Pure	664	8616	13	0.114	398
				50 : 50	979	7267	7	−0.469	
CoPIM-TB-1	NMP	100 °C vacuum 24 h	—	Pure	575	7835	14	0.126	
				50 : 50	654	6271	10	−0.281	
CoPIM-TB-2	NMP	100 °C vacuum 24 h	—	Pure	448	6767	15	0.170	
				50 : 50	536	5818	11	−0.192	
C-CoPIM-TB-1	NMP	4/1 MeOH-glycidol at 60 °C for 8 h; 80 °C 4 h; 120 °C overnight	—	Pure	233	5437	23	0.499	
				50 : 50	264	5241	20	0.335	
C-CoPIM-TB-2	NMP	4/1 MeOH-glycidol at 60 °C for 8 h; 80 °C 4 h; 120 °C overnight	—	Pure	169	4251	25	0.482	
				50 : 50	184	3931	21	0.302	
PIM-1/Matrimid (10 : 90)	THF/NMP	Fibers were immersed in tap water for 3 days; 3 consecutive 30 min solvent exchange by circulating in MeOH and *n*-hexane; dried at RT 24 h	0.06	Pure	11.3	227	20	−0.767	404
				50 : 50	8.1	212	26	−0.542	
PIM-TMN-Trip	$CHCl_3$	MeOH 24 h	161	Pure	722	10 910	15	0.340	463
				60 : 40	489	11 300	23	0.750	
PIM-COOH (330 d)	THF	130 °C 12 h	40–60	Pure	2.1	81	39	−0.523	138
				50 : 50	1.9	90	49	−0.270	
TMGHIM@ZIF-67/PIM-1 (10 wt%)	$CHCl_3$	RT 24 h; 70 °C 8 h	170–200	Pure	1218	12 849	11	0.062	422
				50 : 50	918	8545	9	−0.200	
DFTTB	$CHCl_3$	MeOH 12 h; RT 24 h	63	Pure	144	3146	21.8	0.242	336
				50 : 50	82	2304	28.1	0.369	
SPIM-1-6	$CHCl_3$	RT 24 h; MeOH 12 h; 80 °C vacuum 2 h; immersed in SO_3/DCM solution for 6 min; RT 48 h; aged 7 days	123	Pure	11.4	624	54.7	0.528	510
				50 : 50	8.6	448	52	0.363	
PIM-SBI-Trip (501 d)	$CHCl_3$	MeOH 24 h; RT 24 h	248	Pure	590	11 500	19.5	0.597	511
				35 : 65	685	13 918	20.3	0.703	
PIM-1/SBI-Trip (401 d)	$CHCl_3$	MeOH 24 h; RT 24 h	180	Pure	430	7700	17.9	0.375	
				35 : 65	403	8103	20.1	0.501	
BNNS/PIM-1 (0.5 wt%) (620 d)	$CHCl_3$	MeOH 18 h; 80 °C vacuum 8 h	73 ± 5	Pure	410	3495	8.5	−0.602	512
				50 : 50	364	4679	12.8	−0.115	
BNNS/PIM-1 (0.8 wt%) (620 d)	$CHCl_3$	MeOH 18 h; 80 °C vacuum 8 h	73 ± 5	Pure	278	3331	12.0	−0.296	
				50 : 50	346	4821	13.9	−0.028	
PIM-1 (1 d)	$CHCl_3$	MeOH 24 h; 130 °C vacuum 12 h	58.0 ± 0.9	Pure	660	9000	13.5	0.167	142
				50 : 50	810	8250	10.2	−0.126	
PIM-1 (381 d)	$CHCl_3$	MeOH 24 h; 130 °C vacuum 12 h	43.8 ± 0.9	Pure	300	4000	13.4	−0.128	
				50 : 50	270	4200	16	0.055	
PIM-NH_2 (1 d)	$CHCl_3$	MeOH 24 h; 130 °C vacuum 12 h	49 ± 2	Pure	300	1070	3.6	−1.825	
				50 : 50	33.5	845	25.2	−0.089	
PIM-NH_2 (290 d)	$CHCl_3$	MeOH 24 h; 130 °C vacuum 12 h	51 ± 2	Pure	33	410	12	−1.039	
				50 : 50	14.7	430	29	−0.197	
PIM-NH_2 (448 d)	$CHCl_3$	MeOH 24 h; 130 °C vacuum 12 h	67.2 ± 0.9	Pure	44	480	11.1	−1.056	
				50 : 50	18.3	509	27.8	−0.177	
PIM-NH_2 (433 d, cond.)	$CHCl_3$	MeOH 24 h; 130 °C vacuum 12; CO_2 conditioning up to ∼29 bar	82 ± 1	Pure	54	410	7.6	−1.466	
				50 : 50	16.9	445	26.3	−0.276	

Table 8 (*continued*)

Polymer	Casting solvent	Treatment and drying conditions	Thickness (μm)	Comp. (mol%)	P(CH_4) (barrer)	P(CO_2) (barrer)	α(CO_2/CH_4)	Score	Ref.
PIM-tBOC (351 d)	$CHCl_3$	MeOH 24 h; 130 °C vacuum 12 h	70 ± 9	Pure	6.1	110	18	−1.127	
				50 : 50	6.1	100	17	−1.214	
PIM-deBOC (acid) (339 d)	$CHCl_3$	MeOH 24 h; 130 °C vacuum 12 h	65.0 ± 0.6	Pure	30	460	15.6	−0.753	
				50 : 50	16.7	480	29	−0.158	
PIM-deBOC (thermal) (343 d)	$CHCl_3$	MeOH 24 h; 130 °C vacuum 12 h	83 ± 2	Pure	31	630	20	−0.409	
				50 : 50	24	650	28	−0.084	
PIM-1 (402 d)	$CHCl_3$	MeOH 24 h; 130 °C vacuum 12 h	46 ± 1	Pure	280	3700	13.3	−0.163	
				50 : 50	250	3900	15.8	0.017	
PIM-COOH (330 d)	$CHCl_3$	MeOH 24 h; 130 °C vacuum 12 h	34.2 ± 0.8	Pure	2.1	81	39	−0.512	
				50 : 50	1.7	90	50	−0.243	
22–35 °C, P_{total} = 4 bar									
TPDA-mPDA	$CHCl_3$	MeOH 24 h; RT 24 h; 120 °C vacuum 24 h	40 ± 5	Pure	11.0	349	32	−0.187	343
				50 : 50	9.7	293	30	−0.293	
TPDA-DAR	$CHCl_3$	MeOH 24 h; RT 24 h; 120 °C vacuum 24 h	40 ± 5	Pure	4.7	215	46	−0.007	
				50 : 50	3.9	180	47	−0.059	
TDA1-APAF	THF	MeOH 10 h; RT dry; 120 °C vacuum 12 h	70 ± 5	Pure	0.7	40	55	−0.445	345
				50 : 50	0.5	37	67	−0.279	
TDA1-APAF (250 d)	THF	MeOH 10 h; RT dry; 120 °C vacuum 12 h	70 ± 5	Pure	0.4	30	75	−0.253	
				50 : 50	0.3	28	88	−0.133	
AO-PIM-1	DMAc	MeOH 24 h; 120 °C vacuum 24 h	80–100	Pure	34	1153	34	0.299	347
				50 : 50	36	847	24	−0.139	
PIM-1 (Swaidan 2014)	$CHCl_3$	MeOH 24 h; 120 °C vacuum 24 h	80–100	Pure	362	5919	16	0.197	
				50 : 50	427	5630	13	−0.022	
6FDA-TrMPD	$CHCl_3$	200 °C vacuum 24 h	85	Pure	23.0	498	22	−0.418	342
				50 : 50	19.1	448	23	−0.381	
6FDA-TrMCA	DMF	200 °C vacuum 24 h	85	Pure	3.2	144	45	−0.175	
				50 : 50	2.9	141	48	−0.122	
KAUST-PI-1	$CHCl_3$	MeOH 24 h; 120 °C vacuum 24 h	70	Pure	98	2329	24	0.221	90
				50 : 50	98	2409	25	0.264	
KAUST-PI-5	$CHCl_3$	MeOH 24 h; 120 °C vacuum 24 h	70	Pure	79	1560	20	−0.102	
				50 : 50	67	1431	21	−0.061	
PIM-6FDA-OH TR 440 °C	THF	*n*-Hexane/DCM (90/10) 24 h; air-dry; 120 °C vacuum 24 h	80–100	Pure	54	816	15	−0.580	372
				50 : 50	44	784	18	−0.440	
PIM-6FDA-OH CMS 600 °C	THF	*n*-Hexane/DCM (90/10) 24 h; air-dry; 120 °C vacuum 24 h	80–100	Pure	133	5028	38	0.923	
				50 : 50	133	4797	36	0.862	
PIM-6FDA-OH CMS 630 °C	THF	*n*-Hexane/DCM (90/10) 24 h; air-dry; 120 °C vacuum 24 h	80–100	Pure	56	2880	51	1.013	
				50 : 50	64	2662	42	0.787	
PIM-6FDA-OH CMS 800 °C	THF	*n*-Hexane/DCM (90/10) 24 h; air-dry; 120 °C vacuum 24 h	80–100	Pure	6.0	552	92	0.971	
				50 : 50	7.0	568	81	0.863	372
PIM-1	$CHCl_3$	MeOH overnight; 120 °C vacuum	—	Pure	397	5135	13	−0.073	513
				50 : 50	312	3943	13	−0.188	
Crosslinked PIM-1 385 °C, 8 h (TOX PIM-1)	$CHCl_3$	MeOH overnight; 120 °C vacuum; 385 °C vacuum 8 h	—	Pure	58	1956	34	0.481	
				50 : 50	68	1646	24	0.110	
Crosslinked PIM-1 385 °C, 24 h (TOX PIM-1)	$CHCl_3$	MeOH overnight; 120 °C vacuum; 385 °C vacuum 24 h	—	Pure	16	1100	69	0.943	
				50 : 50	33	1182	36	0.359	
TPDA-APAF 250 °C	THF	120 °C vacuum 24 h; 250 °C vacuum 24 h	40–60	Pure	0.9	46	53	−0.429	34
				50 : 50	0.6	39	61	−0.354	
TPDA-APAF	THF	120 °C vacuum 24 h	40–60	Pure	2.6	99	38	−0.464	
				50 : 50	2.1	89	42	−0.401	

Table 8 (*continued*)

Polymer	Casting solvent	Treatment and drying conditions	Thickness (μm)	Comp. (mol%)	$P(CH_4)$ (barrer)	$P(CO_2)$ (barrer)	$\alpha(CO_2/CH_4)$	Score	Ref.
TPDA-ATAF 250 °C	$CHCl_3$	120 °C vacuum 24 h; 250 °C vacuum 24 h	40–60	Pure	3.8	125	33	−0.518	
				50 : 50	3.6	121	34	−0.509	
TPDA-ATAF	$CHCl_3$	120 °C vacuum 24 h	40–60	Pure	11	325	30	−0.279	
				50 : 50	10	299	30	−0.298	
PIM-1 (Tien-Binh 2018)	$CHCl_3$	MeOH 24 h; 100 °C vacuum 24 h	—	Pure	536	6576	12	−0.034	423
				50 : 50	409	5840	14	0.066	
UiO-66/PIM-1 (20 wt%)	$CHCl_3$	MeOH 24 h; 100 °C vacuum 24 h	—	Pure	610	7100	12	−0.056	
				50 : 50	610	7055	12	−0.064	
UiO-66-NH_2/PIM-1 (20 wt%)	$CHCl_3$	MeOH 24 h; 100 °C vacuum 24 h	—	Pure	638	7660	12	0.000	
				50 : 50	585	7686	13	0.085	
PIM-*co*-UiO-66 (20 wt%)	$CHCl_3$	MeOH 24 h; 100 °C vacuum 24 h	—	Pure	828	15 815	19	0.691	
				50 : 50	831	15 799	19	0.686	
PIM-1 (Tien-Binh 2016)	DCM	60 °C vacuum 24 h	50	Pure	536	6576	12	−0.034	434
				50 : 50	411	5822	14	0.057	
MOF-74/PIM-1 (10 wt%)	$CHCl_3$	60 °C vacuum 24 h	—	Pure	707	9400	13	0.168	
				50 : 50	961	9231	10	−0.143	
MOF-74/PIM-1 (20 wt%, acid treated)	$CHCl_3$	60 °C vacuum 24 h	—	Pure	802	7506	9	−0.240	
				50 : 50	756	7632	10	−0.163	
MOF-74/PIM-1 (20 wt%)	$CHCl_3$	60 °C vacuum 24 h	—	Pure	1114	21 269	19	0.796	
				50 : 50	963	18 401	19	0.745	
OAPS/PIM-1 (5 wt %)	THF	110 °C vacuum	70–80	Pure	227	3519	16	−0.037	437
				50 : 50	303	3603	12	−0.277	
6FDA-DAT1-OH	THF	120 °C vacuum 24 h; 200 °C vacuum 24 h	75 ± 5	Pure	1.4	70	50	−0.332	344
				50 : 50	1.5	70	46	−0.412	
6FDA-DAT1	$CHCl_3$	MeOH 10 h; 120 °C vacuum 12 h	65 ± 5	Pure	2.8	102	36	−0.498	333
				50 : 50	2.5	96	38	−0.474	
6FDA-DAT2	$CHCl_3$	MeOH 10 h; 120 °C vacuum 12 h	65 ± 5	Pure	5.2	156	30	−0.531	
				50 : 50	4.6	139	30	−0.570	

Table 9 CO_2/N_2 performance and upper-bound score for reported microporous polymers

Polymer	Casting solvent	Treatment and drying conditions	Thickness (μm)	Comp.	$P(N_2)$ (barrer)	$P(CO_2)$ (barrer)	$\alpha(CO_2/N_2)$	Score	Ref.
35 °C, P_{total} = 2 bar									
DFTTB	$CHCl_3$	MeOH 12 h; RT 24 h	63	Pure	109	3146	28.9	0.198	336
				15 : 85	89	2875	32.2	0.271	
PIM-NH_2 (448 d)	$CHCl_3$	MeOH 24 h; 130 °C vacuum 12 h	67.2 ± 0.9	Pure	42	483	11.6	−1.282	142
				50 : 50	16	520	32.9	−0.274	
PIM-NH_2 (433 d, cond.)	$CHCl_3$	MeOH 24 h; 130 °C vacuum 12 h and conditioning	82 ± 1	Pure	46	411	8.9	−1.586	
				50 : 50	14	435	31.5	−0.374	
25 °C, P_{total} = 4 bar									
OAPS/PIM-1 (5 wt%)	THF	110 °C vacuum	70–80	Pure	173	3533	20	−0.092	437
				50 : 50	211	3698	18	−0.222	
MAPDA/PIM-1 (15 wt%)	$CHCl_3$	RT 12 h	—	Pure	268	7203	27	0.404	442
				50 : 50	223	6640	30	0.473	
25 °C, *P*total = 6 bar									
Matrimid 5218/PIM-EA(H_2)-TB Blend (30 d)	DCM	RT 24 h	—	Pure	6.8	198	29	−0.712	412
				15 : 85	4.6	208	45	−0.280	
PIM-EA(H_2)-TB (30 d)	DCM	RT 24 h	—	Pure	53	1391	26	−0.164	
				15 : 85	42	1173	28	−0.148	
PIM-SBI-Trip (501 d)	$CHCl_3$	MeOH 24 h; air-dried 24 h	248	Pure	471	11 500	24.4	0.467	511
				15 : 85	498	13 801	27.7	0.647	
PIM-1/SBI-Trip (401 d)	$CHCl_3$	MeOH 24 h; air-dried 24 h	180	Pure	338	7700	22.8	0.270	
				15 : 85	338	8952	26.5	0.462	
22–35 °C, P_{total} = 6.9–8.3 bar									
PIM-300-2.0 d	DCM	MeOH, 120 °C	50–60	Pure	96	4000	42	0.623	392
				50 : 50	75	2924	39	0.454	
PIM-1 (Song 2013)	$CHCl_3$	vacuum overnight	∼50	Pure	313	4333	14	−0.391	390
				50 : 50	147	3077	21	−0.113	
PIM-1, UV, 30 min	$CHCl_3$	UV treatment in air, vacuum overnight	∼50	Pure	58	1555	27	−0.105	
				50 : 50	45	1335	30	−0.060	
PIM-1 (Song 2014)	$CHCl_3$	MeOH overnight; 120 °C vacuum 24 h (1 mbar)	50	Pure	356	5135	14	−0.296	393 and 513
				50 : 50	239	3979	17	−0.249	
TOX-PIM-1	$CHCl_3$	MeOH overnight; 385 °C vacuum 24 h (1 mbar)	50	Pure	30	1100	37	0.076	
				50 : 50	39	979	25	−0.575	
Ultem/PIM-1 (90 : 10)	$CHCl_3$	120 °C vacuum 24 h	45 ± 5	Pure	0.12	4.0	25	−0.296	406
				50 : 50	0.09	3.0	27	−0.245	
Ultem/PIM-1 (80 : 20)	$CHCl_3$	120 °C vacuum 24 h	45 ± 5	Pure	0.19	6.6	25	0.073	
				50 : 50	0.17	6.5	31	−0.320	
OAPS/PIM-1 (5 wt%)	THF	110 °C vacuum	70–80	Pure	157	3266	21	−2.157	437
				50 : 50	185	3202	17	−2.154	

Table 10 H_2/CH_4 permeation performance and upper-bound score for reported microporous polymers

Polymer	Casting solvent	Treatment and drying conditions	Thickness (μm)	Comp. (mol%)	$P(H_2)$ (barrer)	$P(CH_4)$ (barrer)	$\alpha(H_2/CH_4)$	Score	Ref.
35 °C, P_{total} = 2 bar									
PIM-NH_2 (448 d)	$CHCl_3$	MeOH 24 h; 130 °C vacuum 12 h	67.2 ± 0.9	Pure	1134	44	26	0.288	142
				50 : 50	1127	54	20.8	0.118	
PIM-NH_2 (443 d, cond.)	$CHCl_3$	MeOH 24 h; 130 °C vacuum 12 h; CO_2 conditioning up to ~29 bar	82 ± 1	Pure	990	54	18.3	−0.064	
				50 : 50	885	53	16.4	−0.220	
PIM-NH_2	$CHCl_3$	MeOH 24 h; 130 °C vacuum 12 h	58.0 ± 0.9	Pure	1785	297	6	−0.496	
				50 : 50	1652	330	5	−0.683	
25 °C, P_{total} = 6 bar									
TX-AOPIM-1 370 °C 48 h	DMF	Drying at 60 °C; MeOH 24 h; 110 °C vacuum 24 h	65 ± 5	Pure	1060	3.2	331	2.130	515
				50 : 50	665	3.2	208	1.473	
35 °C, P_{total} = 7 bar									
AO-PIM-1	DMF	MeOH 24 h; 120 °C overnight	25 ± 5	Pure	926	42	22	0.024	514
				50 : 50	609	130	4.7	−1.401	
SCA4/AO-PIM-1 (1 wt%)	DMF		25 ± 5	Pure	866	23	38	0.385	
				50 : 50	567	67	8.4	−1.012	
SCA4/AO-PIM-1 (2 wt%)	DMF		25 ± 5	Pure	781	3.4	233	1.665	
				50 : 50	543	14	40	0.107	
SCA4/AO-PIM-1 (3 wt%)	DMF		25 ± 5	Pure	693	2.7	260	1.665	
				50 : 50	470	6.1	77	0.506	
SCA4/AO-PIM-1 (5 wt%)	DMF		25 ± 5	Pure	542	1.8	296	1.598	
				50 : 50	393	3.5	114	0.672	

Table 11 C_3H_6/C_3H_8 permeation performance and upper-bound score for reported microporous polymers tested at 35 °C at a total pure-gas pressure of 2 bar and a total mixed-gas pressure of 4 bar

Polymer	Casting solvent	Treatment and drying conditions	Thickness (μm)	Comp. (mol%)	$P(C_3H_6)$ (barrer)	$P(C_3H_8)$ (barrer)	$\alpha(C_3H_6/C_3H_8)$	Score	Ref.
PIM-PI-1	$CHCl_3$	MeOH 24 h; 120 °C vacuum 24 h	130	Pure	393	51	8	0.264	329
				50 : 50	260	108	2	−0.963	
KAUST-PI-1	$CHCl_3$	MeOH 24 h; 120 °C vacuum 24 h	100	Pure	817	66	12	0.906	
				50 : 50	676	146	5	−0.101	
PIM-6FDA-OH	THF	*n*-Hexane/DCM (90/10) 24 h; 120 °C vacuum 24 h	—	Pure	5.1	0.27	19	0.106	159
				50 : 50	3.69	0.36	10	−0.554	
PIM-6FDA-OH 250 °C (Swaidan 2015)	THF	*n*-Hexane/DCM (90/10) 24 h; 120 °C vacuum 24 h; 250 °C vacuum 24 h	—	Pure	3.5	0.12	29	0.439	
				50 : 50	2.31	0.16	14	−0.361	
PIM-6FDA-OH CMS 600 °C	THF	*n*-Hexane/DCM (90/10) 24 h; 120 °C vacuum 24 h	—	Pure	45	1.3	35	1.221	373
				50 : 50	50	2.1	24	0.870	
PIM-6FDA-OH TR 400 °C	THF	*n*-Hexane/DCM (90/10) 24 h; 120 °C vacuum 24 h	—	Pure	14	0.97	14	0.055	
				50 : 50	12	1.1	11	−0.231	
PIM-6FDA-OH 250 °C (Ma 2018)	THF	250 °C 24 h	40–60	Pure	3.5	0.10	35	0.616	414
				50 : 50	1.9	0.10	19	−0.122	
ZIF-8/PIM-6FDA-OH (33 wt%)	THF	250 °C 24 h	40–60	Pure	10	0.30	33	0.818	
				50 : 50	8.7	0.40	22	0.370	
ZIF-8/PIM-6FDA-OH (65 wt%)	THF	250 °C 24 h	40–60	Pure	38	0.90	42	1.364	
				50 : 50	30	1.0	30	0.976	

sorption effects can outweigh plasticization in highly diffusion-selective materials, the design of sorption-selective materials with strong plasticization resistance remains a promising approach to assuage the impact of plasticization in condensable mixtures.

5.2.4. Robeson upper bound performance at low *versus* high pressures. In an analogous fashion to the mixed- *versus* pure-gas test comparison performed in Section 5.2.3, this section compares low-pressure permeation tests (*e.g.*, CO_2 partial pressure of 1–2 bar) to high-pressure permeation tests (*e.g.*, CO_2 partial pressures at ~10 bar) for microporous polymers. The differences in the low- *versus* high-pressure tests between pure- and mixed-gas cases are also examined. Fig. 75 presents the CO_2/CH_4 mixed-gas permeation data for hydrogen bonding and non-hydrogen bonding samples, while Fig. 77 shows the difference in upper bound scores for samples tested at low and high pressures.

The polymers with hydrogen bonding moieties (Fig. 75a and b) considered in this review showed a decrease in CO_2 permeability and CO_2/CH_4 selectivity with increasing pressure. Many of the pure-gas studies (Fig. 75a and c) showed a smaller decrease in CO_2/CH_4 selectivity with increasing pressure compared to the respective mixed-gas studies (Fig. 75b and d), including comparisons for polymers such as PIM-6FDA-OH,[346] PIM-PMDA-OH,[346] TPDA-APAF,[345] and TPDA-DAR.[345] In the mixed-gas case, some of the

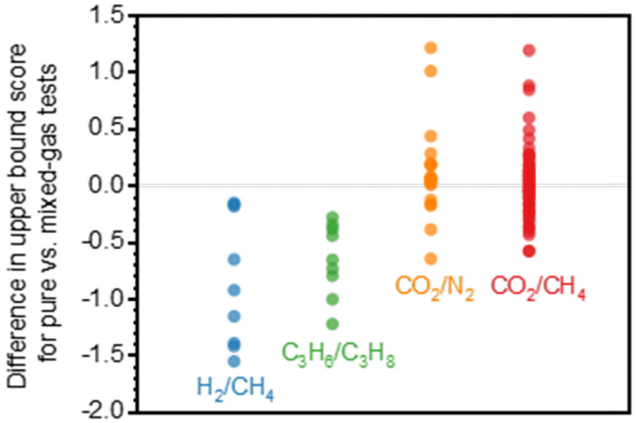

Fig. 74 Difference in mixed-gas and pure-gas upper bound score for H_2/CH_4, C_3H_6/C_3H_8, CO_2/N_2, and CO_2/CH_4 gas pairs for reported polymers tested at low pressures.

polymers considered such as TPDA-DAR,[343] TDA1-APAF (250 days aged),[345] AO-PIM-1,[347] and 6FDA-TrMCA[342] retained good separation performance on the 2018 CO_2/CH_4 mixed-gas upper bound despite the decrease in permselectivity due to plasticization.

In contrast, polymers that do not contain hydrogen bonding groups (Fig. 75c and d) exhibited a larger spread in pure-gas performance changes from 1–2 to ~10 bar. However, it is important to note that, for the polymers without hydrogen bonding moieties, not all samples tested under pure-gas conditions were tested in mixtures. Additionally, there were three times as many polymers without hydrogen bonding moieties (*i.e.*, 35 unique studies) reported in the datasets compared to those with hydrogen bonding moieties (*i.e.*, 11 unique studies). Generally, the difference in upper bound score for non-hydrogen bonding polymers ranged from −0.5 to 0.3 for pure-gas tests and from −0.9 to −0.2 for mixed-gas tests (Fig. 77). For hydrogen bonding polymers, however, the range in upper bound score differences was much smaller, from only −0.3 to −0.1 for pure-gas tests and from −0.5 to −0.1 for mixed-gas tests. This result demonstrates large differences in trends between high-pressure pure- and mixed-gas permeation tests for hydrogen bonding and non-hydrogen bonding polymers, further illustrating the influence of hydrogen bonding on plasticization resistance.

When mixed-gas tests were considered, the overall score differences for both hydrogen bonding and non-hydrogen bonding polymers were negative (Fig. 77), indicating a decrease in upper bound performance. This trend can be attributed to plasticization. PIM-1 samples are highlighted with a blue outline for both pure- and mixed-gas tests, where the same general trend of decreased CO_2/CH_4 performance in mixtures at high pressures is observed (Fig. 77). Taken together, mixed-gas tests allow for evaluation of the effects of plasticization on the transport of the co-permeating species, and therefore such tests can provide a more comprehensive view of changes in CO_2/CH_4 mixed-gas selectivity. In the pure-gas case, plasticization trends will only be observed based on CO_2 plasticization pressure curves and, as a result, the potential change in CH_4 permeation is concealed when calculating permselectivity.

CO_2/CH_4 upper bound plots for post-synthetically modified (PSM) microporous polymers and multi-component systems, which include MMMs and co-polymers, are presented in Fig. 76. In both PSM and multi-component systems, pure-gas tests display a wide variation in scores ranging from −0.6 to 0.1 and from −0.3 to 0.2, respectively. Both mitigation strategies appear to influence plasticization effects in a similar fashion. When comparing the ranges in the difference in upper bound scores between pure- and mixed-gas tests, PSM displayed a range of −0.6 to 0.1 for pure-gas tests *versus* −0.9 to −0.1 for mixed-gas tests. However, in regard to multi-component systems, pure-gas tests displayed a range of −0.3 to 0.2 while mixed-gas tests displayed a much larger range of −1.1 to 0.3. This finding suggests that plasticization adversely affects multi-component systems more than PSM polymers. However, it is important to note that not all samples tested under pure-gas conditions were also tested in mixtures, limiting our confidence in this conclusion. Therefore, only general trends can be drawn from Fig. 77 and only samples with both pure- and mixed-gas data can be used to draw direct conclusions. When considering a directly comparable set of polymers for PSM, for example, TPDA-APAF *versus* TPDA-ATAF treated at 250 °C, mixed-gas tests showed a 31% and a 30% loss in CO_2/CH_4 permselectivity *versus* a 20% and 12% permselectivity loss in the calculated pure-gas case, respectively.[34] In addition, for the samples considered, CMS materials generally showed larger permselectivity differences compared to PSM samples that underwent thermal treatments at lower temperatures (*e.g.*, TR and thermal annealing). For instance, in mixed-gas tests, the CMS derived from PIM-6FDA-OH at 600 °C and 800 °C had an additional 12% and 30% decrease in performance from pure-gas calculations to mixed-gas measurements, respectively. On the other hand, the thermally-rearranged PIM-6FDA-OH and the thermally annealed TPDA-APAF showed a smaller decrease of 2% and 11% in CO_2/CH_4 permselectivity compared to the pure-gas calculations, respectively. Larger permselectivity differences were also observed when considering directly comparable examples for multi-component systems compared to those for PSM systems, as shown in Fig. 76. For instance, for OAPS/PIM-1 (5 wt%),[437] the calculated pure-gas permselectivity increased by 12% while the mixed-gas permselectivity at high pressure decreased by 24%. In this case, the calculated pure-gas selectivity appears to be higher because the sample is tested past its plasticization pressure point. Thus, the pure-gas CO_2 permeability increases, but the CH_4 permeability remains unaffected in the pure-gas case. In contrast, the experimental mixed-gas selectivity unambiguously shows the decrease in mixed-gas permselectivity as a result of plasticization.

Plasticization trends for C_3H_6/C_3H_8 mixtures are highlighted against the 2003 pure-gas and 2012 mixed-gas upper bound in Fig. 78. Once again, a reduction in selectivity is observed as pressure increases from 1 bar C_3H_6 partial pressure to 2.5 to 3 bar C_3H_6 partial pressure. For all reported samples containing PIM-6FDA-OH, a decrease in C_3H_6 permeability is also observed, likely due to competitive sorption with C_3H_8.[159,329,414] In contrast, for PIM-PI-1 and KAUST-PI-1, C_3H_6 permeability increases

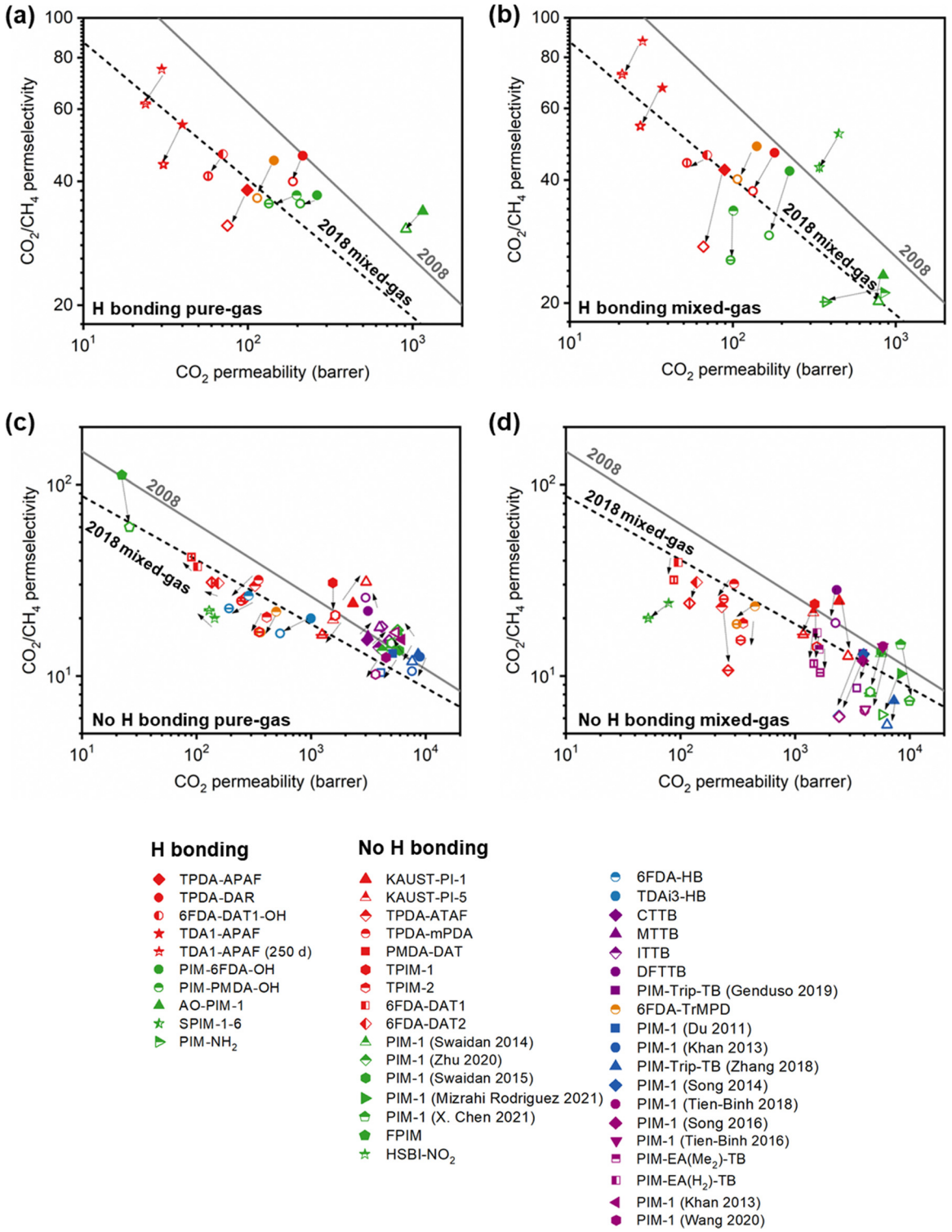

Fig. 75 CO_2/CH_4 Robeson upper bound plots for pure polymers. Filled/half-filled symbols represent data at 1–2 bar CO_2 partial pressure, while unfilled symbols represent data at ~10 bar CO_2 partial pressure. Arrows point from data at 1–2 bar CO_2 partial pressure to ~10 bar CO_2 partial pressure. (a) Polymers with hydrogen bonding groups, calculated pure-gas data. (b) Polymers with hydrogen bonding groups, experimental mixed-gas data (50 : 50 CO_2/CH_4). (c) Polymers without hydrogen bonding groups, calculated pure-gas data. (d) Polymers without hydrogen bonding groups, mixed-gas data (50 : 50 CO_2/CH_4).

as a result of significant plasticization which overcomes competitive sorption. While PIM-PI-1 and KAUST-PI-1 have high intrachain rigidity, they do not contain any hydrogen bonding moieties, rendering them susceptible to plasticization.[329] PIM-6FDA-OH, however, contains –OH groups that hydrogen bond, assisting in CTC formation that helps suppress plasticization.[159,329] Of note, even with plasticization effects, seven of the nine samples considered surpass the 2012 mixed-gas upper bound limit for this

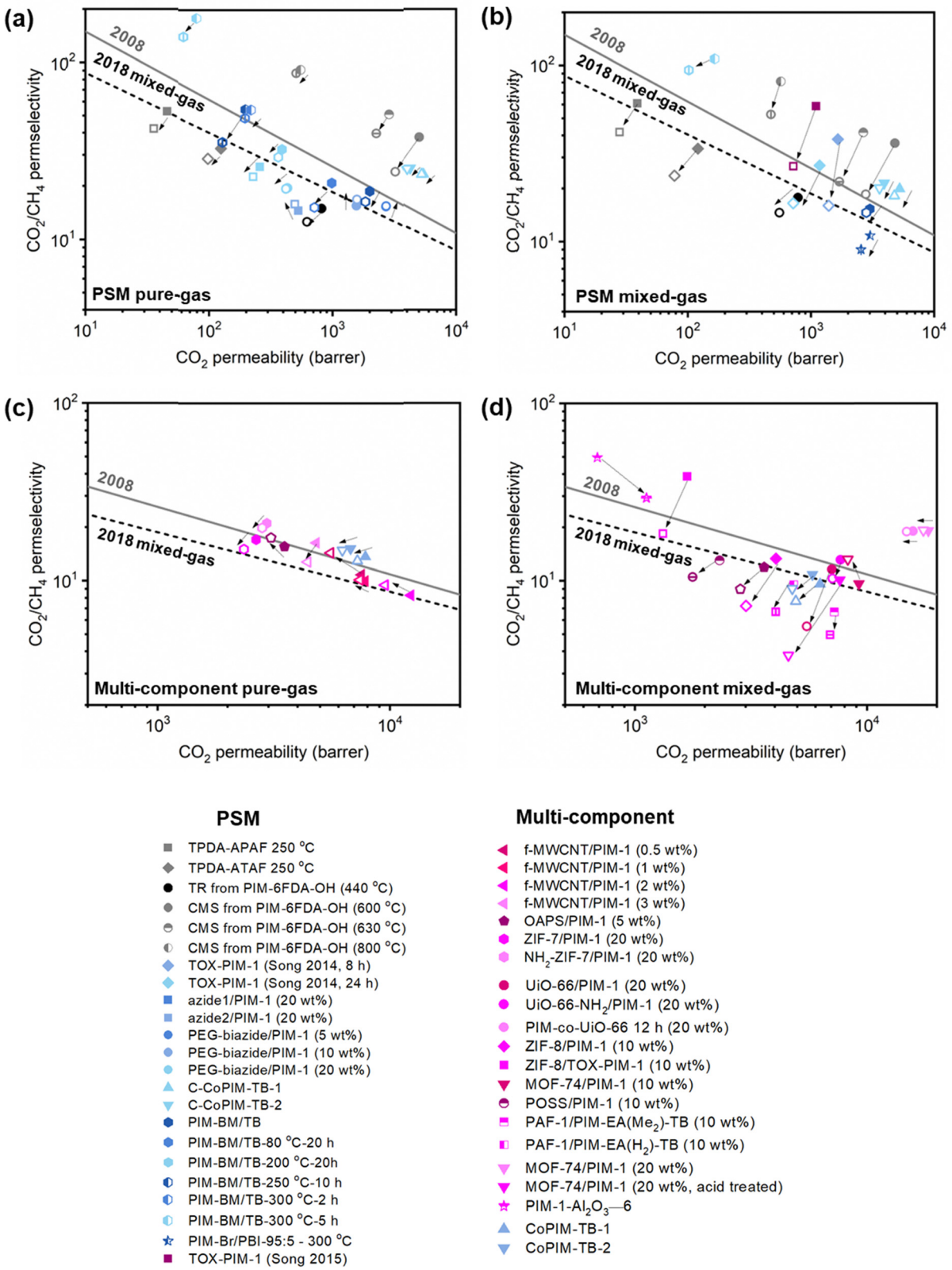

Fig. 76 CO_2/CH_4 Robeson upper bound plots for polymers that underwent PSM and for multi-component systems. Filled/half-filled symbols represent data at 1–2 bar CO_2 partial pressure (except for PIM-1/azide1 and PIM-1/azide2, which were at 3 bar CO_2 partial pressure), while unfilled symbols represent data at 10 bar CO_2 partial pressure. Arrows point from data at 1–2 bar CO_2 partial pressure to 10 bar CO_2 partial pressure. (a) Polymers with PSM, calculated pure-gas data. (b) Polymers with PSM, experimental mixed-gas data (50 : 50 CO_2/CH_4). (c) Multi-component systems, calculated pure-gas data. (d) Multi-component systems, experimental mixed-gas data (50 : 50 CO_2/CH_4).

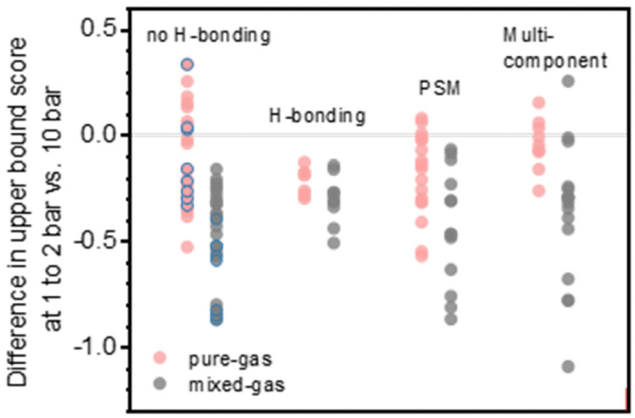

Fig. 77 Difference in CO_2/CH_4 upper bound score at a CO_2 pressure of 1 to 2 bar compared to 10 bar for microporous polymers. Points outlined in blue represent different literature reports of data for PIM-1.

gas mixture. Moreover, when considering the PIM-6FDA-OH samples modified under various conditions, the TR analogue and the ZIF-assisted films showed the smallest decrease in performance metrics in mixed-gas scenarios, suggesting the promise of these strategies for boosting plasticization resistance. While plasticization effects were more pronounced for the CMS analogue of PIM-6FDA-OH compared to the original pristine polymer, performance remained above the 2003 upper bound given the initial enhancements resulting from carbonization of the material.

5.3. Long-term stability of microporous polymers

While this review will not cover long-term performance of microporous polymers in-depth (readers are referred to the following reference for more information),[202] polymer stability is nevertheless an important factor to consider for industrial applications. In this section, we briefly summarize important studies (in both academic and industrial labs) pertaining to long-term performance and stability of microporous polymers.

In 2022, Chen *et al.* developed dibenzomethanopentacene (DBMP)-based PIM copolymer films, and found that over an aging period of over 1000 days, the permeability of DBMP-based PIM copolymers was reduced only by 36–50%, while PIM-1 experienced a reduction in permeability of ~74% on average, suggesting that the incorporation of the rigid DBMP motif can help reduce physical aging effects.[516] Bezzu *et al.* reported that after long-term physical aging (>3.5 years), PIMs containing SBF motifs aged similarly to PIM-1, except for PIM-SBF-5 (Fig. 37), which saw a ~39% decrease in CO_2 permeability (compared to ~79% for PIM-1).[368] This slower aging exhibited by PIM-SBF-5 could be attributed to the bulky *t*-butyl groups that maintain distance between polymer chains that prevent collapse, while other PIM-SBF polymers contain smaller methyl groups.[368] Swaidan *et al.* reported in 2015 that, despite the increased rigidity exhibited by TPIM-1 over PIM-1, the O_2 permeability for TPIM-1 decreased by 95% over the course of 780 days (compared to 70% for PIM-1 over the course of 1380 days), suggesting that intrachain rigidity alone is insufficient in mitigating physical aging.[517] However, there are some distinct counter-examples that note connections between interchain rigidity and observed reductions in physical aging effects for long-term tests. In 2013, Li and Chung reported differences in aging behavior for PIM-1 and PIM-UV4 h (a PIM-1 film that was UV-treated for 4 hours). Over the course of 100 days of aging in an ambient environment, the CH_4 permeability of PIM-1 decreased by ~60% and the CH_4 permeability of PIM-UV4 h decreased by only 25%.[389] This finding suggests that the UV-treated PIM membrane had a more stable structure than PIM-1. When comparing O_2/N_2 selectivity, PIM-UV4 h selectivity increased by ~5% and PIM-1 selectivity increased by 30%, matching trade-off expectations in permeability and selectivity during aging.[389]

In 2021, Foster *et al.* synthesized PIM-1 thin film composite (TFC) membranes and found that both selectivity and aging behavior could be varied by changing the topology of the polymer.[518] For instance, polymerization performed without

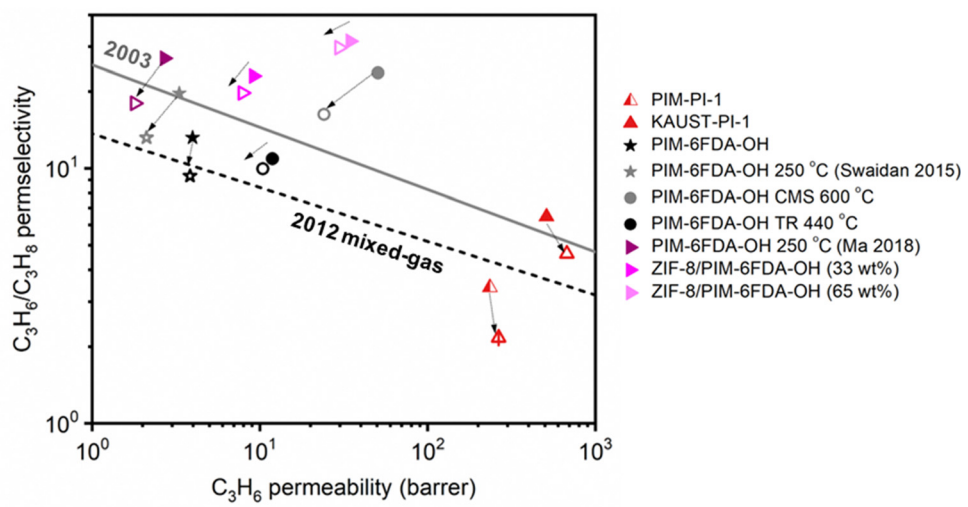

Fig. 78 C_3H_6/C_3H_8 upper bound plot. Filled/half-filled symbols represent data at 1 bar C_3H_6 partial pressure, while unfilled symbols represent data at 2.5 to 3 bar C_3H_6 partial pressure. Arrows point from data at 1 bar C_3H_6 partial pressure to 2.5 to 3 bar C_3H_6 partial pressure.

nitrogen gas led to polymers with higher degrees of branching which could form into small loops.[518] While high molecular weight PIM-1 TFC membranes exhibited a 76% decrease in CO_2 permeability in the first 7 days of aging, a blend containing 80 wt% of high molecular weight PIM-1 and 20 wt% PIM-1 containing small loops exhibited a 47% decrease in CO_2 permeability.[518]

The incorporation of fillers has also been shown to mitigate physical aging. In 2020, Chen *et al.* fabricated MOF-801/PIM-1 MMMs and aged them for 100 days in a dry environment. It was found that while the CO_2 permeability of PIM-1 decreased by 60%, the CO_2 permeability of MOF-801/PIM-1 MMM (with 5 wt% MOF-801) decreased by only 30%, suggesting that MOF-801 helped to rigidify PIM-1.[519] In 2023, Cong *et al.* incorporated a trisilver complex (trisilver pyrazolate, Ag_3pz_3) into PIM-1 films to act as a C_3H_6 carrier filler.[520] When the films were aged in an ambient environment, the permeability of C_3H_6 dropped in the first 60 days ($\sim$15%) and then stabilized, while the C_3H_8 permeability remained stable throughout the 120 days of aging.[520]

In an industrial context, membrane modules often operate continuously for extended periods of time. Therefore, it is also important to test the long-term stability of polymer membranes under the presence of plasticizing gases to evaluate their resistance to plasticization. In 2019, Li *et al.* continuously operated an AO-PIM-1 membrane under a feed mixture containing 20 mol% H_2S, 20 mol% CO_2, and 60 mol% CH_4 at a feed pressure of 8.6 bar and a temperature of 35 °C over the course of 10 days.[521] It was found that the permeabilities of all gases stabilized after 7 days, and the mixed-gas H_2S/CH_4 (40 to 50) and CO_2/CH_4 (20) selectivities remained relatively consistent throughout the 10 days.[521] It was hypothesized that the stability of permeabilities and selectivities during the long-term stability testing could be attributed to the free volume of the AO-PIM-1 membrane being continuously occupied by gases, which could reduce the densification of the membrane.[521] Chen *et al.* reported that after 120 h of continuous gas permeation testing, MOF-801/PIM-1 membranes (with 5 wt% MOF) maintained stable performance with an average CO_2 permeability of 9682 barrer throughout the test.[519] In addition, Cong *et al.* reported that during long-term stability testing of Ag_3pz_3/PIM-1 membranes under single gas conditions, both C_3H_6 and C_3H_8 permeabilities remained stable throughout the 24 days of testing.[520] Therefore, incorporating hydrogen bonding motifs (in the case of AO-PIM-1) or fillers (in the case of both MOF-801 and Ag_3pz_3) in PIM membranes can help maintain stability even when exposed to a continuous feed of plasticizing gases.

While this review does not cover refrigerant gases extensively, a study done by Gutiérrez-Hernández *et al.* in 2023 monitored the long-term separation performance of branched PIM-1 under a 50 : 50 mixture feed of difluoromethane and pentafluoroethane at 1.3 bar and 30 °C, which was changed to a different mixture (68.9 vol% difluoromethane and 31.1 vol% 2,3,3,3-tetrafluoropropene) after four days.[522] In the first four days, the permeability of difluoromethane increased by $\sim$45% to 1325 barrer, but after the mixture was switched, the difluoromethane permeability dropped to 1244 barrer due to an increase in difluoromethane concentration, which would be expected to decrease permeability based on dual-mode sorption.[522] The permeability of difluoromethane then remained relatively constant throughout the rest of the long-term stability testing (7 days total), suggesting an opportunity and a need to further study PIM-1 and other microporous polymers for refrigerant applications.[522]

6. Conclusions and recommendations

Penetrant-induced plasticization remains a critical challenge for polymer membrane performance under realistic high-pressure and condensable feed conditions that are relevant to industry. This review presents a comprehensive summary of the phenomenon of plasticization in emerging microporous polymers, including an in-depth analysis of plasticization trends measured for pure- and mixed-gas permeation and sorption testing conditions. Additionally, in-depth characterization techniques are described to evaluate plasticization at a fundamental level. General mitigation strategies to reduce plasticization effects are also highlighted, including new synthetic approaches, post-synthetic modifications, and multi-component systems such as composites, blends, and copolymers.

While gas permeation tests are an indirect method employed by membrane scientists to probe plasticization in polymer membranes, experiments that directly probe chain mobility in the presence of plasticizing gases can provide direct mechanistic information. For example, studies have been performed on traditional linear polymers to evaluate how gases such as CO_2 influence mechanical properties and the glass transition temperature. However, there are very few related studies on microporous polymers. Tests such as dynamic mechanical analysis (DMA) and dilation experiments can probe chain mobility in the presence of plasticizing gases, which could fill this unmet research need. It is recommended that researchers use additional methods besides gas permeation tests to probe chain mobility in the presence of plasticizing gases, such as DMA, differential scanning calorimetry (DSC), dilation experiments, and molecular dynamics (MD) simulations.

When considering methods to mitigate plasticization effects in microporous polymers, previous research has focused on various strategies including the introduction of (1) rigid backbone moieties to induce intrachain rigidity, (2) hydrogen bonding backbone moieties to increase interchain rigidity, (3) thermal and chemical crosslinking, and (4) filler incorporation (such as metal–organic frameworks (MOFs)) or polymer–polymer blending. When viewed holistically, the most significant differences in transport performance were observed for systems with increased interchain rigidity induced by hydrogen bonding moieties, such as –OH. In fact, the variation in mixed-gas normalized permeabilities for CO_2 and CH_4 were much more significant in the absence of hydrogen bonding, suggesting that the introduction of secondary forces improves plasticization resistance. Other strategies including filler incorporation and crosslinking appeared to stabilize plasticization effects, but clear trends were not observed when comparing across classes of different fillers. Introducing methods to increase *inter*chain

rigidity can be a useful technique to mitigate plasticization effects, but in general, reducing *intra*chain mobility through the incorporation of bulky chain moieties does not significantly improve plasticization resistance. Therefore, we recommend that researchers further investigate the incorporation of secondary forces into microporous polymers, including the incorporation of hydrogen bonding motifs.

The plasticization pressure, which is the pressure at which permeability begins to increase with increasing feed pressure, is often the first metric used to determine if a membrane is plasticization resistant. However, the plasticization pressure alone does not account for changes in permeability of the less condensable penetrant in a mixture experiment. For mixed-gas experiments, some unambiguous indications of plasticization include an increase in permeability of the less condensable penetrant and a decrease in the overall permselectivity with increasing feed pressure. Additionally, when running pure- and mixed-gas tests, maximum feed pressures tested are around 25 bar, but plasticization behavior can significantly change at higher pressures. Therefore, in addition to high-pressure pure-gas tests, it is recommended that researchers perform mixed-gas tests with application-inspired conditions at relevant feed pressures and temperatures.

In addition to both pure- and mixed-gas permeation tests, it is also critical to report specific testing conditions and protocols when evaluating sorption and permeation at high pressures. While performing high-pressure tests is routine in the polymer membrane community, the hold times between each data point for testing are seldom reported. Because plasticization is directly associated to polymer chain motion and dynamics, slight changes in the amount of time a polymer is exposed to a plasticizing gas can significantly influence the resulting high-pressure data, thus biasing plasticization results. For example, PIM-1 has plasticization pressures for CO_2 at 35 °C that range from <2 bar to 27 bar, despite these tests being run for the same polymer composition. It is recommended that researchers report the hold times of each pressure point for high-pressure sorption and permeation tests. Having this information will allow more consistent and reliable comparisons of plasticization effects between polymer structures and chemistries.

When considering mixed-gas testing in microporous materials, this review provides a comprehensive survey of mixtures and testing conditions that have been considered for polymers in the literature. While CO_2/CH_4 has been investigated in great depth, other binary and complex ternary mixtures are seldom explored, despite representing more realistic industrial scenarios. In general, the review of previous work showed that in binary CO_2/CH_4 mixtures, both sorption and diffusion selectivity play an important role in defining separation metrics. In mixtures containing H_2S, sorption selectivity can play a much more significant role over diffusion selectivity in determining overall performance. As such, in addition to running mixed-gas tests with application-inspired feed pressures and temperatures, it is also recommended that mixture compositions reflect compositions found in industry. For example, investigating plasticizing impurities commonly found in natural gas such as H_2S and BTEX aromatics would strengthen the current fundamental and practical understanding of plasticization for that specific application. Additional mixtures including condensable C_2–C_4 gases would also assist in evaluating membrane promise for emerging applications.[475]

It has been proposed that gases with high solubility and critical temperatures induce plasticization in polymer membranes. Before the era of microporous polymers, a critical gas concentration of 38 ± 7 $cm_{(STP)}^3$ $cm_{(polymer)}^{-3}$ was proposed to correlate with CO_2 pure-gas plasticization curves, regardless of the polymer. While there has been some disagreement about the use of this specific critical concentration with non-microporous polymers,[80] many recent studies on microporous polymers indicate that this critical concentration of CO_2 is much higher.[34,48,90,328,342,346] In this review, high-pressure plasticization data for microporous polymers was evaluated and the CO_2 concentration observed at the plasticization pressure was found to be consistently higher than the critical concentration originally suggested by Bos *et al.* (Fig. 67). It is recommended that researchers perform sorption experiments during materials development to evaluate the effects of gas concentration on plasticization. Mixed-gas sorption experiments are ideal to replicate realistic conditions, and more of these experiments are encouraged, but as these tests are often not as accessible, models such as the mixed-gas dual-mode sorption model or NELF model can be used for predicting mixed-gas sorption behavior.

Lastly, most of the membranes tested at the lab scale are bulk films with thicknesses on the micron scale (*i.e.*, >1 μm). However, in an industrial setting, thinner membranes (*i.e.*, <1 μm) are required to maximize productivity. Moreover, thinner membranes are more susceptible to plasticization,[460,523] and thus the thicker membranes that are often tested are not fully representative of how the same material will perform in an industrial setting. Finally, membrane modules operating in a real process are used continuously for extended periods of time, indicating an application need to explore testing under continuous gas flow. We encourage researchers to examine the plasticization properties of thick and thin films using sorption experiments and long-term permeation tests in the presence of plasticizing contaminants.

In conclusion, microporous polymers represent a class of promising materials for gas separations due to their solution processability and high performance relative to the Robeson upper bound. However, despite their rigid backbone structures, microporous materials and emerging polymers are often still susceptible to penetrant-induced plasticization. Although further research is needed to fully understand and mitigate plasticization effects, a great deal of progress has been made to address these effects and enable membrane technology for emerging applications.

List of abbreviations

6FDA	Hexafluoroisopropylidene diphthalic dianhydride
APAF	2,2-Bis(3-amino-4-hydroxyphenyl)-hexafluoropropane

Ar	Argon
ATAF	5,5′-(Hexafluoroisopropylidene)-di-*o*-toluidine
$\alpha_{i,j}$	Membrane selectivity comparing penetrants i and j
α_s	Activity of the penetrant
b	Langmuir affinity constant
BDS	Broadband dielectric spectroscopy
BET	Brunauer–Emmett–Teller
BTEX	Benzenes, toluene, ethylbenzene, xylenes
C	Concentration of penetrant sorbed inside a material
C'_H	Langmuir sorption capacity
C_2H_4	Ethylene
C_2H_6	Ethane
C_3H_6	Propylene
C_3H_8	Propane
CA	Cellulose acetate
CAG	Combined acid gas selectivity
CH_4	Methane
$CHCl_3$	Chloroform
CMS	Carbon molecular sieve
CO	Carbon monoxide
CO_2	Carbon dioxide
C_p	Specific heat capacity
cPIM	Carboxylated PIM
CTA	Cellulose triacetate
CTC	Charge transfer complex
D^*	Diffusion constant at infinite dilution
DABA	3,5-Diaminobenzoic acid
DAM	2,4,6-Trimethyl-*m*-phenylenediamine
DAR	Dihydroxyl-functionalized 4,6-diaminoresorcinol
DCM	Dichloromethane
D_i	Diffusion coefficient of component i
DMA	Dynamic mechanical analysis
DMC	Dimethyl carbonate
DMS	Dual-mode sorption
DSC	Differential scanning calorimetry
f	Frequency
fcu	Face-centered cubic
FFV	Fractional free volume
f_{max}	Maximal dielectric loss
H_2	Hydrogen
H_2O	Water
H_2S	Hydrogen sulfide
HAB	3,3′-Dihydroxy-4,4′-diamino-biphenyl
He	Helium
HN	Havriliak–Negami
i-C_4H_{10}	Isobutane
IR	Infrared
KAUST	King Abdullah University of Science and Technology
k_d	Henry's constant
Kr	Krypton
k_{sw}	Swelling coefficient
l	Thickness
MAS	Magic angle spinning
MD	Molecular dynamics
MEMS	Microelectromechanical systems
MMM	Mixed-matrix membrane
MOF	Metal–organic framework
MT	Modulated-temperature
n-C_4H_{10}	Butane
N_2	Nitrogen
Ne	Neon
N_i	Flux of component i
NELF	Non-equilibrium lattice fluid model
NMP	*N*-Methyl-2-pyrrolidone
NMR	Nuclear magnetic resonance
NO_x	Nitrogen oxides
O_2	Oxygen
OAPS	Amine-functionalized POSS (polyhedral oligomeric silsesquioxane) particles
p	Pressure
PC	Polycarbonate
p-DCX	α,α′-Dichloro-*p*-xylene
PDMS	Polydimethylsiloxane
PEG	Polyethylene glycol
PEI	Polyetherimide
PEMA	Poly(ethyl methacrylate)
PEO	Poly(ethylene oxide)
PhE-POSS	Polyhedral oligomeric silsesquioxane with phenethyl substituents
P_i	Permeability of component i
PI	Polyimide
PIM	Polymer of intrinsic microporosity
PLA	Polylactic acid
PMMA	Poly(methyl methacrylate)
PPC	Pressure perturbation calorimetry
PPMA	Poly(propyl methacrylate)
PPSM	Post-synthetic packing structure modification
PS	Polystyrene
PSA	Pressure swing adsorption
PSf	Polysulfone
PSM	Post-synthetic modification
PTMSP	Poly(1-trimethylsilyl)-1-propyne
PVC	Poly(vinyl chloride)
RH	Relative humidity
RT	Room temperature
ρ	Polymer density
ρ^0	Initial polymer density
SBF	Spirobifluorene
SBI	Spirobisindane
S_i	Sorption coefficient of component i
SO_2	Sulfur dioxide
SO_x	Sulfur oxides
SR	Self-reference
σ	Stress
TAC	Triacetate
TB	Tröger's base
T_β	Temperature at which β relaxation occurs
T_{cryst}	Crystallization temperature
T_c	Critical temperature
T_γ	Temperature at which γ relaxation occurs
T_g	Glass transition temperature

THF	Tetrahydrofuran
T_m	Melting temperature
TOX	Thermal-oxidatively crosslinked
TPDA	9,10-Diisopropyl-triptycene-based dianhydride
TR	Thermal rearrangement
Trip	Triptycene
TrMCA	3,5-Diamino-2,4,6-trimethylbenzoic acid
TSA	Thermal swing adsorption
TSC	Thermally stimulated discharge current
TTS	Time-temperature superposition
TZ	Tetrazole
UiO	University of Oslo
USD	United States dollar
VFTH	Vogel–Fulcher–Tamman–Hesse
ν_i	Molecular volume of species i
V_p	Molar volume of polymer
V_s	Molar volume of solvent
WLF	Williams–Landel–Ferry
x_i	Concentration of component i in the feed
y_i	Concentration of component i in the permeate
ZIF	Zeolitic imidazolate framework

Conflicts of interest

There are no conflicts of interest to declare.

Acknowledgements

We gratefully acknowledge support for this study from the National Science Foundation CAREER Award under Award Number CBET-2146422, the U.S. Department of Energy, Office of Science, Office of Basic Energy Science, Separation Science program under Award Number DE-SC0019087, and the Department of the Navy, Office of Naval Research under ONR awards N00014-20-1-2418 and N00014-21-1-2666.

References

1 G. Towler and R. Sinnott, *Chemical Engineering Design Principles, Practice and Economics of Plant and Process Design*, Elsevier Ltd, 2nd edn, 2013.
2 J. D. Seader, E. J. Henley and D. K. Roper, *Separation Process Principles*, Wiley, 3rd edn, 2011.
3 D. S. Sholl and R. P. Lively, *Nature*, 2016, **532**, 435–437.
4 U. S. E. I. Administration, Energy consumption estimates by sector, **https://www.eia.gov/totalenergy/data/annual/index.php**.
5 U.S. Energy Information Administration, International Energy Outlook 2022, **https://www.eia.gov/outlooks/ieo/**, (accessed 20 May 2022).
6 U.S. Energy Information Administration, Annual Energy Outlook 2021, **https://www.eia.gov/outlooks/aeo/**, (accessed 23 January 2022).
7 D. F. Sanders, Z. P. Smith, R. Guo, L. M. Robeson, J. E. McGrath, D. R. Paul and B. D. Freeman, *Polymer*, 2013, **54**, 4729–4761.
8 S. Mokhatab and W. A. Poe, *Handbook of Natural Gas Transmission and Processing*, Elsevier Science Ltd, 2012, pp. 253–290.
9 C. Z. Liang, T. S. Chung and J. Y. Lai, *Prog. Polym. Sci.*, 2019, **97**, 101141.
10 M. Galizia, W. S. Chi, Z. P. Smith, T. C. Merkel, R. W. Baker and B. D. Freeman, *Macromolecules*, 2017, **50**, 7809–7843.
11 R. W. Baker, *Ind. Eng. Chem. Res.*, 2002, **41**, 1393–1411.
12 Materials & Chemicals Market Research Reports & Materials & Chemicals Industry Analysis, **https://www.marketresearch.com/Heavy-Industry-c1595/Materials-Chemicals-c91/**, (accessed 23 January 2022).
13 B. D. Freeman, *Macromolecules*, 1999, **32**, 375–380.
14 A. Y. Alentiev and Y. P. Yampolskii, *J. Membr. Sci.*, 2000, **165**, 201–216.
15 L. M. Robeson, Z. P. Smith, B. D. Freeman and D. R. Paul, *J. Membr. Sci.*, 2014, **453**, 71–83.
16 A. X. Wu, J. A. Drayton and Z. P. Smith, *AIChE J.*, 2019, **65**, 1–12.
17 L. M. Robeson, *J. Membr. Sci.*, 1991, **62**, 165–185.
18 L. M. Robeson, *J. Membr. Sci.*, 2008, **320**, 390–400.
19 A. Roy, S. R. Venna, G. Rogers, L. Tang, T. C. Fitzgibbons, J. Liu, H. McCurry, D. J. Vickery, D. Flick and B. Fish, *Proc. Natl. Acad. Sci. U. S. A.*, 2021, **118**, 1–9.
20 H. Zhai and E. S. Rubin, *Environ. Sci. Technol.*, 2013, **47**, 3006–3014.
21 B. D. Bhide and S. A. Stern, *J. Membr. Sci.*, 1991, **62**, 37–58.
22 C. A. Scholes, M. T. Ho, D. E. Wiley, G. W. Stevens and S. E. Kentish, *Int. J. Greenh. Gas Control*, 2013, **17**, 341–348.
23 L. Zhao, E. Riensche, L. Blum and D. Stolten, *J. Membr. Sci.*, 2010, **359**, 160–172.
24 T. C. Merkel, H. Lin, X. Wei and R. Baker, *J. Membr. Sci.*, 2010, **359**, 126–139.
25 P. M. Budd, B. S. Ghanem, S. Makhseed, N. B. McKeown, K. J. Msayib and C. E. Tattershall, *Chem. Commun.*, 2004, 230–231.
26 P. M. Budd, E. S. Elabas, B. S. Ghanem, S. Makhseed, N. B. McKeown, K. J. Msayib, C. E. Tattershall and D. Wang, *Adv. Mater.*, 2004, **16**, 456–459.
27 Y. Rogan, L. Starannikova, V. Ryzhikh, Y. Yampolskii, P. Bernardo, F. Bazzarelli, J. C. Jansen and N. B. McKeown, *Polym. Chem.*, 2013, **4**, 3813–3820.
28 R. Swaidan, B. Ghanem, E. Litwiller and I. Pinnau, *Macromolecules*, 2015, **48**, 6553–6561.
29 M. Carta, M. Croad, R. Malpass-Evans, J. C. Jansen, P. Bernardo, G. Clarizia, K. Friess, M. Lanč and N. B. McKeown, *Adv. Mater.*, 2014, **26**, 3526–3531.
30 E. Lasseuguette, R. Malpass-Evans, M. Carta, N. B. McKeown and M. C. Ferrari, *Membranes*, 2018, **8**, 1–11.
31 S. L. Li, Z. Zhu, J. Li, Y. Hu and X. Ma, *Polymer*, 2020, **193**, 122369.
32 Y. Rogan, R. Malpass-Evans, M. Carta, M. Lee, J. C. Jansen, P. Bernardo, G. Clarizia, E. Tocci, K. Friess, M. Lanč and N. B. McKeown, *J. Mater. Chem. A*, 2014, **2**, 4874–4877.

33 M. Carta, R. Malpass-Evans, M. Croad, Y. Rogan, J. C. Jansen, P. Bernardo, F. Bazzarelli and N. B. McKeown, *Science*, 2013, **339**, 303–307.
34 R. Swaidan, B. Ghanem, E. Litwiller and I. Pinnau, *J. Membr. Sci.*, 2015, **475**, 571–581.
35 C. G. Bezzu, M. Carta, A. Tonkins, J. C. Jansen, P. Bernardo, F. Bazzarelli and N. B. Mckeown, *Adv. Mater.*, 2012, **24**, 5930–5933.
36 B. S. Ghanem, N. B. McKeown, P. M. Budd and D. Fritsch, *Macromolecules*, 2008, **41**, 1640–1646.
37 N. Du, H. B. Park, G. P. Robertson, M. M. Dal-Cin, T. Visser, L. Scoles and M. D. Guiver, *Nat. Mater.*, 2011, **10**, 372–375.
38 K. Mizrahi Rodriguez, S. Lin, A. X. Wu, G. Han, J. J. Teesdale, C. M. Doherty and Z. P. Smith, *Angew. Chem., Int. Ed.*, 2021, **60**, 6593–6599.
39 Y. He, F. M. Benedetti, S. Lin, C. Liu, Y. Zhao, H. Z. Ye, T. Van Voorhis, M. G. De Angelis, T. M. Swager and Z. P. Smith, *Adv. Mater.*, 2019, **31**, 1–8.
40 Y. Huang and D. R. Paul, *J. Membr. Sci.*, 2004, **244**, 167–178.
41 D. Cangialosi, H. Schut, A. Van Veen and S. J. Picken, *Macromolecules*, 2003, **36**, 142–147.
42 A. Bos, I. G. M. Pünt, M. Wessling and H. Strathmann, *J. Membr. Sci.*, 1999, **155**, 67–78.
43 B. W. Rowe, B. D. Freeman and D. R. Paul, *Polymer*, 2009, **50**, 5565–5575.
44 B. W. Rowe, B. D. Freeman and D. R. Paul, *Polymer*, 2010, **51**, 3784–3792.
45 M. Wessling, M. Lidon Lopez and H. Strathmann, *Sep. Purif. Technol.*, 2001, **24**, 223–233.
46 N. R. Horn and D. R. Paul, *Polymer*, 2011, **52**, 5587–5594.
47 N. R. Horn and D. R. Paul, *Macromolecules*, 2012, **45**, 2820–2834.
48 S. Yi, X. Ma, I. Pinnau and W. J. Koros, *J. Mater. Chem. A*, 2015, **3**, 22794–22806.
49 C. A. Scholes, G. W. Stevens and S. E. Kentish, *Fuel*, 2012, **96**, 15–28.
50 R. Faiz and K. Li, *Desalination*, 2012, **287**, 82–97.
51 J. Hou, P. Liu, M. Jiang, L. Yu, L. Li and Z. Tang, *J. Mater. Chem. A*, 2019, **7**, 23489–23511.
52 T. C. Merkel, M. Zhou and R. W. Baker, *J. Membr. Sci.*, 2012, **389**, 441–450.
53 C. A. Scholes, K. H. Smith, S. E. Kentish and G. W. Stevens, *Int. J. Greenh. Gas Control*, 2010, **4**, 739–755.
54 W. Qiu, M. Kosuri, F. Zhou and W. J. Koros, *J. Membr. Sci.*, 2009, **327**, 96–103.
55 P. Shao and R. Y. M. Huang, *J. Membr. Sci.*, 2007, **287**, 162–179.
56 X. Qiao, T. S. Chung, W. F. Guo, T. Matsuura and M. M. Teoh, *J. Membr. Sci.*, 2005, **252**, 37–49.
57 M. Zhang, L. Deng, D. Xiang, B. Cao, S. S. Hosseini and P. Li, *Processes*, 2019, **7**, 51–82.
58 N. N. Li, R. B. Long and E. J. Henley, *Ind. Eng. Chem.*, 1965, **57**, 18–29.
59 N. N. Li and E. J. Henley, *AIChE J.*, 1964, 666–670.
60 R. M. Barrer, R. Mallinder and P. S. L. Wong, *Polymer*, 1967, **8**, 321–336.
61 W. J. Koros and D. R. Paul, *J. Polym. Sci., Polym. Phys. Ed.*, 1978, **16**, 1947–1963.
62 A. G. Wonders and D. R. Paul, *J. Membr. Sci.*, 1979, **5**, 63–75.
63 R. T. Chern, W. J. Koros, E. S. Sanders and R. Yui, *J. Membr. Sci.*, 1983, **15**, 157–169.
64 J. S. Chiou, J. W. Barlow and D. R. Paul, *J. Appl. Polym. Sci.*, 1985, **30**, 2633–2642.
65 G. K. Fleming and W. J. Koros, *Macromolecules*, 1986, **19**, 2285–2291.
66 E. S. Sanders, *J. Membr. Sci.*, 1988, **37**, 63–80.
67 S. Zhou and S. A. Stern, *J. Polym. Sci., Part B: Polym. Phys.*, 1989, **27**, 205–222.
68 A. C. Puleo and D. R. Paul, *J. Membr. Sci.*, 1989, **47**, 301–332.
69 P. B. Smith and D. J. Moll, *Macromolecules*, 1990, **23**, 3250–3256.
70 G. K. Fleming and W. J. Koros, *J. Polym. Sci., Part B: Polym. Phys.*, 1990, **28**, 1137–1152.
71 R. T. Chern and C. N. Provan, *Macromolecules*, 1991, **24**, 2203–2207.
72 M. Wessling, S. Schoeman, T. van der Boomgaard and C. A. Smolders, *Gas Sep. Purif.*, 1991, **5**, 222–228.
73 J. H. Petropoulos, *J. Membr. Sci.*, 1992, **75**, 47–59.
74 A. Y. Houde, S. S. Kulkarni and M. G. Kulkarni, *J. Membr. Sci.*, 1992, **71**, 117–128.
75 M. Wessling, I. Huisman, T. V. D. Boomgaard and C. A. Smolders, *J. Polym. Sci., Part B: Polym. Phys.*, 1995, **33**, 1371–1384.
76 A. Bos, I. G. M. Pünt, M. Wessling and H. Strathmann, *Sep. Purif. Technol.*, 1998, **14**, 27–39.
77 A. Bos, I. G. M. Pünt, M. Wessling and H. Strathmann, *J. Membr. Sci.*, 1999, **155**, 67–78.
78 C. Staudt-Bickel and W. J. Koros, *J. Membr. Sci.*, 1999, **155**, 145–154.
79 J. D. Wind, C. Staudt-Bickel, D. R. Paul and W. J. Koros, *Ind. Eng. Chem. Res.*, 2002, **41**, 6139–6148.
80 J. D. Wind, S. M. Sirard, D. R. Paul, P. F. Green, K. P. Johnston and W. J. Koros, *Macromolecules*, 2003, **36**, 6433–6441.
81 J. D. Wind, C. Staudt-Bickel, D. R. Paul and W. J. Koros, *Macromolecules*, 2003, **36**, 1882–1888.
82 J. D. Wind, D. R. Paul and W. J. Koros, *J. Membr. Sci.*, 2004, **228**, 227–236.
83 A. Bos, I. Pünt, H. Strathmann and M. Wessling, *AIChE J.*, 2001, **47**, 1088–1093.
84 T. Visser, G. H. Koops and M. Wessling, *J. Membr. Sci.*, 2005, **252**, 265–277.
85 H. Lin, E. Van Wagner, B. D. Freeman, L. G. Toy and R. P. Gupta, *Science*, 2006, **311**, 639–642.
86 T. Visser, N. Masetto and M. Wessling, *J. Membr. Sci.*, 2007, **306**, 16–28.
87 T. Visser and M. Wessling, *Macromolecules*, 2007, **40**, 4992–5000.
88 W. Qiu, C. C. Chen, L. Xu, L. Cui, D. R. Paul and W. J. Koros, *Macromolecules*, 2011, **44**, 6046–6056.

89 M. Minelli and G. C. Sarti, *J. Membr. Sci.*, 2013, **435**, 176–185.
90 R. Swaidan, B. Ghanem, M. Al-Saeedi, E. Litwiller and I. Pinnau, *Macromolecules*, 2014, **47**, 7453–7462.
91 R. R. Tiwari, Z. P. Smith, H. Lin, B. D. Freeman and D. R. Paul, *Polymer*, 2015, **61**, 1–14.
92 Y. Xiao, B. T. Low, S. S. Hosseini, T. S. Chung and D. R. Paul, *Prog. Polym. Sci.*, 2009, **34**, 561–580.
93 J. K. Adewole, A. L. Ahmad, S. Ismail and C. P. Leo, *Int. J. Greenh. Gas Control*, 2013, **17**, 46–65.
94 A. F. Ismail and W. Lorna, *Sep. Purif. Technol.*, 2002, **27**, 173–194.
95 E. P. Favvas, F. K. Katsaros, S. K. Papageorgiou, A. A. Sapalidis and A. C. Mitropoulos, *React. Funct. Polym.*, 2017, **120**, 104–130.
96 U. W. R. Siagian, A. Raksajati, N. F. Himma, K. Khoiruddin and I. G. Wenten, *J. Nat. Gas Sci. Eng.*, 2019, **67**, 172–195.
97 C. A. Scholes, S. E. Kentish and G. W. Stevens, *Sep. Purif. Rev.*, 2009, **38**, 1–44.
98 K. Hunger, N. Schmeling, H. B. T. Jeazet, C. Janiak, C. Staudt and K. Kleinermanns, *Membranes*, 2012, **2**, 727–763.
99 Y. S. Chang, P. Kumari, C. J. Munro, G. Szekely, L. F. Vega, S. Nunes and L. F. Dumée, *J. Membr. Sci.*, 2023, **666**, 121125.
100 Y. Liu, Z. Liu, G. Liu, W. Qiu, N. Bhuwania, D. Chinn and W. J. Koros, *J. Membr. Sci.*, 2020, **593**, 117430.
101 G. Reiter and P. G. De Gennes, *Eur. Phys. J. E*, 2001, **6**, 25–28.
102 A. Serghei and F. Kremer, *Macromol. Chem. Phys.*, 2008, **209**, 810–817.
103 P. M. Budd, N. B. McKeown and D. Fritsch, *J. Mater. Chem.*, 2005, **15**, 1977–1986.
104 F. Doghieri and G. C. Sarti, *Macromolecules*, 1996, **29**, 7885–7896.
105 L. C. E. Struik, *Polym. Eng. Sci.*, 1977, **17**, 165–173.
106 R. W. Baker and B. T. Low, *Macromolecules*, 2014, **47**, 6999–7013.
107 Y. Huang and D. R. Paul, *Ind. Eng. Chem. Res.*, 2007, **46**, 2342–2347.
108 T. P. Lodge and P. C. Hiemenz, *Polymer chemistry*, CRC Press, Boca Raton, 3rd edn, 2019.
109 J. Zhou, A. T. Haldeman, E. H. Wagener and S. M. Husson, *J. Membr. Sci.*, 2014, **454**, 398–406.
110 O. S. Fleming and S. G. Kazarian, *Polym. Sci.*, 2006, **42**, 205–238.
111 F. Chen, D. Peng, Y. Ogata, K. Tanaka, Z. Yang, Y. Fujii, N. L. Yamada, C. H. Lam and O. K. C. Tsui, *Macromolecules*, 2015, **48**, 7719–7726.
112 I. Kikic, F. Vecchione, P. Alessi, A. Cortesi and F. Eva, *Ind. Eng. Chem. Res.*, 2003, **42**, 3022–3029.
113 R. G. Wissinger and M. E. Paulaitis, *J. Polym. Sci., Part B: Polym. Phys.*, 1991, **29**, 631–633.
114 P. Alessi, A. Cortesi, I. Kikic and F. Vecchione, *J. Appl. Polym. Sci.*, 2003, **88**, 2189–2193.
115 S. Araujo, N. Delpouve, S. Domenek, A. Guinault, R. Golovchak, R. Szatanik, A. Ingram, C. Fauchard, L. Delbreilh and E. Dargent, *Macromolecules*, 2019, **52**, 6107–6115.
116 P. Flory, *Principles of Polymer Chemistry*, Cornell University Press, Ithaca, 1953.
117 E. Favre, P. Schaetzel, Q. T. Nguygen, R. Clément and J. Néel, *J. Membr. Sci.*, 1994, **92**, 169–184.
118 J. M. Zielinski and J. L. Duda, *AIChE J.*, 1992, **38**, 405–415.
119 M. Rubinstein and R. H. Colby, *Polymer Physics*, Oxford University Press, Oxford, UK, 2003.
120 H. B. Eitouni and N. P. Balsara, *Physical Properties of Polymers Handbook*, Springer, New York, NY, 2nd edn, 2007, pp. 339–356.
121 M. Mulder, *Pervaporation Membrane Separation Processes*, Elsevier, Amsterdam, 1991, pp. 225–250.
122 A. G. Mikos and N. A. Peppas, *Biomaterials*, 1988, **9**, 419–423.
123 S. S. Jawalkar, K. V. S. N. Raju, S. B. Halligudi, M. Sairam and T. M. Aminabhavi, *J. Phys. Chem. B*, 2007, **111**, 2431–2439.
124 Y. Yampolskii, I. Pinnau and B. Freeman, *Materials Science of Membranes for Gas and Vapor Separation*, John Wiley & Sons Ltd, Chichester, 2006.
125 T. C. Merkel, V. I. Bondar, K. Nagai, B. D. Freeman and I. Pinnau, *J. Polym. Sci., Part B: Polym. Phys.*, 2000, **38**, 415–434.
126 J. R. Li, R. J. Kuppler and H. C. Zhou, *Chem. Soc. Rev.*, 2009, **38**, 1477–1504.
127 A. G. Cubitt, C. Henderson, L. A. K. Staveley, I. M. A. Fonseca, A. G. M. Ferreira and L. Q. Lobo, *J. Chem. Thermodyn.*, 1987, **19**, 703–710.
128 W. M. Haynes, *CRC Handbook of Chemistry and Physics*, CRC Press, Boca Raton, 95th edn, 2014.
129 National Institute of Standards and Technology, **https://www.nist.gov/**, (accessed 10 June 2022).
130 D. W. Breck, *Zeolite Molecular Sieves – Structure, Chemistry, and Use*, John Wiley & Sons, New York, 1974.
131 G. Rutkai, M. Thol, R. Span and J. Vrabec, *Mol. Phys.*, 2017, **115**, 1104–1121.
132 D. W. Van Krevelen, *Properties of Polymers*, Elsevier, Amsterdam, 3rd edn, 1990.
133 B. E. Poling, J. M. Prausnitz and J. P. O'Connell, *The Properties of Gases and Liquids*, McGraw-Hill, New York, 5th edn, 2000.
134 Q. Qian, P. A. Asinger, M. J. Lee, G. Han, K. Mizrahi Rodriguez, S. Lin, F. M. Benedetti, A. X. Wu, W. S. Chi and Z. P. Smith, *Chem. Rev.*, 2020, **120**, 8161–8266.
135 J. G. Wijmans and R. W. Baker, *J. Membr. Sci.*, 1995, **107**, 1–21.
136 W. Deen, *Analysis of transport phenomena*, Oxford University Press, New York, 1998.
137 H. W. H. Lai, F. M. Benedetti, Z. Jin, Y. C. Teo, A. X. Wu, M. G. De Angelis, Z. P. Smith and Y. Xia, *Macromolecules*, 2019, **52**, 6294–6302.
138 K. Mizrahi Rodriguez, A. X. Wu, Q. Qian, G. Han, S. Lin, F. M. Benedetti, H. Lee, W. S. Chi, C. M. Doherty and Z. P. Smith, *Macromolecules*, 2020, **53**, 6220–6234.
139 S. Lin, T. Joo, F. M. Benedetti, L. C. Chen, A. X. Wu, K. M. Rodriguez, Q. Qian, C. M. Doherty and Z. P. Smith, *Polymer*, 2021, **212**, 123121.
140 D. R. Paul, *ACS Symp. Ser.*, 1979, **83**, 294–302.
141 W. J. Koros, *J. Polym. Sci., Part A-2*, 1980, **18**, 981–992.
142 K. Mizrahi Rodriguez, F. M. Benedetti, N. Roy, A. X. Wu and Z. P. Smith, *J. Mater. Chem. A*, 2021, **9**, 23631–23642.

143 E. Ricci, F. M. Benedetti, M. E. Dose, M. G. De Angelis, B. D. Freeman and D. R. Paul, *J. Membr. Sci.*, 2020, **612**, 118374.
144 D. R. Paul and W. J. Koros, *J. Polym. Sci., Part A-2*, 1976, **14**, 675–685.
145 T. A. Barbari, W. J. Koros and D. R. Paul, *J. Membr. Sci.*, 1989, **42**, 69–86.
146 S. A. Stern and V. Saxena, *J. Membr. Sci.*, 1980, **7**, 47–59.
147 M. H. Cohen and D. Turnbull, *J. Chem. Phys.*, 1959, **31**, 1164–1169.
148 I. C. Sanchez and R. H. Lacombe, *Macromolecules*, 1978, **11**, 1145–1156.
149 M. G. Baschetti, F. Doghieri and G. C. Sarti, *Ind. Eng. Chem. Res.*, 2001, **40**, 3027–3037.
150 M. G. De Angelis, T. C. Merkel, V. I. Bondar, B. D. Freedman, F. Doghieri and G. C. Sarti, *Macromolecules*, 2002, **35**, 1276–1288.
151 M. Galizia, M. G. De Angelis and G. C. Sarti, *J. Membr. Sci.*, 2012, **405–406**, 201–211.
152 A. Bos, I. G. M. Pünt, P. Pünt, M. Wessling and H. Strathmann, *J. Polym. Sci., Part B: Polym. Phys.*, 1998, **36**, 1547–1556.
153 N. R. Horn and D. R. Paul, *Polymer*, 2011, **52**, 1619–1627.
154 A. C. Puleo and D. R. Paul, *J. Membr. Sci.*, 1989, **47**, 301–332.
155 S. Damle and W. J. Koros, *Ind. Eng. Chem. Res.*, 2003, **42**, 6389–6395.
156 K. S. Liao, J. Y. Lai and T. S. Chung, *J. Membr. Sci.*, 2016, **515**, 36–44.
157 Y. Naito, Y. Kamiya, K. Terada, K. Mizoguchi and J. S. Wang, *J. Appl. Polym. Sci.*, 1996, **61**, 945–950.
158 J. T. Vaughn and W. J. Koros, *J. Membr. Sci.*, 2014, **465**, 107–116.
159 R. J. Swaidan, X. Ma, E. Litwiller and I. Pinnau, *J. Membr. Sci.*, 2015, **495**, 235–241.
160 G. Genduso and I. Pinnau, *J. Membr. Sci.*, 2020, **610**, 118269.
161 M. Balçık, S. Velioğlu, S. B. Tantekin-Ersolmaz and M. G. Ahunbay, *Polymer*, 2020, **205**, 122789.
162 E. Ricci, N. Vergadou, G. G. Vogiatzis, M. G. De Angelis and D. N. Theodorou, *Macromolecules*, 2020, **53**, 3669–3689.
163 S. Neyertz and D. Brown, *J. Membr. Sci.*, 2020, **614**, 118478.
164 G. Kupgan, A. G. Demidov and C. M. Colina, *J. Membr. Sci.*, 2018, **565**, 95–103.
165 K. Simons, K. Nijmeijer, J. G. Sala, H. van der Werf, N. E. Benes, T. J. Dingemans and M. Wessling, *Polymer*, 2010, **51**, 3907–3917.
166 M. Houben, R. van Geijn, M. van Essen, Z. Borneman and K. Nijmeijer, *J. Membr. Sci.*, 2021, **620**, 118922.
167 Z. P. Smith, G. Hernández, K. L. Gleason, A. Anand, C. M. Doherty, K. Konstas, C. Alvarez, A. J. Hill, A. E. Lozano, D. R. Paul and B. D. Freeman, *J. Membr. Sci.*, 2015, **493**, 766–781.
168 O. Hölck, M. R. Siegert, M. Heuchel and M. Böhning, *Macromolecules*, 2006, **39**, 9590–9604.
169 J. G. Wijmans, *J. Membr. Sci.*, 2004, **237**, 39–50.
170 M. Wessling, T. V. D. Boomgaard, M. H. V. Mulder and C. A. Smolders, *Makromol. Chem., Macromol. Symp.*, 1993, **70–71**, 379–396.
171 P. Ju, L. Jiang and T. B. Lu, *Inorg. Chem.*, 2015, **54**, 6291–6295.
172 J. Jeromenok and J. Weber, *Langmuir*, 2013, **29**, 12982–12989.
173 G. Adam and J. H. Gibbs, *J. Chem. Phys.*, 1965, **43**, 139–146.
174 J. H. Gibbs and E. A. DiMarzio, *J. Chem. Phys.*, 1958, **28**, 373–383.
175 J. A. Forrest and K. Dalnoki-Veress, *Adv. Colloid Interface Sci.*, 2001, **94**, 167–195.
176 T. P. Lodge, *Macromolecules*, 2017, **50**, 9525–9527.
177 S. Napolitano, E. Glynos and N. B. Tito, *Rep. Prog. Phys.*, 2017, **80**, 1–51.
178 E. Vidal Russell and N. E. Israeloff, *Nature*, 2000, **408**, 695–698.
179 R. Böhmer, R. V. Chamberlin, G. Diezemann, B. Geil, A. Heuer, G. Hinze, S. C. Kuebler, R. Richert, B. Schiener, H. Sillescu, H. W. Spiess, U. Tracht and M. Wilhelm, *J. Non.-Cryst. Solids*, 1998, **235–237**, 1–9.
180 W. C. V. Wang, E. J. Kramer and W. H. Sachse, *J. Polym. Sci., Part A-2*, 1982, **20**, 1371–1384.
181 H. A. Mannan, H. Mukhtar, T. Murugesan, R. Nasir, D. F. Mohshim and A. Mushtaq, *Chem. Eng. Technol.*, 2013, **36**, 1838–1846.
182 Y. Yampolskii, *Macromolecules*, 2012, **45**, 3298–3311.
183 K. Golzar, H. Modarress and S. Amjad-Iranagh, *J. Mol. Model.*, 2017, **23**, 1–25.
184 H. Yin, Y. Z. Chua, B. Yang, C. Schick, W. J. Harrison, P. M. Budd, M. Böhning and A. Schönhals, *J. Phys. Chem. Lett.*, 2018, **9**, 2003–2008.
185 H. Yin, B. Yang, Y. Z. Chua, P. Szymoniak, M. Carta, R. Malpass-Evans, N. B. McKeown, W. J. Harrison, P. M. Budd, C. Schick, M. Böhning and A. Schönhals, *ACS Macro Lett.*, 2019, **8**, 1022–1028.
186 K. Toi, G. Morel and D. R. Paul, *J. Appl. Polym. Sci.*, 1982, **27**, 2997–3005.
187 Y. Maeda and D. R. Paul, *J. Polym. Sci., Part B: Polym. Phys.*, 1987, **25**, 957–980.
188 S. Alexander Stern, *J. Membr. Sci.*, 1994, **94**, 1–65.
189 R. P. White and J. E. G. Lipson, *Macromolecules*, 2016, **49**, 3987–4007.
190 J. S. Vrentas and J. L. Duda, *J. Polym. Sci., Polym. Phys. Ed.*, 1977, **15**, 403–416.
191 N. Ramesh, P. K. Davis, J. M. Zielinski, R. P. Danner and J. L. Duda, *J. Polym. Sci., Part B: Polym. Phys.*, 2011, **49**, 1629–1644.
192 R. P. Danner, *Fluid Phase Equilib.*, 2014, **362**, 19–27.
193 L. M. Robeson, Q. Liu, B. D. Freeman and D. R. Paul, *J. Membr. Sci.*, 2015, **476**, 421–431.
194 P. M. Budd, K. J. Msayib, C. E. Tattershall, B. S. Ghanem, K. J. Reynolds, N. B. McKeown and D. Fritsch, *J. Membr. Sci.*, 2005, **251**, 263–269.
195 T. Corrado and R. Guo, *Mol. Syst. Des. Eng.*, 2020, **5**, 22–48.
196 A. Bondi, *J. Phys. Chem.*, 1964, **68**, 441–451.
197 D. W. Van Krevelen and K. Te Nijenhuis, *Properties of Polymers*, Elsevier BV, Amsterdam, 4th edn, 2009.
198 S. S. Jordan and W. J. Koros, *Macromolecules*, 1995, **28**, 2228–2235.

199 N. R. Horn, *J. Membr. Sci.*, 2016, **518**, 289–294.
200 A. X. Wu, S. Lin, K. Mizrahi Rodriguez, F. M. Benedetti, T. Joo, A. F. Grosz, K. R. Storme, N. Roy, D. Syar and Z. P. Smith, *J. Membr. Sci.*, 2021, **636**, 119526.
201 J. Y. Park and D. R. Paul, *J. Membr. Sci.*, 1997, **125**, 23–39.
202 Z. X. Low, P. M. Budd, N. B. McKeown and D. A. Patterson, *Chem. Rev.*, 2018, **118**, 5871–5911.
203 Y. P. Yampolskii, *Russ. Chem. Rev.*, 2007, **76**, 59–78.
204 A. Thran, C. Kroll and F. Faupel, *J. Polym. Sci., Part B: Polym. Phys.*, 1999, **37**, 3344–3358.
205 S. Matteucci, Y. Yampolskii, B. D. Freeman and I. Pinnau, *Materials Science of Membranes for Gas and Vapor Separation*, John Wiley & Sons Ltd, 2006, pp. 1–47.
206 C. C. Hu, C. S. Chang, R. C. Ruaan and J. Y. Lai, *J. Membr. Sci.*, 2003, **226**, 51–61.
207 T. T. Moore and W. J. Koros, *J. Appl. Polym. Sci.*, 2007, **104**, 4053–4059.
208 A. M. Kratochvil and W. J. Koros, *Macromolecules*, 2010, **43**, 4679–4687.
209 S. Velioğlu, M. G. Ahunbay and S. B. Tantekin-Ersolmaz, *J. Membr. Sci.*, 2012, **417–418**, 217–227.
210 K. S. Chang, C. C. Hsiung, C. C. Lin and K. L. Tung, *J. Phys. Chem. B*, 2009, **113**, 10159–10169.
211 A. K. Doolittle, *J. Appl. Phys.*, 1951, **22**, 1471–1475.
212 D. L. Hogenboom, W. Webb and J. A. Dixon, *J. Chem. Phys.*, 1967, **46**, 2586–2598.
213 W. Herreman, W. Grevendonk and A. De Bock, *J. Chem. Phys.*, 1970, **53**, 185–189.
214 A. A. Miller, *J. Phys. Chem.*, 1963, **67**, 1031–1035.
215 M. H. Lee, D. H. Han and B. Cho, *J. Appl. Polym. Sci.*, 1993, **50**, 1803–1806.
216 F. R. Schwarzl and F. Zahradnik, *Rheol. Acta*, 1980, **19**, 137–152.
217 M. L. Williams, R. F. Landel and J. D. Ferry, *J. Am. Chem. Soc.*, 1955, **77**, 3701–3707.
218 M. A. Bohn, *Propellants, Explos., Pyrotech.*, 2019, **44**, 696–705.
219 T. G. Fox and S. Loshaek, *J. Polym. Sci.*, 1955, **15**, 371–390.
220 F. Xie, T. He, H. F. Zhang, F. K. Lee, B. Du, O. K. C. Tsui, Y. Yokoe, K. Tanaka, A. Takahara and T. Kajiyama, *Macromolecules*, 2002, **35**, 1491–1492.
221 K. Tanaka, A. Taura, S. R. Ge, A. Takahara and T. Kajiyama, *Macromolecules*, 1996, **29**, 3040–3042.
222 W. F. Yong and H. Zhang, *Prog. Mater. Sci.*, 2021, **116**, 100713.
223 S. Zhao, J. Liao, D. Li, X. Wang and N. Li, *J. Membr. Sci.*, 2018, **566**, 77–86.
224 W. F. Yong, F. Y. Li, Y. C. Xiao, P. Li, K. P. Pramoda, Y. W. Tong and T. S. Chung, *J. Membr. Sci.*, 2012, **407–408**, 47–57.
225 W. F. Yong and T. S. Chung, *Polymer*, 2015, **59**, 290–297.
226 T. O. McDonald, R. Akhtar, C. H. Lau, T. Ratvijitvech, G. Cheng, R. Clowes, D. J. Adams, T. Hasell and A. I. Cooper, *J. Mater. Chem. A*, 2015, **3**, 4855–4864.
227 T. G. Fox, *Bull. Am. Phys. Soc.*, 1956, **1**, 123.
228 N. B. Singh, N. P. Singh and K. Singh, *Z. Phys. Chem.*, 1997, **199**, 139–144.
229 R. F. Boyer, *Polym. Eng. Sci.*, 1968, **8**, 161–185.
230 J. Heijboer, *Br. Polym. J.*, 1969, **1**, 3–14.
231 R. F. Boyer, *Polymer*, 1976, **17**, 996–1008.
232 J. Heijboer, *Int. J. Polym. Mater. Polym. Biomater.*, 1977, **6**, 11–37.
233 J. M. G. Cowie, *J. Macromol. Sci., Part B: Phys.*, 1980, **18**, 569–623.
234 D. J. Meier, *Molecular Basis of Transitions and Relaxation*, CRC Press, 1967.
235 J. M. Pereña, *Die Angew. Makromol. Chem.*, 1982, **106**, 61–66.
236 G. Xu, C. C. Gryte, A. S. Nowick, S. Z. Li, Y. S. Pak and S. G. Greenbaum, *J. Appl. Phys*, 1989, **66**, 5290–5296.
237 C. Bas, C. Tamagna, T. Pascal and N. Dominique Alberola, *Polym. Eng. Sci.*, 2003, **43**, 344–355.
238 S. Z. D. Cheng, T. M. Chalmers, Y. Gu, Y. Yoon, F. W. Harris, J. Cheng, M. Fone and J. L. Koenig, *Macromol. Chem. Phys.*, 1995, **196**, 1439–1451.
239 J. P. Habas, J. Peyrelasse and M. F. Grenier-Loustalot, *High Perform. Polym.*, 1996, **8**, 515–532.
240 A. C. Comer, D. S. Kalika, B. W. Rowe, B. D. Freeman and D. R. Paul, *Polymer*, 2009, **50**, 891–897.
241 H. W. Starkweather Jr, *Macromolecules*, 1981, **14**, 1277–1281.
242 H. W. Starkweather, *Polymer*, 1991, **32**, 2443–2448.
243 P. Gill, T. T. Moghadam and B. Ranjbar, *J. Biomol. Technol.*, 2010, **21**, 167–193.
244 W. Brostow, S. H. Goodman and J. Wahrmund, *Handbook of Thermoset Plastics*, Elsevier, 2014, pp. 191–252.
245 Y. Z. Zhan, Y. Du and Y. H. Zhuang, *Methods Phase Diagr. Determ.*, 2007, 108–150.
246 Humboldt Unniversitat zu Berlin, *Adv. Lab DSC Investig. Polym.*, 2009, 1–17.
247 Q. Zheng, Y. Zhang, M. Montazerian, O. Gulbiten, J. C. Mauro, E. D. Zanotto and Y. Yue, *Chem. Rev.*, 2019, **119**, 7848–7939.
248 S. Yu, Y. Wu, S. Wang, M. Lu and L. Zuo, *Sens. Actuators, A*, 2019, **291**, 150–155.
249 M. Ravindar Reddy, A. R. Subrahmanyam, M. Maheshwar Reddy, J. Siva Kumar, V. Kamalaker and M. Jaipal Reddy, *Mater. Today Proc.*, 2016, **3**, 3713–3718.
250 G. B. McKenna and S. L. Simon, *Handbook of Thermal Analysis and Calorimetry*, Elsevier, 2002, vol. 3, pp. 49–109.
251 Y. Zhai, L. Okoro, A. Cooper and R. Winter, *Biophys. Chem.*, 2011, **156**, 13–23.
252 E. Huang, X. Liao, C. Zhao, C. B. Park, Q. Yang and G. Li, *ACS Sustainable Chem. Eng.*, 2016, **4**, 1810–1818.
253 Y. Mi and S. Zheng, *Polymer*, 1998, **39**, 3709–3712.
254 V. A. Byershtein, L. M. Yegorova, V. M. Yegorov and A. B. Sinani, *Polym. Sci. U.S.S.R.*, 1989, **31**, 2719–2728.
255 K. P. Menard and N. R. Menard, *Encyclopedia of Polymer Science and Technology*, John Wiley & Sons Ltd, New York, 2015, pp. 1–33.
256 K. Ghosal, R. T. Chern, B. D. Freeman, W. H. Daly and I. I. Negulescu, *Macromolecules*, 1996, **29**, 4360–4369.
257 H. J. Jo, C. Y. Soo, G. Dong, Y. S. Do, H. H. Wang, M. J. Lee, J. R. Quay, M. K. Murphy and Y. M. Lee, *Macromolecules*, 2015, **48**, 2194–2202.

258 Z. Mi, S. Wang, Z. Hou, Z. Liu, S. Jin, X. Wang, D. Wang, X. Zhao, Y. Zhang, H. Zhou and C. Chen, *Polymers*, 2019, **11**, 1–19.
259 T. Lim, V. Frosini, V. Zaleckas, D. Morrow and J. A. Sauer, *Polym. Eng. Sci.*, 1973, **13**, 51–58.
260 G. N. Gubanova, S. V. Kononova, M. Cristea, D. Timpu, K. A. Romashkova, E. N. Korytkova, T. P. Maslennikova and N. N. Saprikina, *Russ. J. Gen. Chem.*, 2015, **85**, 1496–1505.
261 A. C. Comer, C. P. Ribeiro, B. D. Freeman, S. Kalakkunnath and D. S. Kalika, *Polymer*, 2013, **54**, 891–900.
262 C. R. Maroon, J. Townsend, K. R. Gmernicki, D. J. Harrigan, B. J. Sundell, J. A. Lawrence, S. M. Mahurin, K. D. Vogiatzis and B. K. Long, *Macromolecules*, 2019, **52**, 1589–1600.
263 X. Hu, W. H. Lee, J. Zhao, J. S. Kim, Z. Wang, J. Yan, Y. Zhuang and Y. M. Lee, *J. Membr. Sci.*, 2020, **604**, 118053.
264 J. R. Fried, H. C. Liu and C. Zhang, *J. Polym. Sci., Part C: Polym. Lett.*, 1989, **27**, 385–392.
265 T. S. Chow, *Macromolecules*, 1980, **13**, 362–364.
266 M. Wessling, Z. Borneman, T. Van Den Boomgaard and C. A. Smolders, *J. Appl. Polym. Sci.*, 1994, **53**, 1497–1512.
267 W. Broughton, *Adhes. Mar. Eng.*, 2012, 99–154.
268 M. Meyers, A. Engineering, S. Diego, E. Conferences, H. Senior, S. Award, T. M. S. D. Scientist, E. Awards, L. H. Award, K. Chawla and M. Science, *Mechanical behavior of materials*, Cambridge University Press, Cambridge, 2009, vol. 46.
269 R. E. Wetton, R. D. L. Marsh and J. G. Van-de-Velde, *Thermochim. Acta*, 1991, **175**, 1–11.
270 P. C. Hiemenz and T. P. Lodge, *Polymer Chemistry*, CRC Press, Boca Raton, 2020, pp. 19–60.
271 S. Al-Enezi, K. Hellgardt and A. G. F. Stapley, *Int. J. Polym. Anal. Charact.*, 2007, **12**, 171–183.
272 J. Ulrich, H. G. Brion and R. Kirchheim, *Polymer*, 1999, **40**, 1807–1814.
273 N. M. B. Flichy, S. G. Kazarian, C. J. Lawrence and B. J. Briscoe, *J. Polym. Sci., Part B: Polym. Phys.*, 2001, **39**, 3020–3028.
274 M. Minelli, S. Oradei, M. Fiorini and G. C. Sarti, *Polymer*, 2019, **163**, 29–35.
275 G. Morel and D. R. Paul, *J. Membr. Sci.*, 1982, **10**, 273–282.
276 J. S. Chiou and D. R. Paul, *J. Appl. Polym. Sci.*, 1986, **32**, 2897–2918.
277 J. Xia, T. S. Chung and D. R. Paul, *J. Membr. Sci.*, 2014, **450**, 457–468.
278 P. Číhal, M. Dendisová, M. Švecová, Z. Hrdlička, T. M. Durďáková, P. M. Budd, W. Harrison, K. Friess and O. Vopička, *Polymer*, 2021, **218**, 1–8.
279 J. W. Schultz, *Encycl. Anal. Chem.*, 2000, 1–19.
280 N. Konnertz, Y. Ding, W. J. Harrison, P. M. Budd, A. Schönhals and M. Böhning, *J. Membr. Sci.*, 2017, **529**, 274–285.
281 Y. Poplavko, *Broadband dielectric spectroscopy*, 2021.
282 S. Havriliak and S. Negami, *J. Polym. Sci., Part C: Polym. Symp.*, 2007, **14**, 99–117.
283 F. Kremer and A. Schönhals, *Broadband dielectric spectroscopy*, Springer-Verlag Berlin Heidelberg, New York, 2002.
284 N. Konnertz, Y. Ding, W. J. Harrison, P. M. Budd, A. Schönhals and M. Böhning, *ACS Macro Lett.*, 2016, **5**, 528–532.
285 Y. Matsumiya, T. Inoue, T. Iwashige and H. Watanabe, *Macromolecules*, 2009, **42**, 4712–4718.
286 J. Schaefer, E. O. Stejskal and R. Buchdahl, *Macromolecules*, 1977, **10**, 384–405.
287 J. Schaefer, E. O. Stejskal and R. Buchdahl, *Macromolecules*, 1975, **8**, 291–296.
288 J. Schaefer and E. O. Stejskal, *J. Am. Chem. Soc.*, 1976, **33**, 1031–1032.
289 A. J. Hill, S. J. Pas, T. J. Bastow, M. I. Burgar, K. Nagai, L. G. Toy and B. D. Freeman, *J. Membr. Sci.*, 2004, **243**, 37–44.
290 S. J. D. Smith, R. Hou, K. Konstas, A. Akram, C. H. Lau and M. R. Hill, *Acc. Chem. Res.*, 2020, **53**, 1381–1388.
291 C. H. Lau, X. Mulet, K. Konstas, C. M. Doherty, M. A. Sani, F. Separovic, M. R. Hill and C. D. Wood, *Angew. Chem., Int. Ed.*, 2016, **55**, 1998–2001.
292 C. H. Lau, P. T. Nguyen, M. R. Hill, A. W. Thornton, K. Konstas, C. M. Doherty, R. J. Mulder, L. Bourgeois, A. C. Y. Liu, D. J. Sprouster, J. P. Sullivan, T. J. Bastow, A. J. Hill, D. L. Gin and R. D. Noble, *Angew. Chem., Int. Ed.*, 2014, **53**, 5322–5326.
293 R. Hou, S. J. D. Smith, C. D. Wood, R. J. Mulder, C. H. Lau, H. Wang and M. R. Hill, *ACS Appl. Mater. Interfaces*, 2019, **11**, 6502–6511.
294 N. Sakaguchi, M. Tanaka, M. Yamato and H. Kawakami, *ACS Appl. Polym. Mater.*, 2019, **1**, 2516–2524.
295 M. Koval'Aková, D. Olčák, V. Hronský, P. Vrábel, O. Fričová, I. Chodák, P. Alexy and G. Sučik, *J. Appl. Polym. Sci.*, 2016, **133**, 1–11.
296 M. D. Sefcik and J. Schaefer, *J. Polym. Sci., Part A-2*, 1983, **21**, 1055–1062.
297 M. D. Sefcik, J. Schaefer, F. L. May, D. Raucher and S. M. Dub, *J. Polym. Sci., Part A-2*, 1983, **21**, 1041–1054.
298 M. G. De Angelis, T. C. Merkel, V. I. Bondar, B. D. Freeman, F. Doghieri and G. C. Sarti, *J. Polym. Sci., Part B: Polym. Phys.*, 1999, **37**, 3011–3026.
299 J. N. Hilfiker, M. Stadermann, J. Sun, T. Tiwald, J. S. Hale, P. E. Miller and C. Aracne-Ruddle, *Appl. Surf. Sci.*, 2017, **421**, 508–512.
300 W. Ogieglo, H. Wormeester, M. Wessling and N. E. Benes, *ACS Appl. Mater. Interfaces*, 2012, **4**, 935–943.
301 N. E. Benes, G. Spijksma, H. Verweij, H. Wormeester and B. Poelsema, *AIChE J.*, 2001, **47**, 1212–1218.
302 R. P. Feynman, R. B. Leighton and M. Sands, *The Feynman Lectures on Physics*, Addison-Wesley Publishing Company, Inc., Reading, MA, 1st edn, 1963.
303 A. R. Berens and H. B. Hopfenberg, *Polymer*, 1978, **19**, 489–496.
304 D. S. Pope, G. K. Fleming and W. J. Koros, *Macromolecules*, 1990, **23**, 2988–2994.
305 W. Ogieglo, B. Ghanem, X. Ma, M. Wessling and I. Pinnau, *ACS Appl. Mater. Interfaces*, 2018, **10**, 11369–11376.
306 J. Crank, *The Mathematics of Diffusion*, Oxford University Press, London, 2nd edn, 1975.

307 A. C. Newns, *Trans. Faraday Soc.*, 1956, **52**, 1533–1545.
308 T. Ormanci-Acar, M. Mohammadifakhr, N. E. Benes and W. M. de Vos, *J. Membr. Sci.*, 2020, **610**, 118277.
309 R. Tamime, Y. Wyart, L. Siozade, I. Baudin, C. Deumie, K. Glucina and P. Moulin, *Membranes*, 2011, **1**, 91–97.
310 N. Du, H. B. Park, M. M. Dal-Cin and M. D. Guiver, *Energy Environ. Sci.*, 2012, **5**, 7306–7322.
311 H. B. Park, C. H. Jung, Y. M. Lee, A. J. Hill, S. J. Pas, S. T. Mudie, E. Van Wagner, B. D. Freeman and D. J. Cookson, *Science*, 2007, **318**, 254–258.
312 J. H. Kim, W. J. Koros and D. R. Paul, *J. Membr. Sci.*, 2006, **282**, 32–43.
313 W. Qiu, C. C. Chen, L. Xu, L. Cui, D. R. Paul and W. J. Koros, *Macromolecules*, 2011, **44**, 6046–6056.
314 N. Alaslai, B. Ghanem, F. Alghunaimi, E. Litwiller and I. Pinnau, *J. Membr. Sci.*, 2016, **505**, 100–107.
315 W. Qiu, L. Xu, C. C. Chen, D. R. Paul and W. J. Koros, *Polymer*, 2013, **54**, 6226–6235.
316 J. Vaughn and W. J. Koros, *Macromolecules*, 2012, **45**, 7036–7049.
317 X. Duthie, S. Kentish, S. J. Pas, A. J. Hill, C. Powell, K. Nagai, G. Stevens and G. Qiao, *J. Polym. Sci., Part B: Polym. Phys.*, 2008, **46**, 1879–1890.
318 J. T. Vaughn, W. J. Koros, J. R. Johnson and O. Karvan, *J. Membr. Sci.*, 2012, **401–402**, 163–174.
319 N. B. McKeown, *Sci. China: Chem.*, 2017, **60**, 1023–1032.
320 B. S. Ghanem, *Polym. Chem.*, 2012, **3**, 96–98.
321 B. S. Ghanem, R. Swaidan, X. Ma, E. Litwiller and I. Pinnau, *Adv. Mater.*, 2014, **26**, 6696–6700.
322 R. Swaidan, M. Al-Saeedi, B. Ghanem, E. Litwiller and I. Pinnau, *Macromolecules*, 2014, **47**, 5104–5114.
323 B. S. Ghanem, R. Swaidan, E. Litwiller and I. Pinnau, *Adv. Mater.*, 2014, **26**, 3688–3692.
324 T. M. Long and T. M. Swager, *J. Am. Chem. Soc.*, 2003, **125**, 14113–14119.
325 M. Carta, M. Croad, J. C. Jansen, P. Bernardo, G. Clarizia and N. B. McKeown, *Polym. Chem.*, 2014, **5**, 5255–5261.
326 B. Comesaña-Gándara, J. Chen, C. G. Bezzu, M. Carta, I. Rose, M. C. Ferrari, E. Esposito, A. Fuoco, J. C. Jansen and N. B. McKeown, *Energy Environ. Sci.*, 2019, **12**, 2733–2740.
327 R. Williams, L. A. Burt, E. Esposito, J. C. Jansen, E. Tocci, C. Rizzuto, M. Lanč, M. Carta and N. B. McKeown, *J. Mater. Chem. A*, 2018, **6**, 5661–5667.
328 Y. Wang, B. S. Ghanem, Y. Han and I. Pinnau, *Polymer*, 2020, **201**, 122619.
329 R. J. Swaidan, B. Ghanem, R. Swaidan, E. Litwiller and I. Pinnau, *J. Membr. Sci.*, 2015, **492**, 116–122.
330 R. L. Burns and W. J. Koros, *J. Membr. Sci.*, 2003, **211**, 299–309.
331 F. Li, C. Zhang and Y. Weng, *Macromol. Chem. Phys.*, 2019, **220**, 1–7.
332 P. Stanovsky, A. Zitkova, M. Karaszova, M. Šyc, J. C. Jansen, B. Comesaña Gándara, N. McKeown and P. Izak, *Sep. Purif. Technol.*, 2020, **242**, 2–7.
333 F. Alghunaimi, B. Ghanem, N. Alaslai, R. Swaidan, E. Litwiller and I. Pinnau, *J. Membr. Sci.*, 2015, **490**, 321–327.
334 G. Genduso, Y. Wang, B. S. Ghanem and I. Pinnau, *J. Membr. Sci.*, 2019, **584**, 100–109.
335 Z. Zhu, J. Zhu, J. Li and X. Ma, *Macromolecules*, 2020, **53**, 1573–1584.
336 X. Ma, Z. Zhu, W. Shi, W. Ji, J. Li, Y. Wang and I. Pinnau, *J. Mater. Chem. A*, 2021, **9**, 5404–5414.
337 Y. Wang, X. Ma, B. S. Ghanem, F. Alghunaimi, I. Pinnau and Y. Han, *Mater. Today Nano*, 2018, **3**, 69–95.
338 Z. Cai, Y. Liu, C. Wang, W. Xie, Y. Jiao, L. Shan, P. Gao, H. Wang and S. Luo, *J. Membr. Sci.*, 2022, **644**, 120115.
339 H. Chen, F. Dai, M. Wang, X. Yan, Z. Ke, C. Chen, G. Qian and Y. Yu, *Eur. Polym. J.*, 2022, **173**, 111231.
340 X. Han, L. Chen, Y. Wang, T. Wang, F. Cui, Z. Jiang and J. Pang, *ACS Mater. Lett.*, 2022, **4**, 61–67.
341 H. W. H. Lai, F. M. Benedetti, J. M. Ahn, A. M. Robinson, Y. Wang, I. Pinnau, Z. P. Smith and Y. Xia, *Science*, 2022, **375**, 1390–1392.
342 M. A. Abdulhamid, G. Genduso, Y. Wang, X. Ma and I. Pinnau, *Ind. Eng. Chem. Res.*, 2020, **59**, 5247–5256.
343 N. Alaslai, B. Ghanem, F. Alghunaimi and I. Pinnau, *Polymer*, 2016, **91**, 128–135.
344 N. Alaslai, X. Ma, B. Ghanem, Y. Wang, F. Alghunaimi and I. Pinnau, *Macromol. Rapid Commun.*, 2017, **38**, 1–5.
345 F. Alghunaimi, B. Ghanem, N. Alaslai, M. Mukaddam and I. Pinnau, *J. Membr. Sci.*, 2016, **520**, 240–246.
346 X. Ma, R. Swaidan, Y. Belmabkhout, Y. Zhu, E. Litwiller, M. Jouiad, I. Pinnau and Y. Han, *Macromolecules*, 2012, **45**, 3841–3849.
347 R. Swaidan, B. S. Ghanem, E. Litwiller and I. Pinnau, *J. Membr. Sci.*, 2014, **457**, 95–102.
348 S. Yi, B. Ghanem, Y. Liu, I. Pinnau and W. J. Koros, *Sci. Adv.*, 2019, **5**, 1–11.
349 M. Minelli, B. R. Pimentel, M. L. Jue, R. P. Lively and G. C. Sarti, *Polymer*, 2019, **170**, 157–167.
350 J. H. Kim, W. J. Koros and D. R. Paul, *J. Membr. Sci.*, 2006, **282**, 21–31.
351 K. Tanaka, M. Okano, H. Toshino, H. Kita and K.-I. Okamoto, *J. Polym. Sci., Part B: Polym. Phys.*, 1992, **30**, 907–914.
352 S. Pandiyan, D. Brown, N. F. A. Van der Vegt and S. Neyertz, *J. Polym. Sci., Part B: Polym. Phys.*, 2009, **47**, 1166–1180.
353 G. M. Iyer, L. Liu and C. Zhang, *J. Polym. Sci.*, 2020, **58**, 2482–2517.
354 K. L. Gleason, Z. P. Smith, Q. Liu, D. R. Paul and B. D. Freeman, *J. Membr. Sci.*, 2015, **475**, 204–214.
355 G. Genduso, B. S. Ghanem and I. Pinnau, *Membranes*, 2019, **9**, 1–14.
356 E. Ricci, A. E. Gemeda, N. Du, N. Li, M. G. De Angelis, M. D. Guiver and G. C. Sarti, *J. Membr. Sci.*, 2019, **585**, 136–149.
357 Y. Weng, W. Ji, C. Ye, H. Dong, Z. Gao, J. Li, C. Luo and X. Ma, *J. Membr. Sci.*, 2022, **644**, 120086.
358 B. Satilmis, M. Lanč, A. Fuoco, C. Rizzuto, E. Tocci, P. Bernardo, G. Clarizia, E. Esposito, M. Monteleone, M. Dendisová, K. Friess, P. M. Budd and J. C. Jansen, *J. Membr. Sci.*, 2018, **555**, 483–496.
359 T. Corrado, Z. Huang, J. Aboki and R. Guo, *Ind. Eng. Chem. Res.*, 2020, **59**, 5351–5361.
360 I. Rose, C. G. Bezzu, M. Carta, B. Comesanã-Gándara, E. Lasseuguette, M. C. Ferrari, P. Bernardo, G. Clarizia,

A. Fuoco, J. C. Jansen, K. E. Hart, T. P. Liyana-Arachchi, C. M. Colina and N. B. McKeown, *Nat. Mater.*, 2017, **16**, 932–937.
361 I. Rose, M. Carta, R. Malpass-Evans, M. C. Ferrari, P. Bernardo, G. Clarizia, J. C. Jansen and N. B. McKeown, *ACS Macro Lett.*, 2015, **4**, 912–915.
362 B. S. Ghanem, M. Hashem, K. D. M. Harris, K. J. Msayib, M. Xu, P. M. Budd, N. Chaukura, D. Book, S. Tedds, A. Walton and N. B. McKeown, *Macromolecules*, 2010, **43**, 5287–5294.
363 S. A. Sydlik, Z. Chen and T. M. Swager, *Macromolecules*, 2011, **44**, 976–980.
364 M. G. Rabbani, T. E. Reich, R. M. Kassab, K. T. Jackson and H. M. El-Kaderi, *Chem. Commun.*, 2012, **48**, 1141–1143.
365 Y. J. Cho and H. B. Park, *Macromol. Rapid Commun.*, 2011, **32**, 579–586.
366 M. O. Sinnokrot, E. F. Valeev and C. D. Sherrill, *J. Am. Chem. Soc.*, 2002, **124**, 10887–10893.
367 T. Chen, M. Li and J. Liu, *Cryst. Growth Des.*, 2018, **18**, 2765–2783.
368 C. G. Bezzu, M. Carta, M. C. Ferrari, J. C. Jansen, M. Monteleone, E. Esposito, A. Fuoco, K. Hart, T. P. Liyana-Arachchi, C. M. Colina and N. B. McKeown, *J. Mater. Chem. A*, 2018, **6**, 10507–10514.
369 A. Fuoco, B. Satilmis, T. Uyar, M. Monteleone, E. Esposito, C. Muzzi, E. Tocci, M. Longo, M. P. De Santo, M. Lanč, K. Friess, O. Vopička, P. Izák and J. C. Jansen, *J. Membr. Sci.*, 2020, **594**, 117460.
370 F. M. Benedetti, Y.-C. M. Wu, S. Lin, Y. He, E. Flear, K. R. Storme, C. Liu, Y. Zhao, T. M. Swager and Z. P. Smith, *JACS Au*, 2022, **2**, 1610–1615.
371 S. Lin, K. R. Storme, Y.-C. M. Wu, F. M. Benedetti, T. M. Swager and Z. P. Smith, *J. Membr. Sci.*, 2023, **668**, 121194.
372 R. Swaidan, X. Ma, E. Litwiller and I. Pinnau, *J. Membr. Sci.*, 2013, **447**, 387–394.
373 R. J. Swaidan, X. Ma and I. Pinnau, *J. Membr. Sci.*, 2016, **520**, 983–989.
374 A. Yerzhankyzy, B. S. Ghanem, Y. Wang, N. Alaslai and I. Pinnau, *J. Membr. Sci.*, 2020, **595**, 117512.
375 S. Luo, J. Liu, H. Lin, B. A. Kazanowska, M. D. Hunckler, R. K. Roeder and R. Guo, *J. Mater. Chem. A*, 2016, **4**, 17050–17062.
376 S. Luo, Q. Zhang, L. Zhu, H. Lin, B. A. Kazanowska, C. M. Doherty, A. J. Hill, P. Gao and R. Guo, *Chem. Mater.*, 2018, **30**, 5322–5332.
377 X. Hu, W. H. Lee, J. Y. Bae, J. S. Kim, J. T. Jung, H. H. Wang, H. J. Park and Y. M. Lee, *J. Membr. Sci.*, 2020, **612**, 118437.
378 Z. P. Smith, D. F. Sanders, C. P. Ribeiro, R. Guo, B. D. Freeman, D. R. Paul, J. E. McGrath and S. Swinnea, *J. Membr. Sci.*, 2012, **415–416**, 558–567.
379 Z. Huang, C. Yin, T. Corrado, S. Li, Q. Zhang and R. Guo, *Chem. Mater.*, 2022, **34**, 2730–2742.
380 W. J. Koros and C. Zhang, *Nat. Mater.*, 2017, **16**, 289–297.
381 M. Rungta, G. B. Wenz, C. Zhang, L. Xu, W. Qiu, J. S. Adams and W. J. Koros, *Carbon*, 2017, **115**, 237–248.
382 C. W. Jones and W. J. Koros, *Carbon*, 1994, **32**, 1419–1425.
383 P. S. Tin, T. S. Chung, Y. Liu and R. Wang, *Carbon*, 2004, **42**, 3123–3131.
384 O. Salinas, X. Ma, E. Litwiller and I. Pinnau, *J. Membr. Sci.*, 2016, **500**, 115–123.
385 O. Salinas, X. Ma, Y. Wang, Y. Han and I. Pinnau, *RSC Adv.*, 2017, **7**, 3265–3272.
386 W. Ogieglo, T. Puspasari, A. Alabdulaaly, T. Phuong Nga Nguyen, Z. Lai and I. Pinnau, *J. Membr. Sci.*, 2022, **652**, 120497.
387 K. Hazazi, Y. Wang, N. M. S. Bettahalli, X. Ma, Y. Xia and I. Pinnau, *J. Membr. Sci.*, 2022, **654**, 120548.
388 F. Y. Li, Y. Xiao, Y. K. Ong and T. S. Chung, *Adv. Energy Mater.*, 2012, **2**, 1456–1466.
389 F. Y. Li and T. S. Chung, *Int. J. Hydrogen Energy*, 2013, **38**, 9786–9793.
390 Q. Song, S. Cao, P. Zavala-Rivera, L. Ping Lu, W. Li, Y. Ji, S. A. Al-Muhtaseb, A. K. Cheetham and E. Sivaniah, *Nat. Commun.*, 2013, **4**, 1–9.
391 N. Du, M. M. Dal-Cin, G. P. Robertson and M. D. Guiver, *Macromolecules*, 2012, **45**, 5134–5139.
392 F. Y. Li, Y. Xiao, T. S. Chung and S. Kawi, *Macromolecules*, 2012, **45**, 1427–1437.
393 Q. Song, S. Cao, R. H. Pritchard, B. Ghalei, S. A. Al-Muhtaseb, E. M. Terentjev, A. K. Cheetham and E. Sivaniah, *Nat. Commun.*, 2014, **5**, 1–12.
394 X. Chen, Z. Zhang, L. Wu, X. Liu, S. Xu, J. E. Efome, X. Zhang and N. Li, *ACS Appl. Polym. Mater.*, 2020, **2**, 987–995.
395 P. Li, T. Zhang and L. Deng, *Ind. Eng. Chem. Res.*, 2020, **59**, 18640–18648.
396 N. Du, M. M. D. Cin, I. Pinnau, A. Nicalek, G. P. Robertson and M. D. Guiver, *Macromol. Rapid Commun.*, 2011, **32**, 631–636.
397 M. M. Khan, G. Bengtson, S. Shishatskiy, B. N. Gacal, M. Mushfequr Rahman, S. Neumann, V. Filiz and V. Abetz, *Eur. Polym. J.*, 2013, **49**, 4157–4166.
398 C. Zhang, L. Fu, Z. Tian, B. Cao and P. Li, *J. Membr. Sci.*, 2018, **556**, 277–284.
399 M. Fang, Z. He, T. C. Merkel and Y. Okamoto, *J. Mater. Chem. A*, 2018, **6**, 652–658.
400 S. Luo, K. A. Stevens, J. S. Park, J. D. Moon, Q. Liu, B. D. Freeman and R. Guo, *ACS Appl. Mater. Interfaces*, 2016, **8**, 2306–2317.
401 C. C. Hu, K. R. Lee, R. C. Ruaan, Y. C. Jean and J. Y. Lai, *J. Membr. Sci.*, 2006, **274**, 192–199.
402 J. Wu, J. Liu and T.-S. Chung, *Adv. Sustain. Syst.*, 2018, **2**, 1–10.
403 J. Liu, Y. Xiao, K. S. Liao and T.-S. Chung, *J. Membr. Sci.*, 2017, **523**, 92–102.
404 W. F. Yong, F. Y. Li, Y. C. Xiao, T.-S. Chung and Y. W. Tong, *J. Membr. Sci.*, 2013, **443**, 156–169.
405 W. F. Yong, F. Y. Li, T.-S. Chung and Y. W. Tong, *J. Mater. Chem. A*, 2013, **1**, 13914–13925.
406 L. Hao, P. Li and T.-S. Chung, *J. Membr. Sci.*, 2014, **453**, 614–623.
407 L. Hao, J. Zuo and T.-S. Chung, *AIChE J.*, 2014, **60**, 3848–3858.

408 W. F. Yong, Z. K. Lee and T.-S. Chung, *ChemSusChem*, 2016, **9**, 1953–1962.
409 X. Mei Wu, Q. Gen Zhang, P. Ju Lin, Y. Qu, A. Mei Zhu and Q. Lin Liu, *J. Membr. Sci.*, 2015, **493**, 147–155.
410 W. F. Yong, F. Y. Li, T. S. Chung and Y. W. Tong, *J. Membr. Sci.*, 2014, **462**, 119–130.
411 J. Sánchez-Laínez, B. Zornoza, M. Carta, R. Malpass-Evans, N. B. McKeown, C. Téllez and J. Coronas, *Ind. Eng. Chem. Res.*, 2018, **57**, 16909–16916.
412 E. Esposito, I. Mazzei, M. Monteleone, A. Fuoco, M. Carta, N. B. McKeown, R. Malpass-Evans and J. C. Jansen, *Polymers*, 2019, **11**, 1–14.
413 C. Zhang, R. P. Lively, K. Zhang, J. R. Johnson, O. Karvan and W. J. Koros, *J. Phys. Chem. Lett.*, 2012, **3**, 2130–2134.
414 X. Ma, R. J. Swaidan, Y. Wang, C. E. Hsiung, Y. Han and I. Pinnau, *ACS Appl. Nano Mater.*, 2018, **1**, 3541–3547.
415 J. Sánchez-Laínez, A. Pardillos-Ruiz, M. Carta, R. Malpass-Evans, N. B. McKeown, C. Téllez and J. Coronas, *Sep. Purif. Technol.*, 2019, **224**, 456–462.
416 Q. Song, S. Cao, R. H. Pritchard, H. Qiblawey, E. M. Terentjev, A. K. Cheetham and E. Sivaniah, *J. Mater. Chem. A*, 2015, **4**, 270–279.
417 S. Xiong, C. Pan, G. Dai, C. Liu, Z. Tan, C. Chen, S. Yang, X. Ruan, J. Tang and G. Yu, *J. Membr. Sci.*, 2022, **645**, 120217.
418 L. Hao, K. S. Liao and T. S. Chung, *J. Mater. Chem. A*, 2015, **3**, 17273–17281.
419 X. Wu, W. Liu, H. Wu, X. Zong, L. Yang, Y. Wu, Y. Ren, C. Shi, S. Wang and Z. Jiang, *J. Membr. Sci.*, 2018, **548**, 309–318.
420 X. Wu, Y. Ren, G. Sui, G. Wang, G. Xu, L. Yang, Y. Wu, G. He, N. Nasir, H. Wu and Z. Jiang, *AIChE J.*, 2020, **66**, 1–10.
421 Y. Wang, Y. Ren, H. Wu, X. Wu, H. Yang, L. Yang, X. Wang, Y. Wu, Y. Liu and Z. Jiang, *J. Membr. Sci.*, 2020, **602**, 117970.
422 J. Han, L. Bai, H. Jiang, S. Zeng, B. Yang, Y. Bai and X. Zhang, *Ind. Eng. Chem. Res.*, 2021, **60**, 593–603.
423 N. Tien-Binh, D. Rodrigue and S. Kaliaguine, *J. Membr. Sci.*, 2018, **548**, 429–438.
424 Z. Wang, H. Ren, S. Zhang, F. Zhang and J. Jin, *J. Mater. Chem. A*, 2017, **5**, 10968–10977.
425 G. Yu, X. Zou, L. Sun, B. Liu, Z. Wang, P. Zhang and G. Zhu, *Adv. Mater.*, 2019, **31**, 1–9.
426 N. Prasetya and B. P. Ladewig, *J. Mater. Chem. A*, 2019, **7**, 15164–15172.
427 P. F. Muldoon, S. R. Venna, D. W. Gidley, J. S. Baker, L. Zhu, Z. Tong, F. Xiang, D. P. Hopkinson, S. Yi, A. K. Sekizkardes and N. L. Rosi, *ACS Mater. Lett.*, 2020, **2**, 821–828.
428 C. Geng, Y. Sun, Z. Zhang, Z. Qiao and C. Zhong, *ACS Sustainable Chem. Eng.*, 2022, **10**, 3643–3650.
429 A. Husna, I. Hossain, I. Jeong and T. H. Kim, *Polymers*, 2022, **14**, 655.
430 M. Khdhayyer, A. F. Bushell, P. M. Budd, M. P. Attfield, D. Jiang, A. D. Burrows, E. Esposito, P. Bernardo, M. Monteleone, A. Fuoco, G. Clarizia, F. Bazzarelli, A. Gordano and J. C. Jansen, *Sep. Purif. Technol.*, 2019, **212**, 545–554.
431 A. Sabetghadam, X. Liu, A. F. Orsi, M. M. Lozinska, T. Johnson, K. M. B. Jansen, P. A. Wright, M. Carta, N. B. McKeown, F. Kapteijn and J. Gascon, *Chem. – Eur. J.*, 2018, **24**, 12796–12800.
432 Y. Fan, C. Li, X. Zhang, X. Yang, X. Su, H. Ye and N. Li, *J. Membr. Sci.*, 2019, **573**, 359–369.
433 N. Prasetya and B. P. Ladewig, *ACS Appl. Mater. Interfaces*, 2018, **10**, 34291–34301.
434 N. Tien-Binh, H. Vinh-Thang, X. Y. Chen, D. Rodrigue and S. Kaliaguine, *J. Membr. Sci.*, 2016, **520**, 941–950.
435 Y. Pu, Z. Yang, V. Wee, Z. Wu, Z. Jiang and D. Zhao, *J. Membr. Sci.*, 2022, **641**, 119912.
436 W. F. Yong, K. H. A. Kwek, K. S. Liao and T. S. Chung, *Polymer*, 2015, **77**, 377–386.
437 Y. Kinoshita, K. Wakimoto, A. H. Gibbons, A. P. Isfahani, H. Kusuda, E. Sivaniah and B. Ghalei, *J. Membr. Sci.*, 2017, **539**, 178–186.
438 M. M. Khan, V. Filiz, G. Bengtson, S. Shishatskiy, M. M. Rahman, J. Lillepaerg and V. Abetz, *J. Membr. Sci.*, 2013, **436**, 109–120.
439 H. Sun, W. Gao, Y. Zhang, X. Cao, S. Bao, P. Li, Z. Kang and Q. J. Niu, *React. Funct. Polym.*, 2020, **147**, 104465.
440 S. Kim, J. Hou, Y. Wang, R. Ou, G. P. Simon, J. G. Seong, Y. M. Lee and H. Wang, *J. Mater. Chem. A*, 2018, **6**, 7668–7674.
441 A. F. Bushell, P. M. Budd, M. P. Attfield, J. T. A. Jones, T. Hasell, A. I. Cooper, P. Bernardo, F. Bazzarelli, G. Clarizia and J. C. Jansen, *Angew. Chem., Int. Ed.*, 2013, **52**, 1253–1256.
442 G. Yu, Y. Li, Z. Wang, T. X. Liu, G. Zhu and X. Zou, *J. Membr. Sci.*, 2019, **591**, 117343.
443 C. H. Lau, K. Konstas, C. M. Doherty, S. Kanehashi, B. Ozcelik, S. E. Kentish, A. J. Hill and M. R. Hill, *Chem. Mater.*, 2015, **27**, 4756–4762.
444 C. H. Lau, K. Konstas, A. W. Thornton, A. C. Y. Liu, S. Mudie, D. F. Kennedy, S. C. Howard, A. J. Hill and M. R. Hill, *Angew. Chem., Int. Ed.*, 2015, **54**, 2669–2673.
445 C. Zhang, B. Liu, G. Wang, G. Yu, X. Zou and G. Zhu, *Chem. Commun.*, 2019, **55**, 7101–7104.
446 R. Hou, S. J. D. Smith, K. Konstas, C. M. Doherty, C. D. Easton, J. Park, H. Yoon, H. Wang, B. D. Freeman and M. R. Hill, *J. Mater. Chem. A*, 2022, **10**, 10107–10119.
447 A. Rohatgi, *WebPlotDigitizer: Version 4.4*.
448 Y. Wang, B. S. Ghanem, Z. Ali, K. Hazazi, Y. Han and I. Pinnau, *Small Struct.*, 2021, **2**, 2100049.
449 X. Ma, R. Swaidan, B. Teng, H. Tan, O. Salinas, E. Litwiller, Y. Han and I. Pinnau, *Carbon*, 2013, **62**, 88–96.
450 P. Li, T. S. Chung and D. R. Paul, *J. Membr. Sci.*, 2013, **432**, 50–57.
451 W. S. Chi, B. J. Sundell, D. Harrigan and S. C. Hayden, *ChemSusChem*, 2019, **12**, 2355–2360.
452 J. E. Bachman, Z. P. Smith, T. Li, T. Xu and J. R. Long, *Nat. Mater.*, 2016, **15**, 845–849.
453 Q. Qian, A. X. Wu, W. S. Chi, P. A. Asinger, S. Lin, A. Hypsher and Z. P. Smith, *ACS Appl. Mater. Interfaces*, 2019, **11**, 31257–31269.

454 S. Shahid and K. Nijmeijer, *J. Membr. Sci.*, 2014, **470**, 166–177.
455 N. Jusoh, Y. F. Yeong, K. K. Lau and A. M. Shariff, *J. Cleaner Prod.*, 2017, **149**, 80–95.
456 B. Kraftschik and W. J. Koros, *Macromolecules*, 2013, **46**, 6908–6921.
457 B. Kraftschik, W. J. Koros, J. R. Johnson and O. Karvan, *J. Membr. Sci.*, 2013, **428**, 608–619.
458 Z. Liu, Y. Liu, W. Qiu and W. J. Koros, *Angew. Chem., Int. Ed.*, 2020, **59**, 14877–14883.
459 A. Hayek, A. Alsamah, N. Alaslai, H. Maab, E. A. Qasem, R. H. Alhajry and N. M. Alyami, *ACS Appl. Polym. Mater.*, 2020, **2**, 2199–2210.
460 R. R. Tiwari, J. Jin, B. D. Freeman and D. R. Paul, *J. Membr. Sci.*, 2017, **537**, 362–371.
461 M. J. Mullins, D. Liu and H.-J. Sue, *Thermosets*, 2012, 28–61.
462 I. Hossain, A. Z. Al Munsur and T.-H. Kim, *Membranes*, 2019, **9**, 113–126.
463 P. Stanovsky, M. Karaszova, Z. Petrusova, M. Monteleone, J. C. Jansen, B. Comesaña-Gándara, N. B. McKeown and P. Izak, *J. Membr. Sci.*, 2021, **618**, 118694–118701.
464 I. Hossain, S. Y. Nam, C. Rizzuto, G. Barbieri, E. Tocci and T. H. Kim, *J. Membr. Sci.*, 2019, **574**, 270–281.
465 X. Ma, K. Li, Z. Zhu, H. Dong, J. Lv, Y. Wang, I. Pinnau, J. Li, B. Chen and Y. Han, *J. Mater. Chem. A*, 2021, **9**, 18313–18322.
466 Y. Weng, Q. Li, J. Li, Z. Gao, L. Zou and X. Ma, *Sep. Purif. Technol.*, 2021, **279**, 119681.
467 C. H. Lau, K. Konstas, C. M. Doherty, S. J. D. Smith, R. Hou, H. Wang, M. Carta, H. Yoon, J. Park, B. D. Freeman, R. Malpass-Evans, E. Lasseuguette, M. C. Ferrari, N. B. McKeown and M. R. Hill, *Nanoscale*, 2020, **12**, 17405–17410.
468 R. Darvishi and E. Pakizeh, *Int. J. Polym. Sci.*, 2020, **2020**, 1–12.
469 A. Husna, I. Hossain, O. Choi, S. M. Lee and T. H. Kim, *Macromol. Mater. Eng.*, 2021, **306**, 1–12.
470 W. Chen, Z. Zhang, C. Yang, J. Liu, H. Shen, K. Yang and Z. Wang, *J. Membr. Sci.*, 2021, **636**, 119581.
471 I. Hossain, S. Park, A. Husna, Y. Kim, H. Kim and T. H. Kim, *ACS Appl. Mater. Interfaces*, 2021, **13**, 49890–49906.
472 L. Wang, X. Guo, F. Zhang and N. Li, *J. Membr. Sci.*, 2021, **638**, 119668.
473 X. Chen, Y. Fan, L. Wu, L. Zhang, D. Guan, C. Ma and N. Li, *Nat. Commun.*, 2021, **12**, 1–11.
474 J. Deng, Z. Huang, B. J. Sundell, D. J. Harrigan, S. A. Sharber, K. Zhang, R. Guo and M. Galizia, *Polymer*, 2021, **229**, 123988.
475 D. S. Sholl and R. P. Lively, *JACS Au*, 2022, **2**, 322–327.
476 N. Nemestóthy, P. Bakonyi, P. Lajtai-Szabó and K. Bélafi-Bakó, *Membranes*, 2020, **10**, 1–10.
477 J. T. Vaughn, D. J. Harrigan, B. J. Sundell, J. A. Lawrence and J. Yang, *J. Membr. Sci.*, 2017, **522**, 68–76.
478 Q. Liu, M. Galizia, K. L. Gleason, C. A. Scholes, D. R. Paul and B. D. Freeman, *J. Membr. Sci.*, 2016, **514**, 282–293.
479 S. Yates, R. Zaki, A. Arzadon, C. Liu and J. Chiou, US8016124B2, 2009.
480 H. Lin, S. M. Thompson, A. Serbanescu-Martin, J. G. Wijmans, K. D. Amo, K. A. Lokhandwala and T. C. Merkel, *J. Membr. Sci.*, 2012, **413–414**, 70–81.
481 R. W. Baker and K. Lokhandwala, *Ind. Eng. Chem. Res.*, 2008, **47**, 2109–2121.
482 C. Y. Chuah, K. Goh, Y. Yang, H. Gong, W. Li, H. E. Karahan, M. D. Guiver, R. Wang and T. H. Bae, *Chem. Rev.*, 2018, **118**, 8655–8769.
483 Yadvika, Santosh, T. R. Sreekrishnan, S. Kohli and V. Rana, *Bioresour. Technol.*, 2004, **95**, 1–10.
484 R. W. Baker, B. Freeman, J. Kniep, Y. I. Huang and T. C. Merkel, *Ind. Eng. Chem. Res.*, 2018, **57**, 15963–15970.
485 C. Zhang, Y. Dai, J. R. Johnson, O. Karvan and W. J. Koros, *J. Membr. Sci.*, 2012, **389**, 34–42.
486 R. Swaidan, B. Ghanem and I. Pinnau, *ACS Macro Lett.*, 2015, **4**, 947–951.
487 Y. Liu, Z. Liu, A. Morisato, N. Bhuwania, D. Chinn and W. J. Koros, *J. Membr. Sci.*, 2020, **601**, 117910.
488 O. Vopička, M. G. De Angelis, N. Du, N. Li, M. D. Guiver and G. C. Sarti, *J. Membr. Sci.*, 2014, **459**, 264–276.
489 E. S. Sanders, W. J. Koros, H. B. Hopfenberg and V. T. Stannett, *J. Membr. Sci.*, 1983, **13**, 161–174.
490 E. S. Sanders, W. J. Koros, H. B. Hopfenberg and V. T. Stannett, *J. Membr. Sci.*, 1984, **18**, 53–74.
491 G. Genduso, E. Litwiller, X. Ma, S. Zampini and I. Pinnau, *J. Membr. Sci.*, 2019, **577**, 195–204.
492 W. J. Koros, R. T. Chern, V. Stannett and H. B. Hopfenberg, *J. Polym. Sci., Part A-2*, 1981, **19**, 1513–1530.
493 E. Ricci and M. G. De Angelis, *Membranes*, 2019, **9**, 1–26.
494 M. G. De Angelis, G. C. Sarti and F. Doghieri, *J. Membr. Sci.*, 2007, **289**, 106–122.
495 M. Galizia, K. A. Stevens, Z. P. Smith, D. R. Paul and B. D. Freeman, *Macromolecules*, 2016, **49**, 8768–8779.
496 A. X. Wu, J. A. Drayton, X. Ren, K. Mizrahi Rodriguez, A. F. Grosz, J. W. Lee and Z. P. Smith, *Macromolecules*, 2021, **54**, 6628–6638.
497 E. Ricci, M. Minelli and M. G. De Angelis, *J. Membr. Sci.*, 2017, **539**, 88–100.
498 H. D. Kamaruddin and W. J. Koros, *J. Membr. Sci.*, 1997, **135**, 147–159.
499 A. E. Gemeda, Ing. Chim. dell'ambiente e della Sicur., 2015, Ph. D., 139.
500 R. D. Raharjo, B. D. Freeman, D. R. Paul, G. C. Sarti and E. S. Sanders, *J. Membr. Sci.*, 2007, **306**, 75–92.
501 E. S. Sanders and W. J. Koros, *J. Polym. Sci., Part B: Polym. Phys.*, 1986, **24**, 175–188.
502 C. P. Ribeiro and B. D. Freeman, *Polymer*, 2010, **51**, 1156–1168.
503 E. Ricci, F. M. Benedetti, A. Noto, T. C. Merkel, J. Jin and M. G. De Angelis, *Chem. Eng. J.*, 2021, **426**, 130715.
504 Y. Lou, P. Hao and G. Lipscomb, *J. Membr. Sci.*, 2014, **455**, 247–253.
505 L. M. Robeson, M. E. Dose, B. D. Freeman and D. R. Paul, *J. Membr. Sci.*, 2017, **525**, 18–24.
506 A. Hayek, G. O. Yahaya, A. Alsamah and S. K. Panda, *J. Appl. Polym. Sci.*, 2020, **137**, 1–13.

507 G. Liu, V. Chernikova, Y. Liu, K. Zhang, Y. Belmabkhout, O. Shekhah, C. Zhang, S. Yi, M. Eddaoudi and W. J. Koros, *Nat. Mater.*, 2018, **17**, 283–289.
508 G. Liu, A. Cadiau, Y. Liu, K. Adil, V. Chernikova, I. D. Carja, Y. Belmabkhout, M. Karunakaran, O. Shekhah, C. Zhang, A. K. Itta, S. Yi, M. Eddaoudi and W. J. Koros, *Angew. Chem., Int. Ed.*, 2018, **57**, 14811–14816.
509 Y. Liu, Z. Chen, W. Qiu, G. Liu, M. Eddaoudi and W. J. Koros, *J. Membr. Sci.*, 2021, **627**, 119201.
510 H. Dong, Z. Zhu, K. Li, Q. Li, W. Ji, B. He, J. Li and X. Ma, *J. Membr. Sci.*, 2021, **635**, 119440.
511 C. G. Bezzu, A. Fuoco, E. Esposito, M. Monteleone, M. Longo, J. Carolus Jansen, G. S. Nichol, N. B. Mckeown, C. G. Bezzu, G. S. Nichol, B. Mckeown, A. Fuoco, E. Esposito, M. Monteleone, M. Longo and J. C. Jansen, *Adv. Funct. Mater.*, 2021, **31**, 2104474.
512 A. W. Ameen, J. Ji, M. Tamaddondar, S. Moshenpour, A. B. Foster, X. Fan, P. M. Budd, D. Mattia and P. Gorgojo, *J. Membr. Sci.*, 2021, **636**, 119527.
513 Q. Song and E. Sivaniah, WO2015129925A1, 2015.
514 J. Wu, T. S. Chung, S. Japip and T. S. Chung, *J. Mater. Chem. A*, 2020, **8**, 6196–6209.
515 M. Huang, K. Lu, Z. Wang, X. Bi, Y. Zhang and J. Jin, *ACS Sustainable Chem. Eng.*, 2021, **9**, 9426–9435.
516 J. Chen, M. Longo, A. Fuoco, E. Esposito, M. Monteleone, B. Comesaña Gándara, J. Carolus Jansen and N. B. McKeown, *Angew. Chem., Int. Ed.*, 2023, **62**, 1–9.
517 R. Swaidan, B. Ghanem, E. Litwiller and I. Pinnau, *Macromolecules*, 2015, **48**, 6553–6561.
518 A. B. Foster, J. L. Beal, M. Tamaddondar, J. M. Luque-Alled, B. Robertson, M. Mathias, P. Gorgojo and P. M. Budd, *J. Mater. Chem. A*, 2021, **9**, 21807–21823.
519 W. Chen, Z. Zhang, L. Hou, C. Yang, H. Shen, K. Yang and Z. Wang, *Sep. Purif. Technol.*, 2020, **250**, 117198.
520 S. Cong, X. Feng, L. Guo, D. Peng, J. Wang, J. Chen, Y. Zhang, X. Shen and G. Yang, *Adv. Sci.*, 2023, **3**, 2–9.
521 S. Yi, B. Ghanem, Y. Liu, I. Pinnau and W. J. Koros, *Sci. Adv.*, 2019, **5**, 1–11.
522 S. V. Gutiérrez-Hernández, F. Pardo, A. B. Foster, P. Gorgojo, P. M. Budd, G. Zarca and A. Urtiaga, *J. Membr. Sci.*, 2023, **675**, 1–9.
523 C. A. Scholes, G. Q. Chen, G. W. Stevens and S. E. Kentish, *J. Membr. Sci.*, 2010, **346**, 208–214.